Modeling and programming shape-morphing structured media

Thesis by
Connor Glenn McMahan

In Partial Fulfillment of the Requirements for the
Degree of
Doctor of Philosophy in Mechanical Engineering

CALIFORNIA INSTITUTE OF TECHNOLOGY
Pasadena, California

2022
Defended August 17, 2021

Connor Glenn McMahan
ORCID: 0000-0001-5024-6138

ACKNOWLEDGEMENTS

First and foremost, I would like to thank my advisor, Prof. Chiara Daraio. Working with her was an experience I will cherish my entire life, and I have learned so much from the way she fosters creativity in the group. I couldn't be more grateful to her for offering the freedom to pursue projects that interested me, for introducing me to a group of amazing collaborators at Caltech and at other universities, and for her continual guidance and encouragement.

Secondly, I would like to thank my dear friend and Partner in Mechanics, Paolo Celli. When I first started doing research in the group, Paolo took me under his wing and is largely responsible for helping me mature into the person and researcher that I am today. I have a great admiration for his outlook on life and science, and hope that I can be as good of a mentor to others as he was to me.

This thesis is certainly the result of a team effort with my collaborators. I am especially grateful for the friendships I made by working closely with four fellow graduate students: Arda Kotikian (Harvard), Ruslan Guseinov (IST Austria), Alice Lamaro (ETH Zurich), and Andy Akerson (Caltech). Working with them was great fun, and I admire the competence, work ethic, and perseverance that they brought to the table. In addition to these students, I would like to thank the other people with whom I collaborated for their mentorship and research contributions: Basile Audoly, Bernd Bickel, Jennifer Lewis, Doug Hofmann, Jesus Perez, Punnathat (Tent) Bordeenithikasem, Adam Oskowitz, Andrew Wisneski, Shant Vartanian, Yi-fan Wang, Emily Davidson, Jalilah Muhammad, Robert Weeks, Roberto Brighenti, Brian Ramirez, Anton Bauhofer, Adri Lauper, Tori Lee, Christina Naify, Ke (Chris) Liu, Ozair Rajani, Kristjan Stone, Aditya Rathi, and Paromita Mitchell. Although we never had the opportunity to work together, my conversations with Sharan Injeti, Hao Zhou, Kevin Korner, Aaron Baumgarten, Vincenzo Costanza, Bailey Montaño, Dennis Kochmann, Kaushik Bhattacharya, Jordan Rainey, and Katia Bertoldi were essential to the progress of my projects.

This work could not have been conducted without the department staff's support. A special thanks to Carolina Oseguera, Lynn Seymour, Jaymie Mateo, and Holly Golcher for their administrative support, and to Bruce Dominguez, John van Deusen, Paul Stovall, and Petros Arakelian for their help with fabrication. Additionally, I would like to thank Manan Arya, Case Bradford, Doug Hofmann, Punnathat (Tent)

Bordeenithikasem, and Peter Dillon for hosting me in their groups over the two summers that I spent at JPL. I would also like to thank Olive Stohlman for being my liaison to the NASA Science Research Fellowship program.

No words can express the gratitude I have for my family's love and for the depth of the friendships that accompanied me during these years. The Daraio group and the MCE community were wonderful to me. Ethan Pickering and I lived together during the entirety of our time in graduate school. We joke that we are unlikely friends due to our differences in personality, but he was always there for me when I needed someone to talk to and he challenged me to grow as a person in a way that few people have.

Finally, I would like to thank my thesis committee—Kaushik Bhattacharya, Sergio Pellegrino, and Guruswami Ravichandran—for serving in this capacity and for providing valuable feedback on this thesis.

ABSTRACT

Shape-morphing and self-propelled locomotion are examples of mechanical behaviors that can be "programmed" in structured media by designing geometric features at micro- and mesostructural length scales. This programmability is possible because the small-scale geometry often imposes local kinematic modes that are strongly favored over other deformations. In turn, global behaviors are influenced by local kinematic preferences over the extent of the structured medium and by the kinematic compatibility (or incompatibility) between neighboring regions of the domain. This considerably expands the design space for effective mechanical properties, since objects made of the same bulk material but with different internal geometry will generally display very different behaviors. This motivates pursuing a mechanistic understanding of the connection between small-scale geometry and global kinematic behaviors. This thesis addresses challenges pertaining to the modeling and design of structured media that undergo large deformations.

The first part of the thesis focuses on the relation between micro- or mesoscale patterning and energetically favored modes of deformation. This is first discussed within the context of twisted bulk metallic glass ribbons whose edges display periodic undulations. The undulations cause twist concentrations in the narrower regions of the structural element, delaying the onset of material failure and permitting the design of structures whose deployment and compaction emerge from the ribbons' chirality. Following this discussion of a periodic system, we study sheets with non-uniform cut patterns that buckle out-of-plane. Motivated by computational challenges associated with the presence of geometric features at disparate length scales, we construct an effective continuum model for these non-periodic systems, allowing us to simulate their post-buckling behavior efficiently and with good accuracy.

The second part of the thesis discusses ways to leverage the connection between micro/mesoscale geometry and energetically favorable local kinematics to create "programmable matter" that undergo prescribed shape changes or self-propelled locomotion when exposed to an environmental stimulus. We first demonstrate the capabilities of an inverse design method that automates the design of structured plates that morph into target 3D geometries over time-dependent actuation paths. Finally, we present devices made of 3D-printed liquid crystal elastomer (LCE) hinges that change shape and self-propel when heated.

PUBLISHED CONTENT AND CONTRIBUTIONS

[1] P. Celli, C. McMahan, B. Ramirez, A. Bauhofer, C. Naify, D. Hofmann, B. Audoly, and C. Daraio. Shape-morphing architected sheets with non-periodic cut patterns. *Soft Matter*, 14(48):9744–9749, 2018. doi: 10.1039/C8SM02082E.
C.M. participated in the design, fabrication, modeling, and testing of the architected sheets, and in writing and revising the manuscript.

[2] P. Celli*, A. Lamaro*, C. McMahan*, P. Bordeenithikasem, D. C. Hofmann, and C. Daraio. Compliant morphing structures from twisted bulk metallic glass ribbons. *Journal of the Mechanics and Physics of Solids*, 145:104129, 2020. doi: 10.1016/j.jmps.2020.104129.
C.M., P.C., and A.L. contributed equally to this work. C.M. performed the analytical modeling and participated in writing and revising the manuscript.

[3] R. Guseinov, C. McMahan, J. Pérez, C. Daraio, and B. Bickel. Programming temporal morphing of self-actuated shells. *Nature Communications*, 11(1):1–7, 2020. doi: 10.1038/s41467-019-14015-2.
C.M. designed the mechanical characterization experiments and participated in the conduction of unit-cell characterization experiments, in data analysis, in mechanical modeling, and in writing and revising the manuscript.

[4] A. Kotikian*, C. McMahan*, E. C. Davidson, J. M. Muhammad, R. D. Weeks, C. Daraio, and J. A. Lewis. Untethered soft robotic matter with passive control of shape morphing and propulsion. *Science Robotics*, 4(33), 2019. doi: 10.1126/scirobotics.aax7044.
C.M. and A.K. contributed equally to this work. C.M. participated in the conception of the project, in designing the experiments, in material characterization experiments, in the design of the proof-of-concept demonstrations, and in writing and revising the manuscript. C.M. also coded the 3D printer nozzle paths and performed mechanical modeling.

[5] C. McMahan, A. Akerson, P. Celli, B. Audoly, and C. Daraio. Effective continuum models for the buckling of non-periodic architected sheets that display quasi-mechanism behaviors. *arXiv*:2107.01704, 2021.
C.M. participated in the conception of the project, performed analytical modeling and experiments, and participated in conducting simulations, and in writing and revising the manuscript.

TABLE OF CONTENTS

Acknowledgements . . . iii
Abstract . . . v
Published Content and Contributions . . . vi
Table of Contents . . . vii
Chapter I: Introduction . . . 1
1.1 Research objectives . . . 1
1.2 Motivation . . . 1
1.3 Research approach, challenges, and methods . . . 4
1.4 Chapter outlines . . . 11
Bibliography . . . 13
Chapter II: Compliant Morphing Structures from Twisted Bulk Metallic Glass Ribbons . . . 20
2.1 Introduction . . . 21
2.2 Ribbon design and material characterization . . . 24
2.3 Twisting mechanics . . . 25
2.4 From ribbons to structures . . . 40
2.5 Conclusions and outlook . . . 45
Bibliography . . . 46
Chapter III: Shape-Morphing Architected Sheets with Non-Periodic Cut Patterns 53
3.1 Introduction . . . 54
3.2 Design paradigm . . . 55
3.3 Non-periodicity . . . 58
3.4 Conclusions . . . 61
3.5 Materials and methods . . . 61
Bibliography . . . 63
Chapter IV: Effective Continuum Models for the Buckling of Non-Periodic Architected Sheets that Display Quasi-Mechanism Behaviors . . . 68
4.1 Introduction . . . 69
4.2 Modeling approach . . . 72
4.3 Finite element implementation . . . 78
4.4 Results . . . 80
4.5 Conclusions . . . 84
Bibliography . . . 85
Chapter V: Programming Temporal Morphing of Self-Actuated Shells . . . 91
5.1 Introduction . . . 92
5.2 Results . . . 93
5.3 Discussion . . . 98
5.4 Methods . . . 100
Bibliography . . . 101

Chapter VI: Untethered Soft Robots with Passive Control of Shape Morphing and Propulsion . . . 106
6.1 Introduction . . . 107
6.2 Results . . . 109
6.3 Discussion . . . 118
6.4 Materials and methods . . . 118
Bibliography . . . 124
Chapter VII: Conclusions . . . 130
7.1 Summary of contributions . . . 130
7.2 Outlook on future research directions . . . 131
Appendix A: Compliant Morphing Structures from Twisted Bulk Metallic Glass Ribbons . . . 135
A.1 Details on the material properties of BMG . . . 135
Bibliography . . . 135
Appendix B: Shape-Morphing Architected Sheets with Non-Periodic Cut Patterns . . . 136
B.1 Additional information on the tensile tests . . . 136
B.2 Details on the finite element model . . . 137
B.3 Kinematic analysis . . . 139
B.4 Cut pattern generation . . . 143
B.5 Influence of the design parameters on the in-plane deformation of periodic specimens . . . 148
B.6 Influence of the design parameters on the out-of-plane deformation of non-periodic sheets . . . 149
B.7 Alternative design for stiff materials and plastic deformations . . . 149
Bibliography . . . 150
Appendix C: Effective Continuum Models for the Buckling of Non-Periodic Architected Sheets that Display Quasi-Mechanism Behaviors . . . 153
C.1 Strong form of equilibrium . . . 153
C.2 Finite element formulation and Solution Procedure . . . 153
C.3 Stability analysis with mixed method constraint . . . 154
Appendix D: Programming Temporal Morphing of Self-Actuated Shells . . . 156
D.1 Shell design . . . 156
D.2 Simulation . . . 159
D.3 Material measurement and modeling . . . 163
D.4 Temporal programming . . . 169
D.5 Fabrication procedure . . . 171
D.6 Mechanical measurements of shells . . . 173
D.7 Supplementary movies . . . 174
Bibliography . . . 174
Appendix E: Untethered Soft Robots with Passive Control of Shape Morphing and Propulsion . . . 176
E.1 Mechanics of thin nematic elastomer bilayers . . . 176
E.2 Supplemental figures . . . 181
Bibliography . . . 181

List of Illustrations 190

Chapter 1

INTRODUCTION

1.1 Research objectives

This thesis discusses the mechanics and design of media that derive their global kinematic behaviors from geometric features at the micro- or mesostructural length scales. The main objectives of the research in this thesis are (i) to understand the connection between micro- or mesoscale patterning and energetically favored local modes of deformation in both passive and active media and (ii) to leverage this understanding to create "programmable matter" that change shape or locomote according to a designer's intention when exposed to an environmental stimulus. The ability to program active materials' responses to loading scenarios or environmental stimuli offers new opportunities to create compliant systems that interact with or navigate through their environments.

1.2 Motivation

Throughout most of history, humans have generally relied on the flexion of slender elements and on the rigid body motions of jointed mechanisms to embed predictable degrees of freedom in tools and structures. Levers, hinges, pulleys, and other mechanical elements have been actuated by humans, animals, wind, and water for thousands of years. In today's industrial setting, actuation has mostly been delegated to engines and electric motors, but the majority of machines still (appropriately) rely on basic mechanisms to realize their intended kinematics.

However, several contemporary engineering practices and applications are driving departures from conventional machine design approaches that rely on the above-mentioned components. Causes of this include volume and mass constraints in aerospace systems that undergo complex switches between stowed and deployed configurations [1, 2], requirements for operating in harsh environments where electronics are inviable, and the drive to reduce part counts in assemblies. In these situations, pure mechanisms (i.e. systems that display zero-elastic energy kinematic modes) are often replaced by compliant elements [3] and active materials that assume target shapes in response to environmental cues such as light, temperature or humidity changes, chemical gradients, electric fields, etc. [4–10].

In a step beyond replacing individual joints with compliant analogues, advanced materials synthesis techniques and additive manufacturing technologies have enabled the design and fabrication of structures that derive their kinematic behaviors from geometric feature *patterns* at the micro- or mesostructural length scales [11, 12]. Structures with patterned geometric features are referred to as structured media when their micro/mesoscale geometric features are much smaller than the overall dimensions of the object as well as the size of global deformation features (e.g. the wavelength of a buckling mode). Namely, structured media display a separation of length scales between the small features of their micro/mesostructure and other relevant dimensions.

Crucially, the kinematic modes that are favored by structured media can be significantly altered by modulating the parameters that define the small-scale features [13]. These structured media become "programmable" when the ability to tailor kinematic behaviors is coupled to a mechanistic understanding of how local geometry influences global effective properties: this enables the creation of structured media that display *desired* kinematic behaviors in response to an environmental stimulus or a simple loading condition. Examples of programmable media include devices that accurately morph into target geometries [14] or are capable of self-propelled locomotion [15] when heated.

Several approaches have been suggested for prescribing large deformations in structured media via micro/mesostructural design. Origami is perhaps the most commonly known framework for doing so, and it provides a clear illustration for the connection between mesoscale geometry and global kinematics (Fig. 1.1a-b). Because it is much easier to fold creases than to stretch planar facets, vastly different folded shapes can be attained by altering the crease patterns [12, 20, 21]. Micro/mesostructural tailoring has been extended to many other forms of soft [5–7, 10, 22–26] and stiff [18, 27, 28] structured media with the purpose of exerting similar control over global deformations. These are discussed in more detail in subsequent chapters.

This control over global deformations via micro/mesostructural design has also been crucial for the rapidly maturing field of soft robotics: Soft robots often have infinite degrees of freedom and are subjected to finite deformations (unlike most of their rigid counterparts), so it can be challenging to predict their kinematics under a continually varying set of boundary conditions and to implement control systems. Since micro- and mesoscale patterning are avenues for favoring desired

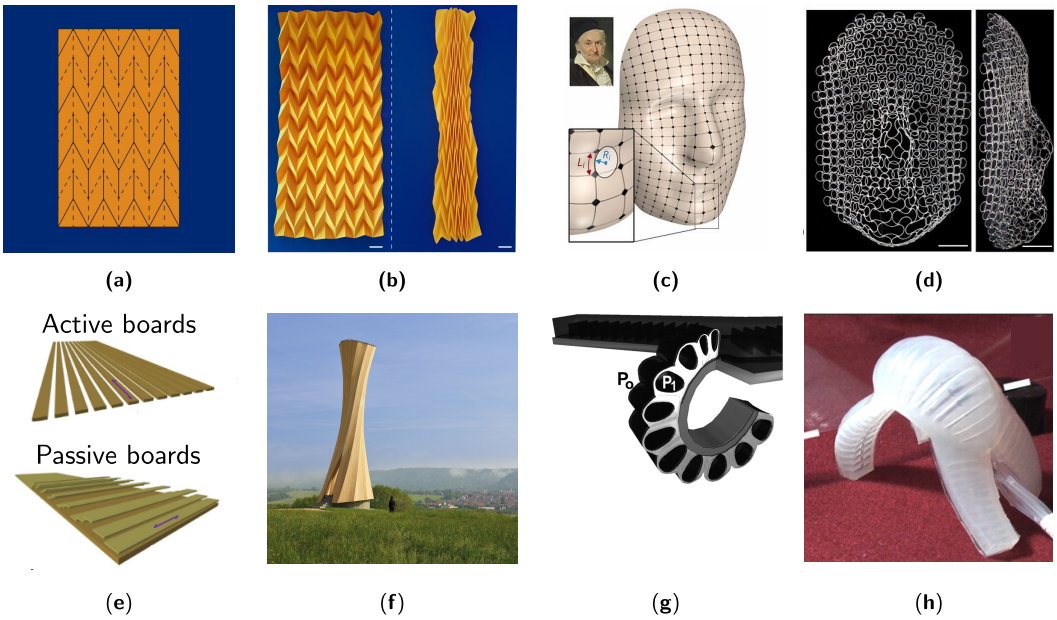

Figure 1.1: Examples of how deformations can be "programmed" via mesostructural patterning. (a) A miura-ori crease pattern that leads to the kinematic behavior shown in (b) [16]. (c) An inverse design framework is used to create the mesostructure of an initially flat beam network that (d) morphs into the shape of Gauss's face [14]. (e) Hygromorphic wooden bilayers [17] are used to shape the panels that compose (f) the 14m tall Urbach Tower [18]. (g) Pneumatic cavities in the limb of (h) a locomoting soft robot enable complex locomotive gaits in response to pressurization and depressurization cycles [19].

kinematics over other deformations [29–31], they enable functions such as object manipulation [32–34] and locomotion [15, 19, 35–37], as shown in Fig 1.1g-h.

Within this context of attaining desired structural functions, an important trait of structured media (broadly speaking) is that they offer engineers a versatile platform for obtaining desired mechanical properties via optimal design [38, 39]. These optimal design techniques have had an especially profound impact on the design of programmable media, as they alleviate engineering intuition's burden in designing non-uniform micro/mesostructures. Through optimal design, very complex global kinematic targets can be attained by creating micro/mesostructures that energetically favor the necessary local deformations [10, 12, 14, 40, 41]. Fig. 1.1c-d shows the effectiveness of inverse design techniques, where the shape of Gauss's face is attained from an initially flat structure.

By using these optimal design techniques to create the micro/mesostructures of *active* media, one can prescribe responses to environmental stimuli such as changes in temperature [14, 22, 23], chemical concentrations [42], etc. Although active medium programming has mostly been shown within the context of desktop-scaled

devices, recent studies have bridged the concept to larger scales. For example, the 14m tall Urbach Tower shown in Fig. 1.1e-f shows an interesting use of hygromorphic wood panels in an architectural context [18, 27].

The ability to program shape-morphing responses to environmental stimuli through the constitutive and geometric tuning of active media is similar to what roboticists are able to achieve by using electronic controllers and motors. This has motivated researchers to program additional operations that are characteristic of robots (e.g. locomotion, object manipulation, logic processing) within untethered devices' active material-based structural frames, rather than requiring additional power sources, control devices, and actuators [43]. An example of this is shown in Fig. 1.2 [15]. In the future, a robust integration of sensing, actuation, computation and communication capabilities as an intrinsic material property of a micro/mesostructure would blur the distinction between structured media and robots.

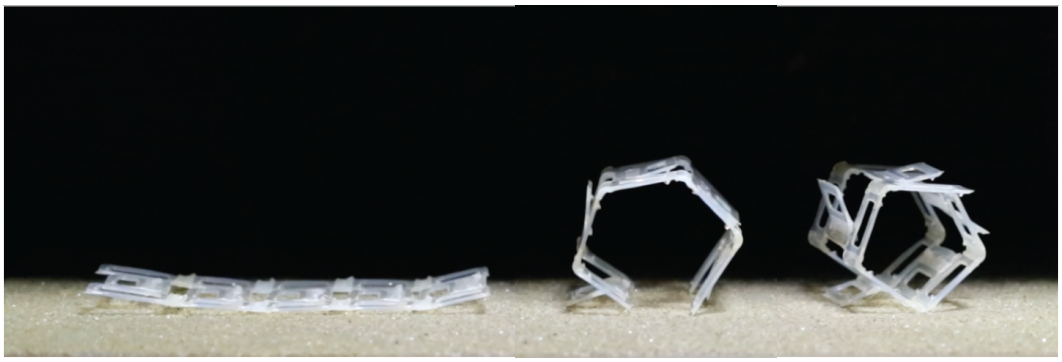

Figure 1.2: A time-lapse overlay showing untethered shape-reconfiguration and locomotion by a programmed structured medium. The mesogen orientation in the liquid crystal elastomer bilayers cause the hinges to fold in response to a thermal stimulus [15].

1.3 Research approach, challenges, and methods

This thesis discusses micro/mesostructural patterning as a tool for enforcing desired deformations. We start with the simpler case of a periodic mesostructure before exploring the mechanical behavior of a class of non-periodic structured media. We then introduce a method for inversely designing the non-uniform mesostructures of initially flat shells that morph into target geometries. Finally, micro/mesoscale patterning is discussed within the application-oriented context of designing soft robots with easy-to-predict kinematics.

Although the internal geometry of a structured medium exerts a strong influence on mechanical behaviors, the bulk materials' elastic (or inelastic) properties also

must be accounted for in compliant systems. This need to account for a structured medium's energetic behavior can considerably complicate the design process, and motivates the performance of experiments and the development of models that help us understand and predict the mechanical behavior of structured media [44]. Throughout this thesis, experimental characterizations of structured media and their unit cells guide the construction of mechanical models that capture their behavior. These models then inform the design of larger or non-uniformly patterned specimens that serve as proof-of-concept demonstrations of interesting mechanical behaviors. The challenges associated with each of these steps and the methods employed on the problems will be discussed in the following subsections.

Specimen fabrication and characterization

Specimen fabrication and their experimental characterization are two of the main challenges associated with many research projects, including with the work in this thesis. Attaining statistically significant results requires collecting a large quantity of data, which is challenging if specimen fabrication and testing is not automated. This challenge is compounded when the research objective is to understand the mechanics of structured media composed of non-uniformly patterned geometric features or that display temporally varying mechanical properties because one must conduct experiments on a broad set of unit cell geometries jubjected to a variety of loading scenarios.

All of the specimens discussed in this thesis are structured plates that assume flat initial configurations. Although these choices of structured media were not primarily driven by ease of fabrication, they do alleviate the above-mentioned difficulties by allowing for the use of planar fabrication techniques such as manual cutting [45], laser cutting [13, 46], lattice layering [40] and the direct ink writing of liquid crystal elastomers [9], which are usually faster processes than additively manufacturing or machining 3D structures. Details on the specific fabrication techniques used for each project are discussed in the following chapters and in the appendices.

Two classes of structured media discussed in this thesis consist of non-uniform tessellations of unit cells. As mentioned above, this can significantly increase the number of characterization experiments that must be conducted for two reasons. First, unit cell geometry exerts a strong influence on effective properties and the broad unit cell design space must be properly sampled (*Problem A*). Secondly, mesostructural non-uniformity tends to cause kinematic incompatibilities between

neighboring regions of a medium. This often causes deformations that deviate from a unit cell's energetically favored kinematic modes (*Problem B*). For example, origami facet bending would occur in a miura-ori tessellation if some of the creases were badly misaligned. This usually requires characterization experiments under a variety of loading conditions.

The first class of structured media where mesostructural non-uniformities occur entails tessellations of unit cells made of bulky blocks that rotate about slender elastic joints. These unit cells display a kinematic mode that is much softer than other deformations. In this energetically favorable soft elastic mode, almost all of the elastic energy is stored in the slender joints. Although the unit cell geometry may vary over the extend of the structured medium, the joints are always uniformly distributed and are subjected to nearly identical strains for a given relative rotation angle between adjacent tiles. After measuring the effective stiffnesses of a few specimens, the mechanical behavior of other unit cell geometries can be predicted by varying the geometric parameters embedded in a strain energy function. This addresses Problem A. For this class of systems, Problem B is simplified by assuming that all deviations from the soft kinematic mode will be very stiff in comparison, so all of these non-ideal behaviors are lumped into being strongly penalized in the strain energy function. More details on this aspect of the problem are presented in a later chapter.

These two problems are approached in a very different way by the second project that involves non-uniform tessellations of unit cells. Due to the large variance in the geometry of the unit cells' deformable components, Problem A was treated through a brute force method that entailed performing a very large number of mechanical characterization experiments to fully sample the range of unit cell geometries and the local tractions observed in our structured media. Meanwhile, Problem B was addressed by programming the structured media to only undergo conformal deformations while morphing from one surface geometry to another. This reduced unwanted shear modes. As an additional safeguard, the unit cell geometries were designed to be shear resistant.

Modeling the mechanics of structured media

The projects in this thesis involve a diverse set of structured media, but there are important commonalities between them that inform the choice of modeling techniques employed: all of the structured media presented here are thin plates

that assume flat initial configurations and undergo finite deformations. Unless stated otherwise, mechanical modeling is simplified by assuming that unit normal vectors to the reference mid-surface are mapped to unit normal vectors in the deformed configuration, with vanishing transverse strains (i.e. the Love-Kirchhoff assumption). This assumption was used to simplify the analytical solutions of some governing equilibrium equations via a perturbation approach, as well as in finite element formulations throughout the text.

As stated previously, micro/mesoscale geometric features exert a tremendous influence on the mechanical behaviors of structured media by energetically favoring some deformation modes over others. However, it is computationally expensive to perform conventional finite element simulations that resolve small geometric features and span a large domain. Homogenization theory [47], discrete elastic rod [28, 48] and Kirchhoff rod networks [49], bar-and-hinge models for origami [50–52], effective continuum models [46, 53–55], and many other modeling approaches have been used as computationally efficient alternatives to fine-grained finite element techniques.

The main mechanical modeling challenges addressed in this thesis revolve around ways to embed the kinematic preferences imposed by the micro/mesostructure geometry into a reduced order model. Each modeling-heavy project approached this problem in a different way, including (i) assuming the approximate shape of the deformed configuration prior to calculating unknown strain field quantities analytically using a perturbation method, (ii) enriching an effective continuum model by attributing an energy penalty to deviations from geometrically-favored kinematic modes, and (iii) by coupling an effective spring network to a finite element simulation of a membrane. In all of these cases, experiments were used to understand the local behavior of structured media and to extract values for model parameters.

Modelling the mechanical behaviors of structured media is especially challenging in cases where the medium has a non-periodic micro/mesostructure (see the discussion of Problems A and B in the previous subsection). This setting arises frequently in shape-morphing structures and in soft robots because simple loading conditions will only trigger complex deformations in media that display non-uniform micro/mesostructures [11, 13, 14, 40]. Some of the projects discussed in this thesis contribute to the body of work on modeling structured media with non-uniform mesostructures, but the mechanics community would benefit from further advances in this area of research.

Mathematical tools for solving equilibrium equations

A variety of mathematical tools are used to solve the equilibrium equations obtained from the above-mentioned modeling approaches. Most solutions rely on in-house or commercial implementations of finite element methods. Details on my collaborators' finite element implementations will be left for the Appendices because many books have been written on the topic and most engineers are aware of these methods. Perturbation expansions are not as broadly familiar to engineers and are used to attain an approximate closed form solution to one of the equilibrium equations in this thesis. The specifics of the approach are discussed in a later chapter. Bender and Orszag's book provides an excellent introduction to this topic [56].

Inverse design of shells that undergo changes in Gaussian curvature

In many cases of shape-morphing systems that have complex deformation targets, it is essentially impossible to design the non-uniform micro/mesoscale geometries that accurately yield the desired behaviors using human intuition alone. This motivates using reduced order models that describe the interplay between internal geometry and energetically favored deformations as a foundation for inverse design approaches, where an algorithm outputs the topology, material properties, or the geometric parameters needed to attain desired deformations [10, 14, 38, 40, 41, 57]. These inverse design processes are effectively methods for "programming" the mechanical responses of a material or structure.

Some of the structured media discussed in this thesis undergo programmed deformations in which their Gaussian curvature changes. A brief introduction to the geometry of shells will be provided here as a mathematical foundation for our inverse design method.

Consider a shell midsurface parametrized by (x, y) over a domain $U \subset \mathbb{R}^2$ that is embedded in $\mathbb{R}^3$ by a map $\overrightarrow{m}$. This is shown in Figure 1.3. At each point, the midsurface has tangent vectors $\partial\overrightarrow{m}/\partial x$ and $\partial\overrightarrow{m}/\partial y$, and a normal unit vector $\overrightarrow{n}$. Any material point $\overrightarrow{s}$ inside a shell of thickness h can be written as a normal offset from the midsurface:

$$\overrightarrow{s}(x, y, z) = \overrightarrow{m}(x, y) + z\overrightarrow{n}(x, y)\ , z \in [-h/2, h/2].$$

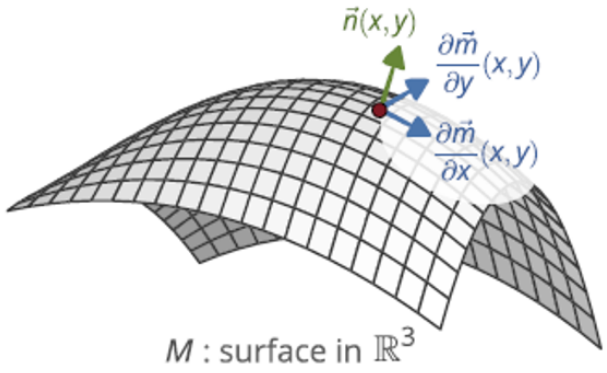

Figure 1.3: M is defined as an embedding m of a region of the plane U into $\mathbb{R}^3$. Image reproduced from [58].

This yields a metric $\mathbf{G}$ on the volume $U \times [-h/2, h/2]$,

$$\mathbf{G}(x, y, z) = (d\overrightarrow{s})^T d\overrightarrow{s} = \begin{pmatrix} \mathbf{g}(x, y, z) & 0 \\ 0 & 1 \end{pmatrix},$$

where the 2×2 tensor $\mathbf{g}$ is given by

$$\mathbf{g}(x, y, z) = (d\overrightarrow{m} + z d\overrightarrow{n})^T (d\overrightarrow{m} + z d\overrightarrow{n}) = \mathbf{a}(x, y) - 2z\mathbf{b}(x, y) + O(z^2) .$$

Here, $\mathbf{a}$ and $\mathbf{b}$ are the first and second fundamental forms of the surface. The Gaussian curvature K (which corresponds to the product of the two principal curvatures at a point) is related to these two tensors by the ratio of their determinants:

$$K = \frac{\det(\mathbf{b})}{\det(\mathbf{a})} .$$

Gauss's *Theorema Egregium* tells us that the Gaussian curvature of a smooth surface is invariant under local isometries [59]. Manfredo do Carmo's *"Differential Geometry of Curves and Surfaces"* provides a succinct proof of the theorem [60]. Returning to the context of shape-morphing elastic shells, this theorem dictates that changes in Gaussian curvature necessarily couple bending deformations to membrane stretching.

Although isometric deformations are out of the question for achieving changes in Gaussian curvature, shape-shifting along conformal (angle preserving) deformation pathways is a compelling option for achieving those target morphing behaviors while

minimizing shear. Importantly, any two regular surfaces are locally conformal [60], scale distortion is smoothly distributed in conformal maps and the discrete differential geometry community has developed a number of freely available tools (such as the one shown in Fig. 1.4) to find conformally equivalent meshes quickly [61, 62]. As a result, many approaches for inversely designing shape-morphing shells rely on these discrete conformal mapping techniques [11, 14, 40, 63] as starting points for design algorithms.

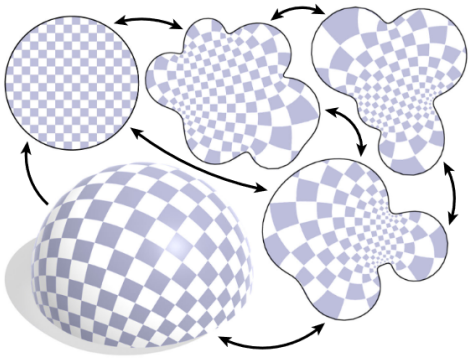

Figure 1.4: Discrete conformal flattening tools take 3D surface meshes as inputs and output conformally equivalent flat meshes. In this example, the user also has the option of prescribing the flattened boundary. Image sourced from [62].

Once a conformal map has been found between the target and reference configurations, choosing a micro/mesostructural class (such as auxetics, spring networks, beam networks, etc.) that will enforce conformal deformations is usually left to engineering intuition. After this class is selected, optimization procedures are generally used to fine tune the non-uniform internal geometries that will impose the target global behaviors.

Active materials

Active materials have been studied for several decades for their ability to deform in response to environmental stimuli. With the creation of 3D printing and other advanced materials processing techniques, the scientific community attained a set of fabrication tools that enables graded control of material chemistry and of geometric features at their micro/mesostructural length scales [7, 10, 25]. This considerably expanded the versatility of active materials beyond homogeneous deformation modes.

These advanced fabrication techniques led to a broad body of work on shape-morphing structures, motile materials, and soft robots [14, 30, 35, 37, 40, 64–66].

In most cases, the material chemistry and small-scale geometry are tailored so that a single task is performed passively when the device is exposed to a stimulus. However, we have recently seen the development of structures that express more complex materials-based control operations, where different environmental stimuli lead to different active material behaviors [5, 15, 26]. Fewer examples of these materials exist, but they include devices that behave as programmable logic gates [42] or that rely on variations in mesoscale geometry or chemistry throughout the structural frame to attain sequential actuation [15, 40, 64].

In the materials described above, the actions rely on passive, open loop control and are generally pre-programmed by the designer. We are starting to see demonstrations of structured media embedded with a capacity for closed loop feedback control [67], as well as material reprogrammability [68]. Advancements in these directions will enable the creation of devices that offer distinct advantages over conventional robotic systems for many applications, such as decentralizing computing, actuation and sensing capabilities over the entire extent of the structural frame rather than at a few discrete locations. This would open the doors to a number of currently unrealized applications, such as creating fully soft untethered systems that can manipulate and navigate through their environments effectively.

However, many challenges associated with active materials present hurdles to reaching this degree of technological sophistication. Active materials often display low energy density [69], irreversible actuation (i.e. must be manually reprogrammed before every actuation cycle) [64, 70, 71], or require tethers to rigid power sources [72]. It can also be challenging to couple them to other materials in larger devices. The liquid crystal elastomer-based soft robot presented toward the end of this thesis overcomes these challenges thanks to recent advances in liquid crystal elastomer 3D printing technology [9, 73, 74], but its operation is limited to very specific environmental conditions.

1.4 Chapter outlines

This thesis presents a series of explorations on the mechanics and design of structured media that display shape-morphing behaviors. The first research project on this topic is discussed in Chapter 2, where we use experiments, numerical simulations and analytical modeling to show how the presence of a mesoscale pattern affects the twisting mechanics of bulk metallic glass ribbons. In this case, the introduction of periodic undulations in the ribbon edge geometry concentrates twist in desired

regions of the structural element and delays the onset of material failure. These ribbons with undulated boundaries are joined to create metallic deployable systems whose shape-changing capabilities are derived from the chirality of the ribbon elements.

Next, we depart from periodic frameworks to investigate the effect of non-uniform patterns on the mechanics of structured media. This is done by studying sheets composed of bulky tiles connected by slender elastic joints. Tile rotations about the joints are low-energy local kinematic modes that are strongly favored over other deformations (we refer to these behaviors as "quasi-mechanisms"). In-plane kinematic incompatibilities arise in non-periodic mesostructures, resulting in out-of-plane buckling. A paradigm for designing these sheets such that buckling occurs in desired regions is presented in Chapter 3. Due to the presence of geometric features at disparate length scales, simulations of the post-buckling behavior of these sheets would be computationally expensive using a standard finite element approach with a fine-grained mesh. In light of this, we construct an effective continuum model for these non-periodic systems in Chapter 4, allowing us to simulate the post-buckling behavior of the specimens at a low computational cost.

One of the principle aims of this research is to develop architected materials with pre-programmed temporal responses to environmental stimuli. While several stimulus-responsive materials have been used for inducing compelling demonstrations of changes in geometry, examples of shape-shifting over time-dependent actuation paths have only been shown in a small number of morphing processes that involve the sequential folding of discrete hinges. We discuss an extension of this capability to architected materials that shape-shift into non-developable geometries and can be treated as programmable *continua* in Chapter 5, substantially broadening the range of achievable geometries in shape-morphing systems.

While the soft robotics community has produced some examples of untethered, passively controlled systems, they are generally limited in their ability to self-propel by a lack of energy density or actuator reversibility. In Chapter 6, we present devices made of 3D-printed liquid crystal elastomer (LCE) hinges. These hinges' actuation responses are programmed by varying their chemistry and printed geometry, and are used to create devices such as a multi-stable origami polyhedron and a soft robot that assembles into a pentagonal prism and self-propels in a rolling motion in response to thermal stimuli.

A summary of contributions and a discussion on avenues for future work concludes the thesis in Chapter 7.

Permissions

Figure 1.1(a-b) obtained from [16] and reproduced under the terms of the Creative Commons Attribution CC-BY-NC-ND.

Figure 1.1(c-d) obtained from [14]. Permission to reproduce the figures is not required for non-commercial and educational use.

Figure 1.1(e) adapted from [17] and reproduced under the terms of the Creative Commons Attribution CC-BY.

Figure 1.1(f) obtained from [18] and reproduced under the terms of the Creative Commons Attribution CC-BY.

Figure 1.1(g-h) obtained from [19]. Permission to reproduce the figures is not required for non-commercial and educational use.

Figure 1.2 adapted from [15]. The copyright is held by me and my co-authors.

Figure 1.3 obtained from [58]. Permission to reproduce the figures is not required for non-commercial and educational use.

Figure 1.4 obtained from [62]. Permission to make digital or hard copies of all or part of this work for personal use is granted without fee provided that copies are not made or distributed for profit or commercial advantage and that copies bear this notice and the full citation.

References

[1] M. Arya, N. Lee, and S. Pellegrino. Crease-free biaxial packaging of thick membranes with slipping folds. *International Journal of Solids and Structures*, 108:24–39, 2017.

[2] M. Arya, F. Mechentel, D. Webb, J. Steeves, D. Lisman, S. Shaklan, S. C. Bradford, E. Kelso, K. Neff, A. Swain, et al. Demonstration of deployment repeatability of key subsystems of a furled starshade architecture. *Journal of Astronomical Telescopes, Instruments, and Systems*, 7(2):021202, 2021.

[3] L. Howell. Compliant mechanisms. In *21st Century Kinematics*, pages 189–216. Springer, 2013.

[4] J. Kupfer and H. Finkelmann. Nematic liquid single crystal elastomers. *Die Makromolekulare Chemie, Rapid Communications*, 12:717–726, 1991.

[5] Y. Yao, J. T. Waters, A. V. Shneidman, J. Cui, X. Wang, N. K. Mandsberg, S. Li, A. C. Balazs, and J. Aizenberg. Multiresponsive polymeric microstructures with encoded predetermined and self-regulated deformability. *Proceedings of the National Academy of Sciences*, 115:12950–12955, 2018. ISSN 0027-8424. doi: 10.1073/pnas.1811823115.

[6] T. Guin, B. A. Kowalski, R. Rao, . D. Auguste, C. A. Grabowski, P. F. Lloyd, V. P. Tondiglia, B. Maruyama, R. A. Vaia, and T. J. White. Electrical control of shape in voxelated liquid crystalline polymer nanocomposites. *ACS Applied Materials and Interfaces*, 10:1187–1194, 2018. ISSN 19448252. doi: 10.1021/acsami.7b13814.

[7] Y. Klein, E. Efrati, and E. Sharon. Shaping of elastic sheets by prescription of non-euclidean metrics. *Science*, 315(5815):1116–1120, 2007. ISSN 0036-8075. doi: 10.1126/science.1135994. URL `http://science.sciencemag.org/content/315/5815/1116`.

[8] L. M. Korpas, R. Yin, H. Yasuda, and J. R. Raney. Temperature-responsive multistable metamaterials. *ACS Applied Materials & Interfaces*, 13(26): 31163–31170, 2021.

[9] A. Kotikian, R. L. Truby, J. W. Boley, T. J. White, and J. A. Lewis. 3D printing of liquid crystal elastomeric actuators with spatially programed nematic order. *Advanced Materials*, 30:1706164, 2018. doi: 10.1002/adma.201706164.

[10] A. S. Gladman, E. A. Matsumoto, R. G. Nuzzo, L. Mahadevan, and J. A. Lewis. Biomimetic 4D printing. *Nature Materials*, 15:413–418, 2016. ISSN 1476-1122. doi: 10.1038/nmat4544.

[11] R. Guseinov, E. Miguel, and B. Bickel. Curveups. *ACM Transactions on Graphics*, 36:1–12, 2017. ISSN 07300301. doi: 10.1145/3072959.3073709.

[12] L. H. Dudte, E. Vouga, T. Tachi, and L. Mahadevan. Programming curvature using origami tessellations. *Nature Materials*, 15:583–588, 2016. ISSN 14764660. doi: 10.1038/nmat4540.

[13] P. Celli, C. McMahan, B. Ramirez, A. Bauhofer, C. Naify, D. Hofmann, B. Audoly, and C. Daraio. Shape-morphing architected sheets with non-periodic cut patterns. *Soft Matter*, 14:9744–9749, 2018. doi: 10.1039/C8SM02082E.

[14] J. W. Boley, W. M. van Rees, C. Lissandrello, M. N. Horenstein, R. L. Truby, A. Kotikian, J. A. Lewis, and L. Mahadevan. Shape-shifting structured lattices via multimaterial 4D printing. *Proceedings of the National Academy of Sciences*, page 201908806, 2019.

[15] A. Kotikian, C. McMahan, E. C. Davidson, Jalilah M. Muhammad, R. D. Weeks, C. Daraio, and J. A. Lewis. Untethered soft robotic matter with passive control of shape morphing and propulsion. *Science Robotics*, 4(33): eaax7044, 2019.

[16] S. J. P. Callens and A. A. Zadpoor. From flat sheets to curved geometries: Origami and kirigami approaches. *Materials Today*, 21(3):241–264, 2018. doi: 10.1016/j.mattod.2017.10.004.

[17] P. Grönquist. *Smart manufacturing of curved mass timber components by self-shaping*. PhD thesis, ETH Zurich, 2020.

[18] D. Wood, P. Grönquist, S. Bechert, L. Aldinger, D. Riggenbach, K. Lehmann, M. Rüggeberg, I. Burgert, J. Knippers, A. Menges, et al. From machine control to material programming: self-shaping wood manufacturing of a high performance curved CLT structure–Urbach Tower. *JSTOR*, 2020.

[19] R. F. Shepherd, F. Ilievski, W. Choi, S. A. Morin, A. A. Stokes, A. D. Mazzeo, X. Chen, M. Wang, and G. M. Whitesides. Multigait soft robot. *Proceedings of the National Academy of Sciences*, 108:20400–20403, 2011. ISSN 0027-8424. doi: 10.1073/pnas.1116564108.

[20] R. J. Lang. *Twists, tilings, and tessellations: Mathematical methods for geometric origami*. CRC Press, 2017.

[21] E. T. Filipov, T. Tachi, and G. H. Paulino. Origami tubes assembled into stiff, yet reconfigurable structures and metamaterials. *Proc. Natl. Acad. Sci. U.S.A.*, 112(40):12321–12326, 2015. doi: 10.1073/pnas.1509465112.

[22] J. Kim, J. A. Hanna, M. Byun, C. D. Santangelo, and R. C. Hayward. Designing responsive buckled surfaces by halftone gel lithography. *Science*, 1201:1200–1205, 2012. doi: 10.1126/science.1215309.

[23] P. Plucinsky, B. A. Kowalski, T. J. White, and K. Bhattacharya. Patterning nonisometric origami in nematic elastomer sheets. *Soft Matter*, 14:3127–3134, 2018. ISSN 17446848. doi: 10.1039/c8sm00103k.

[24] J.-H. Na, A. A. Evans, J. Bae, M. C. Chiappelli, C. D. Santangelo, R. J. Lang, T. C. Hull, and R. C. Hayward. Programming reversibly self-folding origami with micropatterned photo-crosslinkable polymer trilayers. *Advanced Materials*, 27:79–85, 2014. ISSN 0935-9648. doi: 10.1002/adma.201403510.

[25] T. H. Ware, M. E. McConney, J. J. Wie, V. P. Tondiglia, and T. J. White. Voxelated liquid crystal elastomers. *Science*, 347:982–984, 2015. ISSN 0036-8075. doi: 10.1126/science.1261019.

[26] B. R. Donovan, V. M. Matavulj, S. K. Ahn, T. Guin, and T. J. White. All-optical control of shape. *Advanced Materials*, 31:1805750, 2019. ISSN 15214095. doi: 10.1002/adma.201805750.

[27] P. Grönquist, P. Panchadcharam, D. Wood, A. Menges, M. Rüggeberg, and F.K. Wittel. Computational analysis of hygromorphic self-shaping wood gridshell structures. *Royal Society Open Science*, 7(7):192210.

[28] C. Baek, A. O. Sageman-Furnas, M. K. Jawed, and P. M. Reis. Form finding in elastic gridshells. *Proc. Natl. Acad. Sci. U.S.A*, 115(1):75–80, 2018. doi: 10.1073/pnas.1713841115.

[29] K. Bhattacharya and R. D. James. The material is the machine. *Science*, 307 (5706):53–54, 2005.

[30] E. Hawkes, B. An, N. M. Benbernou, H. Tanaka, S. Kim, E. D. Demaine, D. Rus, and R. J. Wood. Programmable matter by folding. *Proceedings of the National Academy of Sciences*, 107:12441–12445, 2010. ISSN 0027-8424. doi: 10.1073/pnas.0914069107.

[31] F. Connolly, C. J. Walsh, and K. Bertoldi. Automatic design of fiber-reinforced soft actuators for trajectory matching. *Proceedings of the National Academy of Sciences*, 114:51–56, 2017. doi: 10.1073/pnas.1615140114.

[32] F. Ilievski, A. D. Mazzeo, R. F. Shepherd, X. Chen, and G. M. Whitesides. Soft robotics for chemists. *Angewandte Chemie–International Edition*, 50: 1890–1895, 2011.

[33] H. Yuk, S. Lin, C. Ma, M. Takaffoli, N. X. Fang, and X. Zhao. Hydraulic hydrogel actuators and robots optically and sonically camouflaged in water. *Nature Communications*, 8:14230, 2017. doi: 10.1038/ncomms14230.

[34] B. T. Phillips, K. P. Becker, S. Kurumaya, K. C. Galloway, G. Whittredge, D. M. Vogt, C. B. Teeple, M. H. Rosen, V. A. Pieribone, D. F. Gruber, and R. J. Wood. A dexterous, glove-based teleoperable low-power soft robotic arm for delicate deep-sea biological exploration. *Scientific Reports*, 8:14779, 2018. doi: 10.1038/s41598-018-33138-y.

[35] S. Palagi, A. G. Mark, S. Y. Reigh, K. Melde, T. Qiu, H. Zeng, C. Parmeggiani, D. Martella, A. Sanchez-Castillo, N. Kapernaum, F. Giesselmann, D. S. Wiersma, E. Lauga, and P. Fischer. Structured light enables biomimetic swimming and versatile locomotion of photoresponsive soft microrobots. *Nature Materials*, 15:647–653, 6 2016. ISSN 14764660. doi: 10.1038/nmat4569.

[36] M. T. Tolley, R. F. Shepherd, B. Mosadegh, K. C. Galloway, M. Wehner, M. Karpelson, R. J. Wood, and G. M. Whitesides. A resilient, untethered soft robot. *Soft Robotics*, 1:213, 2014. ISSN 2169-5172. doi: 10.1089/soro.2014.0008.

[37] C. Ahn, K. Li, and S. Cai. Light or thermally powered autonomous rolling of an elastomer rod. *ACS Applied Materials and Interfaces*, 10:25689–25696, 8 2018. ISSN 19448252. doi: 10.1021/acsami.8b07563.

[38] F. Agnelli, M. Tricarico, and A. Constantinescu. Shape-shifting panel from 3d printed undulated ribbon lattice. *Extreme Mechanics Letters*, 42:101089, 2021.

[39] S. S. Injeti, P. Celli, K. Bhattacharya, and C. Daraio. Tuning acoustic impedance in load-bearing structures. *arXiv preprint arXiv:2106.10573*, 2021.

[40] R. Guseinov, C. McMahan, J. Pérez, C. Daraio, and B. Bickel. Programming temporal morphing of self-actuated shells. *Nature Communications*, 11(1): 1–7, 2020.

[41] G. P. T. Choi, L. H. Dudte, and Lakshminarayanan Mahadevan. Programming shape using kirigami tessellations. *Nature Materials*, 18(9):999–1004, 2019. doi: 10.1038/s41563-019-0452-y.

[42] Y. Jiang, L. M. Korpas, and J. R. Raney. Bifurcation-based embodied logic and autonomous actuation. *Nature Communications*, 10(1):1–10, 2019.

[43] M. A. McEvoy and N. Correll. Materials that couple sensing, actuation, computation, and communication. *Science*, 347(6228), 2015.

[44] P. M. Reis, F. Brau, and P. Damman. The mechanics of slender structures. *Nature Physics*, 14(12):1150–1151, 2018. doi: 10.1038/s41567-018-0369-4.

[45] P. Celli, A. Lamaro, C. McMahan, P. Bordeenithikasem, D. C. Hofmann, and C. Daraio. Compliant morphing structures from twisted bulk metallic glass ribbons. *Journal of the Mechanics and Physics of Solids*, 145:104129, 2020.

[46] C. McMahan, A. Akerson, P. Celli, B. Audoly, and C. Daraio. Effective continuum models for the buckling of non-periodic architected sheets that display quasi-mechanism behaviors. *arXiv*, 2107.01704, 2021.

[47] S. Müller, N. Triantafyllidis, and G. Geymonat. Homogenization of nonlinearly elastic materials, microscopic bifurcation and macroscopic loss of rank-one convexity. *Archive for Rational Mechanics and Analysis*, 122, 09 1993. doi: 10.1007/BF00380256.

[48] C. Lestringant and D. M. Kochmann. Modeling of flexible beam networks and morphing structures by geometrically exact discrete beams. *Journal of Applied Mechanics*, 87(8):081006, 2020. doi: 10.1115/1.4046895.

[49] T. Yu, L. Dreier, F. Marmo, S. Gabriele, S. Parascho, and S. Adriaenssens. Numerical modeling of static equilibria and bifurcations in bigons and bigon rings. *Journal of the Mechanics and Physics of Solids*, 152:104459, 2021.

[50] M. Schenk and S. D. Guest. Origami folding: A structural engineering approach. *Origami*, 5:291–304, 2011.

[51] E. T. Filipov, K. Liu, T. Tachi, M. Schenk, and G. H. Paulino. Bar and hinge models for scalable analysis of origami. *International Journal of Solids and Structures*, 124:26–45, 2017. doi: 10.1016/j.ijsolstr.2017.05.028.

[52] Y. Liu, B. Shaw, M. D. Dickey, and J. Genzer. Sequential self-folding of polymer sheets. *Science Advances*, 3:e1602417, 2017.

[53] R. Khajehtourian and D. M. Kochmann. A continuum description of substrate-free dissipative reconfigurable metamaterials. *Journal of the Mechanics and Physics of Solids*, 147:104217, 2021.

[54] Y. Bar-Sinai, G. Librandi, K. Bertoldi, and M. Moshe. Geometric charges and nonlinear elasticity of two-dimensional elastic metamaterials. *Proceedings of the National Academy of Sciences*, 117(19):10195–10202, 2020. doi: 10.1073/pnas.1920237117.

[55] M. Czajkowski, C. Coulais, M. van Hecke, and D. Z. Rocklin. Conformal elasticity of mechanism-based metamaterials. *arXiv preprint arXiv:2103.12683*, 2021.

[56] C. M. Bender and S. A. Orszag. *Advanced mathematical methods for scientists and engineers*. McGraw-Hill Book Company, New York, NY, 1978.

[57] L. Jin, A. E. Forte, B. Deng, A. Rafsanjani, and K. Bertoldi. Kirigami-inspired inflatables with programmable shapes. *Advanced Materials*, 32(33):2001863, 2020. doi: 10.1002/adma.202001863.

[58] W. M. van Rees, E. Vouga, and L. Mahadevan. Growth patterns for shape-shifting elastic bilayers. *Proceedings of the National Academy of Sciences*, 114(44):11597–11602, 2017. doi: 10.1073/pnas.1709025114.

[59] C. F. Gauss. *Disquisitiones generales circa superficies curvas*. Typis Dietericianis, 1828.

[60] M. P. do Carmo. *Differential geometry of curves and surfaces: Revised and updated second edition*. Courier Dover Publications, 2016.

[61] B. Springborn, P. Schröder, and U. Pinkall. Conformal equivalence of triangle meshes. *ACM Transactions on Graphics*, 27(3):77:1–77:11, August 2008.

[62] R. Sawhney and K. Crane. Boundary first flattening. *ACM Transactions on Graphics (ToG)*, 37(1):1–14, 2017.

[63] M. Konaković, K. Crane, B. Deng, S. Bouaziz, D. Piker, and M. Pauly. Beyond developable: Computational design and fabrication with auxetic materials. *ACM Transactions on Graphics*, 35(4):89, 2016. doi: 10.1145/2897824.2925944.

[64] Q. Ge, C. K. Dunn, H. J. Qi, and M. L. Dunn. Active origami by 4D printing. *Smart Materials and Structures*, 23:094007, 2014. ISSN 1361665X. doi: 10.1088/0964-1726/23/9/094007.

[65] C. Yuan, D. J. Roach, C. K. Dunn, Q. Mu, X. Kuang, C. M. Yakacki, T. J. Wang, K. Yu, and H. J. Qi. 3D printed reversible shape changing soft actuators assisted by liquid crystal elastomers. *Soft Matter*, 13:5558–5568, 2017. ISSN 1744-683X. doi: 10.1039/c7sm00759k.

[66] N. Kellaris, V. G. Venkata, G. M. Smith, S. K. Mitchell, and C. Keplinger. Peano-HASEL actuators: Muscle-mimetic, electrohydraulic transducers that linearly contract on activation. *Science Robotics*, 3:3276, 2018. URL http://robotics.sciencemag.org/.

[67] A. Kotikian, J. M. Morales, A. Lu, J. Mueller, Z. S. Davidson, J. W. Boley, and J. A. Lewis. Innervated, self-sensing liquid crystal elastomer actuators with closed loop control. *Advanced Materials*, page 2101814, 2021.

[68] T. Chen, M. Pauly, and P. M. Reis. A reprogrammable mechanical metamaterial with stable memory. *Nature*, 589(7842):386–390, 2021.

[69] M. Wehner, R. L. Truby, D. J. Fitzgerald, B. Mosadegh, G. M. Whitesides, J. A. Lewis, and R. J. Wood. An integrated design and fabrication strategy for entirely soft, autonomous robots. *Nature*, 536:451–455, 2016. ISSN 14764687.

[70] T. Chen, O. R. Bilal, K. Shea, and C. Daraio. Harnessing bistability for directional propulsion of soft, untethered robots. *Proceedings of the National Academy of Sciences*, 115(22):5698–5702, 2018.

[71] J. Wu, C. Yuan, Z. Ding, M. Isakov, Y. Mao, T. Wang, M. L. Dunn, and H. J. Qi. Multi-shape active composites by 3D printing of digital shape memory polymers. *Scientific Reports*, 6: 24224, 2016. ISSN 2045-2322. doi: 10.1038/srep24224. URL http://www.pubmedcentral.nih.gov/articlerender.fcgi?artid=4829848&tool=pmcentrez&rendertype=abstract.

[72] A. O'Halloran, F. O'Malley, and P. McHugh. A review on dielectric elastomer actuators, technology, applications, and challenges. *Journal of Applied Physics*, 104(7):9, 2008.

[73] M. O. Saed, C. P. Ambulo, H. Kim, R. De, V. Raval, K. Searles, D. A. Siddiqui, J. M. O. Cue, M. C. Stefan, M. R. Shankar, and T. H. Ware. Molecularly-engineered, 4D-printed liquid crystal elastomer actuators. *Advanced Functional Materials*, 29:1806412, 2019. ISSN 16163028. doi: 10.1002/adfm.201806412.

[74] C. P. Ambulo, J. J. Burroughs, J. M. Boothby, H. Kim, M. R. Shankar, and T. H. Ware. Four-dimensional printing of liquid crystal elastomers. *ACS Applied Materials and Interfaces*, 9:37332–37339, 2017. ISSN 19448252. doi: 10.1021/acsami.7b11851.

Chapter 2

COMPLIANT MORPHING STRUCTURES FROM TWISTED BULK METALLIC GLASS RIBBONS

P. Celli*, A. Lamaro*, C. McMahan*, P. Bordeenithikasem, D. C. Hofmann, and C. Daraio. Compliant morphing structures from twisted bulk metallic glass ribbons. *Journal of the Mechanics and Physics of Solids*, 145:104129, 2020. doi: 10.1016/j.jmps.2020.104129.
C.M., P.C., and A.L. contributed equally to this work. C.M. performed the analytical modeling and participated in writing and revising the manuscript.

Chapter preamble

In the first research project discussed in this thesis, we analyze the mechanics of ribbon elements that display periodic boundary undulations. These mechanical analyses are used to probe the limits to which the ribbons can be twisted prior to failing, but are not incorporated into algorithms that inversely design ribbon networks. Subsequent chapters discuss modeling and design techniques for non-periodic systems.

Chapter abstract

In this work, we investigate the use of pre-twisted metallic ribbons as building blocks for shape-changing structures. We manufacture these elements by twisting initially flat ribbons about their (lengthwise) centroidal axis into a helicoidal geometry, then thermoforming them to make this configuration a stress-free reference state. The helicoidal shape allows the ribbons to have preferred bending directions that vary throughout their length. These bending directions serve as compliant joints and enable several deployed and stowed configurations that are unachievable without pre-twist, provided that compaction does not induce material failure. We fabricate these ribbons using a bulk metallic glass (BMG), for its exceptional elasticity and thermoforming attributes. Combining numerical simulations, an analytical model based on a geometrically nonlinear plate theory and torsional experiments, we analyze the finite-twisting mechanics of various ribbon geometries. We find that, in ribbons with undulated edges, the twisting deformations can be better localized onto desired regions prior to thermoforming. Finally, we join multiple ribbons to create deployable systems with complex morphing attributes enabled by the intrinsic

chirality of our twisted structural elements. Our work proposes a framework for creating fully metallic, yet compliant structures that may find application as elements for space structures and compliant robots.

2.1 Introduction

Shape-changing structures are mechanical systems designed to undergo predictable changes of shape when subjected to external or internal stimuli. Typically, such structures are made of separate elements that can move relative to each other and are connected via kinematic joints, and the acts of deployment and retraction do not require the various elements to be dismounted [1–4]. They find use as everyday objects (e.g., foldable chairs and expandable toys), architectural elements (e.g., retractable roofs and pop-up domes), space structures (e.g., deployable booms, solar sails and starshades) and medical devices (e.g., stents and capsules for drug delivery). In space systems, deployable structures are necessary to satisfy increasingly stringent packaging ratios and weight requirements imposed by cubesats. One way to reduce weight and complexity in deployable systems is to replace multiple jointed parts with continua featuring compliant hinges. Here, we call these systems "compliant morphing structures." Examples of compliant structure classes are: origami, which feature axially-rigid, but potentially-flexible panels connected by foldable creases [5–7]; kirigami, where creases are combined with cuts to expand the range of achievable morphed shapes [8–10]; compliant mechanism-like structures, where bulky components are connected via thin flexures [11–18]; and creaseless foldable shell structures such as tape springs and slotted cylinders [19–22]. Through careful design, some of these compliant systems achieve extreme changes of shape that are typically unattainable with other strategies. Examples are systems that transform from flat configurations into 3D shapes [16, 17, 23–26] and compact objects that deploy into large surfaces [27].

In compliant structures, high stresses are typically concentrated at the creases/flexures. This makes it challenging to design low-part-count systems that possess complex and reversible morphing attributes and are simultaneously made of materials that provide the load-bearing capacity or durability required by certain structural applications. An attempt in this direction is the relization of additively manufactured, metallic origami [28]. Another example is represented by bulk metallic glass kirigami sheets [29]. Other researchers have attempted to use composites to create morphing systems [9, 30]. These structures typically require the union of multiple elements via pin-joints to achieve complex morphing scenarios [31] due to limita-

tions in fabrication processes [32]. Others have considered origami systems with more complex compliant hinge geometries to reduce stresses [33, 34].

To create compliant morphing structures made of materials relevant to structural engineering, systems that feature extremely compliant, yet robust and manufacturable hinges are needed. In recent years, ribbons (slender structural elements where length $\gg$ width $\gg$ thickness) have emerged as building blocks for morphing structures, as they can be bent and buckled [21, 35, 36], twisted [37–45], and sheared [46]. Their dimensions can be tailored to avoid the onset of plasticity when deformed. For example, sheets with ribbon-like features made of various materials (including metals) can be transformed into 3D objects via compressive buckling when triggered by the release of a pre-stretched substrate [47–51]. The main issue with this approach in a structural setting is its limited scalability and its reliance on a substrate for deployment. The structural capacity of ribbon-based compliant systems can be improved when ribbons are joined and used as building blocks for free-standing structures, but few efforts have been made in this direction [31, 52–55]. One constraint is the fact that a ribbon can only be significantly compacted by bending it about the axis aligned with the "width" direction, thus limiting the stowing configurations of ribbon-based structures.

In this work, we propose the combination of a design framework and a material choice to create ribbon-based compliant morphing structures. Our fundamental structural element is a pre-twisted bulk metallic glass (BMG) ribbon. Applying finite twists to the ribbon sketched in Fig. 2.1(a) about its longitudinal axis produces the beam-like structural element in Fig. 2.1(b). If we construct a fixed coordinate system with orthonormal basis vectors $\{\mathbf{e}_i\}$ and align the twist axis of the ribbon with $\mathbf{e}_1$, some ribbon cross-sections have preferred bending directions about $\mathbf{e}_2$ and others about $\mathbf{e}_3$. We will refer to these regions as "faces" throughout this article. This expanded set of bending axes and the inherent chirality imparted via twisting allows for extreme compaction of the ribbon. BMGs have attractive properties for compliant structures [29, 56] due to a broad elastic range, up to 2% strain [57–59]. Additionally, BMGs can be made into complex, stress-free geometries via thermoforming, where the alloy is heated above its glass transition temperature, reshaped, and quenched to avoid crystallization [60]. In this work, we choose $Zr_{65}Cu_{17.5}Ni_{10}Al_{7.5}$ BMG [61] since it is widely studied in the literature and is commercially available in melt-spun ribbon form [62]. First, we provide a complete mechanistic analysis of the twisting process, and propose a ribbon configuration

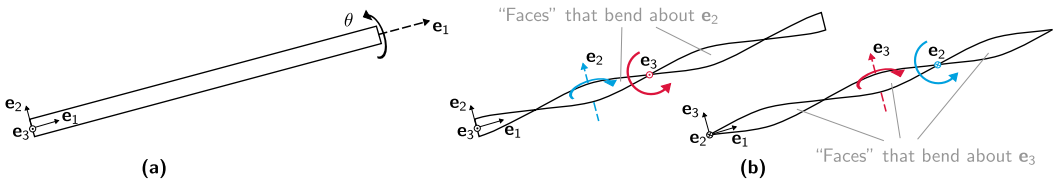

Figure 2.1: Twisting ribbons to create structural elements with an expanded set of bending axes. (a) Original ribbon configuration, where $\{\mathbf{e}_i\}$ are the orthonormal basis vectors of a coordinate system aligned with the centerline of the ribbon. (b) Ribbon configuration after a $\theta = 3\pi$-degree twist about $\mathbf{e}_1$, viewed from two different directions. In a twisted configuration, we call "faces" those regions that can bend about $\mathbf{e}_2$ or $\mathbf{e}_3$.

with undulated edges that allows us to localize the majority of the twist onto desired regions. The influence of various design parameters is analyzed via finite-element (FE) simulations and through an analytical model based on a geometrically nonlinear plate theory. We compare these results with torsion experiments on BMG ribbons. Once we have a complete mechanistic description of twisting, we thermoform ribbons into twisted shapes, and assemble them into structural prototypes of deployable mechanical systems, such as collapsible rings, spheres and auxetic structures. With this preliminary work we (i) shed light on the twisting mechanics of non-straight ribbons, (ii) illustrate the potential of twisted ribbons as structural elements for deployable structures, (iii) demonstrate that the combination of advanced materials such as BMGs and carefully-designed architectures can be leveraged to design compliant shape-morphing systems made of metals. Owing to the richness of achievable deformations we envision that, upon proper scaling, these structural systems could find application as components of deployable space structures (e.g., booms or rings for mesh-antennae) or as components for compliant, yet fully metallic robots.

In Section 2.2, we illustrate the fundamental design parameters of our undulated ribbons and we provide an experimental characterization of the mechanical properties of BMG. In Section 2.3, we provide background information and results on the twisting mechanics of ribbons. We use FE simulations to understand the influence of the various design parameters and compare it to twisting experiments we conducted on BMG ribbons. We then adapt an analytical model introduced by Mockensturm to our case of undulated ribbons, and use it to analyze the influence of the design parameters on their elastic response. In Section 2.4, we describe our thermoforming setup and show that it enables the fabrication of pre-twisted ribbons that are subsequently spot-welded into structures that display extreme morphing capacity. Conclusions and future outlook are reported in Section 2.5.

2.2 Ribbon design and material characterization

One of the ribbon geometries used in our work is shown in Fig. 2.2. As in Fig. 2.1, we define an orthonormal vector basis $\{\mathbf{e}_i\}$, with material coordinates x_i. The

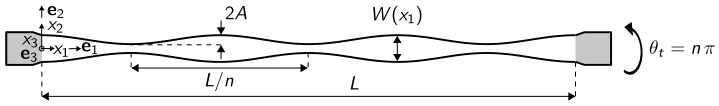

Figure 2.2: Undulated ribbon characterized by thin necks and wide faces, with all the relevant geometrical parameters. The gray extremities/tabs of the ribbon are not part of the model, but facilitate clamping of the fabricated specimens. θ_t is the target twisting angle to align all necks with the $\mathbf{e}_1$–$\mathbf{e}_3$ plane and all faces with the $\mathbf{e}_1$–$\mathbf{e}_2$ plane.

ribbon has thickness H and its length is $L = 180\,\text{mm}$, unless otherwise specified (excluding the shaded gray tabs used for clamping purposes). The long edges of the ribbon have a sinusoidal profile with amplitude A and wavelength L/n, where n is the number of necks. The width of the ribbon follows the function $W(x_1) = w + 2A[\cos(2\pi n x_1/L) - 1]$, where $w = 9\,\text{mm}$ unless otherwise specified. In order to achieve a twisted state where all necks represent faces that can bend about the $\mathbf{e}_3$ axis, an undulated ribbon needs to be twisted through a target angle $\theta_t = n\,\pi$.

All ribbons in our work are manufactured from a melt-spun roll of the $Zr_{65}Cu_{17.5}$-$Ni_{10}Al_{7.5}$ alloy. The roll and a micrographic image showing the melt-spinning-induced irregularities of the cross-section are shown in Fig. 2.3(a). For modeling

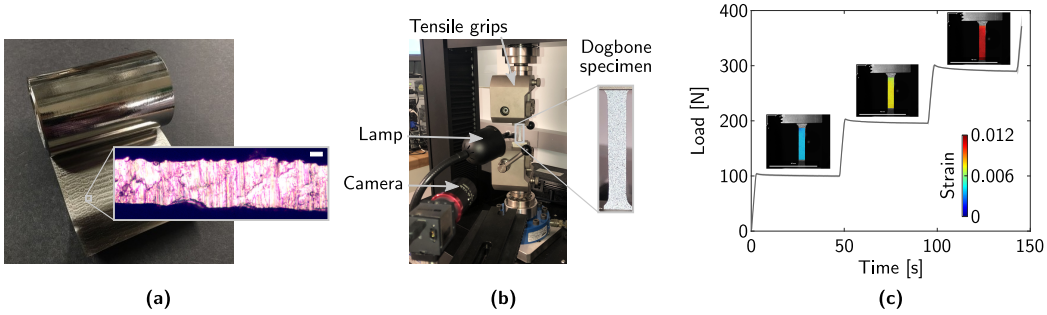

Figure 2.3: Material characterization. (a) BMG roll ($Zr_{65}Cu_{17.5}Ni_{10}Al_{7.5}$). The micrograph shows the irregular cross section of the roll (Scale bar: $10\,\mu$m). (b) Tensile test setup to characterize the BMG sheets. (c) Load-time curve indicating our testing procedure; the specimen is pulled and the force is held constant at various force values to record images for the DIC procedure. The insets show the DIC-computed axial strain field.

purposes, we cut several BMG pieces from the same roll and measure their thickness using a microscope, finding an average thickness of $54\,\mu$m. All specimens used in

this work are obtained by creating drawings in MATLAB, cutting PETG masks with a Silhouette Cameo cutter, using these masks to mark the edges of the ribbons on the BMG roll, and manually cutting the roll. Since the mechanical performance of our ribbons is affected by the cross-sectional imperfections visible in Fig. 2.3(a), we measure the mechanical properties of several dogbone-shaped specimens. We do so with the universal testing machine shown in Fig. 2.3(b) (ADMET eXpert 8612 Table-Top Axial Torsion Test System, with a 25 kN axial load cell), equipped with grippers for tension tests. Our setup also features a high-definition camera (Edmund Optics EO-5023M) to record photographs that are analyzed via 2D digital image correlation (DIC). First, we perform a tensile test to understand the behavior of the material and to identify the limits of the linear elastic regime (see A.1). We realize that the material behaves linear-elastically up until the breaking point, which occurs at a breaking strain $\varepsilon_b \approx 1.7\%$ and at a stress $\sigma_b \approx 1.2\,\text{GPa}$. In light of this, we test three specimens of equal dimensions following the load path illustrated in Fig. 2.3(c). A specimen is pulled up to loads of 100, 200 and 300 N. At those values, the force is kept constant for 45 seconds to allow us to record a picture of the specimen. We compare these images to the undeformed configuration using the DIC software nCorr [63] to extract the strains in the plane of the specimen. As a result, we can measure Young's modulus E and Poisson's ratio ν for the material by averaging these quantities across specimens. We obtain the following values: $E = 78\,\text{GPa}$ and $\nu = 0.355$.

2.3 Twisting mechanics

This Section is dedicated to the analysis of the twisting mechanics of undulated ribbons, with the goal of understanding what geometries yield BMG ribbons that can be twisted into desired shapes, where the bending axes of adjacent faces are perpendicular to each other as sketched in Fig. 2.1(b).

For some boundary conditions, it is observed that twisting a ribbon leads to mechanical instabilities that result in the appearance of wrinkle-like patterns. This behavior was first observed by A. E. Green in 1936 [64, 65], and has received renewed attention since the early 2000's. Mockensturm's work on the topic is the most general from a modeling standpoint, where a fully-nonlinear plate theory is used to model the twisting behavior and elastic instabilities of arbitrarily-wide ribbons subjected to large twists [37, 66, 67]. A very comprehensive article on this phenomenon by Chopin and Kudrolli [42] used experiments and scaling arguments to map various buckling modes of twisted, pre-stretched ribbons clamped at their

edges. Their conclusions are that there is a critical pre-stretch at which there is a transition between lateral and longitudinal buckling modes, and that the ribbon geometry strongly influences the critical twists and achievable post-buckled shapes.

In our work, we are interested in avoiding these instabilities. In fact, for our ribbons to morph into structural elements with multiple preferred bending axes, we need to avoid any localization of curvature that would compromise their deployability and their post-twisting response. However, special considerations need to be made since our ribbons feature non-straight edges—a scenario that is seldom considered in the existing literature [44]. Therefore, we use numerical simulations to predict the principal strains and the deformed shapes achievable by twisting undulated ribbons. These simulations are validated via torsional experiments on BMG specimens. To gain a better understanding of the mechanics involved and of the influence of the design parameters, we adapt the model developed by Mockensturm [37] to the case of ribbons with non-constant cross-sections.

Numerical modeling

Our numerical, finite element (FE) simulations are conducted using the commercial software Abaqus. The ribbon configurations we consider have the dimensions reported in Section 2.2, and varying numbers of necks n and undulation amplitudes A. We consider four-node reduced-integration shell elements (of the S4R type) with 7 through-the-thickness integration points. These elements are suitable for geometrically-nonlinear analyses. The material response is considered to be linear over finite strains, an assumption that is acceptable for a material like BMG (see A.1). Each ribbon is clamped at the bottom edge, while all nodes of the top edge are fixed to a fictitious reference point where we apply the load. The solution is carried out in two separate steps. First, we use an implicit/static analysis to model the axial pre-stretching step necessary to avoid longitudinal instabilities. This is enforced by applying an initial displacement of 0.1 mm between clamped boundaries. Then, we use an explicit/dynamic analysis to model the twisting process. This is done in order to speed up the computation time with respect to the standard implicit solver. We use a mass-scaling approach to accelerate computations, where the density of the material is artificially scaled to increase the stable time increment. To ensure that the model reflects the quasi-static nature of the twisting process, we monitor the total kinetic energy of our system and make sure it remains below 5% of the total energy in each simulation.

First, we analyze the response of a straight ribbon; this is summarized in Fig. 2.4(a,c). In Fig. 2.4(a), we illustrate the undeformed configuration. The ribbon is clamped at

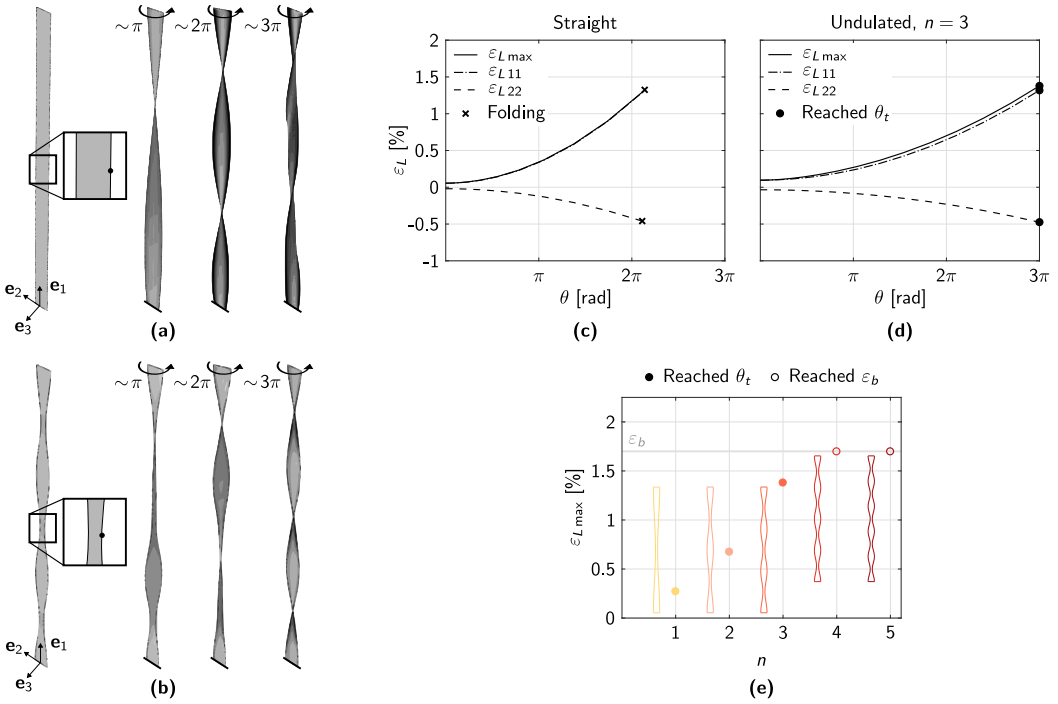

Figure 2.4: Numerical (FE) results on twisting. (a) Initial and deformed configurations for an initially-straight ribbon subjected to pre-stretch and torsion. Darker colors indicate regions of higher maximum principal strain, and serve the sole purpose of qualitatively showing where the strains are largest. (b) Same as (a), but for an undulated ribbon with $n = 3$ and $A = w/6$. The circular markers in the undeformed configurations indicate the locations where strains are the largest. (c) Logarithmic strain versus twist angle for a straight ribbon. The crosses indicate when the ribbon reached an unwanted self-folded configuration. (d) Logarithmic strain versus twist angle for an undulated ribbon with $n = 3$ and $A = w/6$. (e) Effects of the number of necks n on the maximum strain, with $A = w/6$ fixed. Recall that the breaking strain for this material is $\varepsilon_b = 1.7\%$.

both bottom and top ends. The load is modeled as a displacement along $\mathbf{e}_1$ followed by twist about $\mathbf{e}_1$ applied to the top end of the ribbon. This figure also illustrates the ribbon for various levels of twisting. Darker colors indicate regions of higher maximum principal strain. One can qualitatively see that, as already known from the literature [42], larger strains concentrate at the edges of the ribbon. Thus, we extract quantitative information on the response at the critical point illustrated in the inset (located at $x_1 = L/2$ and $x_2 = -W(x_1)/2$ in the undeformed configuration). Considering the total twisting angle θ between the top and bottom edges as our variable, we monitor the evolution of the maximum principal ($\varepsilon_{L\,\max}$), axial ($\varepsilon_{L\,11}$) and lateral ($\varepsilon_{L\,22}$) strains and plot them in Fig. 2.4(c). All strains are logarithmic.

We can see that the maximum principal strain coincides with the axial strain, and that they are both nonzero at $\theta = 0$ due to the pre-stretch. On the other hand, the lateral strain is compressive. This behavior is due to Poisson's effects that balance the twisting-induced tension, and it is known to lead to lateral buckling [42]. This behavior is actually visible in our numerical results in the form of a self-folding that takes place after $\theta = 2\pi$ (see also the deformed shape at 3π in Fig. 2.4(a)). After self-folding occurs, the strains assume values that are strongly dependent on the assumed contact parameters, and are therefore deemed unrealistic.

In Fig. 2.4(b,d), we report the response of an undulated ribbon with $n = 3$ necks and undulation amplitude $A = w/6$. In this case, the maximum strains are achieved at the edge of a neck region. The strain plot illustrates that the maximum strains achieved are less than those in the straight ribbon and remain below the breaking strain of 1.7‰. Moreover, no self-folding is observed prior to the target angle $\theta_t = 3\pi$ due to smaller lateral compressive strains. The final twisted configuration is illustrated in Fig. 2.4(b) and, as expected, it features necks parallel to the $\mathbf{e}_1$–$\mathbf{e}_3$ plane and wide faces parallel to $\mathbf{e}_1$–$\mathbf{e}_2$.

Now that we have illustrated the benefits of the undulated edge geometry, we use our numerical model to analyze the effects of the number of necks n on the twisting response. A more detailed parametric analysis is then carried out analytically in Section 2.3. In Fig. 2.4(e), the markers indicate the maximum principal strain as a function of the number of necks. Each value is recorded at a target twist angle that is dependent on the number of necks. We also superimpose the color-coded silhouettes of the ribbons as a visual aid. Increasing the number of necks causes the maximum principal strain to increase. For the 4 and 5 neck cases, we reach the breaking strain before reaching the target angles of 4π and 5π, respectively. This indicates that, for the ribbon dimensions we selected, more than 3 necks (wavelengths less than 6 cm) are not admissible.

Experimental validation

To experimentally validate our numerical predictions, we perform torsional tests on ribbons of various geometries. These tests are carried out using the same apparatus we used for the axial experiments described in Section 2.2, using grippers designed for torsion. The comparison between experimental and numerical results for three ribbon geometries is shown in Fig. 2.5. In all cases, we plot the axial reaction force developed during twisting, as a function of the twisting angle. For the straight

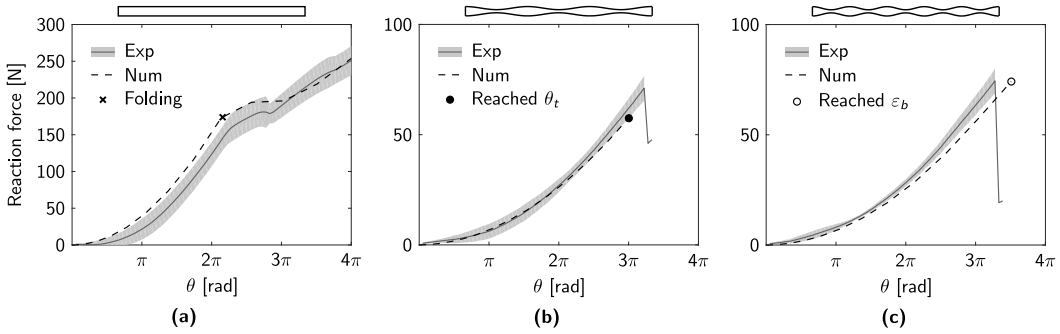

Figure 2.5: Experimental validation of the numerical predictions on twisting. (a) Axial reaction force versus twist angle for a straight ribbon. The dark gray line is the mean and the shaded light gray area indicates the standard deviation of measurements performed on three specimens. The cross marker indicates the θ angle at which the simulation indicates self-folding. (b), (c) Same as (a), but for a 3-neck and 5-neck ribbon, respectively. Both cases feature $A = w/6$. A sharp drop in the experimental curve indicates failure.

ribbon configuration, shown in Fig. 2.5(a), we can see that the numerical response follows the experimental trend both during the monotonic force increase that is observed before self-folding and during the non-monotonic regime that occurs after the ribbon self-folds. The self-folding point achieved numerically is indicated by the cross marker. Despite the incidence of self-folding, the experiments illustrate that the ribbon does not fail in the 0-4π twist range. When considering a ribbon with $n = 3$ and $A = w/6$, as illustrated in Fig. 2.5(b), we can see that numerics and experiments agree well. Moreover, as predicted in Section 2.3, the experiments confirm that this ribbon does not fail at the target angle of 3π. Finally, in Fig. 2.5(c), we confirm the numerical prediction that a ribbon with $n = 5$ and $A = w/6$ fails (reaching the breaking strain) long before reaching the target angle 5π.

These experiments serve as a partial validation of our numerical model. They provide insight into the axial response of the ribbons, but offer no information on the lateral stresses that arise during twisting. Since twisting induces out of plane deformations, we cannot reliably use 2D DIC; moreover, 3D DIC would only be useful for small twists. For these reasons, we develop an analytical model to verify the numerical prediction that ribbons with undulated edge geometries experience considerably smaller compressive stresses in the lateral direction, thus delaying the onset of buckling due to twist.

Analytical modeling

The model we employ to analyze the state of strain in the ribbons prior to thermoforming is heavily based on a fully nonlinear, geometrically exact description of

rectangular ribbons that was developed by Mockensturm [37]. We re-derive this model while making minor modifications in order to extend it to ribbons with edges that are symmetric, but not straight. We provide an overview of the model and its assumptions, compare the analytical and computational predictions, and perform a more extensive parametric analysis on undulated ribbons, while highlighting some limitations of the approach.

Reference and deformed configurations

A ribbon's material particle positions in an untwisted reference configuration are $\mathbf{X} = x_\alpha \mathbf{e}_\alpha + x_3 \mathbf{e}_3$. Throughout this text, the indices α and β pertain to the mid-surface of the ribbon, the index '3' corresponds to the direction normal to the surface, and we use the Einstein summation convention for repeated indices. The coordinates x_i are convected and material, and $0 < x_1 < L,\ |x_2| < W(x_1)/2,\ |x_3| < H/2$ for a ribbon of uniform length L and thickness H, and varying width $W(x_1)$. Our fixed coordinate frame $\{\mathbf{e}_i\}$ is orthonormal. The mapping $\boldsymbol{\chi}^*(x_i) = \boldsymbol{\chi}(x_\alpha) + x_3 \hat{\mathbf{v}}^3$ describes these particles in the twisted configuration, where $\boldsymbol{\chi}(x_\alpha)$ is the deformation mapping of the midplane of the ribbon, and $\hat{\mathbf{v}}^3$ is the outward unit normal to the surface $\mathcal{S}$ defined by $\boldsymbol{\chi}(x_\alpha)$. It is assumed that unit normals to the surface $x_\alpha \mathbf{e}_\alpha$ are mapped to unit normals of $\mathcal{S}$, with vanishing transverse strains. This is an assumption that is valid within the thin plate approximation framework and is called the Love-Kirchhoff hypothesis.

After the ribbon is subjected to a pre-stretch and torsion, its mid-surface assumes a helicoidal geometry, where the expression for $\boldsymbol{\chi}(x_\alpha)$ is shown in Eq. 2.1 below. For a cross-section located at x_1, $f(x_1, x_2)$ is the mapping of the particles in the lateral direction x_2, $\lambda_1(x_1)$ is the local axial pre-stretch, and $\theta(x_1)$ is the local twist angle relative to the supported edge at $x_1 = 0$. Throughout this text, when the material coordinate is not specified, we are evaluating the twist angle function at the end of the ribbon. Namely, $\theta \equiv \theta(L)$.

$$\boldsymbol{\chi}(x_\alpha) = \lambda_1(x_1) x_1 \mathbf{e}_1 + f(x_1, x_2) \cos(\theta(x_1)) \mathbf{e}_2 + f(x_1, x_2) \sin(\theta(x_1)) \mathbf{e}_3 \ . \qquad (2.1)$$

The expression above is slightly different from what is used by Mockensturm, as it accounts for variations in λ_1, f, and θ' as a function of axial position x_1. These functions are calculated in the following subsection.

Pre-stretch and twist as a function of axial position

Static equilibrium implies that the total axial force F acting on each cross-section is independent of position x_1. Therefore, the local linear axial strain du_1/dx_1 due to pre-stretch can be written as:

$$\frac{du_1(x_1)}{dx_1} = \frac{F}{EHW(x_1)} \,. \tag{2.2}$$

The total stretch λ_{tot} of the ribbon is obtained by integration:

$$\lambda_{tot} = \frac{1}{L}\left(L + \int_0^L \frac{du_1}{dx_1} dx_1\right) = 1 + \frac{F}{EHL}\int_0^L \frac{1}{W(x_1)} dx_1 \,. \tag{2.3}$$

This total pre-stretch is prescribed in our experiments, and therefore we know the total force F that is being exerted at all ribbon cross-sections:

$$F = \frac{EHL(\lambda_{tot} - 1)}{\int_0^L \frac{1}{W(x_1)} dx_1} \,. \tag{2.4}$$

Knowing F, the local axial pre-stretch $\lambda_1(x_1)$ of an infinitesimally long cross-section at x_1 is obtained from the previously calculated quantities:

$$\lambda_1(x_1) = 1 + \frac{du_1(x_1)}{dx_1} = 1 + \frac{L(\lambda_{tot} - 1)}{W(x_1)\int_0^L \frac{1}{W(x_1)} dx_1} \,. \tag{2.5}$$

Recalling the assumption that unit normals to the reference surface are mapped to unit normals of the deformed surface and that transverse strains vanish, we calculate the twist of the ribbon as a function of x_1. We note that the shear modulus G is a constant and that the torque T is the same at all ribbon cross-sections, so the twist rate of a ribbon is given by:

$$\theta'(x_1) = \frac{T}{GJ(x_1)} \,. \tag{2.6}$$

The polar moment of inertia for a slender rectangular cross section ($W \gg H$) is $J = WH^3/3$. Since we prescribe the total twist of the ribbon's supported edges $\theta(L)$, we can calculate the ratio T/G (for brevity, we omit the algebraic steps that are similar to the calculation of F above) and thus know the twist rate as a function of axial position x_1:

$$\theta'(x_1) = \frac{\theta(L)}{W(x_1)} \frac{1}{\int_0^L \frac{1}{W(x_1')} dx_1'} \,. \tag{2.7}$$

We integrate this expression to find that the twist of the ribbon at x_1 relative to the fixed support at $x_1 = 0$ is:

$$\theta(x_1) = \theta(L) \frac{\int_0^{x_1} \frac{1}{W(x_1')} dx_1'}{\int_0^L \frac{1}{W(x_1')} dx_1'} \,. \tag{2.8}$$

Kinematic measures

Now that expressions for $\lambda_1(x_1)$ and $\theta(x_1)$ are given in Eqs. 2.5 and 2.8, we must calculate $f(x_1, x_2)$ to complete our description of the deformed surface $\boldsymbol{\chi}$, represented by Eq. 2.1. Here, we follow Mockensturm's calculations closely but, unlike in his work, we account for the non-constant nature of λ_1 and θ'.

Each term that appears in the final elastic equilibrium equation is a function of the covariant and/or contravariant basis vectors of the ribbon's deformed configuration. The covariant basis on $\mathcal{S}$ is given by $\mathbf{v}_\alpha = \partial\boldsymbol{\chi}/\partial x_\alpha$, and the reciprocal, contravariant basis $\mathbf{v}^\alpha$ to $\mathcal{S}$ is constructed such that $\hat{\mathbf{v}}_3 \cdot \mathbf{v}_\alpha = 0,\ \hat{\mathbf{v}}_3 = \hat{\mathbf{v}}^3,\ \mathbf{v}^i \cdot \mathbf{v}_j = \delta^i_j$. Here, δ^i_j is the Kronecker delta. To simplify our calculations, we note that $\partial f(x_1, x_2)/\partial x_1$ is very small compared to $f(x_1, x_2)$ and $\partial f(x_1, x_2)/\partial x_2$ everywhere in the ribbon (this is supported by shear being negligible in our numerical simulations). We also can calculate that $x_1\lambda_1'(x_1) \ll \lambda_1(x_1)$ everywhere in the ribbon and that $x_1\theta''(x_1) \ll \theta'(x_1)$ in the regions surrounding the narrowest and widest cross-sections of the ribbon. In particular, $\lambda_1'(x_1) = \theta''(x_1) = \partial f(x_1, x_2)/\partial x_1 = 0$ where $W'(x_1) = 0$ (the width extrema). Note that the numerical results tell us that stresses are global minima or maxima at these exact cross-sections. In the following, we keep our derivation general to a small region surrounding these width extrema, and we ignore these small terms in the expressions for the basis vectors v_i and v^i. Note that, given the above simplifications, we denote $f'(x_1, x_2) \equiv \partial f(x_1, x_2)/\partial x_2$ for the purpose of concise notation.

Our covariant basis vectors $\mathbf{v}_i$ are:

$$\mathbf{v}_1 = \begin{Bmatrix} \lambda_1(x_1) \\ -f(x_1, x_2)\theta'(x_1)\sin\left(\theta(x_1)\right) \\ f(x_1, x_2)\theta'(x_1)\cos\left(\theta(x_1)\right) \end{Bmatrix}, \quad \mathbf{v}_2 = \begin{Bmatrix} 0 \\ f'(x_1, x_2)\cos\left(\theta(x_1)\right) \\ f'(x_1, x_2)\sin\left(\theta(x_1)\right) \end{Bmatrix}, \tag{2.9}$$

$$\mathbf{v}_3 = \frac{1}{\sqrt{\left(\lambda_1(x_1)^2 + \theta'(x_1)^2 f(x_1, x_2)^2\right) f'(x_1, x_2)}} \begin{Bmatrix} -\theta'(x_1) f(x_1, x_2) f'(x_1, x_2) \\ -\lambda_1(x_1) f'(x_1, x_2)\sin\left(\theta(x_1)\right) \\ \lambda_1(x_1) f'(x_1, x_2)\cos\left(\theta(x_1)\right) \end{Bmatrix}.$$

We then calculate the contravariant basis vectors:

$$\mathbf{v}^1 = \frac{1}{\lambda_1(x_1)^2 + f(x_1, x_2)^2\theta'(x_1)^2} \begin{Bmatrix} \lambda_1(x_1) \\ -f(x_1, x_2)\theta'(x_1)\sin\left(\theta(x_1)\right) \\ f(x_2)\theta'(x_1)\cos\left(\theta(x_1)\right) \end{Bmatrix}, \tag{2.10}$$

$$\mathbf{v}^2 = \frac{1}{f'(x_1,x_2)} \begin{Bmatrix} 0 \\ \cos\Big(\theta(x_1)\Big) \\ \sin\Big(\theta(x_1)\Big) \end{Bmatrix},$$

$$\mathbf{v}^3 = \frac{1}{\sqrt{\Big(\lambda_1(x_1)^2 + \theta'(x_1)^2 f(x_1,x_2)^2\Big) f'(x_1,x_2)}} \begin{Bmatrix} -\theta'(x_1) f(x_1,x_2) f'(x_1,x_2) \\ -\lambda_1(x_1) f'(x_1,x_2) \sin\Big(\theta(x_1)\Big) \\ \lambda_1(x_1) f'(x_1,x_2) \cos\Big(\theta(x_1)\Big) \end{Bmatrix}.$$

The first and second fundamental forms $a_{\alpha\beta}$ and $b_{\alpha\beta}$, respectively, and the Christoffel symbols of the second kind Γ^k_{ij} are used to provide local descriptions of $\mathcal{S}$, and are given by:

$$a_{\alpha\beta} = \mathbf{v}_\alpha \cdot \mathbf{v}_\beta \ , \quad b_{\alpha\beta} = \Gamma^3_{\alpha\beta} = \mathbf{v}_{\alpha,\beta} \cdot \hat{\mathbf{v}}_3 \ , \tag{2.11}$$

$$\Gamma^\lambda_{\alpha\beta} = \mathbf{v}_{\alpha,\beta} \cdot \mathbf{v}^\lambda \ , \quad \Gamma^\beta_{3\alpha} = -b^\beta_\alpha = \hat{\mathbf{v}}_{3,\alpha} \cdot \mathbf{v}^\beta \ , \quad \Gamma^3_{3i} = \Gamma^i_{33} = 0 \ .$$

In the definitions shown above (and throughout the remainder of the text), the underscore comma designates partial differentiation with respect to the corresponding coordinate component ($\mathbf{v}_{,i} \equiv \partial \mathbf{v}/\partial x_i$). We note that our tensors $b_{\alpha\beta}$ and b^β_α have identical matrix components. See [68] for a more thorough discussion of the relationship between the second fundamental form and Christoffel symbols of the second kind. The matrix components of these forms are given below:

$$[a_{\alpha\beta}] = \begin{bmatrix} \lambda_1(x_1)^2 + f(x_1,x_2)^2 \theta'(x_1)^2 & 0 \\ 0 & f'(x_1,x_2)^2 \end{bmatrix}, \tag{2.12}$$

$$[b_{\alpha\beta}] = [\Gamma^3_{\alpha\beta}] = \frac{\lambda_1(x_1)\theta'(x_1) f'(x_1,x_2)}{\sqrt{\lambda_1(x_1)^2 + \theta'(x_1)^2 f(x_1,x_2)^2}} \begin{bmatrix} 0 & 1 \\ 1 & 0 \end{bmatrix},$$

$$[\Gamma^1_{\alpha\beta}] = \frac{f(x_1,x_2) f'(x_1,x_2) \theta'(x_1)^2}{\lambda_1^2 + f(x_1,x_2)^2 \theta'(x_1)^2} \begin{bmatrix} 0 & 1 \\ 1 & 0 \end{bmatrix},$$

$$[\Gamma^2_{\alpha\beta}] = \frac{1}{f'(x_1,x_2)} \begin{bmatrix} -f(x_1,x_2)\theta'(x_1)^2 & 0 \\ 0 & f''(x_1,x_2) \end{bmatrix},$$

$$\Gamma^3_{3i} = \Gamma^i_{33} = 0.$$

When the ribbons are mapped into the deformed configuration, the first fundamental form $a_{\alpha\beta}$ characterizes the in-plane stretches and the second fundamental form $b_{\alpha\beta}$ describes the inner products between the partial derivatives of the covariant basis vectors and the unit normal, thus capturing out-of-plane bending. The mixed

component form b_α^β defined in Eq. 2.12 has the same matrix components as $b_{\alpha\beta}$ in our case and captures the inner products between the partial derivatives of the local unit normal and the contravariant basis vectors, essentially describing the rotation of the unit normal as we move along the surface. The connection between these forms and the tensors for in-plane strain $\mathbf{C}$ and bending $\mathbf{\Lambda}$ commonly used in plate and shell mechanics is described more precisely below [69]:

$$\mathbf{C} = a_{\alpha\beta}(\mathbf{e}_\alpha \otimes \mathbf{e}_\beta) \ , \quad \mathbf{\Lambda} = -(b_{\alpha\beta} + b_{\beta\alpha})(\mathbf{e}_\alpha \otimes \mathbf{e}_\beta) \ . \tag{2.13}$$

Material model and stress resultants

Mockensturm's usage of a Saint-Venant-Kirchhoff material model is also appropriate for our ribbons due to the large regime of elastic linearity displayed by the BMG. This model uses the following strain energy function:

$$\varphi(\mathbf{C}, \mathbf{\Lambda}) = \frac{KH^2}{24}\left(\nu\frac{(\mathbf{\Lambda}\cdot\mathbf{I})^2}{4} + (1-\nu)\frac{\mathbf{\Lambda}\cdot\mathbf{\Lambda}}{4}\right) + \ldots \\ \frac{K}{2}\left(\nu\frac{(\mathbf{C}\cdot\mathbf{I}-3)^2}{4} + (1-\nu)\frac{(\mathbf{C}-\mathbf{I})\cdot(\mathbf{C}-\mathbf{I})}{4}\right), \tag{2.14}$$

where $K = EH/(1-\nu^2)$, E is Young's modulus, and ν is Poisson's ratio. The in-plane and bending stress resultants are:

$$\mathbf{N} = 2\frac{\partial\varphi(\mathbf{C}, \mathbf{\Lambda})}{\partial\mathbf{C}} \ , \qquad \mathbf{M} = 2\frac{\partial\varphi(\mathbf{C}, \mathbf{\Lambda})}{\partial\mathbf{\Lambda}} \ . \tag{2.15}$$

In matrix component form, these resultants are:

$$N_{11} = \frac{K}{2}\lambda_1(x_1)^2 - 1 + \theta'(x_1)^2 f(x_1, x_2)^2 + \nu\left(f'(x_1, x_2)^2 - 1\right) \ , \\ N_{12} = N_{21} = 0 \ , \\ N_{22} = \frac{K}{2}\nu\left(\lambda_1(x_1)^2 - 1 + \theta'(x_1)^2 f(x_1, x_2)^2\right) + f'(x_1, x_2)^2 - 1, \\ M_{11} = M_{12} = 0 \ ,$$

$$M_{12} = M_{21} - \frac{KH^2(1-\nu)\lambda_1(x_1)\theta'(x_1)f'(x_1, x_2)}{12\sqrt{\lambda_1(x_1)^2 + \theta'(x_1)^2 f(x_1, x_2)^2}} \ . \tag{2.16}$$

We must now enforce our assumptions that transverse strains vanish and that unit normals to the reference configuration remain unit normals after deformation. The following constraint stress tensor is used to this purpose in this restricted kinematics plate theory and is calculated through the equilibrium equations in the next section:

$$\mathbf{Q} = Q^\alpha(\mathbf{e}_\alpha \otimes \mathbf{e}_3 + \mathbf{e}_3 \otimes \mathbf{e}_\alpha) + Q^3\mathbf{e}_3 \otimes \mathbf{e}_3 \ . \tag{2.17}$$

Resolving the PDEs governing equilibrium onto the contravariant basis

The two equations describing equilibrium are derived fully in Mockensturm's doctoral dissertation [66] and are given below:

$$[N^{\alpha\Gamma}\mathbf{v}_\alpha + Q^\Gamma\hat{\mathbf{v}}_3 + M^{\alpha\Gamma}\hat{\mathbf{v}}_{3,\alpha}]_{,\Gamma} = 0\,, \tag{2.18}$$

$$[M^{\alpha\Gamma}\mathbf{v}_\alpha]_{,\Gamma} - [Q^\alpha\mathbf{v}_\alpha + Q^3\hat{\mathbf{v}}_3] = 0\,. \tag{2.19}$$

By resolving Eq. 2.19 onto $\mathbf{v}^\beta$ and $\mathbf{v}^3$ we obtain, respectively:

$$Q^\beta = M^{\beta\Gamma}_{,\Gamma} + M^{\alpha\Gamma}\Gamma^\beta_{\alpha\Gamma}\,, \tag{2.20}$$

$$Q^3 = M^{\alpha\Gamma}b_{\alpha\Gamma}\,.$$

By inserting $\mathbf{Q}$ into Eq. 2.18, resolving the PDEs onto the contravariant basis $\mathbf{v}^i$ and eliminating the zero-valued terms, we obtain the following statement of equilibrium:

$$\begin{aligned} &N^{11}_{,1} + N^{22}_{,2} + N^{11}\Gamma^2_{11} + N^{22}\Gamma^2_{22} + 2(M^{12}_{,12} + M^{12}_{,1}\Gamma^1_{12} + M^{12}\Gamma^1_{12,1}) + \ldots \\ &\quad - 2(M^{12}_{,1} + M^{12}_{,2} + M^{12}\Gamma^1_{12})b^2_1 - M^{12}(b^2_{1,1} + b^2_{1,2} + \Gamma^2_{11}b^2_1 + \Gamma^2_{22}b^2_1) = 0\,. \end{aligned} \tag{2.21}$$

The difference between our result at this point and what is shown in Mockensturm's work is the inclusion of terms where there are partial derivatives of the stress tensors in the x_1 direction due to the non-constant functions $\lambda_1(x_1)$ and $\theta'(x_1)$.

Computing the lateral stretch using a perturbation method

We proceed by stating that for this analytical model to be accurate, the amplitude of the edge undulations must be much smaller than the wavelength. This holds for most of our ribbons and we discuss the limitations of the model in Section 2.3. In light of this consideration, we make a few simplifications driven by $W'(x_1)$ being small everywhere. We now focus our analysis at the width extrema (where $W'(x_1) = 0$). At these specific cross-sections, $N^{11}_{,1} = M^{12}_{,1} = M^{12}_{,12} = b^2_{1,1} = \Gamma^1_{12,1} = 0$ and the equilibrium statement given by Eq. 2.21 becomes:

$$N^{22}_{,2} + N^{11}\Gamma^2_{11} + N^{22}\Gamma^2_{22} - 2(M^{12}_{,2} + M^{12}\Gamma^1_{12})b^2_1 - M^{12}(b^2_{1,2} + \Gamma^2_{11}b^2_1 + \Gamma^2_{22}b^2_1) = 0\,. \tag{2.22}$$

This is the same as what Mockensturm obtained for rectangular, homogeneous ribbons. By also noting that $W''(x_1)$ is small, the boundary conditions on the traction free lateral edges in regions where $W'(x_1) = 0$ are:

$$N^{22} - 2b^2_1M^{12} = 0\,, \quad M^{12}_{,1} = 0\,, \quad M^{22} = 0\,. \tag{2.23}$$

Inserting the expressions for fundamental forms, Christoffel symbols and stress resultants calculated in previous sections (see Eqs. 2.12 and 2.16), we obtain a single nonlinear ODE for the lateral stretch of the ribbons. (We assume the dependence of all variables on x_1 to be fixed and remove the dependence of the variables on this coordinate in our notation for simplicity.)

$$\begin{aligned}
&\frac{6f''(x_2)\left(\nu(\lambda_1^2-1+\theta'^2 f(x_2)^2)+f'(x_2)^2-1\right)}{f'(x_2)}+\dots\\
&\quad-\frac{6\theta'^2 f(x_2)\left(\lambda_1^2-1+\theta'^2 f(x_2)^2+\nu(f'(x_2)^2-1)\right)}{f'(x_2)}+\dots\\
&\quad+\frac{4H^2\lambda_1^2\theta'^2(1-\nu)f'(x_2)f''(x_2)}{\lambda_1^2+\theta'^2 f(x_2)^2}+\dots\\
&\quad-\frac{H^2\lambda_1^2\theta'^4(1-\nu)f(x_2)f'(x_2)\left(\lambda_1^2+\theta'^2 f(x_2)^2+f'(x_2)^2\right)}{(\lambda_1^2+\theta'^2 f(x_2)^2)^2}+\dots\\
&\quad+12f'(x_2)(\theta'^2\nu f(x_2)+f''(x_2))=0\,. \qquad (2.24)
\end{aligned}$$

The boundary condition $N^{22}-2b_1^2M^{12}=0$ at the lateral edges becomes:

$$3(f'(\pm W/2)^2-1+\nu(\theta'^2 f(\pm W/2)^2+\lambda_1^2-1))+\frac{H^2\lambda_1^2\theta'^2(1-\nu)f'(\pm W/2)^2}{\theta'^2 f(\pm W/2)^2+\lambda_1^2}=0\,. \qquad (2.25)$$

We set changes of variables $e\equiv(\lambda_1^2-1)/2$, $\eta=H/W$, and define a non-dimensional parameter $T_p=W\theta'$. To proceed with the solution of this differential equation, we note that T_p is small and e and η are on the order of T_p^2. This determination of order stems from the pre-stretch being very small and from the ribbons having very slender cross-sections, and has been validated numerically for the ribbon geometries we study. We then use a perturbation $f(x_2)=\sum_{I=0}^{\infty}f_{(2I)}(x_2)$ which has a slightly different form compared to what Mockensturm proposed. Inserting this into Eqs. 2.24 and 2.25 gives us an ODE for each order of the lateral stretches $f_{(2I)}(x_2)$:

Zeroth order :

$$\begin{aligned}
&(3f'_{(0)}(x_2)^2-1)f''_{(0)}(x_2)=0\,,\\
&\textbf{BCs}: f'_{(0)}(\pm W/2)^2-1=0\,,\quad f_{(0)}=0\,,\\
&\textbf{Solution}: f_{(0)}(x_2)=x_2\,.
\end{aligned} \qquad (2.26)$$

Second order :

$$f''_{(2)}(x_2) + \frac{\nu T_p^2}{W^2} x_2 = 0 \,,$$
$$\textbf{BCs} : f'_{(2)}(\pm W/2) + \frac{T_p^2 \nu}{8} + e\nu = 0 \,, \quad f_{(2)} = 0 \,,$$
$$\textbf{Solution} : f_{(2)}(x_2) = -e\nu x_2 - \frac{\nu T_p^2 x_2^3}{6W^2} \,. \tag{2.27}$$

Fourth order :

$$f''_{(4)}(x_2) + \frac{T_p^4 \left(2\nu^2 - 3\right)}{6W^4} x_2^3 - \frac{eT_p^2}{W^2} x_2 = 0 \,,$$
$$\textbf{BCs:}\ f'_{(4)}(\pm W/2) + \frac{1}{24}\nu^2(12e^2 - 3eT_p^2 - \frac{T_p^4}{16}) = 0 \,, \quad f_{(4)} = 0 \,,$$
$$\textbf{Solution} : f_{(4)}(x_2) = \frac{1}{1920}\Bigg(\left(15T_p^4(\nu^2 - 1) + 240eT_p^2(\nu^2 - 1) - 960e^2\nu^2\right)x_2 + \ldots$$
$$\frac{320eT_p^2}{W^2} x_2^3 + \frac{16T_p^4(3 - 2\nu^2)}{W^4} x_2^5\Bigg) \,. \tag{2.28}$$

Now that we have calculated f to fourth order, we can insert the function into the expressions for strains (Eq. 2.13) and stresses (Eq. 2.16) in order to compare predictions from this analytical model to those from the numerical simulations.

Analytical results and comparison with the numerical ones

We first compare the strains predicted by numerical simulations and by this analysis for the case of ribbons with straight edges in Fig. 2.6(a-b). We do the same for a ribbon with three necks and edge undulation amplitude $A = w/6$ (where w is the maximum width of the ribbon) in Fig. 2.6(c-d). In both of these scenarios, we plot the principal logarithmic strains as a function of clamp twist angle at the region of the ribbon that experiences the greatest principal strains (marked with dots in Fig. 2.6(a,c)), showing good agreement between the numerical and analytical methods. From Fig. 2.6(b), we can see that the analytics, unlike the numerics, do not capture any self-folding behavior. In Fig. 2.6(d), we can see that analytics and numerics follow the same trend, especially for the lateral strains. Discrepancies in

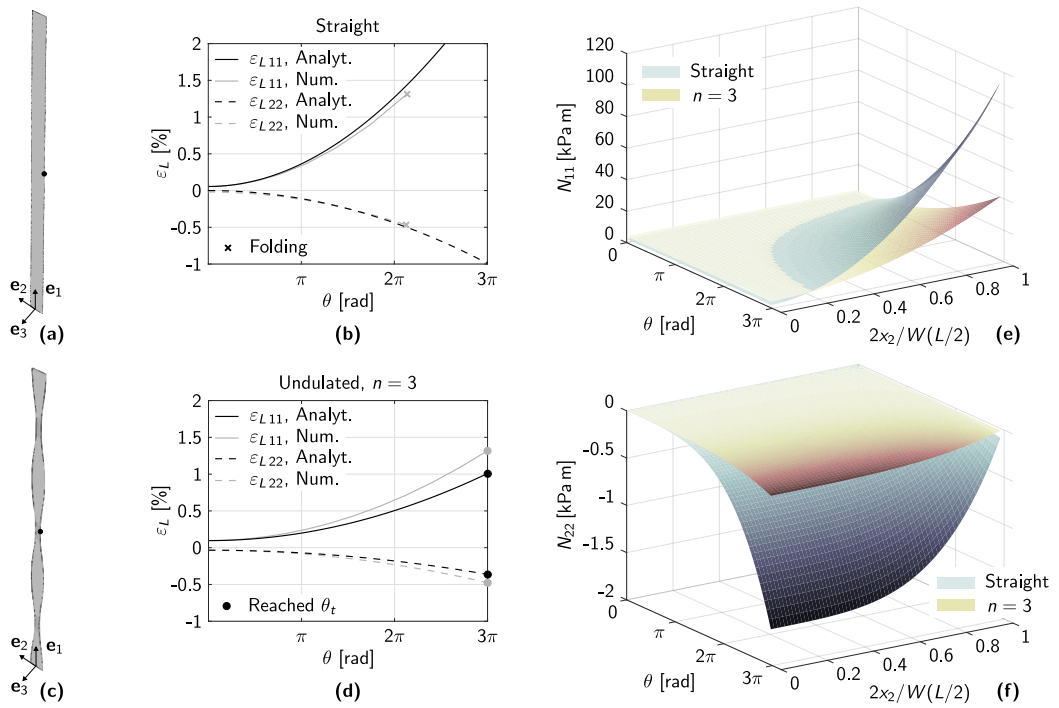

Figure 2.6: Comparison between analytical and numerical results. (a) Schematic diagram of a straight ribbon. (b) Principal logarithmic strains at the free edges of a straight ribbon. (c) Schematic diagram of a ribbon with undulated edges and $A = w/6$. (d) Principal logarithmic strains at the free edges of a "neck" region. In (b), (d), the strains are plotted as a function of total relative twist of the clamped edges. (e) Analytical prediction of the axial stress resultant as a function of twist and normalized lateral position in ribbons with straight edges and ribbons with three neck regions. For the undulated-edge ribbon, we plot the stresses at a neck cross-section, where the stresses are greatest. (f) Analytical prediction of the lateral stress resultant as a function of twist and normalized lateral position in ribbons with straight edges and ribbons with three neck regions. The greatest lateral compressive stresses (plotted here) in undulated-edge ribbons emerge in the center of the neck regions.

this case have to be ascribed to the fact that our theory is only valid for small $A\,n/L$, i.e., for small amplitude to wavelength ratios of the undulation.

Having shown a consistency between the two methods of analysis, we can now use our analytical results to study the stress evolution within the most vulnerable (narrowest) cross-section. Fig. 2.6(e-f) shows that the introduction of undulated edges reduces the principal stress resultants considerably. In particular, Fig. 2.6(f) highlights the emergence of compressive lateral stresses toward the center of the ribbon as twist is increased. These lateral stresses induce buckling at a critical twist. It is clear that the stresses are much greater for ribbons with straight edges than for ribbons of equal length, maximum width and thickness, but with undulated edges. This highlights the benefits of our design strategy when trying to obtain twisted

ribbons that do not buckle during twisting. Our analytical model can be extended to the analysis of buckling, as done by Mockensturm [37], but this is beyond the scope of this work.

Parametric study

We now leverage our analytical model to perform a broader parametric analysis than the one reported in Section 2.3. The results of this analysis are reported in Fig. 2.7. First, in Fig. 2.7(a), we analyze the effects of A on the maximum principal strain,

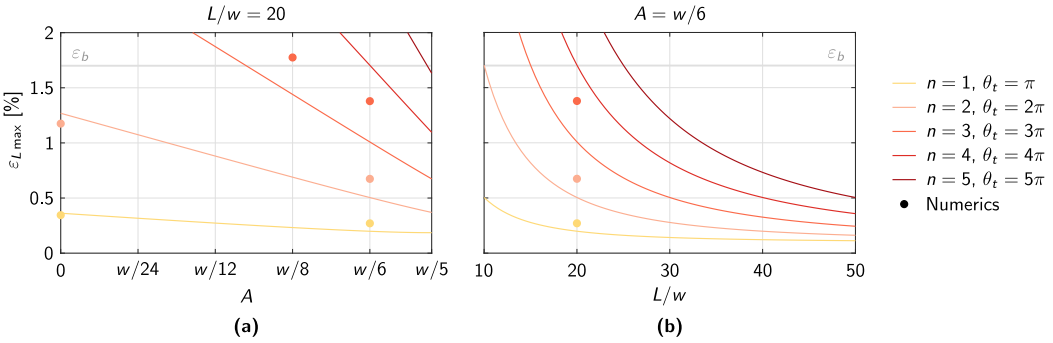

Figure 2.7: Extended parametric analysis. All curves are obtained using our analytical model. The dots are numerical data points and are useful to understand the limitations of the analytical model. (a) Effects of the amplitude of undulation A on the maximum principal strain, for various n and with $L/w = 20$ fixed. (b) Effects of L/w for various n, with $A = w/6$ fixed.

for various n and keeping the aspect ratio $L/w = 20$ fixed. All values correspond to points at the edge of a neck region. We can observe that increasing the undulation amplitude from 0 (straight ribbon) to $w/5$ causes the maximum strains to decrease. We also observe that increasing n causes the level of strain to increase during twisting, noting that θ_t increases proportionally with n. This is consistent with what is shown in Fig. 2.4(e). The superimposed circular markers follow the same color coding of the analytical lines and represent numerical data points. They allow us to evaluate the performance of the analytical model. We can see once again that the analytical model is more accurate for ribbons where the edge undulation amplitude is much smaller than the undulation wavelength, and tends to significantly underestimate the maximum principal strain for smaller values of $L/(n\,A)$. Also note that the analytical model does not capture whether self-folding occurs before the breaking strain is reached.

In Fig. 2.7(b), we analyze the effects of L/w, the aspect ratio of the ribbon, on the maximum principal strain. In this case, we fix $A = w/6$. We can see that

increasing L/w causes an exponential decrease of the maximum principal strain. While increasing L/w helps delay the onset of failure, it comes at the expense of having compact ribbon geometries.

2.4 From ribbons to structures

We now have the theoretical and numerical tools to choose geometrical configurations that yield desired shapes upon twisting. Based on previous considerations, we choose ribbons where $n = 3$ and $A = w/6$. In this section, we describe the thermoforming process and the setup we designed for twisted ribbon fabrication. We also investigate the potential of single twisted ribbons and assemblies of them as deployable mechanical systems. We do so by analyzing the bending behavior of pre-twisted ribbons and by illustrating prototypes of deployable mechanical systems capable of reversible compaction and deployment cycles.

Thermoforming

The steps required to thermoform an initially-flat ribbon into a twisted configuration are illustrated in Fig. 2.8(a). A picture of the fabrication setup is shown in Fig. 2.8(b). First, a ribbon is manually cut. Then, we use a custom setup to clamp its supporting tabs (described in Section 2.2) and apply a pre-stretch to avoid longitudinal instabilities during the twisting process. The ribbon is then twisted to its target angle and is subsequently immersed in a hot salt bath (Dynalene MS-2). The bath temperature is continuously monitored using a thermocouple and is kept constant at a value that is between the BMG's glass transition T_g and its crystallization temperature T_x. This is required for the material to be thermoformable while avoiding the onset of crystallization, which would cause the material to become brittle. For our BMG alloy, we perform Differential Scanning Calorimetry experiments and measure $T_g = 370\,°\text{C}$ and $T_x = 445\,°\text{C}$. Thus, we keep the salt bath at $\sim 400\,°\text{C}$. Our thermoforming protocol consists of immersing a specimen in the bath for 10 seconds, and then quenching it in water at room temperature. This procedure leads to stress-free BMG ribbons that assume the desired twisted shape while preserving the material's elasticity. Note that thermoforming also corrects any curvature induced by the melt-spinning process. Pictures of the 3-neck ribbon before and after thermoforming are shown in Fig. 2.8(c). The insets in the twisted configuration image show that the neck regions can bend about the $\mathbf{e}_3$ axis and the wide faces can bend about $\mathbf{e}_2$, as desired. One interesting aspect of these twisted ribbons is that they have an inherent chirality, which is imposed by choosing the twisting direction

during fabrication. The case shown in Fig. 2.8(c), for example, is such that the normal to the surface of the ribbon rotates in a counterclockwise fashion along $\mathbf{e}_1$.

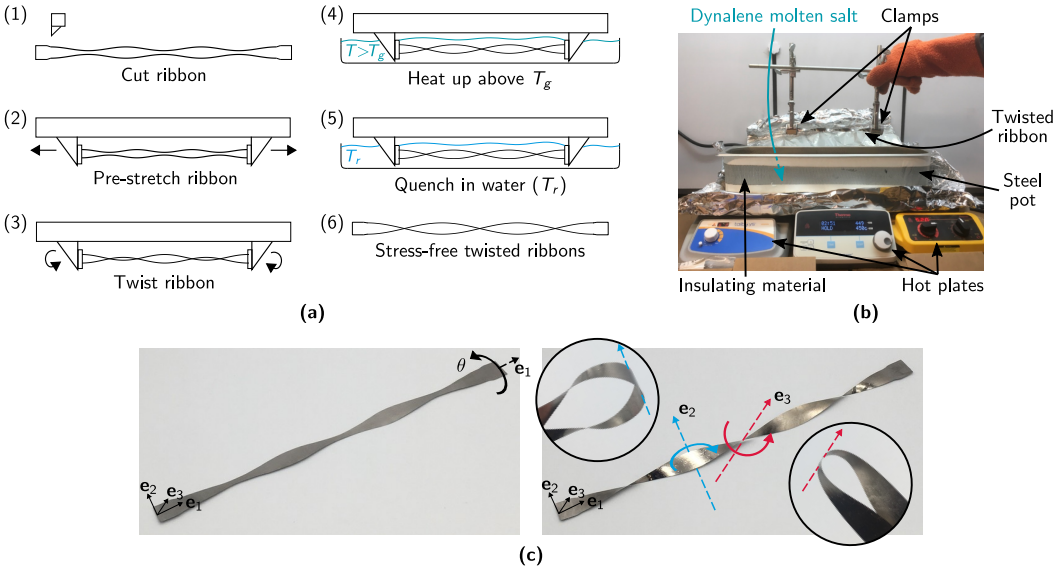

Figure 2.8: BMG ribbon thermoforming. (a) Sketch illustrating the various steps of the thermoforming process, from an initial planar ribbon to a final twisted and stress-free configuration. (b) Thermoforming setup. (c) BMG ribbon before and after thermoforming, with insets illustrating how wide faces and neck regions can be bent about $\mathbf{e}_2$ and $\mathbf{e}_3$, respectively.

Bending behavior of twisted ribbons

To allow for repeated stowage and deployment of our structures, it is important that bending the necks about $\mathbf{e}_3$ and the wide faces about $\mathbf{e}_2$ does not produce strains that exceed the breaking strain of the material. To verify that this is the case, we perform bending simulations on the pre-twisted ribbons, using the same FE model discussed in Section 2.3. To speed up computations, we only consider portions of the selected ribbon geometry. A segment of the pre-twisted stress-free ribbon that includes a single neck and terminates at the midpoints of two consecutive wide faces (thus having length $L/3 = 60\,\text{mm}$) is illustrated at the top of Fig. 2.9(a). To simulate bending of a neck about $\mathbf{e}_3$, we constrain all points belonging to the top and bottom edges of the ribbon segment to remain in the $\mathbf{e}_1$–$\mathbf{e}_2$ plane, and we force the two left extremes of the top and bottom edges to displace towards each other (d is the distance between these two points). The bent configurations for d values of 20 mm and 0 mm are also shown in Fig. 2.9(a). The evolution of the maximum principal strain in the ribbon and of the moment M_3 about $\mathbf{e}_3$ as d decreases are illustrated in Fig. 2.9(b). We can see that the strains produced during

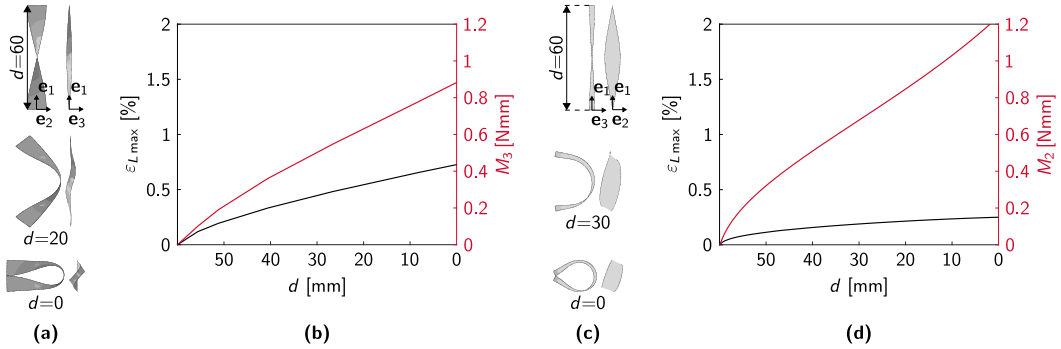

Figure 2.9: Numerical (FE) bending response of different regions of the same twisted ribbon (with $n = 3$ and $A = w/6$). (a) Snapshots of the bending deformation of the neck about $\mathbf{e}_3$. All dimensions are in mm. (b) Performance of the neck region as a joint, indicating the maximum strain involved and the moment about the rotation axis. (c) Snapshots illustrating how a wide face bends about $\mathbf{e}_2$. (d) Bending performance of the wide face.

bending remain below the breaking strain threshold of 1.7%. The moment versus displacement plot (*de facto* a moment-angle plot), is obtained by monitoring the resultant force along $\mathbf{e}_1$ at the left extreme of the top edge of the ribbon, and by multiplying it by the displacement along $\mathbf{e}_2$ of the center of the neck. We can see that the moments are two orders of magnitude smaller compared to hinges that are designed specifically for aerospace applications [22]. This implies that small moments are needed to go from the fully-deployed to the stowed configuration and that the deployed structure has limited stiffness. This behavior could be improved either by increasing the structure's dimensions (especially the ribbon's thickness—a choice that would require monitoring strains to prevent failure), or by altering the design to introduce a curvature about $\mathbf{e}_1$ that could yield a bistable behavior similar to that displayed by tape-spring hinges. This would require a modification of the thermoforming setup that is not discussed in this article.

We also simulate bending of the wide faces about $\mathbf{e}_2$, as illustrated in Fig. 2.9(c,d). In this case, the maximum principal strains achieved are extremely low, since bending a wide face produces low curvatures. However, moments are larger than those in Fig. 2.9(b), indicating that bending a wide face is more difficult than bending a neck. From Fig. 2.9(a) and (c), we can see that both necks and faces do not behave like perfect planar hinges. Due to the chirality of the ribbons, these regions feature asymmetric bending profiles (e.g., the neck region in Fig. 2.9(a) does not remain symmetric about the $\mathbf{e}_1$–$\mathbf{e}_2$ plane). This aspect can be leveraged to introduce additional degrees of freedom and enrich the shape-changing capacity of structures made from twisted ribbons.

Figure 2.10: Elastic stowage and deployment of twisted ribbons. In all cases, deformations are reversible and do not induce any plastic deformation. Note that we use tape to keep together the stowed configurations for illustration purposes. (a) A twisted ribbon can be compacted by folding it about the necks/hinges, and by finally bending the wide faces. (b) Assembling four ribbons in a circle leads to a ring structure that can be compacted following the same procedure shown in (a). (c) The chirality of the ribbons can be leveraged to create a sphere that can be compacted by applying a twisting load, similarly to Hoberman's Twist-O. (d) Planar auxetic lattice made of twisted ribbons. The dashed lines highlight the global curvature achievable by taping together selected pairs of necks.

Tabletop-scale structural prototypes

Now that we verified that pre-twisted ribbons can bend without breaking, we investigate several deployment-stowage scenarios for single twisted ribbons and assemblies of them. First, we consider a single ribbon, shown in Fig. 2.10(a). In order to compact this one-dimensional structural element, we first fold one of the wide faces

onto another, leveraging the hinge-like behavior of one of the necks. We repeat this process sequentially for all wide faces, until we obtain the configuration indicated in the second image from the right. At that point, we bend the stack of wide faces to further compact the system, obtaining the stowed configuration illustrated in the right-most panel. The longest dimension of this compacted ribbon is one order of magnitude smaller than the initial size, highlighting its potential as a deployable system. It is to be noted that the stowed configurations are kept together with double sided tape for illustration purposes, and that the ribbon goes back to the original configuration upon tape removal, owing to the fact that we are not exceeding the breaking strain.

The full potential of these systems as deployable structures can be achieved by combining multiple twisted ribbons in order to create two- and three-dimensional systems. A reliable way of joining multiple ribbons is via spot-welding. By joining four ribbons feturing the same chirality, we obtain the ring shown in Fig. 2.10(b), that has an initial diameter of 25 cm. By folding wide faces on top of each other and leveraging the joint-like behavior of the necks as we did in Fig. 2.10(a), we can compact the ring, and obtain the final configuration shown in the right-most panel. One can also create three-dimensional structures, as shown in Fig. 2.10(c). This sphere is obtained by first creating two rings from ribbons that all have the same chirality. Then, the rings are joined at two couples of wide faces. There are many ways to compact this system, but a particularly interesting one can be achieved by pushing down on the sphere from its top-most point, while simultaneously applying a rotation. This behavior is reminiscent of Hoberman's Twist-O toys, i.e., spheres made by pin-jointed polymeric crosses that can also be compacted by twisting one of their units. In our case, applying a counterclockwise or clockwise twist produces different stowed configurations owing to the chirality of the ribbons. This further highlights the potential that twisted ribbons have to create structures with many stowage configurations.

Finally, in Fig. 2.10(d), we show that twisted ribbons can be used as building blocks for structures with negative Poisson's ratio (a behavior known as auxeticity). From the undeformed lattice, the planar stowed configuration that displays an auxetic behavior (i.e., global shrinkage along $\mathbf{e}_1$ and $\mathbf{e}_2$) is obtained by taping together alternating pairs of necks, as illustrated in the central panel of the figure. If fewer pairs of necks are joined together, the structure curves into a three-dimensional surface, owing to the chirality and non-planar nature of our hinges. This phenomenon can

potentially be tailored by assembling ribbons with different chirality, can be leveraged to create freeform structures from planar precursors, and deserves a separate treatment in future work.

2.5 Conclusions and outlook

This work represents a first attempt at utilizing thin structural elements made of bulk metallic glass to create compliant deployable structures. We do this by taking initially-flat ribbons and twisting them into structural elements that feature regions that behave as compliant hinges with different preferred bending axes, and assembling these ribbons into more complex three-dimensional structures. Along the way, we use numerical and analytical models to understand the mechanics of twisting and to design ribbons that can be twisted and thermoformed into desired configurations. We also use simulations to verify that pre-twisted ribbons do not fail when they are bent and used as deployable structural systems. Here, we only consider twisted ribbons as building blocks for our structures. However, it could be possible to include ribbons with different deployability attributes, e.g., axial extension, to create structures featuring more complex deformation patterns.

Acknowledgments

This research was carried out at the California Institute of Technology and the Jet Propulsion Laboratory under a contract with the National Aeronautics and Space Administration, and funded through the President's and Director's Fund Program. Reference herein to any specific commercial product, process, or service by trade name, trademark, manufacturer, or otherwise, does not constitute or imply its endorsement by the United States Government or the Jet Propulsion Laboratory, California Institute of Technology. P.C. and C.D. acknowledge support from the Foster and Coco Stanback Space Innovation Fund. This work was also supported by a NASA Space Technology Research Fellowship to C.M. We thank Michael Mello for helping with material characterization and for fruitful discussions. We thank Basile Audoly and Paolo Ermanni for helpful suggestions, and Brian Ramirez, Sharan Injeti, Hao Zhou, Cristina Naify, and Giordano Bellucci for useful discussions.

Permissions

This chapter was previously published in the Journal of the Mechanics and Physics of Solids [70]. Permission from Elsevier is not required for inclusion in this thesis.

References

[1] Z. You and S. Pellegrino. Foldable bar structures. *International Journal of Solids and Structures*, 34(15):1825–1847, 1997. ISSN 0020-7683. doi: 10.1016/S0020-7683(96)00125-4.

[2] S. Pellegrino. *Deployable Structures*. Springer Vienna, 2001. doi: 10.1007/978-3-7091-2584-7.

[3] Z. You and Y. Chen. *Motion Structures: Deployable Structural Assemblies of Mechanisms*. Spon Press, 2012. doi: 10.1201/9781482266610.

[4] G. E. Fenci and N. G. R. Currie. Deployable structures classification: A review. *International Journal of Space Structures*, 32(2):112–130, 2017. doi: 10.1177/0266351117711290.

[5] S. Guest and S. Pellegrino. Inextensional wrapping of flat membranes. In *Structural Morphology / Morphologie Structurale, Proceedings of the First International Seminar on Structural Morphology*, pages 203–215, 1992.

[6] M. Schenk and S. D. Guest. Geometry of miura-folded metamaterials. *Proceedings of the National Academy of Sciences of the United States of America*, 110(9):3276–3281, 2013. doi: 10.1073/pnas.1217998110.

[7] E. T. Filipov, T. Tachi, and G. H. Paulino. Origami tubes assembled into stiff, yet reconfigurable structures and metamaterials. *Proceedings of the National Academy of Sciences of the United States of America*, 112(40):12321–12326, 2015. doi: 10.1073/pnas.1509465112.

[8] D. M. Sussman, Y. Cho, T. Castle, X. Gong, E. Jung, S. Yang, and R. D. Kamien. Algorithmic lattice kirigami: A route to pluripotent materials. *Proceedings of the National Academy of Sciences of the United States of America*, 112(24):7449–7453, 2015. doi: 10.1073/pnas.1506048112.

[9] R. M. Neville, F. Scarpa, and A. Pirrera. Shape morphing kirigami mechanical metamaterials. *Scientific Reports*, 6:31067, 2016. doi: 10.1038/srep31067.

[10] A. Rafsanjani and K. Bertoldi. Buckling-induced kirigami. *Physical Review Letters*, 118:084301, 2017. doi: 10.1103/PhysRevLett.118.084301.

[11] L. Howell. *Compliant Mechanisms*. Wiley, 2001.

[12] A. Ion, J. Frohnhofen, L. Wall, R. Kovacs, M. Alistar, J. Lindsay, P. Lopes, H-T. Chen, and P. Baudisch. Metamaterial mechanisms. In *Proceedings of the 29th Annual Symposium on User Interface Software and Technology*, UIST '16, pages 529–539, 2016. doi: 10.1145/2984511.2984540.

[13] M. Konaković, K. Crane, B. Deng, S. Bouaziz, D. Piker, and M. Pauly. Beyond developable: Computational design and fabrication with auxetic materials. *ACM Transactions on Graphics*, 35(4):89, 2016. doi: 10.1145/2897824.2925944.

[14] J. T. B. Overvelde, J. C. Weaver, C. Hoberman, and K. Bertoldi. Rational design of reconfigurable prismatic architected materials. *Nature*, 541:347–352, 2017. doi: 10.1038/nature20824.

[15] X. Shang, L. Liu, A. Rafsanjani, and D. Pasini. Durable bistable auxetics made of rigid solids. *Journal of Materials Research*, 33(3):300–308, 2018. doi: 10.1557/jmr.2017.417.

[16] M. Konaković-Luković, J. Panetta, K. Crane, and M. Pauly. Rapid deployment of curved surfaces via programmable auxetics. *ACM Transactions on Graphics*, 37(4):106, 2018. doi: 10.1145/3197517.3201373.

[17] P. Celli, C. McMahan, B. Ramirez, A. Bauhofer, C. Naify, D. Hofmann, B. Audoly, and C. Daraio. Shape-morphing architected sheets with non-periodic cut patterns. *Soft Matter*, 14:9744–9749, 2018. doi: 10.1039/C8SM02082E.

[18] S. Kamrava, R. Ghosh, J. Xiong, S. M. Felton, and A. Vaziri. Origami-equivalent compliant mechanism. *Applied Physics Letters*, 115(17):171904, 2019. doi: 10.1063/1.5115790.

[19] S. Schleicher, J. Lienhard, S. Poppinga, T. Speck, and J. Knippers. A methodology for transferring principles of plant movements to elastic systems in architecture. *Computer-Aided Design*, 60:105–117, 2015. ISSN 0010-4485. doi: 10.1016/j.cad.2014.01.005. Material Ecology.

[20] K. A. Seffen and S. Pellegrino. Deployment dynamics of tape springs. *Proceedings of the Royal Society of London. Series A: Mathematical, Physical and Engineering Sciences*, 455(1983):1003–1048, 1999. doi: 10.1098/rspa.1999.0347.

[21] M. G. Walker and K. A. Seffen. The flexural mechanics of creased thin strips. *International Journal of Solids and Structures*, 167:192–201, 2019. doi: https://doi.org/10.1016/j.ijsolstr.2019.03.016.

[22] M. Sakovsky and S. Pellegrino. Closed cross-section dual-matrix composite hinge for deployable structures. *Composite Structures*, 208:784–795, 2019. doi: 10.1016/j.compstruct.2018.10.040.

[23] L. H. Dudte, E. Vouga, T. Tachi, and L. Mahadevan. Programming curvature using origami tessellations. *Nature Materials*, 15:583–588, 2016. doi: 10.1038/nmat4540.

[24] S. J. P. Callens and A. A. Zadpoor. From flat sheets to curved geometries: Origami and kirigami approaches. *Materials Today*, 21(3):241–264, 2018. doi: 10.1016/j.mattod.2017.10.004.

[25] J. W. Boley, W. M. van Rees, C. Lissandrello, M. N. Horenstein, R. L. Truby, A. Kotikian, J. A. Lewis, and L. Mahadevan. Shape-shifting structured lattices via multimaterial 4d printing. *Proceedings of the National Academy of Sciences*, 116(42):20856–20862, 2019. doi: 10.1073/pnas.1908806116.

[26] R. Guseinov, C. McMahan, J. Pérez, C. Daraio, and B. Bickel. Programming temporal morphing of self-actuated shells. *Nature Communications*, 11(1): 1–7, 2020. doi: 10.1038/s41467-019-14015-2.

[27] M. Arya, N. Lee, and S. Pellegrino. Crease-free biaxial packaging of thick membranes with slipping folds. *International Journal of Solids and Structures*, 108:24–39, 2017. doi: 10.1016/j.ijsolstr.2016.08.013.

[28] J. A. Harris and G. J. McShane. Metallic stacked origami cellular materials: Additive manufacturing, properties, and modelling. *International Journal of Solids and Structures*, 2019. doi: 10.1016/j.ijsolstr.2019.09.007.

[29] S. H. Chen, K. C. Chan, D. X. Han, L. Zhao, and F. F. Wu. Programmable super elastic kirigami metallic glasses. *Materials & Design*, 169:107687, 2019. doi: 10.1016/j.matdes.2019.107687.

[30] A. A. Deleo, J. O'Neil, H. Yasuda, M. Salviato, and J. Yang. Origami-based deployable structures made of carbon fiber reinforced polymer composites. *Composites Science and Technology*, 191:108060, 2020. doi: 10.1016/j.compscitech.2020.108060.

[31] C. McHale, D. A. Hadjiloizi, R. Telford, and P. M. Weaver. Morphing composite cylindrical lattices: Enhanced modelling and experiments. *Journal of the Mechanics and Physics of Solids*, page 103779, 2019. doi: 10.1016/j.jmps.2019.103779.

[32] G. Knott and A. Viquerat. Helical bistable composite slit tubes. *Composite Structures*, 207:711–726, 2019. doi: 10.1016/j.compstruct.2018.09.045.

[33] I. L. Delimont, S. P. Magleby, and L. L. Howell. Evaluating compliant hinge geometries for origami-inspired mechanisms. *Journal of Mechanisms and Robotics*, 7(1):011009, 2015. doi: 10.1115/1.4029325.

[34] T. G. Nelson, A. Avila, L. L. Howell, J. L. Herder, and D. Farhadi Machekposhti. Origami-inspired sacrificial joints for folding compliant mechanisms. *Mechanism and Machine Theory*, 140:194–210, 2019. doi: 10.1016/j.mechmachtheory.2019.05.023.

[35] Y. Morigaki, H. Wada, and Y. Tanaka. Stretching an elastic loop: Crease, helicoid, and pop out. *Physical Review Letters*, 117:198003, 2016. doi: 10.1103/PhysRevLett.117.198003.

[36] A. Gillman, G. Wilson, K. Fuchi, D. Hartl, A. Pankonien, and P. Buskohl. Design of soft origami mechanisms with targeted symmetries. *Actuators*, 8 (1):3, 2018. doi: 10.3390/act8010003.

[37] E. M. Mockensturm. The elastic stability of twisted plates . *Journal of Applied Mechanics*, 68(4):561–567, 2000. doi: 10.1115/1.1357517.

[38] S. Zhao, S. Zhang, Z. Yao, and L. Zhang. Equilibrium conformation of polymer chains with noncircular cross section. *Physical Review E*, 74:032801, 2006. doi: 10.1103/PhysRevE.74.032801.

[39] S. Cranford and M. J. Buehler. Twisted and coiled ultralong multilayer graphene ribbons. *Modelling and Simulation in Materials Science and Engineering*, 19(5):054003, 2011. doi: 10.1088/0965-0393/19/5/054003.

[40] A. P. Korte, E. L. Starostin, and G. H. M. van der Heijden. Triangular buckling patterns of twisted inextensible strips. *Proceedings of the Royal Society A: Mathematical, Physical and Engineering Sciences*, 467(2125):285–303, 2011. doi: 10.1098/rspa.2010.0200.

[41] O. O. Kit, T. Tallinen, L. Mahadevan, J. Timonen, and P. Koskinen. Twisting graphene nanoribbons into carbon nanotubes. *Physical Review B*, 85:085428, 2012. doi: 10.1103/PhysRevB.85.085428.

[42] J. Chopin and A. Kudrolli. Helicoids, wrinkles, and loops in twisted ribbons. *Physical Review Letters*, 111:174302, 2013. doi: 10.1103/PhysRevLett.111.174302.

[43] S. Armon, H. Aharoni, M. Moshe, and E. Sharon. Shape selection in chiral ribbons: from seed pods to supramolecular assemblies. *Soft Matter*, 10:2733–2740, 2014. doi: 10.1039/C3SM52313F.

[44] M. A. Dias and B. Audoly. "Wunderlich, Meet Kirchhoff": A general and unified description of elastic ribbons and thin rods. *Journal of Elasticity*, 119 (1):49–66, 2015. doi: 10.1007/s10659-014-9487-0.

[45] J. Boddapati, S. Mohanty, and R. K. Annabattula. An analytical model for shape morphing through combined bending and twisting in piezo composites. *Mechanics of Materials*, 2020. ISSN 0167-6636. doi: 10.1016/j.mechmat.2020.103350.

[46] T. Yu and J. A. Hanna. Bifurcations of buckled, clamped anisotropic rods and thin bands under lateral end translations. *Journal of the Mechanics and Physics of Solids*, 122:657 – 685, 2019. ISSN 0022-5096. doi: 10.1016/j.jmps.2018.01.015.

[47] Y. Zhang, Z. Yan, K. Nan, D. Xiao, Y. Liu, H. Luan, H. Fu, X. Wang, Q. Yang, J. Wang, W. Ren, H. Si, F. Liu, L. Yang, H. Li, J. Wang, X. Guo, H. Luo, L. Wang, Y. Huang, and J. A. Rogers. A mechanically driven form of kirigami as a route to 3D mesostructures in micro/nanomembranes. *Proceedings of the National Academy of Sciences of the United States of America*, 112(38): 11757–11764, 2015. doi: 10.1073/pnas.1515602112.

[48] Y. Liu, Z. Yan, Q. Lin, X. Guo, M. Han, K. Nan, K-C. Hwang, Y. Huang, Y. Zhang, and J. A. Rogers. Guided formation of 3D helical mesostructures by mechanical buckling: Analytical modeling and experimental validation. *Advanced Functional Materials*, 26(17):2909–2918, 2016. doi: 10.1002/adfm.201505132.

[49] Y. Shi, F. Zhang, K. Nan, X. Wang, J. Wang, Y. Zhang, Y. Zhang, H. Luan, K-C. Hwang, Y. Huang, J. A. Rogers, and Y. Zhang. Plasticity-induced origami for assembly of three dimensional metallic structures guided by compressive buckling. *Extreme Mechanics Letters*, 11:105–110, 2017. doi: 10.1016/j.eml.2016.11.008.

[50] H. Fu, K. Nan, W. Bai, W. Huang, K. Bai, L. Lu, C. Zhou, Y. Liu, F. Liu, J. Wang, M. Han, Z. Yan, H. Luan, Y. Zhang, Y. Zhang, J. Zhao, X. Cheng, M. Li, J. W. Lee, Y. Liu, D. Fang, X. Li, Y. Huang, Y. Zhang, and J. A. Rogers. Morphable 3D mesostructures and microelectronic devices by multistable buckling mechanics. *Nature Materials*, 17:268–276, 2018. doi: 10.1038/s41563-017-0011-3.

[51] X. Guo, X. Wang, D. Ou, J. Ye, W. Pang, Y. Huang, J. Rogers, and Y. Zhang. Controlled mechanical assembly of complex 3D mesostructures and strain sensors by tensile buckling. *NPJ Flexible Electronics*, 2:14, 2018. doi: 10.1038/s41528-018-0028-y.

[52] J. I. Lipton, R. MacCurdy, Z. Manchester, L. Chin, D. Cellucci, and D. Rus. Handedness in shearing auxetics creates rigid and compliant structures. *Science*, 360(6389):632–635, 2018. doi: 10.1126/science.aar4586.

[53] Y. Zhang, Q. Wang, M. Tichem, and F. van Keulen. Design and characterization of multi-stable mechanical metastructures with level and tilted stable configurations. *Extreme Mechanics Letters*, page 100593, 2019. doi: 10.1016/j.eml.2019.100593.

[54] C. Aza, A. Pirrera, and M. Schenk. Multistable morphing mechanisms of Nonlinear Springs. *Journal of Mechanisms and Robotics*, 11(5):051014, 2019. doi: 10.1115/1.4044210.

[55] C. T. Nguyen, D. T. Ho, S. T. Choi, Chun D-M., and S. Y. Kim. Pattern transformation induced by elastic instability of metallic porous structures. *Computational Materials Science*, 157:17–24, 2019. doi: 10.1016/j.commatsci.2018.10.023.

[56] E. R. Homer, M. B. Harris, S. A. Zirbel, J. A. Kolodziejska, H. Kozachkov, B. P. Trease, J-P. C. Borgonia, G. S. Agnes, L. L. Howell, and D. C. Hofmann. New methods for developing and manufacturing compliant mechanisms utilizing bulk metallic glass. *Advanced Engineering Materials*, 16(7):850–856, 2014. doi: 10.1002/adem.201300566.

[57] M. Telford. The case for bulk metallic glass. *Materials Today*, 7(3):36–43, 2004. doi: 10.1016/S1369-7021(04)00124-5.

[58] M. F. Ashby and A. L. Greer. Metallic glasses as structural materials. *Scripta Materialia*, 54(3):321–326, 2006. doi: 10.1016/j.scriptamat.2005.09.051.

[59] J. J. Kruzic. Bulk metallic glasses as structural materials: A review. *Advanced Engineering Materials*, 18(8):1308–1331, 2016. doi: 10.1002/adem.201600066.

[60] J. Schroers. Processing of bulk metallic glass. *Advanced Materials*, 22(14):1566–1597, 2010. doi: 10.1002/adma.200902776.

[61] A. Inoue, T. Zhang, N. Nishiyama, K. Ohba, and T. Masumoto. Preparation of 16 mm diameter rod of amorphous $Zr_{65}Al_{7.5}Ni_{10}Cu_{17.5}$ alloy. *Materials Transactions, JIM*, 34(12):1234–1237, 1993. doi: 10.2320/matertrans1989.34.1234.

[62] P. Bordeenithikasem, Y. Shen, H-L. Tsai, and D. C. Hofmann. Enhanced mechanical properties of additively manufactured bulk metallic glasses produced through laser foil printing from continuous sheetmetal feedstock. *Additive Manufacturing*, 19:95–103, 2018. doi: 10.1016/j.addma.2017.11.010.

[63] J. Blaber, B. Adair, and A. Antoniou. Ncorr: Open-source 2d digital image correlation matlab software. *Experimental Mechanics*, 55:1105–1122, 2015. doi: 10.1007/s11340-015-0009-1.

[64] A. E. Green and G. I. Taylor. The equilibrium and elastic stability of a thin twisted strip. *Proceedings of the Royal Society of London. Series A - Mathematical and Physical Sciences*, 154(882):430–455, 1936. doi: 10.1098/rspa.1936.0061.

[65] A. E. Green and G. I. Taylor. The elastic stability of a thin twisted strip. *Proceedings of the Royal Society of London. Series A - Mathematical and Physical Sciences*, 161(905):197–220, 1937. doi: 10.1098/rspa.1937.0141.

[66] E. M. Mockensturm. *On the finite twisting of translating plates*. PhD thesis, University of California, Berkeley, 1998.

[67] E. M. Mockensturm and C. D. Mote. Steady motions of translating, twisted webs. *International Journal of Non-Linear Mechanics*, 34(2):247–257, 1999. doi: 10.1016/S0020-7462(98)00020-1.

[68] F. I. Niordson. *Shell Theory*. Elsevier, 1985.

[69] P. M. Naghdi. Finite deformation of elastic rods and shells. In D. E. Carlson and R. T. Shield, editors, *Proceedings of the IUTAM Symposium on Finite Elasticity*, 1982. ISBN 978-94-009-7538-5.

[70] P. Celli, A. Lamaro, C. McMahan, P. Bordeenithikasem, D.C. Hofmann, and C. Daraio. Compliant morphing structures from twisted bulk metallic glass ribbons. *Journal of the Mechanics and Physics of Solids*, 145:104129, 2020.

Chapter 3

SHAPE-MORPHING ARCHITECTED SHEETS WITH NON-PERIODIC CUT PATTERNS

P. Celli, C. McMahan, B. Ramirez, A. Bauhofer, C. Naify, D. Hofmann, B. Audoly, and C. Daraio. Shape-morphing architected sheets with non-periodic cut patterns. *Soft Matter*, 14(48):9744–9749, 2018. doi: 10.1039/C8SM02082E.
C.M. participated in the design, fabrication, modeling, and testing of the architected sheets, and in writing and revising the manuscript.

Chapter preamble

Following the discussion on periodically patterned ribbon elements in the previous chapter, we now turn our attention to structured media composed of patterns of non-uniform unit cells. This chapter serves as an introduction to this class of structured media and provides a design paradigm for inducing in-plane kinematic incompatibilities that lead to the out-of-plane buckling of these elastic sheets. A more thorough mechanical modeling effort is presented in Chapter 4, where an effective continuum model is constructed to capture the buckling behavior of these systems.

Chapter abstract

Structuring geometrical features in a two-dimensional elastic sheet, which buckles in response to external actuation, allows faster and more scalable fabrication of three-dimensional objects. Here, we investigate the out-of-plane shape morphing capabilities of single-material elastic sheets with architected cut patterns. The sheets are laser-cut into an array of tiles connected by flexible hinges, which enable large deformations with small applied forces. We demonstrate that a non-periodic cut pattern can make a sheet buckle into selectable three-dimensional shapes, such as domes or patterns of wrinkles, when pulled at specific boundary points. These global buckling modes are observed in experiments, predicted by numerical simulations, and rationalized by a kinematic analysis that highlights the role of the geometric frustration arising from non-periodicity. The study focuses initially on elastic sheets, and is later extended to sheets made of elastic-plastic materials, which can retain their shape upon load removal. Our results provide a novel method for obtaining

three-dimensional objects from initially-flat sheets by the application of tensile loads.

3.1 Introduction

Imparting elastic sheets with a mesoscale architecture by folding [1, 2], perforating [3–5], or patterning them [6–8], enables the creation of materials with unusual characteristics, such as extreme extensibility [9], deployability [10, 11], and auxeticity [12]. These properties can be leveraged to design sheets that morph into complex three-dimensional objects. For example, origami sheets can be turned into nearly-arbitrary shapes [13, 14], but are typically challenging to fold [15] or actuate [16–18]. Patterned elastomeric sheets [6, 19], bilayers [20], and sheets with smart hinges [21–23] can morph into three-dimensional surfaces via non-mechanical stimuli, but their fabrication is complex. Ribbon- and membrane-like flat mesostructures, made of elastic or brittle materials, can buckle out of plane and produce three-dimensional geometries when subject to mechanical actuation in compression [24, 25] or tension [26, 27]. However, compressive actuation requires pre-stretched substrates and non-trivial assembly processes, and the geometries obtained via tensile loads are limited to thin, arch-like features.

In contrast to shape-morphing origami or bilayer films, sheets with architected cut patterns can be easily fabricated via subtractive technologies. Their out-of-plane deformation can be triggered by manual forming [28, 29], via the actuation of smart hinges [30], or by applying compressive boundary loads [25, 31, 32]. Recently, it has been demonstrated that sheets with periodic perforations can also buckle locally in tension [27, 33–36], producing crease patterns that can be used for soft robotic locomotion [37] or as coatings for sunlight control [36]. However, since these buckling modes take place at the scale of the unit cells, the size of the transverse features they can produce cannot significantly exceed the typical length of the cuts. Non-periodic cut patterns have been seldom explored in this context: non-periodicity is known to lead to geometric frustration [38, 39], i.e., the desired deformation mode is impeded by the geometric incompatibility between neighboring cells. In the few cases where non-periodic cut patterns have been explored, frustration has been avoided [40–42]. In particular, the effect of geometric frustration on the out-of-plane deformations of thin architected sheets has been ignored so far.

In this work, we study the tensile response of elastic sheets featuring non-periodic cut patterns, and intentionally leverage geometric frustration to induce controllable, global shape changes via buckling. In most of our designs, we use point-like

boundary loads that induce large deformations in selected sub-domains of the sheets. The inhomogeneous distribution of strains results into global buckling modes that make the sheets bend out of plane: we use this principle to obtain both dome-like surfaces, and patterns of wrinkles confined to pre-determined regions of the sheets. We show that the buckling pattern can be changed by applying the load at different points. We also extend the method to initially cylindrical—rather than planar—sheets and to cut patterns arranged into non-rectangular grids, and we demonstrate the formation of persistent three-dimensional surfaces by using sheets made of elastic-plastic materials [35].

3.2 Design paradigm

We start by analyzing a simple cut pattern featuring a large-amplitude, planar mode of deformation. A 108-by-108 mm, 1.55 mm-thick natural rubber sheet is laser-cut [43] following a pattern of (*i*) diamond-shaped cut-outs and (*ii*) straight cut lines ending close to the diamonds' vertices. These two types of cuts are visible in black in the insets of Fig. 3.1. The result is an array of 18×18 rhomboid tiles, visible in

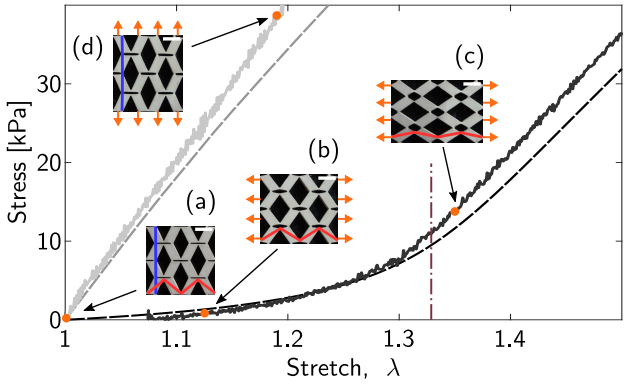

Figure 3.1: Uniaxial tension test of a periodic sheet whose undeformed geometry is shown in (a). The plot in the background shows the loading curve when the applied tension is either along the horizontal direction (black lines) or along the vertical direction (grey lines), both from experiments (solid lines) and from finite element simulations (dashed lines). The vertical dash-dot line shows the maximum stretch predicted by the kinematic analysis, where a geometric-to-elastic transition takes place. Insets (a-d) show snapshots of a 4×4-tile portion of the sheet at different levels of deformation (scale bar is 6 mm). The red and blue overlaid lines are obtained by joining the diagonals in a particular row and column of tiles, respectively, and are used to predict the maximum stretch by a kinematic analysis.

grey in the pictures, connected by thin hinges. The experimental traction curves (Fig. 3.1) for unaxial tension reveal a strongly anisotropic and non-linear behavior (see Appendix B.1 for more details). When the tension is applied in the in-plane direction referred to as the x-direction (horizontal direction in the figure, black lines)

the response is initially compliant up to a stretch value $\lambda \sim 1.3$, and then becomes much stiffer. When the tension is applied in the perpendicular y-direction (vertical direction in the figure, gray lines), the response is stiff and approximately linear for the range of stretch investigated; no initial compliant regime is observed. We simulated the mechanical response of the architected sheet numerically as well, by meshing a rectangular domain with periodic cut-outs, and by using a finite-element (FE) model for a neo-Hookean material in plane strain (the plane strain assumption is applicable as the in-plane width of the hinges is smaller than their out-of-plane thickness, see Appendix B.2). The traction curves predicted by simulation are in good agreement with the experiments (Fig. 3.1).

The salient features of the loading curves can be explained by a kinematic analysis, in which the sheet is modeled as an array of rigid tiles connected by pin joints. Such networks can feature modes of deformation known as *mechanisms* [44], which are mapped to low-energy configurations of the elastic sheet involving bending and shear [5] at the joints only. A mechanism relies on the coordinated rotation of the tiles in response to applied tension (Fig. 3.1, Appendix B.3 and [45, 46]). In particular, the maximum stretch attainable via a mechanism can be derived by a geometric argument, considering the broken lines connecting the diagonals of the tiles in a given row or column, see red and blue lines overlaid in Fig. 3.1(a). As the length of these lines is preserved by mechanisms, the maximum stretch in the x or y direction is attained when the corresponding line is fully stretched out. For the cut design used in Fig. 3.1, this maximum stretch is calculated by a geometric argument as $\lambda_x = 1.33$ in the x-direction, as indicated by the dash-dotted line in the figure; this is indeed where the compliant-to-stiff transition is observed in the experimental and numerical traction curves. For this particular cut design, the line of diagonals in the y-direction is already straight in the initial configuration, see the blue line in Fig. 3.1(a), meaning that no mechanism can be activated when the tension is applied in the y-direction; this is consistent with the absence of an initial compliant regime in the grey curves in Fig. 3.1.

Next, we introduce a family of periodic cut patterns parameterized by design variables. Our generic pattern, sketched in Fig. 3.2(a), is obtained by cutting out diamonds with alternating directions, centered at the nodes of a grid of $N_x \times N_y$ rectangles, each with dimensions $l_x \times l_y$. The two families of diamonds are assigned different widths, w_x and w_y, so that the previous design comprising line-cuts can be recovered as the special case $w_y = 0$. The length of the diamonds is such that a

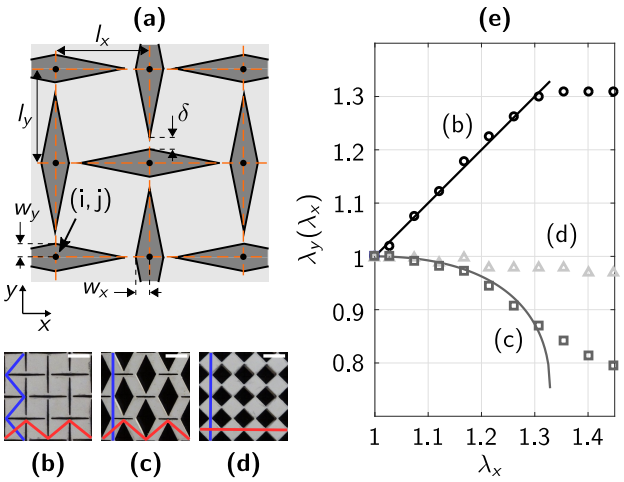

Figure 3.2: Unit cell generalization. (a) Sketch of a generic periodic architecture parameterized by design variables. (b-d) Digital images of details of three periodic undeformed specimens, corresponding to different values of (w_x, w_y) listed in Appendix B.4; scale bar is 6 mm. (e) Transverse stretch λ_y as a function of the axial stretch λ_x for simple traction along the x-direction, and for the same set of specimens: experiments (open symbols) versus predictions of the kinematic model (solid curves).

gap (hinge) of width δ is present between adjacent diamonds. Three examples of periodic geometries cut out in natural rubber sheets are shown in Fig. 3.2(b-d), for $N_x = N_y = 18$, $l_x = l_y = 6\,\text{mm}$, and out-of-plane thickness $t = 1.55\,\text{mm}$; note that the shape of the tiles, shown in light grey, can now vary from rhomboid to square. Experimental traction curves for three particular cutting patterns are plotted in the plane of stretches (λ_x, λ_y) in Fig. 3.2(e), and compared with the predictions of the kinematic analysis (see Appendix B.3 for a detailed derivation),

$$\lambda_y\,(\lambda_x) = \frac{d_v}{l_y}\,\sin\left[\gamma + \arccos\left(\frac{\lambda_x l_x}{d_h}\right)\right], \tag{3.1}$$

where $d_h = \sqrt{l_x^2 + [l_y - 2w_y - \delta]^2}$ and $d_v = \sqrt{l_y^2 + [l_x - 2w_x - \delta]^2}$ are the lengths of the diagonals of a tile, and γ is the angle between these diagonals. The design variables have a strong influence on tension tests. The cut pattern in Fig. 3.2(b) gives rise to an auxetic mechanism [12] having a negative Poisson's ratio $\nu = -1$; this is reflected by the positive slope of the black curve in Fig. 3.2(d). By contrast, the mechanism associated with the cut pattern in Fig. 3.1 and 3.2(c) has a positive Poisson's ratio. For both these cut patterns, the kinematic model in Equation (3.1) provides an accurate prediction of the transverse stretch $\lambda_y(\lambda_x)$ up to around $\lambda_x \sim 1.3$, where the joints start to stretch, see Fig. 3.2(e). Finally, the cut pattern in Fig. 3.2(d) is stiff when loaded in tension since the maximum stretch $\lambda_x = 1$ predicted by the kinematic analysis is attained in the undeformed configuration (the

diagonals of adjacent tiles are aligned). The effect of the design parameters δ and t on the in-plane response is investigated in Appendix B.5.

3.3 Non-periodicity

Having analyzed a family of *periodic* cut patterns parameterized by the design variables w_x and w_y, we now investigate *non-uniform* designs, obtained by specifying arbitrary values of w_x and w_y in every cell of a rectangular grid; the cell size $l_x \times l_y$ is uniform throughout the sheet. Upon deformation, we expect that every unit cell of these non-periodic sheets will try to follow the mechanism corresponding to the local values of w_x and w_y, as described by Equation (3.1). However, mechanisms corresponding to neighboring cells are not geometrically compatible in general (see Appendix B.3). Thus, we investigate how this incompatibility is resolved at the global level by buckling. As a first example, we consider a cut geometry where w_x is constant while w_y varies sinusoidally in the y-direction, see Fig. 3.3(a1), using a 1.55 mm-thick natural rubber sheet with $N_x = 36$, $N_y = 18$, $l_x = 6\,\text{mm}$, $l_y = 2\,l_x$. This choice of maps for w_x and w_y ensures that the top and bottom parts of the sheet are virtually undeformable, see the inset in Fig. 3.3(a1), while the center is highly stretchable. When the sheet is stretched by point-like forces, as in Fig. 3.3(a2), the strong geometric incompatibility between the center and the edges produces a global buckling mode spanning the central region. Note that this buckling instability takes place in tension, unlike in the classical Euler buckling. For a given cut pattern, the dependence of the buckled configuration on the sheet's thickness t is similar to what can be expected from the classical theory of plates without cut-outs, see Appendix B.6 for details. As t increases, the onset of buckling occurs at larger critical stretches, consistent with the fact that the effective bending modulus is larger. An increased thickness also yields larger deflections and makes the buckling pattern spread further away from the the line of application of the force.

More complex buckling patterns can be obtained by letting both w_x and w_y vary along the sheet, either smoothly or abruptly. As an example, we study a sheet comprising two stretchable and auxetic islands surrounded by unstretchable and non-auxetic regions, see Fig. 3.3(b1). This geometry induces strong geometric incompatibilities: when the sheet is stretched, the auxetic islands tend to swell in the transverse direction. This swelling is prevented by the surrounding stiff regions, and compressive in-plane stress appears, as confirmed by the FE simulations in Fig. 3.3(b2). Ultimately, this leads to a buckling pattern made up of two domes localized on the auxetic islands, see Fig. 3.3(b2). As another example, we study the

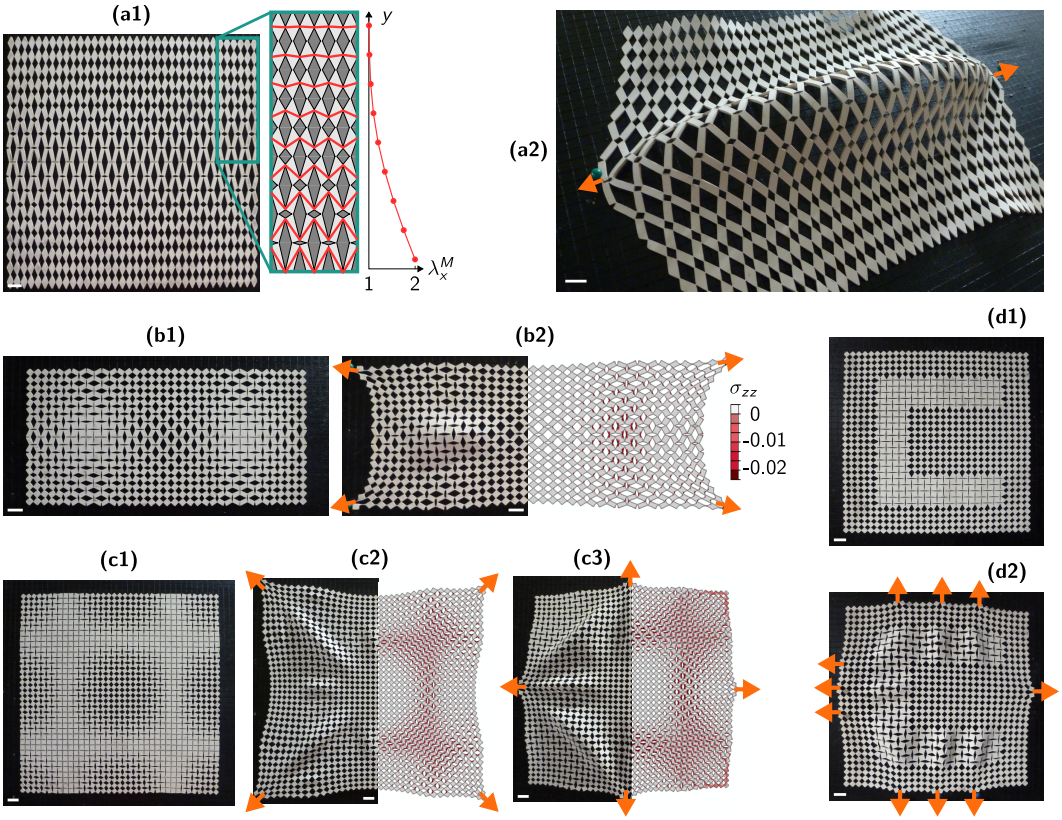

Figure 3.3: Out-of-plane morphing of sheets with non-periodic cut patterns. (a1) Cut pattern with gradient in the y direction. The inset to the right of the undeformed configuration highlights the tile diagonals (in red), that are inextensible by the local kinematic analysis, as well as a plot of the corresponding maximum stretch $\lambda_x^M(y)$: this shows that the sheet is highly stretchable in the center, but inextensible along its upper and lower edges. (a2) A dome shape obtained when the sheet is pulled from two boundary points. (b1) Undeformed configuration of a specimen featuring two soft and auxetic regions in its interior, which give rise to two localized bumps upon pulling at the four corners (b2). (c1-c3) Undeformed and deformed configurations of another specimen, highlighting the influence of the boundary loading on the pattern of wrinkles. The right-halves of (b2), (c2) and (c3) are the stress maps of $\sigma_{zz} = \nu(\sigma_{xx} + \sigma_{yy})$ (under the plane strain assumption); negative values of the average in-plane stress $(\sigma_{xx} + \sigma_{yy})$ are taken as an indicator for buckling. (d1-d2) Shaping wrinkles: a C-shaped soft and auxetic region is embedded in a sheet by a suitable choice of the maps of w_x and w_y in the reference configuration (d1). The wrinkles localize upon the application of boundary loads (d2). The orange arrows indicate the boundary loads. Scale bar: 12 mm.

response of a sheet with a more complex cut pattern obtained by varying both w_x and w_y sinusoidally along both the horizontal and vertical directions. The experimental results in (c2) and (c3), corresponding to actuation at the structures' corners or boundary mid-points, respectively, show markedly different wrinkle patterns, thereby highlighting the role of the applied force in selecting the pattern. Finally, in

Fig. 3.3(d1-d2), we show the response of a sheet featuring a C-shaped auxetic region separated from the rest of the sheet, which is unstretchable, by a sharp boundary. In this case, pulling the specimen as indicated by the orange arrows leads to wrinkles localized along the C-like domain. The wavelength of the wrinkles is comparable to the width of the C-shaped domain. These examples show that the buckling patterns can be tailored by engineering the sheet's local properties through the maps of w_x and w_y, and by choosing the points of application of the load.

Our approach can be extended to solids of revolution. For example, we pattern a sheet by varying w_x and w_y in vertical stripes, alternating regions of auxetic and not-auxetic behavior. We then roll the sheet, forming a tube, and pull on its ends. The applied tractions force the tube to expand at prescribed, auxetic sections and to contract at others [47], see Fig. 3.4(a). Stretching the tube further produces

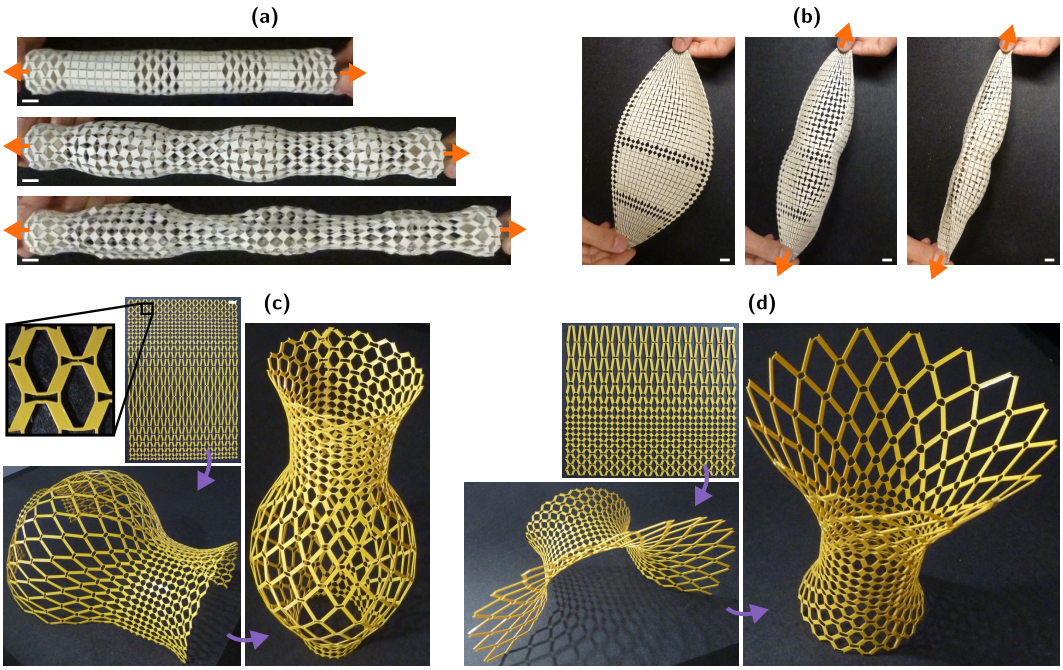

Figure 3.4: Cylindrical structures and extension to plastic sheets. (a) An architected tube can expand or contract radially based on an initial stripe pattern. Beyond a critical tensile load, an azimuthal buckling pattern appears in the expanded regions. (b) Petal-shaped specimen generated from a non-rectangular grid. This sheet morphs into a pea pod-shaped object when pulled from its ends. (c-d) Sculpting axisymmetric shapes from a sheet made of an elastic-plastic material; the shapes are obtained by using graded cut patterns and by stretching out the sheets locally by hand. Scale bars: 12 mm.

a non-axisymmetric buckling bifurcation, with an azimuthal wavelength roughly comparable to the stripes' width. Cut patterns can also be attached to non-Cartesian

grids, as illustrated in the example in Fig. 3.4(b), where the petal-like sheet closes up into a pea pod shape when pulled at its ends.

The design strategy is not limited to elastic materials such as rubber. Permanent three-dimensional shapes can be obtained by using an elastic-plastic material [35]. This requires modifying the hinge design to avoid breakage: the new design, shown in the insets in Fig. 3.4(c), was inspired by [48] and is discussed in Appendix B.7. The deformation of two sheets featuring the same initial cut pattern, one made of natural rubber and one made of stiff PETG are compared in Fig. B.12. While they feature a similar buckling pattern, the second sheet deforms irreversibly, leaving a permanent pattern after load removal. We leverage the elastic-plastic behavior to sculpt axisymmetric shapes out of a planar PETG sheet, see Fig. 3.4(c-d). As earlier with the tube, the cut patterns are graded along the axis, which allows us to select the radial expansion (hence the target radius) as a function of the axial coordinate. To obtain an even larger stretchability contrast, we use non-regular rectangular grids, i.e., we set $l_y(y)$ to take on larger values in the regions of large stretch. The irreversible deformations are obtained by stretching the sheet locally by hand, and a similar effect could be achieved using localized smart-material actuators or pressurized membranes. These structures are reminiscent of gridshells [49] and are easier to fabricate, especially at small scales.

3.4 Conclusions

In this work, we have demonstrated that geometric incompatibility can be leveraged to create three-dimensional objects from sheets with non-periodic cut-outs. By choosing the properties of the cuts locally, one can prescribe a map of maximum stretch, which is resolved when the sheet bends out of plane in response to boundary loads or local stretching. While the shapes we have obtained are relatively simple, these design principles could be extended to different families of mechanisms, and could be coupled to optimization and inverse-design strategies to obtain more complex shapes. Due to the flexibility of the fabrication process, which involves cutting mono-layer sheets, this approach could be used to produce three-dimensional structures at vastly different scales.

3.5 Materials and methods

Specimen fabrication. A Universal ILS9 120W laser cutter is used to create perforations. We mainly use 1.55 mm-thick natural rubber sheets (McMaster-Carr, item no. 8633K71), but some 3.1 mm- and 0.75 mm-thick ones were also used (Grainger,

items no. 1XWE5 and 8611K18). For the 1.55 mm-thick specimens, the machine is set to cut at 35% power and 5% speed, with an air assist flow rate of 100% to avoid burning the specimens. For the 3.1 mm-thick specimens, 45% power and 2.3% speed are selected. For the 0.75 mm-thick specimens, 30% power and 5% speed are selected. Since the laser beam has a finite cutting diameter, the hinges are not characterized by sharp corners but are de-facto beams having a finite length. The tube specimens are closed using double-sided tape glued to some tiles. PETG sheets (0.5 mm-thick) were perforated with the same laser cutter, with 3.0% power and 2.2% speed, and were also closed into surfaces of revolution using double-sided tape.

Material testing. Uniaxial tensile tests are conducted using an Instron ElectroPuls (Model E3000) system equipped with a 250 N load cell at a constant deformation rate of $2\,\mathrm{mm\,s^{-1}}$. The specimens are stretched by pulling on some of the hinges using a customized fixture which allows for lateral expansion or contraction of the sheets being pulled (see Appendix B.1). The tensile forces and displacements are measured with 1 mN and 5 μm accuracy, respectively, at an acquisition rate of 1 kHz. The force-displacement data obtained from the Instron WaveMatrix software is converted to stress-stretch data using the original sample dimensions. The data obtained is then subsampled to remove some of the noise (one every 10 measurements is kept). Finally, the stretch is adjusted to account for the self-weight elongation experienced by some specimens featuring a pronounced mechanism-like behavior along the direction parallel to the load.

Acknowledgements

This research was carried out at the California Institute of Technology and the Jet Propulsion Laboratory under a contract with the National Aeronautics and Space Administration, and funded through the President's and Director's Fund Program. This work is partially supported through the Foster and Coco Stanback Space Innovation Fund. We thank D. Pasini of McGill University for useful suggestions, A. Constantinescu of École Polytechnique, and members of C.D.'s research group at Caltech for their input and suggestions. We also thank B. Dominguez of Caltech for his assistance during laser cutting.

Permissions

This chapter was previously published in Soft Matter [50]. Permission from the Royal Society of Chemistry is not required for inclusion in this thesis.

References

[1] M. Schenk and S. D. Guest. Geometry of miura-folded metamaterials. *Proceedings of the National Academy of Sciences*, 110(9):3276–3281, 2013. doi: 10.1073/pnas.1217998110.

[2] J. L. Silverberg, A. A. Evans, L. McLeod, R. C. Hayward, T. Hull, C. D. Santangelo, and I. Cohen. Using origami design principles to fold reprogrammable mechanical metamaterials. *Science*, 345(6197):647–650, 2014. doi: 10.1126/science.1252876.

[3] T. Mullin, S. Deschanel, K. Bertoldi, and M. C. Boyce. Pattern transformation triggered by deformation. *Physical Review Letters*, 99:084301, 2007. doi: 10.1103/PhysRevLett.99.084301.

[4] D. M. Sussman, Y. Cho, T. Castle, X. Gong, E. Jung, S. Yang, and R. D. Kamien. Algorithmic lattice kirigami: A route to pluripotent materials. *Proceedings of the National Academy of Sciences*, 112(24):7449–7453, 2015. doi: 10.1073/pnas.1506048112.

[5] C. Coulais, C. Kettenis, and M. van Hecke. A characteristic length scale causes anomalous size effects and boundary programmability in mechanical metamaterials. *Nature Physics*, 14:40–44, 2017. doi: 10.1038/nphys4269.

[6] J. Kim, J. A. Hanna, M. Byun, C. D. Santangelo, and R. C. Hayward. Designing responsive buckled surfaces by halftone gel lithography. *Science*, 335(6073): 1201–1205, 2012. doi: 10.1126/science.1215309.

[7] Q. Ge, H. J. Qi, and M. L. Dunn. Active materials by four-dimension printing. *Applied Physics Letters*, 103(13):131901, 2013. doi: 10.1063/1.4819837.

[8] A. S. Gladman, E. A. Matsumoto, R. G. Nuzzo, L. Mahadevan, and J. A. Lewis. Biomimetic 4d printing. *Nature Materials*, 15:413–418, 2016. doi: 10.1038/nmat4544.

[9] Y. Tang and J. Yin. Design of cut unit geometry in hierarchical kirigami-based auxetic metamaterials for high stretchability and compressibility. *Extreme Mechanics Letters*, 12:77–85, 2017. doi: 10.1016/j.eml.2016.07.005.

[10] E. T. Filipov, T. Tachi, and G. H. Paulino. Origami tubes assembled into stiff, yet reconfigurable structures and metamaterials. *Proceedings of the National Academy of Sciences*, 112(40):12321–12326, 2015. doi: 10.1073/pnas.1509465112.

[11] J. T. B. Overvelde, J. C. Weaver, C. Hoberman, and K. Bertoldi. Rational design of reconfigurable prismatic architected materials. *Nature*, 541:347–352, 2017. doi: 10.1038/nature20824.

[12] J. N. Grima, V. Zammit, R. Gatt, A. Alderson, and K. E. Evans. Auxetic behaviour from rotating semi-rigid units. *Physica Status Solidi B*, 244(3): 866–882, 2007. doi: 10.1002/pssb.200572706.

[13] L. H. Dudte, E. Vouga, T. Tachi, and L. Mahadevan. Programming curvature using origami tessellations. *Nature Materials*, 15:583–588, 2016. doi: 10.1038/nmat4540.

[14] S. J. P. Callens and A. A. Zadpoor. From flat sheets to curved geometries: Origami and kirigami approaches. *Materials Today*, 21(3):241–264, 2018. doi: 10.1016/j.mattod.2017.10.004.

[15] E. D. Demaine and T. Tachi. Origamizer: A practical algorithm for folding any polyhedron. In *33rd International Symposium on Computational Geometry (SoCG 2017)*, volume 77, pages 34:1–34:16, 2017. doi: 10.4230/LIPIcs.SoCG.2017.34.

[16] E. Hawkes, B. An, N. M. Benbernou, H. Tanaka, S. Kim, E. D. Demaine, D. Rus, and R. J. Wood. Programmable matter by folding. *Proceedings of the National Academy of Sciences*, 107(28):12441–12445, 2010. doi: 10.1073/pnas.0914069107.

[17] M. Stern, M. B. Pinson, and A. Murugan. The complexity of folding self-folding origami. *Physical Review X*, 7:041070, 2017. doi: 10.1103/PhysRevX.7.041070.

[18] P. Plucinsky, B. A. Kowalski, T. J. White, and K. Bhattacharya. Patterning nonisometric origami in nematic elastomer sheets. *Soft Matter*, 14:3127–3134, 2018. doi: 10.1039/C8SM00103K.

[19] T. H. Ware, M. E. McConney, J. J. Wie, V. P. Tondiglia, and T. J. White. Voxelated liquid crystal elastomers. *Science*, 347(6225):982–984, 2015. doi: 10.1126/science.1261019.

[20] W. M. van Rees, E. Vouga, and L. Mahadevan. Growth patterns for shape-shifting elastic bilayers. *Proceedings of the National Academy of Sciences*, 114(44):11597–11602, 2017. doi: 10.1073/pnas.1709025114.

[21] S. M. Felton, M. T. Tolley, B. Shin, C. D. Onal, E. D. Demaine, D. Rus, and R. J. Wood. Self-folding with shape memory composites. *Soft Matter*, 9: 7688–7694, 2013. doi: 10.1039/C3SM51003D.

[22] J. H. Na, A. A. Evans, J. Bae, M. C. Chiappelli, C. D. Santangelo, R. J. Lang, T. C. Hull, and R. C. Hayward. Programming reversibly self-folding

origami with micropatterned photo-crosslinkable polymer trilayers. *Advanced Materials*, 27(1):79–85, 2014. doi: 10.1002/adma.201403510.

[23] S. Ahmed, Z. Ounaies, and M. Frecker. Investigating the performance and properties of dielectric elastomer actuators as a potential means to actuate origami structures. *Smart Materials and Structures*, 23(9):094003, 2014. doi: 10.1088/0964-1726/23/9/094003.

[24] S. Xu, Z. Yan, K. Jang, W. Huang, H. Fu, J. Kim, Z. Wei, M. Flavin, J. McCracken, R. Wang, A. Badea, Y. Liu, D. Xiao, G. Zhou, J. Lee, H. U. Chung, H. Cheng, W. Ren, A. Banks, X. Li, U. Paik, R. G. Nuzzo, Y. Huang, Y. Zhang, and J. A. Rogers. Assembly of micro/nanomaterials into complex, three-dimensional architectures by compressive buckling. *Science*, 347(6218):154–159, 2015. doi: 10.1126/science.1260960.

[25] Y. Zhang, Z. Yan, K. Nan, D. Xiao, Y. Liu, H. Luan, H. Fu, X. Wang, Q. Yang, J. Wang, W. Ren, H. Si, F. Liu, L. Yang, H. Li, J. Wang, X. Guo, H. Luo, L. Wang, Y. Huang, and J. A. Rogers. A mechanically driven form of kirigami as a route to 3D mesostructures in micro/nanomembranes. *Proceedings of the National Academy of Sciences*, 112(38):11757–11764, 2015. doi: 10.1073/pnas.1515602112.

[26] M. A. Dias, M. P. McCarron, D. Rayneau-Kirkhope, P. Z. Hanakata, D. K. Campbell, H. S. Park, and D. P. Holmes. Kirigami actuators. *Soft Matter*, 13:9087–9092, 2017. doi: 10.1039/C7SM01693J.

[27] X. Guo, X. Wang, D. Ou, J. Ye, W. Pang, Y. Huang, J. Rogers, and Y. Zhang. Controlled mechanical assembly of complex 3D mesostructures and strain sensors by tensile buckling. *NPJ Flexible Electronics*, 2:14, 2018. doi: 10.1038/s41528-018-0028-y.

[28] M. Konaković, K. Crane, B. Deng, S. Bouaziz, D. Piker, and M. Pauly. Beyond developable: Computational design and fabrication with auxetic materials. *ACM Transactions on Graphics*, 35(4):89, 2016. doi: 10.1145/2897824.2925944.

[29] F. Wang, X. Guo, J. Xu, Y. Zhang, and C. Q. Chen. Patterning curved three-dimensional structures with programmable kirigami designs. *Journal of Applied Mechanics*, 84(6):061007, 2017. doi: 10.1115/1.4036476.

[30] J. Cui, J. G. M. Adams, and Y. Zhu. Pop-up assembly of 3D structures actuated by heat shrinkable polymers. *Smart Materials and Structures*, 26(12):125011, 2017. doi: 10.1088/1361-665X/aa9552.

[31] R. M. Neville, F. Scarpa, and A. Pirrera. Shape morphing kirigami mechanical metamaterials. *Scientific Reports*, 6:31067, 2016. doi: 10.1038/srep31067.

[32] H. Fu, K. Nan, W. Bai, W. Huang, K. Bai, L. Lu, C. Zhou, Y. Liu, F. Liu, J. Wang, M. Han, Z. Yan, H. Luan, Y. Zhang, Y. Zhang, J. Zhao, X. Cheng, M. Li, J. W. Lee, Y. Liu, D. Fang, X. Li, Y. Huang, Y. Zhang, and J. A. Rogers. Morphable 3D mesostructures and microelectronic devices by multistable buckling mechanics. *Nature Materials*, 17:268–276, 2018. doi: 10.1038/s41563-017-0011-3.

[33] M. K. Blees, A. W. Barnard, P. A. Rose, S. P. Roberts, K. L. McGill, P. Y. Huang, A. R. Ruyack, J. W. Kevek, B. Kobrin, Muller D. A., and P. L. McEuen. Graphene kirigami. *Nature*, 524:204–207, 2015. doi: 10.1038/nature14588.

[34] T. C. Shyu, P. F. Damasceno, P. M. Dodd, A. Lamoreaux, L. Xu, M. Shlian, M. Shtein, S. C. Glotzer, and N. A. Kotov. A kirigami approach to engineering elasticity in nanocomposites through patterned defects. *Nature Materials*, 14: 785–789, 2015. doi: 10.1038/nmat4327.

[35] A. Rafsanjani and K. Bertoldi. Buckling-induced kirigami. *Physical Review Letters*, 118:084301, 2017. doi: 10.1103/PhysRevLett.118.084301.

[36] Y. Tang, G. Lin, S. Yang, Y. K. Yi, R. D. Kamien, and J. Yin. Programmable kiri-kirigami metamaterials. *Advanced Materials*, 29(10):1604262, 2017. doi: 10.1002/adma.201604262.

[37] A. Rafsanjani, Y. Zhang, B. Liu, S. M. Rubinstein, and K. Bertoldi. Kirigami skins make a simple soft actuator crawl. *Science Robotics*, 3(15), 2018. doi: 10.1126/scirobotics.aar7555.

[38] C. Coulais, E. Teomy, K. de Reus, Y. Shokef, and M. van Hecke. Combinatorial design of textured mechanical metamaterials. *Nature*, 535:529–532, 2016. doi: 10.1038/nature18960.

[39] R. Guseinov, E. Miguel, and B. Bickel. Curveups: Shaping objects from flat plates with tension-actuated curvature. *ACM Transactions on Graphics*, 36(4): 64, 2017. doi: 10.1145/3072959.3073709.

[40] Y. Cho, J-H. Shin, A. Costa, T. A. Kim, V. Kunin, J. Li, S. Y. Lee, S. Yang, H. N. Han, I-S. Choi, and D. J. Srolovitz. Engineering the shape and structure of materials by fractal cut. *Proceedings of the National Academy of Sciences*, 111(49):17390–17395, 2014. doi: 10.1073/pnas.1417276111.

[41] A. Ion, J. Frohnhofen, L. Wall, R. Kovacs, M. Alistar, J. Lindsay, P. Lopes, H-T. Chen, and P. Baudisch. Metamaterial mechanisms. In *UIST '16*, pages 529–539, 2016. ISBN 978-1-4503-4189-9. doi: 10.1145/2984511.2984540.

[42] M. J. Mirzaali, S. Janbaz, M. Strano, L. Vergani, and A. A. Zadpoor. Shape-matching soft mechanical metamaterials. *Scientific Reports*, 8:965, 2018. doi: 10.1038/s41598-018-19381-3.

[43] A. Rafsanjani and D. Pasini. Bistable auxetic mechanical metamaterials inspired by ancient geometric motifs. *Extreme Mechanics Letters*, 9:291–296, 2016. doi: 10.1016/j.eml.2016.09.001.

[44] S. Pellegrino and C.R. Calladine. Matrix analysis of statically and kinematically indeterminate frameworks. *International Journal of Solids and Structures*, 22(4):409–428, 1986. doi: 10.1016/0020-7683(86)90014-4.

[45] R. G. Hutchinson and N. A. Fleck. The structural performance of the periodic truss. *Journal of the Mechanics and Physics of Solids*, 54(4):756–782, 2006. doi: 10.1016/j.jmps.2005.10.008.

[46] V. Kapko, M. M. J. Treacy, M. F. Thorpe, and S. D. Guest. On the collapse of locally isostatic networks. *Proceedings of the Royal Society A*, 465(2111): 3517–3530, 2009. doi: 10.1098/rspa.2009.0307.

[47] J. Liu and Y. Zhang. Soft network materials with isotropic negative Poisson's ratios over large strains. *Soft Matter*, 14:693–703, 2018. doi: 10.1039/C7SM02052J.

[48] X. Shang, L. Liu, A. Rafsanjani, and D. Pasini. Durable bistable auxetics made of rigid solids. *Journal of Materials Research*, 33(3):300—-308, 2018. doi: 10.1557/jmr.2017.417.

[49] C. Baek, A. O. Sageman-Furnas, M. K. Jawed, and P. M. Reis. Form finding in elastic gridshells. *Proceedings of the National Academy of Sciences*, 115 (1):75–80, 2018. doi: 10.1073/pnas.1713841115.

[50] P. Celli, C. McMahan, B. Ramirez, A. Bauhofer, C. Naify, D. Hofmann, B. Audoly, and C. Daraio. Shape-morphing architected sheets with non-periodic cut patterns. *Soft Matter*, 14:9744–9749, 2018. doi: 10.1039/C8SM02082E.

Chapter 4

EFFECTIVE CONTINUUM MODELS FOR THE BUCKLING OF NON-PERIODIC ARCHITECTED SHEETS THAT DISPLAY QUASI-MECHANISM BEHAVIORS

C. McMahan, A. Akerson, P. Celli, B. Audoly, and C. Daraio. Effective continuum models for the buckling of non-periodic architected sheets that display quasi-mechanism behaviors. *arXiv*:2107.01704, 2021.
C.M. participated in the conception of the project, performed analytical modeling and experiments, and participated in conducting simulations, and in writing and revising the manuscript.

Chapter preamble

This chapter focuses on the construction of an effective continuum model for the structured media introduced in the previous chapter. This model captures the out-of-plane buckling instabilities that arise due to in-plane kinematic incompatibilities in non-periodic mesostructures and computes post-buckled equilibrium. The model is not included in an inverse design method for designing these buckling sheets. Chapter 5 will broach this topic for a different class of structured media.

Chapter abstract

In this work, we construct an effective continuum model for architected sheets that are composed of bulky tiles connected by slender elastic joints. Due to their mesostructure, these sheets feature quasi-mechanisms – low-energy local kinematic modes that are strongly favored over other deformations. In sheets with non-uniform mesostructure, kinematic incompatibilities arise between neighboring regions, causing out-of-plane buckling. The effective continuum model is based on a geometric analysis of the sheets' unit cells and their energetically favorable modes of deformation. Its major feature is the construction of a strain energy that penalizes deviations from these preferred modes of deformation. The effect of non-periodicity is entirely described through the use of spatially varying geometric parameters in the model. Our simulations capture the out-of-plane buckling that occurs in non-periodic specimens and show good agreement with experiments. While we only consider one class of quasi-mechanisms, our modeling approach could be applied to a diverse set of shape-morphing systems that are of interest to the mechanics community.

4.1 Introduction

Advanced manufacturing and synthesis technologies have given engineers the ability to design media with complex micro- and mesostructures that strongly influence bulk constitutive properties [1–3]. For example, the micro/mesoscale geometry can be designed to attain extreme or unconventional global mechanical behaviors such as high stiffness-to-weight ratios [1] and bistable auxeticity [4]. These fabrication processes have considerably expanded the design space for shape-shifting media [5–7] and deployable structures [8, 9]. In this context, mesoscale design has been used to create compliant features that replace conventional hinges, extensional elements and flexures [10–12], or to create structures whose mechanical behaviors can be tailored by adjusting the geometry of a pattern [13–21].

In structured media, the mesoscale geometry can be designed to energetically favor desired local modes of deformation [22, 23]. We refer to these behaviors as "quasi-mechanisms" when they accompany a non-negligible change in the system's energetic state. This distinguishes quasi-mechanisms from pure mechanisms, which are zero-energy kinematic modes. We emphasize that quasi-mechanisms are local behaviors: these energetic preferences can be spatially modulated by designing non-uniform mesostructures.

Within this context, origami [10, 14, 24, 25], kirigami [15, 26–28] and auxetic motifs [4, 16, 29–32] are the most popular classes of mesostructures that lead to quasi-mechanisms. However, demonstrations of shape-shifting materials have also been achieved using thermally responsive bilayer lattices [20] and in 3D structures such as snapology origami [33]. Quasi-mechanisms can be used to attain non-homogeneous strain field objectives (even under uniform loading conditions) by relying on non-uniform internal structures that spatially modulate local effective material properties. Morphing from a planar state to a doubly curved 3D geometry is an example of where this non-uniformity is important: Gauss' *Theorema Egregium* tells us that changing a surface's Gaussian curvature requires a non-isometric mapping [34], which in turn requires mesostructural non-uniformity if the actuation is driven by a spatially uniform stimulus [9, 20].

However, optimally designing non-uniform micro/mesostructures that lead to desired global behaviors can be challenging. The presence of geometric features at disparate length scales means that conventional finite element approaches become computationally expensive due to the need for meshes that resolve the finest features and yet span the entire structure. Homogenization theory provides a way to

determine effective properties of periodic structures [35], but in practice it is often only viable in the limited context of linear elasticity, as the presence of non-linearity and instabilities significantly complicates the methods [36]. In light of this, engineers have used a variety of reduced order modeling techniques to investigate forward elastic equilibrium and stability problems, as well as to inversely design non-uniform mesostructures at a lesser computational expense. These techniques range from bar-and-hinge [37–39] and structural frame [40] models that capture the mechanics of folded sheets, to representations of structural element networks that are based on effective springs [41], equivalent lattices [42], Chebyshev nets [43], discrete elastic rods [43, 44], and Kirchhoff rods [45].

Despite the above-mentioned advancements in modeling using networks of reduced order elements, there are limitations to the existing approaches. They can be computationally expensive in cases where the structure is much larger than the mesoscale unit cell size and a reduced order element (such as a discrete elastic rod) is needed for every constituent of the physical network (e.g., in hierarchical systems). Additionally, some of these models lack the generality needed to make themselves useful to the study of other systems. For example, bar-and-hinge origami models would not be suitable for extensional spring networks. It can also be challenging to calibrate constants such that accurate results are achieved using these models.

For these reasons, the mechanics community has pursued the development of effective continuum models. These models are powerful approaches to capturing the behavior of structures with internal geometric patterns in instances where there is a sufficient separation of length scales between the local geometric parameters and the global behaviors [46]. When this separation of scales exists, an energy density function can be constructed to capture the mechanical behaviors of the structure as if it were a bulk material, thus removing the need to resolve the geometric features at the smaller length scales with a fine mesh. This coarse meshing allows for significantly faster finite element simulations of complex physical behaviors. To this end, effective continuum models have been used to understand the behavior of periodic structured media that display quasi-mechanism behaviors [47] and can capture their responses to non-uniform loading conditions [48, 49]. However, these effective continuum modeling frameworks have not been applied to modeling the quasi-mechanism behaviors of graded media.

This article demonstrates how geometric analyses of unit cells can be used to construct effective continuum models for architected sheets with graded mesostructures.

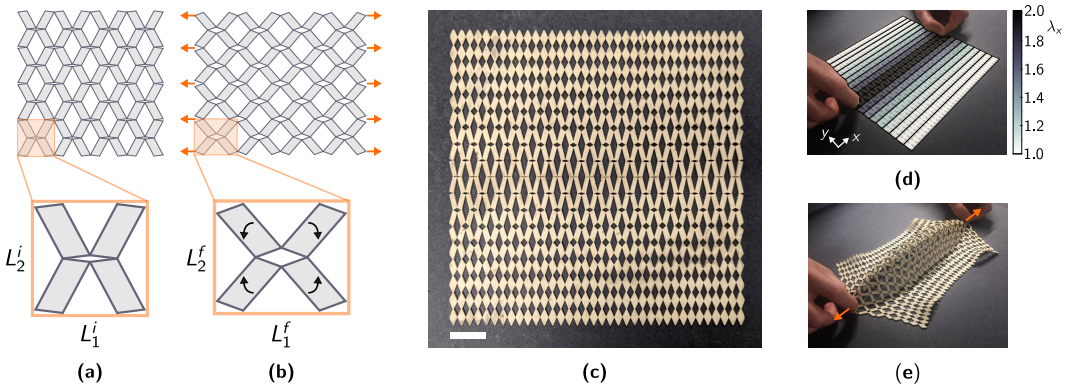

Figure 4.1: The mechanical behaviors of periodic and non-periodic architected sheets. (a-b) A sheet with a periodic cut pattern that displays a quasi-mechanism mode of deformation: rotation of tiles about slender elastic joints. As the tiles rotate, the unit cell dimensions change from L_α^i to L_α^f. Although tile rotations are low-energy kinematic modes compared to other deformations, the energetic cost associated with the deformation of the joints is not negligible. (c) Introducing a gradient in the cut pattern modulates the quasi-mechanism kinematics over the sheet. The scale bar represents 3 cm. (d) The mesostructural non-uniformity shown in (c) affects the extent to which tiles can rotate in different regions of the sheet, creating kinematic incompatibilities between the quasi-mechanism behaviors of different regions. Here, λ_x is the maximum stretch a unit cell can attain in the direction of loading through quasi-mechanism behaviors. (e) These in-plane kinematic incompatibilities lead to out-of-plane buckling. The design of the buckling sheets shown in (c-e) was first discussed in our prior work [16].

We illustrate this approach by studying generalizations of the auxetic sheets introduced by Grima *et al.* [29] to spatially varying distributions of diamond-shaped cuts [16, 50, 51]. The tessellated unit cells consist of bulky tiles connected by slender joints, and display two elastic regimes: a soft regime that occurs when the tiles rotate about the joints (as shown in Fig. 4.1a-b), and a stiff regime when the joints are subjected to tension. We design heterogeneous cut patterns to provoke in-plane kinematic incompatibilities under simple point-loading scenarios, which leads to out-of-plane buckling in a region of the structure [16] (shown in Fig. 4.1e).

This article is organized as follows. In Section 4.2, we discuss our effective continuum model for non-periodically patterned sheets that display quasi-mechanism behaviors. Our modeling approach entails first performing a geometric analysis of unit cells to derive their energetically favorable kinematic modes. Specifically, we derive the effect of geometric parameters on the rotational behavior of the tiles about the joints. Next, we begin constructing our strain energy density function by attributing an energy penalty to deviations from the above-mentioned kinematic modes, which may occur due to kinematic incompatibilities between neighboring

regions of the sheets. Since the joints are not ideal pins, the rotation of tiles is an elastic process, albeit softer than deviations from this preferred local behavior. We use a common constitutive model for elastic materials to approximate the elastic energy associated with the tile rotations. We extract the value of a few non-geometric constants from tensile experiments on periodically patterned structures and these parameters are then used to simulate the non-periodic structure. This type of effective material modeling enables us to use a coarse mesh to solve for pre-buckled equilibrium, the onset of instabilities, and post-buckled equilibrium. The numerical approach is discussed in Section 4.3, and we compare these numerical results to a new set of experiments in Section 4.4, highlighting the good agreement between coarse mesh finite element simulations and experiments. Our concluding remarks and perspective for future work are presented in Section 4.5. While our modeling method is demonstrated for the class of quasi-mechanisms discussed above, we believe it would be straightforward to apply it to many other quasi-mechanisms that are of interest to the mechanics community, such as origami tessellations [25] and shape-shifting bilayer lattices [20].

4.2 Modeling approach

In this section, we discuss how a strain energy density function can be extracted by modeling the effect that mesoscale geometric features have on a structure's energetically favorable local modes of deformation. Our approach is presented for modeling effective continua within the context of initially flat sheets with diamond-shaped cut patterns, although it could be generalized to other types of 2D or 3D architected media.

Quasi-mechanism kinematics

Our aim is to create an effective continuum model that captures the quasi-mechanism kinematics of sheets with diamond-shaped cut patterns (Fig. 4.2a). These sheets are tessellations of unit cells that are composed of four bulky tiles connected by slender elastic joints (Fig. 4.2b). The structures may be either periodic or non-periodic tessellations of unit cells (as in Fig. 4.2a or Fig. 4.1c, respectively). In either case, the quasi-mechanism local modes of deformation can be derived from a simple geometric analysis relating unit cell geometry to the rigid body rotations of the bulky tiles about the joints (Fig. 4.2b-c).

Five spatially varying geometric parameters constitute a geometry vector field $\phi(x_\alpha)$ and define the quasi-mechanism kinematics of our sheets. Namely ϕ =

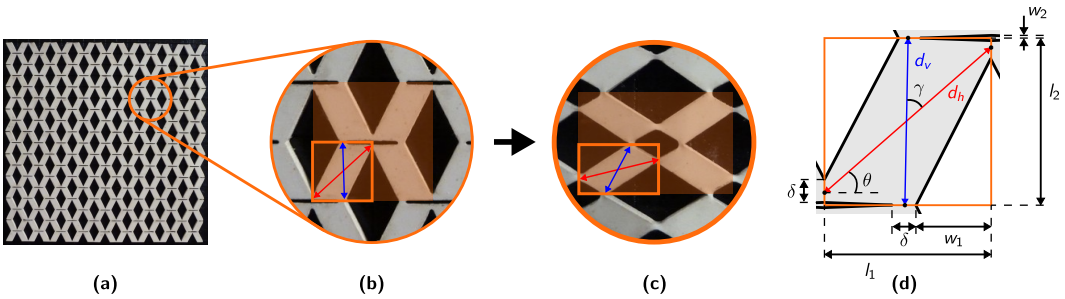

Figure 4.2: Quasi-mechanism kinematics. (a) An example of a sheet with a uniform pattern of diamond-shaped cuts. (b) A unit cell (shaded) consists of four tiles (boxed). (c) The quasi-mechanism kinematics consist of tile rotations about the slender elastic joints. This deformation mode can be entirely described by the projection of the tile diagonals onto the fixed orthogonal coordinate frame. This rotational mode has a non-negligible energetic cost, but one that is still much lesser than deformations where the joints are under tension or shear. (d) The reference configuration of the boxed tile shown in (b). Five parameters define the geometry of a unit cell: l_1 and l_2 are the reference configuration lengths of the unit cell grid spacing in the $\mathbf{e}_1$ and $\mathbf{e}_2$ directions, δ is the width of the slender joints, and w_1 and w_2 are the half-widths of the two diamond-shaped cuts that define the tiles' inclinations. The diagonals d_v and d_h and the angle γ between these two can be computed from those parameters. Finally, θ is the angle between the red diagonal, d_h, and the $\mathbf{e}_1$ direction. As the tile rotates from one configuration to another, this angle varies (as shown in b-c). The projected lengths of the tile's deformed configuration in the $\mathbf{e}_1$ and $\mathbf{e}_2$ directions are $d_h \cos(\theta)$ and $d_v \sin(\gamma + \theta)$, respectively. This allows us to compute the unit cell stretches: only the rotation of one tile about a joint needs to be analyzed to determine the quasi-mechanism kinematics of the unit cell. (a-d) Adapted from [16] by permission of The Royal Society of Chemistry.

$\{l_1, l_2, \delta, w_1, w_2\}$, where $l_1(x_\alpha)$ and $l_2(x_\alpha)$ are the lengths of the unit cell grid spacing in the $\mathbf{e}_1$ and $\mathbf{e}_2$ directions, $\delta(x_\alpha)$ is the width of the slender joints, and $w_1(x_\alpha)$ and $w_2(x_\alpha)$ are the half-widths of the two diamond-shaped cuts that define the tiles' inclinations. These parameters are illustrated in Fig. 4.2d. A few geometric parameters that are functions of the five mentioned above are also shown in Fig. 4.2d and will be discussed below.

We seek to identify a function $g(\mathbf{C}, \phi)$ such that the local quasi-mechanisms are described by the implicit relation $g(\mathbf{C}, \phi) = 0$. Here, $\mathbf{C}$ is the right Cauchy-Green strain tensor. To do so, we first define a unit cell as a 2×2 arrangement of quadrilateral tiles. Due to the symmetry of the unit cell, we can fully describe its quasi-mechanism kinematics by analyzing the geometry and rotation of a single tile. We use the bottom left tile in the unit cell, such as the one boxed in Fig. 4.2b-c. For a unit cell located at x_α with geometry defined by $\phi(x_\alpha) = \{l_1(x_\alpha), l_2(x_\alpha), \delta(x_\alpha), w_1(x_\alpha), w_2(x_\alpha)\}$,

the respective lengths d_h and d_v of the diagonals illustrated in Fig. 4.2d in red and blue are

$$d_h(\phi) = \sqrt{l_1^2 + (l_2 - 2w_2 - \delta)^2} \quad \text{and} \quad d_v(\phi) = \sqrt{l_2^2 + (l_1 - 2w_1 - \delta)^2}\,. \tag{4.1}$$

The angle γ between these two diagonals is given in terms of the geometric parameters ϕ as

$$\gamma(\phi) = \frac{\pi}{2} - \arctan\left(\frac{l_2 - 2w_2 - \delta}{l_1}\right) - \arctan\left(\frac{2w_1 + \delta - l_1}{l_2}\right)\,. \tag{4.2}$$

As the tile rotates about the joint, the angle θ between the diagonal d_h and the $\mathbf{e}_1$ direction varies, as shown in Fig. 4.2b-c. During this tile rotation, the projected lengths of the tile diagonals on the fixed orthogonal frame $\mathbf{e}_i$ change, and the unit cell will have effective stretches λ_1 and λ_2 of

$$\lambda_1(\theta) = \frac{d_h \cos\theta}{l_1} \quad \text{and} \quad \lambda_2(\theta) = \frac{d_v \sin(\gamma + \theta)}{l_2}\,. \tag{4.3}$$

We can invert the function for $\lambda_1(\theta)$ to obtain $\theta(\lambda_1)$ as

$$\theta(\lambda_1) = \arccos\left(\frac{\lambda_1 l_1}{d_h}\right)\,. \tag{4.4}$$

Substituting (4.4) into the expression for $\lambda_2(\theta)$ in (4.3) leads to the following explicit formula for $\lambda_2(\lambda_1)$:

$$\lambda_2(\lambda_1) = \frac{d_v}{l_2} \sin\left[\gamma + \arccos\left(\frac{\lambda_1 l_1}{d_h}\right)\right]\,. \tag{4.5}$$

We first derived this explicit function for the quasi-mechanism kinematics in our prior work [16]. Through trigonometric identities and algebraic manipulation, this can be written in implicit form:

$$\left(\frac{l_1\lambda_1}{d_h}\right)^2 + \left(\frac{l_2\lambda_2}{d_v}\right)^2 - 2\sin(\gamma)\frac{l_1\lambda_1}{d_h}\frac{l_2\lambda_2}{d_v} - \cos^2(\gamma) = 0\,. \tag{4.6}$$

In our reference frame, the implicit function (4.6) can be rewritten using the components of $\mathbf{C}$, since $\mathbf{C_{11}} = \lambda_1^2 \mathbf{e}_1 \otimes \mathbf{e}_1$ and $\mathbf{C_{22}} = \lambda_2^2 \mathbf{e}_2 \otimes \mathbf{e}_2$:

$$g(\mathbf{C}, \phi) = \frac{l_1^2 \mathbf{C_{11}}}{d_h^2(\phi)} + \frac{l_2^2 \mathbf{C_{22}}}{d_v^2(\phi)} - 2\sin\Big(\gamma(\phi)\Big)\frac{l_1 l_2}{d_h(\phi) d_v(\phi)}\sqrt{\det \mathbf{C}} - \cos^2\Big(\gamma(\phi)\Big) = 0\,. \tag{4.7}$$

The quasi-mechanism kinematics expressed in (4.7) describe the unit cells' preferred modes of local deformation as a function of geometric parameters. We emphasize that a unit cell may not deform according to this function. For example, this may occur if neighboring unit cells have a different geometry and cause kinematic incompatibility or if global loading conditions make these modes of deformation energetically unfavorable. In these cases, $g(\mathbf{C}, \phi) \neq 0$. In Section 4.2, we will model the stiffening that occurs when (4.7) cannot be satisfied by embedding this kinematic description as a penalty term in our strain energy function.

Kinematics of a thin elastic plate

Our aim is to embed the quasi-mechanism behavior described by (4.7) into an effective continuum model. We consider a thin elastic plate whose material particle positions of the mid-plane in an initially flat reference configuration are $\mathbf{X} = x_\alpha \mathbf{e}_\alpha$. The indices α and β in this subsection relate to the mid-plane of the plate (we use the Einstein summation convention for repeated indices), and the index '3' corresponds to the direction normal to the reference surface. The coordinate frame $\{\mathbf{e}_i\}$ is fixed and orthonormal. The domains for the material coordinates x_α are $x_1 \in [0, a]$ and $x_2 \in [0, b]$, where a and b are constants. The thickness t is much smaller than the other material domain dimensions, and we seek the mid-surface mapping $\boldsymbol{\chi}(x_\alpha)$:

$$\boldsymbol{\chi}(x_\alpha) = \Big(x_\alpha + u_\alpha(x_\beta)\Big)\mathbf{e}_\alpha + w(x_\beta)\mathbf{e}_3 \,, \tag{4.8}$$

where u_α and w are the in-plane and out-of-plane components of the mid-plane displacement vector, respectively. The deformation gradient tensor $\tilde{\mathbf{F}} = \nabla\boldsymbol{\chi}$ can be expressed in terms of the gradients of u_α and w. We label $\mathbf{F}$ as the in-plane component of the deformation gradient tensor ($\mathbf{F} \equiv \mathbf{I} + \nabla u_\alpha$). Since we have two material coordinates embedded in three spatial dimensions, the deformation gradient assumes the following form:

$$\tilde{\mathbf{F}} = \begin{bmatrix} 1 + u_{1,1} & u_{1,2} \\ u_{2,1} & 1 + u_{2,2} \\ w_{,1} & w_{,2} \end{bmatrix} = \begin{bmatrix} \mathbf{F} \\ \nabla w \end{bmatrix} . \tag{4.9}$$

We use the right Cauchy-Green deformation tensor, $\mathbf{C}$, as our measure for in-plane strain, and the Laplacian of the out-of-plane deflections, Δw, as our bending strain measure:

$$\mathbf{C} = \tilde{\mathbf{F}}^{\mathbf{T}}\tilde{\mathbf{F}} = \mathbf{F}^{\mathbf{T}}\mathbf{F} + \nabla w \otimes \nabla w \,, \qquad \Delta w = \frac{\partial^2 w}{\partial x_1^2} + \frac{\partial^2 w}{\partial x_2^2} \,. \tag{4.10}$$

Strain energy

Now that we have an implicit function (4.7) describing the quasi-mechanism behavior and a formulation of thin plate kinematics, we can construct a strain energy density function for our sheets. The first step is to attribute an energy penalty Ψ_p for deviations from the quasi-mechanism behavior. As discussed in Section 4.2, $g(\mathbf{C}, \phi) = 0$ when local deformations correspond to quasi-mechanism behaviors, and $g(\mathbf{C}, \phi) \neq 0$ when there is a deviation from these energetic preferences. Therefore we can write our energy penalty Ψ_p as

$$\Psi_p = \frac{1}{2\eta} g^2(\mathbf{C}, \phi) \,, \tag{4.11}$$

where η is a small parameter. For our perforated sheets, $g(\mathbf{C}, \phi)$ is given in (4.7). Therefore,

$$\Psi_p = \frac{1}{2\eta}\left(\frac{l_1^2 \mathbf{C_{11}}}{d_h^2} + \frac{l_2^2 \mathbf{C_{22}}}{d_v^2} - 2\sin(\gamma)\frac{l_1 l_2}{d_h d_v}\sqrt{\det \mathbf{C}} - \cos^2(\gamma) \right)^2 . \tag{4.12}$$

For elastic bodies, deforming according to these preferential modes will still entail non-zero energy. Thus, we must also assign a soft elastic energy density Ψ_s to this scenario (this softness is relative to the energy expense of deviating from quasi-mechanism behaviors). A compressible Neo-Hookean model provides the flexibility to approximate our experimental data from tensile tests well while using only two material parameters. Therefore, the total membrane strain energy density function $\Psi_m(\mathbf{C}, \phi) = \Psi_p(\mathbf{C}, \phi) + \Psi_s(\mathbf{C})$ is

$$\Psi_m(\mathbf{C}, \phi) = \Psi_p(\mathbf{C}, \phi) + \frac{\mu}{2}(\bar{I}_1 - 2) + \frac{\lambda}{2}(J-1)^2 \,, \tag{4.13}$$

where $J = \sqrt{\det(\mathbf{C})}$, $\bar{I}_1 = \mathrm{tr}(\mathbf{C})J^{-1}$, μ and λ are the Lamé parameters and Ψ_p is given in (4.12). Our bending energy density function is

$$\Psi_b = \frac{B(\Delta w)^2}{2} , \tag{4.14}$$

where B is a bending stiffness constant. Our strain energy per unit thickness is the sum of Ψ_m and Ψ_b, integrated over the 2D domain spanned by the mid-plane of the sheet, Ω:

$$\mathcal{E}(\mathbf{u}, w) = \int_\Omega \Big(\Psi_m(\mathbf{C}, \phi) + \Psi_b(\Delta w) \Big)\, dA . \tag{4.15}$$

All of the parameters in the energy function are either geometric or can be extracted from three simple tensile experiments: one on a dogbone specimen of the bulk rubber with no cut patterns, and two (conducted in orthogonal directions) on a sheet with periodic but anisotropic cuts.

Contact model

In the case where the sheet lies on a rigid surface, we wish to enforce the contact condition $w \geq 0$. While techniques such as the active set method directly impose this constraint, we opt to relax this condition and instead use a rather simple penalty-based contact model. Thus, for problems where the sheet is lying on a flat surface, we consider a contact penalty energy for negative out-of-plane deflections:

$$\Psi_c(w) = \frac{P}{2}(dw^-)^2, \qquad dw^- = \min(0, w + \varepsilon) , \tag{4.16}$$

where P is the penalty stiffness and $\varepsilon > 0$ is a small tolerance length. Notice that the contact energy is nonzero only when $w < -\varepsilon$. This ensures that the contact condition does not interfere with the stability of the initially flat, unbuckled plate, and only becomes active post-bifurcation. We add this contact energy onto (4.15) to give the total energy functional

$$\mathcal{E}(\mathbf{u}, w) = \int_\Omega \Psi_m(\mathbf{C}, \phi) + \Psi_b(\Delta w) + \Psi_c(w)\, dA . \tag{4.17}$$

We will discuss the variations of this energy to compute equilibrium and stability in Section 4.3.

4.3 Finite element implementation

In this section, we present the equilibrium conditions for the system. Using a mixed formulation, we compute the solution using standard first order Lagrange polynomial finite elements. More details for our solution procedure and stability analysis are provided in the appendices. We implement this formulation in the deal.II open source finite element library [52].

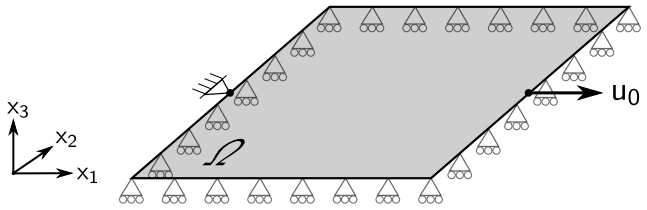

Figure 4.3: An example of a domain and of a set of boundary conditions used in our simulations. In-plane displacements are prescribed on a portion of the boundary and in-plane traction-free edges are observed on the remainder. Additionally, we constrain out-of-plane displacements and have no applied moments on the entire boundary. This drawing displays the boundary conditions used to model the sheet with non-uniform cut patterns shown in Fig 4.1c-e.

We consider a rectangular domain in a displacement-controlled setting. The in-plane displacements $\mathbf{u}$ are prescribed on $\partial_u\Omega \subset \partial\Omega$ and we have in-plane traction free edges on the remainder, $\partial_f\Omega = \partial\Omega\backslash\partial_u\Omega$. Additionally, we constrain out-of-plane displacements w and have moment-free edges on the entire boundary. Fig 4.3 shows an example of a domain and of a set of boundary conditions used in some of our simulations. While the boundary conditions may be altered for a more general case, the mixed formulation discussed in Subsection 4.3 may not be appropriate for situations such as clamped boundaries.

Equilibrium and mixed formulation

The equilibrium condition is the stationarity of our energy functional from (4.17) in both $\mathbf{u}$ and w,

$$\frac{\mathrm{d}}{\mathrm{d}\kappa}\Big[\mathcal{E}(\mathbf{u}+\kappa\delta\mathbf{u}, w+\kappa\delta w)\Big]_{\kappa=0} = 0 \qquad \text{for all} \quad \delta\mathbf{u} \in \mathcal{U}_0, \quad \delta w \in H_0^2(\Omega)\ , \tag{4.18}$$

where $\mathcal{U}_0$ is the set of kinematically admissible in-plane displacement variations

$$\mathcal{U}_0 = \left\{\mathbf{u} \in \left(H^1(\Omega)\right)^2,\ \mathbf{u} = 0 \text{ on } \partial_u\Omega\right\}, \tag{4.19}$$

and we search for solutions $\mathbf{u} \in \mathcal{U}$ and $w \in \mathcal{W}$ where

$$\mathcal{U} = \left\{ \mathbf{u} \in \left(H^1(\Omega) \right)^2, \ \mathbf{u} = \mathbf{u}_0 \text{ on } \partial_u \Omega \right\}, \quad \mathcal{W} = \left\{ w \in H^2(\Omega), \ w = w_0 \text{ on } \partial\Omega \right\}. \tag{4.20}$$

A common issue for plate problems is the bi-harmonic operator on w that arises from the Gateaux derivative of the bending energy. In this case, the weak form contains a product of the second derivative of w and its variation, so that the usual Galerkin finite element method with even quadratic Lagrange polynomial shape functions is not appropriate.[1] Therefore, we turn to a mixed formulation that is widely used for linear biharmonic problems [53]. We introduce a scalar function $v \in H^1_0(\Omega)$ and set it equal to Δw by considering an augmented energy

$$\widehat{\mathcal{E}}(\mathbf{u}, w) = \sup_{v \in H^1_0(\Omega)} \int_\Omega \Psi_m(\mathbf{C}) + \Psi_c(w) - B \left(\nabla w \cdot \nabla v - \frac{1}{2} |v|^2 \right) \, dA \, . \tag{4.21}$$

Stationarity of $\widehat{\mathcal{E}}$ in both $\mathbf{u}$ and w, along with the suprema condition on v, gives the weak form of equilibrium

$$\begin{aligned}
0 &= \int_\Omega \left(2\mathbf{F} \frac{\partial \Psi_m}{\partial \mathbf{C}} \right) : \nabla \delta \mathbf{u} \, dA && \forall \delta \mathbf{u} \in \mathcal{U}_0 \, , \\
0 &= \int_\Omega \left(2 \frac{\partial \Psi_m}{\partial \mathbf{C}} \nabla w \right) \cdot \nabla \delta w + \frac{\partial \Psi_c}{\partial w} - B \nabla v \cdot \nabla \delta w \, dA && \forall \delta w \in H^1_0(\Omega) \, , \\
0 &= \int_\Omega -B \nabla w \cdot \nabla \delta v - B v \delta v \, dA && \forall \delta v \in H^1_0(\Omega) \, .
\end{aligned} \tag{4.22}$$

The first two lines in (4.22) are the equilibrium relations for in-plane and out-of-plane displacements, respectively. The final line is the constraint that $v = \Delta w$ weakly. The strong form of these relations can be found in Appendix C.1. Notice that (4.22) only contains first derivatives of the displacements and their variations. It is shown in [53] that we may now consider $w \in H^1(\Omega)$. Therefore, we use a Galerkin finite element formulation with p = 1 shape functions for the fields $\mathbf{u}$, w and v. We solve the nonlinear system with typical Newton-Raphson iterations. Details on the finite element formulation and solution procedure can be found in Appendix C.2.

Stability analysis

To probe the stability of an equilibrium configuration, it is common practice to calculate the eigenvalues of the tangent stiffness matrix. A negative eigenvalue

[1] Standard Lagrange polynomial shape functions have discontinuous first-derivatives at the boundaries of elements. This would result in integrating the product of two Dirac delta functions, which is undefined.

implies an instability, and the equilibrium solution can then be perturbed in the direction of the corresponding eigenvector to explore the buckled solution. However, the mixed formulation complicates this procedure. To assess stability, we must restrict the eigenvectors to the subspace upon which the constraint $v = \Delta w$ is satisfied. To this end, we consider an effective stiffness matrix on this subspace. By solving the linear constraint explicitly, we can condense v out of the system matrix. Then, we calculate eigenvalues of this reduced stiffness matrix to asses stability. We use the linear constraint to map the corresponding eigenvector back to the full variable set and perturb the system. The magnitude of the perturbation is chosen to be on the same order as the displacement increment. The direction of the perturbation is decided such that the w component at the middle of the sheet is positive. The full details of the stability analysis can be found in Appendix C.3.

4.4 Results

In this section, we discuss the extraction of effective material model constants from experiments on sheets with uniform cut patterns and we compare experimental and numerical results on the post-buckling behavior of sheets with non-periodic mesostructure.

Extracting model constants from experiments on sheets with uniform cut patterns

As discussed in Section 4.2, our energy given in (4.17) requires the extraction of four parameters from experiments: the Lamé moduli (λ and μ), the energy penalty parameter (η), and the bending stiffness (B). We obtained λ, μ and η from tensile tests on the specimen with uniform cut patterns shown in Fig. 4.2a, where $l_1 = l_2 = 6$ mm, $\delta = l_1/8$, $w_1 = (l_1 - \delta)/2$, and $w_2 = 0$ mm. The sheets have a thickness of $t = 1.55$ mm, width dimensions of 108 mm in each direction and are made of natural rubber gum. The diamond-shape cuts were made using a laser cutter.

The specimen was placed on a custom apparatus that grips the edges with roller pins, thus allowing free sliding in the direction perpendicular to the tension. To obtain λ and μ, the sheet was loaded in the direction that induces quasi-mechanism behavior (rotation of the tiles about the elastic joints). Since the sheet's cut pattern is uniform, no kinematic incompatibilities arise and only the soft elastic mode is present. The values of $\mu = 17$ kPa and $\lambda = 0.1$ kPa provided a good fit to our data, as shown in Fig. 4.4. To attain η, the sheet was loaded in the perpendicular direction, where

tiles do not rotate because their diagonals are aligned in the direction of loading and the elastic joints are in tension. We attain a good fit of our data by setting $\eta = 0.002$ kPa^{-1}. Fig. 4.4 shows a comparison of effective continuum simulations of the in-plane elastic behaviors with experiments and Abaqus/Standard simulations from prior work [16], where the mesh fully resolves the fine features of the specimen geometry.

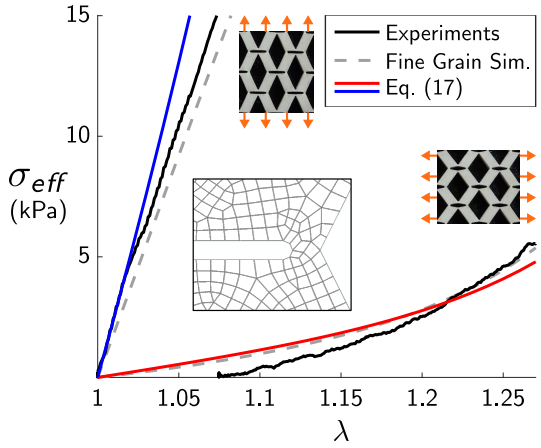

Figure 4.4: Effective stress vs. stretch for a sheet with a periodic cut pattern. The insets show four unit cells of this structure, see Fig. 4.2a for an image of the entire sheet. We compare our effective continuum model (solid red and blue lines) represented by (4.17) to experiments (solid black lines) and fine-grain finite element simulations (gray dashes) that fully resolve the small geometric features in our sheets. These experiments and the fine-grain simulations (using Abaqus/Standard) were conducted in our prior work [16]). The experimental curve for the soft loading direction does not start at $\lambda = 1$ due to the effect of gravity in a vertically loaded tensile testing machine. The inset on the bottom left of the figure shows a small region of the mesh used in the Abaqus simulations to capture the geometry of the elastic joints. The large number of elements needed for these fine grain simulations motivates the usage of effective continuum models. The insets in this image were adapted from [16] by permission of The Royal Society of Chemistry.

We adjust the classic bending stiffness for a Kirchhoff-Love plate [54] by including a scaling factor $\alpha(f)$ that accounts for the reduced bending stiffness of a sheet with porosity f. Therefore, the bending stiffness of the patterned sheet can be written in the following form:

$$B = \frac{\alpha(f) E t^2}{12(1-\nu^2)} \,. \tag{4.23}$$

Here, $E = 2$ MPa is Young's modulus (obtained from linear regime tensile tests on a 55 mm $\times$ 9.2 mm $\times$ 1.5 mm dogbone sample of natural rubber), t is the sheet thickness, and $\nu = 0.5$ is Poisson's ratio. A recent paper by Shrimali, et al. [55]

showed that the effective bending stiffness of thin perforated plates is much more dependent on the plate's porosity f than on the shape or size of the perforations. This holds both for plates where the sheet thickness is much smaller than the unit cell dimension, and vice versa. Given the porosity of our sheets ($f \approx 0.5$), we adopt a scaling value of $\alpha(f) = 0.25$, as suggested by the results in [55]. Their results also justify our use of a uniform bending stiffness. Again, (4.17) is the strain energy per unit thickness, hence the scaling of B with t^2. Based on these considerations, no additional experiment is required to obtain the bending stiffness.

Out-of-plane buckling of sheets with graded mesostructure

We now consider a more interesting pattern of cuts that is non-periodic, and where spatial variations in the local quasi-mechanism behavior lead to kinematic incompatibilities. To model the behavior of these sheets, we update the geometry vector $\phi(x_\alpha) = \{l_1(x_\alpha), l_2(x_\alpha), \delta(x_\alpha), w_1(x_\alpha), w_2(x_\alpha)\}$. We have three specimens of equal thickness $t = 1.55$ mm, but varying aspect ratios. Now, $l_1 = \{4.5 \text{ mm}, 6 \text{ mm}, 7.5 \text{ mm}\}$ for the three sheets (the overall width dimensions of the square sheets scale linearly with l_1 to 162 mm, 216 mm, and 270 mm, respectively). The other parameters are $l_2 = 2l_1$, $\delta = l_1/8$, $w_1 = (l_1 - \delta)/2$, and $w_2(x_\alpha) = \frac{l_1-\delta}{2}\left(1 - \sin\frac{\pi x_2}{18 l_2}\right)$. The non-uniform geometry is accounted for by considering spatially varying $w_2(x_\alpha)$ in the finite element formulation. We note that, although the geometric parameter $w_2(x_\alpha)$ is non-uniform, we still use a uniform soft elastic energy density, Ψ_s, because it represents the energetic cost of the non-ideal mechanism and the joint density is still uniform.

The geometric gradation of the mesostructure leads to variations in the local quasi-mechanism behavior over the extent of the sheet. This causes in-plane kinematic incompatibilities, which lead to out-of plane buckling after each sheet's critical stretch is reached, as shown in Fig. 4.5a-b. We show the buckled mode nucleation and the evolution of the post-buckled height of the central point in the sheets as a function of boundary point displacement in Fig. 4.5c. We compare simulations of our effective continuum model (computed using the deal.II finite element library [52] on a 36×36 uniform quadrilateral mesh) to measurements of the physical samples (using a level-calibrated mounted caliper) and see excellent agreement between the two, especially at larger boundary displacements. As expected, the stretch at which buckling occurs is delayed by increasing the thickness-to-width ratio. The difference between the computational predictions and experimental measurements of buckling nucleation and height at lower stretch values can be partially attributed

to the fact that our simulations do not account for friction with the table or gravity. These two physical processes are important since the material is soft and bending is a low-energy deformation for shells with small gaussian curvature. As the dome height increases, the structure becomes less susceptible to the effect of gravity.

Finally, to better visualize how the post-buckling behavior evolves and is affected by the aspect ratio of the sheet, we show laser scans of the physical specimens and deformed simulation meshes at three different boundary point displacements in Fig. 4.6. Accurate quantitative comparisons are challenging due to the manual stitching process that follows the acquisition of laser scan data patches, which introduces slight distortions and puts certain regions of the scanned sheet at an inclined plane relative to the rest of the structure. As expected, the post-buckled domes are wider (relative to the overall width of the sheets) for specimens that have larger thickness-to-width ratios, showing good qualitative agreement between experiments and simulations. Furthermore, the onset of buckling occurs at greater stretches as t/l_1 increases.

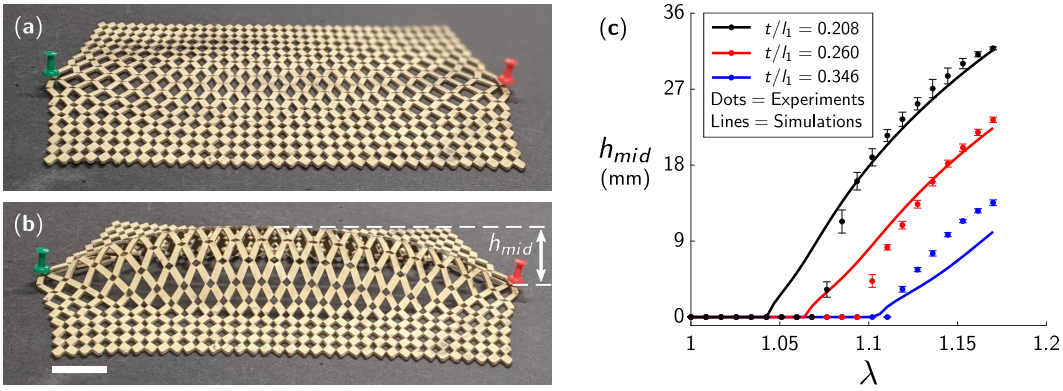

Figure 4.5: Buckling behavior of sheets with non-uniform cut patterns. (a) Up to a certain stretch λ, point displacements lead to in-plane deformations. (b) Following a critical value of λ, the in-plane kinematic incompatibilities will lead to out-of-plane buckling. The scale bar represents 3 cm. (c) Comparison of dome height between effective continuum simulations (solid lines) and experiments (dots) for sheets of three aspect ratios. Here, h_{mid} is the height of a sheet's center point, λ is the stretch of the sheet's center line in the $\mathbf{e}_1$ direction, t is the sheet thickness, and l_1 is the length of the unit cell grid spacing in the $\mathbf{e}_1$ direction.

These results show that this effective continuum modeling framework is a powerful tool for understanding the physics of quasi-mechanisms in non-periodic media. In our previous work [16], we only captured in-plane deformation mappings using standard, fine-grained finite element procedures since the large number of elements needed to resolve the small mesostructural features (in the range between 10^5 and 10^6 elements depending on the structure being simulated) caused the calculation

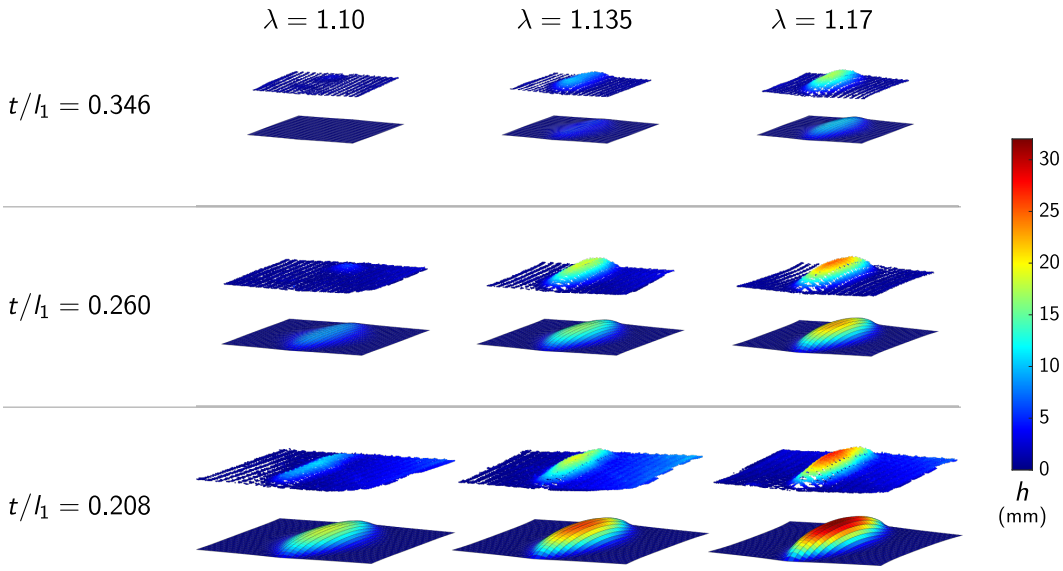

Figure 4.6: Post-buckling behavior of sheets with three thickness-to-width ratios. These are the same three sheets represented in Fig. 4.5c. Here, t is the sheet thickness, l_1 is the length of the unit cell grid spacing in the $\mathbf{e}_1$ direction, and λ is the applied stretch at the midpoint of the sheet edge. In each entry of the stretch vs. aspect ratio grid, the laser scans are plotted directly above the simulated deformed meshes. As expected, we see that sheets with higher thickness-to-width ratios will nucleate at larger stretches and will buckle into wider domes relative to the overall sheet width.

of out-of-plane buckling modes to have an inviable computational cost. Using the effective continuum approach we can get accurate results merely using a 36×36 uniform quadrilateral mesh, a reduction of two to three orders of magnitude in the number of elements used. Each of the bifurcation curves in Fig 4.5 took roughly 5 minutes to compute running on a single core of a Intel® Xeon® 5218 processor. Meanwhile, we could not make simulations for the post-buckling behavior of our sheets converge in a reasonable amount of time using a standard fine-grained FEM approach.

4.5 Conclusions

We present an effective continuum modeling framework for architected media that display quasi-mechanism behaviors and demonstrate its validity on sheets that are patterned with diamond-shaped cuts. The model incorporates a penalty for deviations from quasi-mechanism behaviors and relies on material model parameters extracted directly from experiments. We show that the approach correctly predicts the mechanical behavior of non-periodic media, even when the model's parameters are derived from experiments on periodic specimens. Our approach permits accurate and efficient simulations of mechanical behaviors that would otherwise be

impractical to model using fine-grained simulations that fully resolve the material's small geometric features.

We note that the implicit relation (4.7) does not define the function $g(\mathbf{C}, \phi)$ uniquely, implying that other choices of the functions Ψ_p from (4.12) and Ψ_m from (4.13) are possible. A good agreement with experiments is still attained, suggesting that the buckling behavior of the sheet is robust with respect to the choice of the function g.

There are a few limitations to this approach. First, it requires a sufficient separation of length scales between the global deformation mode dimensions and the unit cell size. Therefore, it would not be able to capture the local buckling modes observed in some kirigami sheets [56] or handle the dome kinking that occurs in our systems if they are fabricated from extremely thin sheets [16]. Furthermore, although we believe that this modeling approach could be applied to a broad range of architected media that display quasi-mechansims, extracting the material model constants from experiments may be more challenging in other systems in comparison to the perforated sheets we have discussed. Finding a suitable soft elastic energy density Ψ_s that is appropriate for the quasi-mechanism regime also requires the modeler to have an intuition for which constitutive models can be appropriately tailored to fit experimental data attained from experiments on their system.

In the future, this modeling framework could be adapted to 3D media and materials with temporally varying mechanical properties, provided that they also display quasi-mechanisms.

Acknowledgements

C.M. and C.D. were supported by the US Army Research Office Grant W911NF-17-1-0147. This work was also supported by a NASA Space Technology Research Fellowship to C.M. We thank Andrei Constantinescu and Kaushik Bhattacharya for helpful discussions, and Paul Stovall for assistance with fabrication.

Permissions

This chapter is currently under review for publication in a journal.

References

[1] T. A. Schaedler, A. J. Jacobsen, A. Torrents, A. E. Sorensen, J. Lian, J. R. Greer, L. Valdevit, and W. B. Carter. Ultralight metallic microlattices. *Science*, 334 (6058):962–965, 2011.

[2] T. H. Ware, M. E. McConney, J. J. Wie, V. P. Tondiglia, and T. J. White. Voxelated liquid crystal elastomers. *Science*, 347(6225):982–984, 2015. doi: 10.1126/science.1261019.

[3] W. P. Moestopo, A. J. Mateos, R. M. Fuller, J. R. Greer, and C. M. Portela. Pushing and pulling on ropes: Hierarchical woven materials. *Advanced Science*, 7(20):2001271, 2020. doi: 10.1002/advs.202001271.

[4] A. Rafsanjani and D. Pasini. Bistable auxetic mechanical metamaterials inspired by ancient geometric motifs. *Extreme Mechanics Letters*, 9:291–296, 2016. doi: 10.1016/j.eml.2016.09.001.

[5] Y. Klein, E. Efrati, and E. Sharon. Shaping of Elastic Sheets by Prescription of Non-Euclidean Metrics. *Science*, 315(5815):1116–1120, 2007. ISSN 0036-8075. doi: 10.1126/science.1135994.

[6] A. S. Gladman, E. A. Matsumoto, R. G. Nuzzo, L. Mahadevan, and J. A. Lewis. Biomimetic 4d printing. *Nature Materials*, 15:413–418, 2016. doi: 10.1038/nmat4544.

[7] P. Plucinsky, B. A. Kowalski, T. J. White, and K. Bhattacharya. Patterning nonisometric origami in nematic elastomer sheets. *Soft Matter*, 14:3127–3134, 2018. doi: 10.1039/C8SM00103K.

[8] M. Schenk, A. D. Viquerat, K. A. Seffen, and S. D. Guest. Review of inflatable booms for deployable space structures: packing and rigidization. *Journal of Spacecraft and Rockets*, 51(3):762–778, 2014.

[9] J. W. Boley, W. M. van Rees, C. Lissandrello, M. N. Horenstein, R. L. Truby, A. Kotikian, J. A. Lewis, and L. Mahadevan. Shape-shifting structured lattices via multimaterial 4d printing. *Proceedings of the National Academy of Sciences*, 116(42):20856–20862, 2019. doi: 10.1073/pnas.1908806116.

[10] H. C. Greenberg, M. L. Gong, S. P. Magleby, and L. L. Howell. Identifying links between origami and compliant mechanisms. *Mechanical Sciences*, 2 (2):217–225, 2011.

[11] P. Celli, A. Lamaro, C. McMahan, P. Bordeenithikasem, D. C. Hofmann, and C. Daraio. Compliant morphing structures from twisted bulk metallic glass ribbons. *Journal of the Mechanics and Physics of Solids*, 145:104129, 2020.

[12] S. Ferraro and S. Pellegrino. Topology and shape optimization of ultrathin composite self-deployable shell structures with cutouts. *AIAA Journal*, pages 1–14, 2021.

[13] S. D. Guest and S. Pellegrino. The folding of triangulated cylinders, part i: geometric considerations. *Journal of Applied Mechanics*, 61:773–777, 1994.

[14] L. H. Dudte, E. Vouga, T. Tachi, and L. Mahadevan. Programming curvature using origami tessellations. *Nature Materials*, 15(5):583–588, 2016. doi: 10.1038/NMAT4540.

[15] F. Wang, X. Guo, J. Xu, Y. Zhang, and C. Q. Chen. Patterning curved three-dimensional structures with programmable kirigami designs. *Journal of Applied Mechanics*, 84(6):061007, 2017. doi: 10.1115/1.4036476.

[16] P. Celli, C. McMahan, B. Ramirez, A. Bauhofer, C. Naify, D. Hofmann, B. Audoly, and C. Daraio. Shape-morphing architected sheets with non-periodic cut patterns. *Soft Matter*, 14:9744–9749, 2018. doi: 10.1039/C8SM02082E.

[17] E. Hawkes, B. An, N. M. Benbernou, H. Tanaka, S. Kim, E. D. Demaine, D. Rus, and R. J. Wood. Programmable matter by folding. *Proceedings of the National Academy of Sciences*, 107(28):12441–12445, 2010. doi: 10.1073/pnas.0914069107.

[18] X. Shang, L. Liu, A. Rafsanjani, and D. Pasini. Durable bistable auxetics made of rigid solids. *Journal of Materials Research*, 33(3):300–308, 2018.

[19] E. Siéfert, E. Reyssat, J. Bico, and B. Roman. Programming stiff inflatable shells from planar patterned fabrics. *Soft Matter*, 16(34):7898–7903, 2020.

[20] R. Guseinov, C. McMahan, J. Pérez, C. Daraio, and B. Bickel. Programming temporal morphing of self-actuated shells. *Nature Communications*, 11(1):1–7, 2020. doi: 10.1038/s41467-019-14015-2.

[21] F. Agnelli, M. Tricarico, and A. Constantinescu. Shape-shifting panel from 3D printed undulated ribbon lattice. *Extreme Mechanics Letters*, 42:101089, 2021.

[22] K. Bertoldi, V. Vitelli, J. Christensen, and M. van Hecke. Flexible mechanical metamaterials. *Nature Reviews Materials*, 2(11):1–11, 2017.

[23] N. Singh and M. van Hecke. Design of pseudo-mechanisms and multistable units for mechanical metamaterials. *Physical Review Letters*, 126:248002, 2021. doi: 10.1103/PhysRevLett.126.248002.

[24] K. Liu, T. Tachi, and G. H. Paulino. Invariant and smooth limit of discrete geometry folded from bistable origami leading to multistable metasurfaces. *Nature Communications*, 10(1):1–10, 2019. doi: 10.1038/s41467-019-11935-x.

[25] S. J. P. Callens and A. A. Zadpoor. From flat sheets to curved geometries: Origami and kirigami approaches. *Materials Today*, 21(3):241–264, 2018. doi: 10.1016/j.mattod.2017.10.004.

[26] T. Castle, Y. Cho, X. Gong, E. Jung, D. M. Sussman, S. Yang, and R. D. Kamien. Making the cut: Lattice kirigami rules. *Physical Review Letters*, 113:245502, 2014. doi: 10.1103/PhysRevLett.113.245502.

[27] Y. Tang and J. Yin. Design of cut unit geometry in hierarchical kirigami-based auxetic metamaterials for high stretchability and compressibility. *Extreme Mechanics Letters*, 12:77–85, 2017. doi: 10.1016/j.eml.2016.07.005.

[28] C. Jiang, F. Rist, H. Pottmann, and J. Wallner. Freeform quad-based kirigami. *ACM Transactions on Graphics*, 39(6), 2020. ISSN 0730-0301. doi: 10.1145/3414685.3417844.

[29] J. N. Grima, V. Zammit, R. Gatt, A. Alderson, and K. E. Evans. Auxetic behaviour from rotating semi-rigid units. *Physica Status Solidi B*, 244(3): 866–882, 2007. doi: 10.1002/pssb.200572706.

[30] K. Bertoldi, P. M. Reis, S. Willshaw, and T. Mullin. Negative Poisson's ratio behavior induced by an elastic instability. *Advanced Materials*, 22(3):361–366, 2010.

[31] M. Konaković, K. Crane, B. Deng, S. Bouaziz, D. Piker, and M. Pauly. Beyond developable: Computational design and fabrication with auxetic materials. *ACM Transactions on Graphics*, 35(4):89, 2016. doi: 10.1145/2897824.2925944.

[32] M. Konaković-Luković, J. Panetta, K. Crane, and M. Pauly. Rapid deployment of curved surfaces via programmable auxetics. *ACM Transactions on Graphics*, 37(4):106, 2018. doi: 10.1145/3197517.3201373.

[33] J. T. B. Overvelde, J. C. Weaver, C. Hoberman, and K. Bertoldi. Rational design of reconfigurable prismatic architected materials. *Nature*, 541(7637): 347–352, 2017.

[34] C. F. Gauss. *Disquisitiones generales circa superficies curvas*. Typis Dietericianis, 1828.

[35] G. Allaire. A brief introduction to homogenization and miscellaneous applications. *ESAIM: Proceedings*, 37:1–49, 09 2012. doi: 10.1051/proc/201237001.

[36] S. Müller, N. Triantafyllidis, and G. Geymonat. Homogenization of nonlinearly elastic materials, microscopic bifurcation and macroscopic loss of rank-one convexity. *Archive for Rational Mechanics and Analysis*, 122, 09 1993. doi: 10.1007/BF00380256.

[37] M. Schenk and S. D. Guest. Origami folding: A structural engineering approach. *Origami*, 5:291–304, 2011.

[38] E. T. Filipov, K. Liu, T. Tachi, M. Schenk, and G. H. Paulino. Bar and hinge models for scalable analysis of origami. *International Journal of Solids and Structures*, 124:26–45, 2017. doi: 10.1016/j.ijsolstr.2017.05.028.

[39] K. Liu and G. H. Paulino. Nonlinear mechanics of non-rigid origami: An efficient computational approach. *Proceedings of the Royal Society A: Mathematical, Physical and Engineering Sciences*, 473(2206):20170348, 2017. doi: 10.1098/rspa.2017.0348.

[40] K. Hayakawa and M. Ohsaki. Form generation of rigid origami for approximation of a curved surface based on mechanical property of partially rigid frames. *International Journal of Solids and Structures*, 2020. doi: 10.1016/j.ijsolstr.2020.12.007.

[41] C. Coulais, C. Kettenis, and M. van Hecke. A characteristic length scale causes anomalous size effects and boundary programmability in mechanical metamaterials. *Nature Physics*, 14(1):40–44, 2018. doi: 10.1038/nphys4269.

[42] K. Leimer and P. Musialski. Reduced-order simulation of flexible metamaterials. In *Symposium on Computational Fabrication*, SCF '20, New York, NY, USA, 2020. Association for Computing Machinery. doi: 10.1145/3424630.3425411.

[43] C. Baek, A. O. Sageman-Furnas, M. K. Jawed, and P. M. Reis. Form finding in elastic gridshells. *Proceedings of the National Academy of Sciences*, 115 (1):75–80, 2018. doi: 10.1073/pnas.1713841115.

[44] C. Lestringant and D. M. Kochmann. Modeling of flexible beam networks and morphing structures by geometrically exact discrete beams. *Journal of Applied Mechanics*, 87(8):081006, 2020. doi: 10.1115/1.4046895.

[45] T. Yu, L. Dreier, F. Marmo, S. Gabriele, S. Parascho, and S. Adriaenssens. Numerical modeling of static equilibria and bifurcations in bigons and bigon rings. *Journal of the Mechanics and Physics of Solids*, 152:104459, 2021.

[46] P. M. Reis, F. Brau, and P. Damman. The mechanics of slender structures. *Nature Physics*, 14(12):1150–1151, 2018. doi: 10.1038/s41567-018-0369-4.

[47] Y. Bar-Sinai, G. Librandi, K. Bertoldi, and M. Moshe. Geometric charges and nonlinear elasticity of two-dimensional elastic metamaterials. *Proceedings of the National Academy of Sciences*, 117(19):10195–10202, 2020. doi: 10.1073/pnas.1920237117.

[48] M. Czajkowski, C. Coulais, M. van Hecke, and D. Rocklin. Conformal elasticity of mechanism-based metamaterials. *arXiv preprint arXiv:2103.12683*, 2021.

[49] R. Khajehtourian and D. M. Kochmann. A continuum description of substrate-free dissipative reconfigurable metamaterials. *Journal of the Mechanics and Physics of Solids*, 147:104217, 2021.

[50] G. P. T. Choi, L. H. Dudte, and L. Mahadevan. Programming shape using kirigami tessellations. *Nature Materials*, 18(9):999–1004, 2019. doi: 10.1038/s41563-019-0452-y.

[51] L. Jin, A. E. Forte, B. Deng, A. Rafsanjani, and K. Bertoldi. Kirigami-inspired inflatables with programmable shapes. *Advanced Materials*, 32(33):2001863, 2020. doi: 10.1002/adma.202001863.

[52] D. Arndt, W. Bangerth, D. Davydov, T. Heister, L. Heltai, M. Kronbichler, M. Maier, J.-P. Pelteret, B. Turcksin, and D. Wells. The deal.II finite element library: Design, features, and insights. *Computers & Mathematics with Applications*, 81:407–422, 2021. doi: 10.1016/j.camwa.2020.02.022.

[53] D. Boffi, F. Brezzi, and M. Fortin. *Mixed Finite Element Methods and Applications*, volume 44. 01 2013. ISBN 978-3-642-36518-8. doi: 10.1007/978-3-642-36519-5.

[54] S. Timoshenko and S. Woinowsky-Krieger. Theory of plates and shells. 1959.

[55] B. Shrimali, M. Pezzulla, S. Poincloux, P. M. Reis, and O. Lopez-Pamies. The remarkable bending properties of perforated plates. *Journal of the Mechanics and Physics of Solids*, 2021.

[56] A. Rafsanjani, Y. Zhang, B. Liu, S. M. Rubinstein, and K. Bertoldi. Kirigami skins make a simple soft actuator crawl. *Science Robotics*, 3(15):eaar7555, 2018. doi: 10.1126/scirobotics.aar7555.

Chapter 5

PROGRAMMING TEMPORAL MORPHING OF SELF-ACTUATED SHELLS

R. Guseinov, C. McMahan, J. Pérez, C. Daraio, and B. Bickel. Programming temporal morphing of self-actuated shells. *Nature Communications*, 11(1):1–7, 2020. doi: 10.1038/s41467-019-14015-2.
C.M. designed the mechanical characterization experiments and participated in the conduction of unit-cell characterization experiments, in data analysis, in mechanical modeling, and in writing and revising the manuscript.

Chapter preamble

This chapter discusses an inverse design technique for the first time in this thesis. The technique enables the programming of self-actuated tri-layer shells that morph into target 3D geometries, allowing a degree of control over the rates at which each region of the structures deforms. Discrete conformal mappings are used as the starting point for the method. The inverse design of the non-uniform mesostructure geometry then relies on an extensive set of unit cell characterization experiments to couple effective spring network representations of the outer shell layers to a finite element mesh description of the mid-layer membrane.

Chapter abstract

Advances in shape-morphing materials, such as hydrogels and shape-memory polymers have enabled prescribing self-directed deformations of initially flat geometries. However, most proposed solutions evolve towards a target geometry without considering time-dependent actuation paths. To achieve more complex geometries and avoid self-collisions, it is critical to encode a spatial and temporal shape evolution within the initially flat shell. Recent realizations of time-dependent morphing are limited to the actuation of few, discrete hinges and cannot form doubly curved surfaces. Here, we demonstrate a method for encoding temporal shape evolution in architected shells that assume complex shapes and doubly curved geometries. The shells are non-periodic tessellations of pre-stressed unit cells that soften in water at rates prescribed locally by mesostructure geometry. A midplane contraction is coupled to the formation of encoded curvatures. We propose an inverse design tool based on a data-driven model for unit cells' temporal responses.

5.1 Introduction

Morphing flat sheets into complex, three-dimensional geometries is a challenge that has been pursued for centuries by artists, and more recently by mathematicians and scientists [1–3]. In engineering, the search for materials suitable for such transformations has been motivated by the ease of two-dimensional fabrication [4], which relies on subtractive processes, such as punching, machining, water jetting or laser cutting. Flat objects can be stacked in volumetrically efficient arrangements, which simplifies transportation and storage. While flat sheets are easy to fabricate and store, many structural and functional applications across scales rely on changing surface curvatures (e.g., tunable mirrors [5, 6] and parabolic antennae [7]). Morphing between flat geometries and desired curved surfaces requires methods for prescribing local deformations.

To reach non-zero Gaussian curvatures from initially flat shells, bending must be coupled to in-plane stretches, according to Gauss' *Theorema Egregium* [8]. Several frameworks have been proposed to achieve this. Notably, the out-of-plane deformations of auxetic and kirigami sheets are defined by the architecture of voids or cut patterns [9–11]. Kinematic frustration has recently been embraced for changing the curvature of initially flat shells [12, 13]. These examples are suitable for light-weight structures, but require mechanical stimuli to achieve 3D shapes through manual forming, boundary loading, or through the release of a pre-stretched sheet. Self-actuation is desirable in morphing shells because it enables untethered structural adaptation to changing environmental stimuli. To this end, responsive materials combine structural, sensing, and actuation capabilities in structures that remain flat until a non-mechanical environmental stimulus triggers the actuation process.

For example, self-actuation has been demonstrated in shells through hydrogel swelling [2, 14] and nematic-to-isotropic phase changes in liquid crystal elastomers [15]. A variety of 4D-printed systems can also be used to achieve desired shapes by coupling locally prescribed in-plane kinematics to changes in curvature [16–22]. Self-actuation has been extended to the folding of origami [23, 24], which is one of the most common and well-studied methods for inducing shape changes in initially flat objects [1, 4, 25, 26]. However, none of these proposed solutions demonstrate control over deformation rates during morphing processes. Consequently, self-collisions may occur in attempts to realize more complex geometries.

The ability to locally control the shape evolution in time drastically expands the design space of self-morphing shells. More broadly, an intrinsic capacity for pre-

programmed temporal responses allows designing materials that can perform complex tasks, like self-deployment and locomotion, without the need for external controllers or power supplies [27]. While time-dependent folding has been demonstrated in structures that are wired to power sources and electronic control devices [28, 29], a small number of architected shells made of materials with intrinsic actuation capabilities have incorporated temporal programming through the sequential folding of discrete hinges [30–32]. However, none of these examples allow for changes in Gaussian curvature. They realize sequential folding of few discrete hinges [32], must be fabricated in their target shape prior to manual programming [30], or rely on ad-hoc empirical designs that do not account for characterizations of their materials' time-dependent constitutive responses [31].

Here, we show that spatio-temporal information can be embedded in the geometry of architected shells that morph from flat to smooth three-dimensional shapes. This programmed temporal evolution enables reaching target geometries that would be impeded by collisions if shells actuated with uniform or unplanned deformation rates. Furthermore, our shells use polymers that actuate when the temperature in their environment is set to a critical value. At room temperature, they remain flat, storing the energy necessary to drive the deformation.

5.2 Results

Spatio-temporal programming of self-actuated shell mechanisms

We propose an inverse design algorithm for shell architectures and the temporal evolution of their shapes (Fig. 5.1a). The algorithm collects user inputs at two stages: the first input is the desired 3D target surface, and the second is the specification of local deformation rates. We term this temporal map input an *actuation time landscape*. The algorithm outputs the mesostructure for initially flat shells that we fabricate and test. These shells have three layers, with a $\sim$ 4.6 mm total thickness. The two outer layers are 3D-printed tessellations of non-uniform unit cells, made of Vero PureWhite (Stratasys). The middle layer is a 0.5 mm thick pre-stretched elastic membrane, which stores the energy required to drive the morphing process. Actuation from the flat to the curved profile is triggered by immersing the shells into 56° *C* water, which causes the outer layers to soften over the course of approximately 30 to 80 s.

The unit cells have a grid spacing of $\sim$ 10 mm, and are composed of cylindrical bases connected at the external shell surfaces by pairs of V-shaped brackets (Fig. 5.1b).

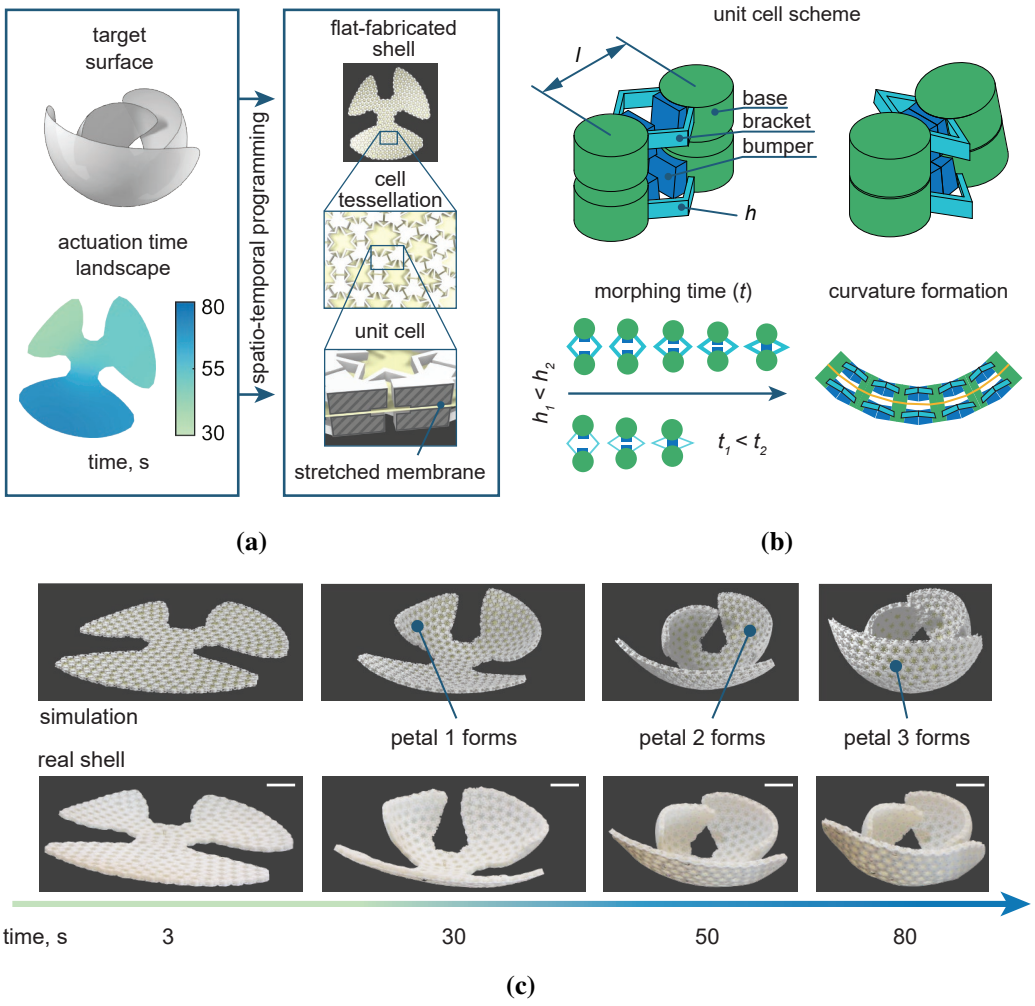

Figure 5.1: Encoding spatial and temporal shape evolution in a flat shell mesostructure. (a) A user-specified target surface and actuation time landscape (a field of deformation completion times) are inputs to an inverse design procedure that defines the mesostructure of flat-fabricated shells that morph into the target geometries. The shells are composed of inhomogeneous tessellations of unit cells with an interior pre-stretched membrane. (b) Each unit cell has an initial central length l. Brackets control actuation time through their softening rate, which is controlled by their thickness, h, and a set of bumpers prescribe final local curvatures upon collision. (c) Morphing of a petalled structure with an actuation time landscape ensuring that larger petals cover their smaller neighbors avoiding collisions on the way. Simulation and experiments are compared at 3, 30, 50, and 80 seconds in water. The structure replicates the encoded actuation time landscape shown in (a). Scale bars, 3 cm.

The bases serve as attachment points to the elastic membrane and as mounting points for the brackets. The brackets serve as nonlinear springs: they hold the structure flat prior to being placed in water, and then they guide the temporal morphing process, softening at rates determined by their geometric parameters when heated (thicker brackets soften at slower rates). There are also bumpers attached to the bases in

the space between the brackets, which collide when the local contraction reaches the target magnitude and control the contact angle between adjacent unit cells. The membrane provides energy for actuation, compressing the brackets as they soften. All of these components play an important role for reaching targeted geometries through spatio-temporal programming. For example, the petalled structure shown in Fig. 5.1c has been programmed so that the petals reach their target shape sequentially, actuating from smallest to largest (Supplementary Movie 1 – see Appendix D.7 to access all videos). If all petals deformed at the same rate, they would collide and would not reach the target geometry. More details on shell design are available in Appendix D.1.

We incorporated a discretized mechanical model of our shells in an inverse design algorithm for obtaining desired temporal morphing. Given a target geometry and a smooth time landscape, the algorithm automatically generates the flat shell mesostructure that will produce the corresponding morphing process. It first composes a continuous target shell out of compressed unit cells. To do this, the target surface is isotropically triangulated, producing a stencil that serves as a placeholder for base locations. With the arrangement of bases in the target shape, the bumper geometries are defined to ensure that they are in contact in this target shape (Fig. 5.1b top-right). Then, a minimal distortion conformal map [33] flattens the stencil. The bases with bumpers are then relocated to the flat stencil and are interconnected by brackets. Note that this stencil has to be free of overlaps to enable fabrication. Therefore, base placement, bumper arrangements and bracket lengths are configured automatically given a target surface input. However, the selection of bracket thicknesses is governed by the designer's specification of the actuation time landscape. Thicker brackets soften at a slower rate than narrower ones, enabling distinct target deformation times to be realized in each region of the shell for collision avoidance, visual impression or other desired functionalities. Given that there can be a broad range of morphing sequences that yield certain target geometries, the morphing process can be designed according to the designer's goals by iterating through actuation time landscapes and observing their effect.

The time evolution of the shells is simulated quasistatically by coupling a finite element simulation of the rubber membrane with a data-driven spring model for the brackets and a rigid body model for bases. Bumper collisions are described as sharp increases in bracket stiffness in the model. A summary of the energy model is given below. Its constitutive parts are the energy associated with bracket compression

(W_c) obtained from fitting and interpolating experimental data, an energy penalty to shearing (W_s) that replicates the effect of the shear-resisting bracket geometry, and the elastic membrane energy (W_m):

$$W(\mathbf{x}) = \sum_{c_{ij}} W_c + \sum_{s_{ij}} W_s + \sum_{\mathcal{T}_i} W_m(\mathbf{G}_i). \tag{5.1}$$

Here, c_{ij} refers to the contractile springs that join the i-th and the j-th bases. Each unit cell is modeled with four of these springs to capture bending effects. Bumper collisions are modelled as a sharp stiffening of these elements. Shear-resisting elements s_{ij} have analogous indexing. $\mathcal{T}_i$ refers to the i-th element of the membrane discretization, and $\mathbf{G}_i$ is the deformation gradient of the membrane evaluated at this element. A complete description of the simulation procedure is available in Appendix D.2.

To construct the constitutive model for bracket softening, we conducted experiments (Fig. 5.2a) on brackets of varying length l (in a range 5–9 mm) and thickness h (0.3–0.65 mm), applying constant forces (1–5 N) and tracking their compression over time spent in water using a Zwick tensile tester (Figs. 5.2b and 5.2c). Fits to the experimental data were then sampled from the space of bracket parameters and immersion times to build a time-dependent force-displacement model used in the simulation (Fig. 5.2d). Material measurement and modelling are discussed more extensively in Appendix D.3. From this sampling, we select bracket thicknesses that yield target deformation timings under the loads generated by the membrane (see Appendix D.4).

Examples of temporally programmed structures

We highlight the effect that different actuation time landscapes have on the final shapes of initially flat shells by comparing the example discussed in Fig. 5.1c to the shell shown in Fig. 5.3a. Both shells have similar flat geometries but different actuation time landscapes are encoded in their mesostructures. In the first example, smaller petals are covered by their larger neighbors. Meanwhile, each petal shown in the second example has an edge that covers a neighbor and one edge that is covered. For the latter case, all the petals have been programmed with the same actuation time landscape so they deform simultaneously. We slightly increased target actuation times for some petal tips to increase the distance between neighboring petals on their morphing paths (Supplementary Movie 2). This way, the interior edge of each petal completes its deformation before being covered by its neighbor. Shape-morphing

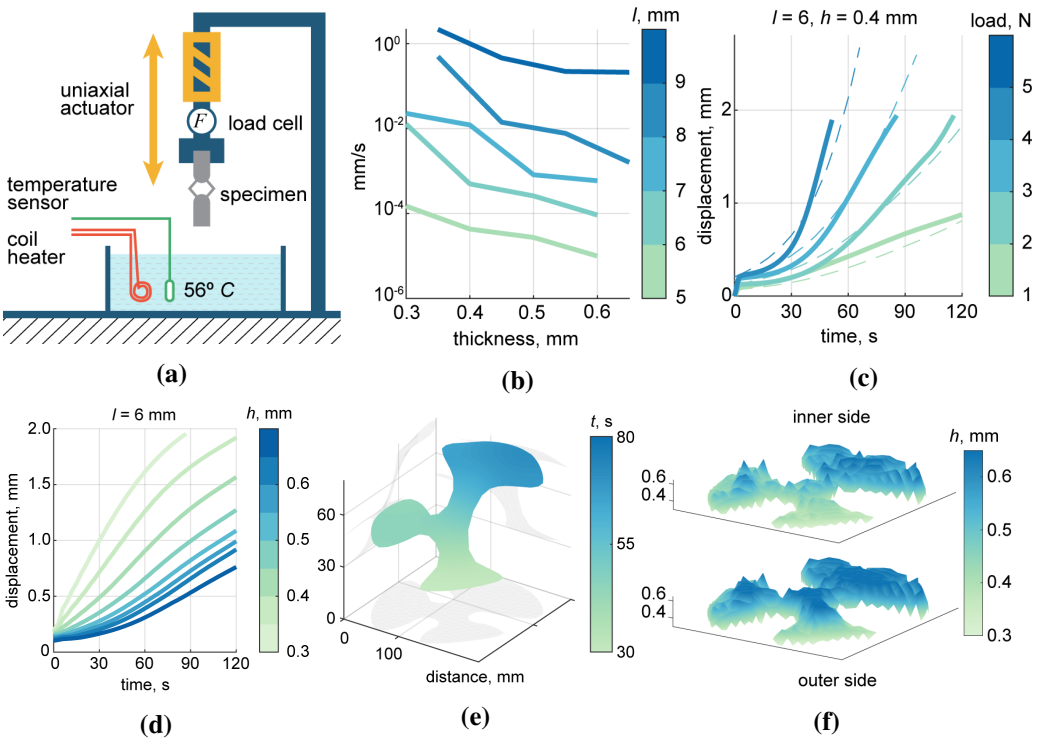

Figure 5.2: Modeling bracket softening and prescribing an actuation time landscape. (a) Load-controlled tensile tests were used to determine the deformation rates of unit cells in 56° C water. (b) Average deformation rates for specimens subject to constant loads of 4 N for $l < 7$ and 5 N for $l \geq 7$ N. These values are close to the inner membrane tractions on each unit cell in real shells. (c) Deformation rate measurements (solid lines) are fit (dashed lines) to produce a model of bracket softening. Here we show the fit for $l = 6$ mm, $h = 0.4$ mm. (d) The model is interpolated and queried to infer the mesostructure that yields target curvatures and deformation completion times in each section of the shell. Here, we show deformations of unit cells with central length $l = 6$ mm and a range of bracket thicknesses from 0.3 mm to 0.65 mm. (e) Smooth actuation time landscape that induces the sequential deformation process demonstrated in Fig. 5.1c. (f) Bracket thickness fields for both sides of the petalled shape. Though the prescribed time landscape is smooth, the field of bracket thickness is highly irregular because bracket thicknesses also depend on initial unit cell lengths and their target deformations.

precision was measured using a 3D scan of the final geometry. The blue markers were matched with their simulated locations. The resulting mean error for the pairwise distances in the experimental realization of the structure shown in Fig. 5.3a was 3.6% relative to the diameter of the target markers' point cloud.

Developable target surfaces can also be achieved using this structural framework. The actuation time landscape for the double-loop spiral shown in Fig. 5.3b is a constant gradient from one end to the other. This allows the interior to curl without colliding with the outer loop (Supplementary Movie 3). The 3D scan reveals a 2.4%

mean error. Geometries with negative Gaussian curvature can also be realized, such as the saddle shown in Fig. 5.3c (Supplementary Movie 4). The relative mean error for the saddle's base positions was 0.8%.

We showcase the complexity of achievable shapes through the self-interweaving structure shown in Fig. 5.3d. This shape requires embedding precise morphing trajectories and time landscapes in the flat-printed structure in order to thread each arm through the loop created by a neighboring one without colliding (Supplementary Movie 5). The experimental replication of this challenging target geometry yields a 9.7% 3D scan mean error, and highlights the versatility of our design and simulation framework.

5.3 Discussion

The realization of complex 3D geometries from flat-fabricated structures, which are easier to manufacture and transport, is a compelling motivation for developing shape-morphing frameworks. However, to be used in a broad range of engineering applications, the morphed structures must remain structurally stable. In our examples, the shells' outer layers soften during deformation in hot water, but become stiff when returned to room temperature (see the details on the shells' fabrication procedure in the Appendix D.5). Data from simple mechanical tests on flat structures are available in Appendix D.6. Structural stability could be further increased by using snap-locking mechanisms instead of bumpers or coating the structure after actuation has completed.

Our method for programming temporal morphing in shells is based on a combination of a pre-stressed midplane and outer layers with effective stiffness differentials that are configured to evolve over time according to user specifications. The encodement is performed using an inverse design algorithm that takes a target surface and an actuation time landscape as inputs and outputs a mesostructure with embedded self-morphing information. The significance of this method is that it enables collision-avoidance during deformations from flat shapes to curved geometries. We built a design system based on a data-driven mechanical model of mesostructures to predict shape evolution in time, enabling temporal morphing design. Applications of self-actuating shells to biomedical and construction industries are close to becoming reality with the fast advances in this field of study. Further generalizations of our approach to other materials such as liquid-crystal elastomers, bio-compatible polymers, and conventional engineering materials whose properties evolve in time

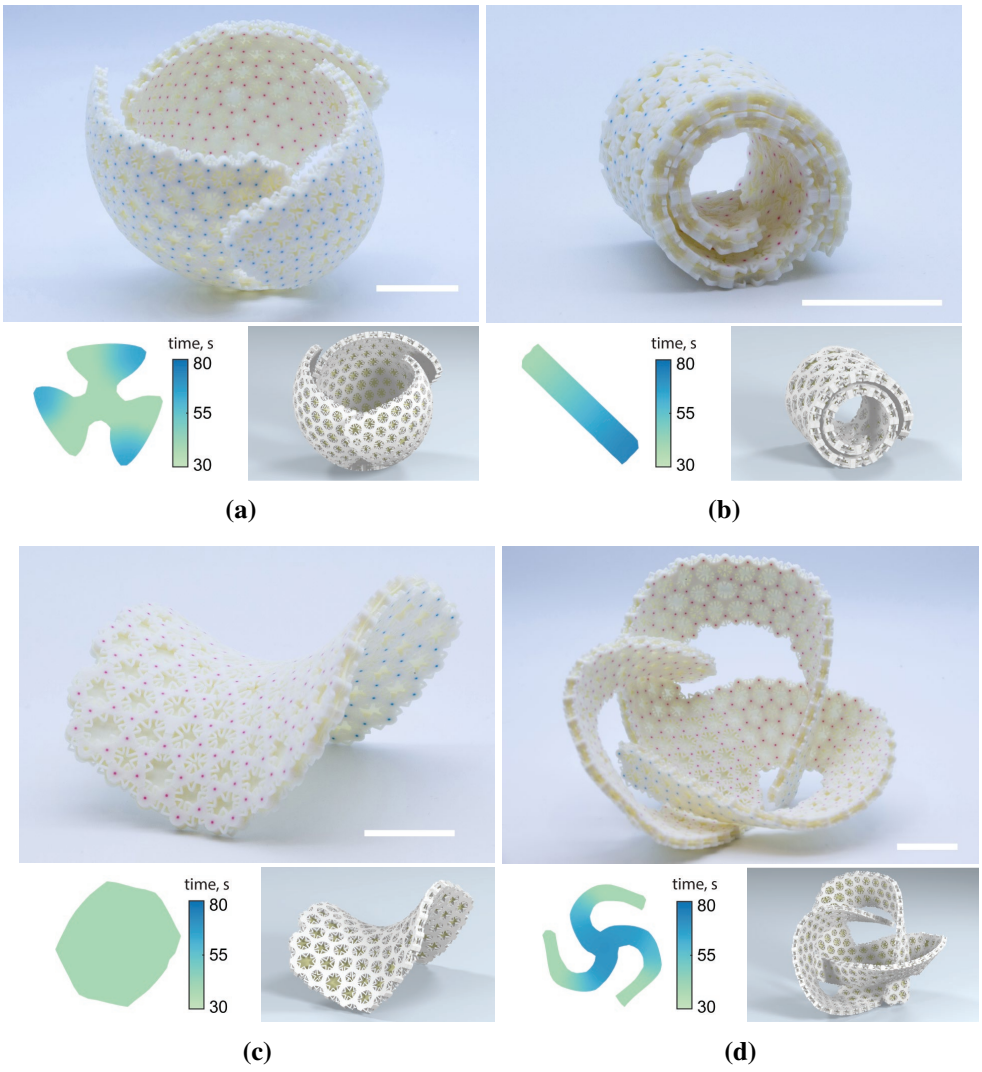

Figure 5.3: Spatio-temporally programmed shells. Each panel shows a real shell (top), its actuation time landscape (bottom-left), and its corresponding simulated shell (bottom-right). (a) Doubly-curved shell where petals morph synchronously to cover each other in a cyclic manner. One corner of each petal is programmed to morph slower to increase the distance between petals during morphing. (b) A double spiral that approximates a developable surface. A gradient time landscape enables the inner spiral to curl first. (c) A saddle shape with negative curvature. (d) A shell with a complex self-interweaving shape prone to multiple collisions in the course of its morphing process. Scale bars, 3 cm.

due to other stimuli such as temperature, humidity, light, pH, etc., could enable rapid manufacturing of load-bearing structures that can only assume desired geometries through temporally planned deformations upon deployment as well as robotic materials temporally programmed for a broader range of functionalities.

5.4 Methods

Experiments

All specimens used for bracket characterization and the outer layers of the shape-morphing structures were 3D-printed using a Stratasys J750 using Vero Pure White material. Colored markers were included in the bases to facilitate visualization. Water was kept at 56° C using a temperature controller, and two Canon 700D cameras were used for imaging.

The mechanical properties of the brackets were measured using a Zwick tensile tester with a custom-built water tank attachment. Experiments measuring strain restitution after unloading were conducted to estimate the plastic fraction of the deformation. These experiments are discussed more extensively in Appendix D.3.

All shells were fabricated by first uniformly stretching a latex sheet of thickness 0.5 mm to 900% its initial area. After cleaning the membrane surfaces with 2-Propanol, the printed lattices are glued to the membrane. In each structure, several bases have holes to align the opposite shell layers using push-pins. Latex surplus surrounding the assembled flat shell is removed, then the shells are submerged into a $350 \times 350 \times 350$ mm water tank to induce shape-morphing. See Appendix D.5 for more details.

Data fitting and simulation

Experimental data was used to generate a force-displacement model of brackets by combining simpler fitting components. First, displacement-force curves were fitted so that the initial state corresponded to the behavior at room temperature. Second, displacement rates dependent on time in water were fitted. Based on the combination of these two fittings, the parameter domain was resampled to yield time-dependent force-displacement relationships. Data from the plasticity experiments were used to build the final elastoplastic model used in the simulation software for inverse design.

In addition to implementing this data-driven bracket compression model in simulations, shear-resisting elements are included to capture brackets' geometry-based shear resistance. Bases are simulated as rigid bodies and a FEM approach is used for the membrane simulation. Bumper collisions are modelled as abrupt bracket stiffness increases. All simulation elements are coupled via shared vertices. We implemented the simulations using a `C++` code developed in-house. A simple user interface was designed to import target surfaces and specify time landscapes. User inputs are automatically processed to configure the simulated structure and display

resulting morphing processes. Once the desired morphing is achieved, the system automatically generates structures for 3D printing.

The data-fitting and simulation procedures are explained in more detail in Appendices D.2 and D.3.

3D scanning

An HP David SLS-3 structured light scanner with two cameras was used to generate textured 3D meshes in OBJ format. Then, the textures were filtered to obtain binary images with markers. Markers were lifted to their actual scanned positions using the 3D mesh and resolved to single points. The obtained point clouds were registered to the clouds generated by the simulation software and points were matched using Munkres' algorithm.

Acknowledgements

R.G. and B.B. were supported by the European Research Council (ERC) under grant agreement No 715767 - MATERIALIZABLE: Intelligent fabrication-oriented Computational Design and Modeling. J.P. was supported by the European Union's Horizon 2020 Marie Sklodowscka-Curie COFUND Action ISTPlus under Grant Agreement No. 754411. C.M. and C.D. were supported by the US Army Research Office Grant W911NF-17-1-0147. C.M. was supported by a NASA Space Technology Research Fellowship.

References

[1] R. J. Lang. A computational algorithm for origami design. In *Proceedings of the Twelfth Annual Symposium on Computational Geometry*, SCG '96, pages 98–105. ACM, 1996. ISBN 0-89791-804-5. doi: 10.1145/237218.237249. URL http://doi.acm.org/10.1145/237218.237249.

[2] Y. Klein, E. Efrati, and E. Sharon. Shaping of elastic sheets by prescription of non-euclidean metrics. *Science*, 315(5815):1116–1120, 2007. ISSN 0036-8075. doi: 10.1126/science.1135994. URL http://science.sciencemag.org/content/315/5815/1116.

[3] C. Baek, A. O. Sageman-Furnas, M. K. Jawed, and P. M. Reis. Form finding

in elastic gridshells. *Proceedings of the National Academy of Sciences*, 115 (1):75–80, 2018. doi: 10.1073/pnas.1713841115.

[4] S. J. P. Callens and A. A. Zadpoor. From flat sheets to curved geometries: Origami and kirigami approaches. *Materials Today*, 21(3):241–264, 2018. doi: 10.1016/j.mattod.2017.10.004.

[5] M. Clampin. Status of the james webb space telescope (jwst). In *Space Telescopes and Instrumentation*, volume 7010, 2008. doi: 10.1117/12.790388. URL `https://doi.org/10.1117/12.790388`.

[6] W. Liu and J. J. Talghader. Current-controlled curvature of coated micromirrors. *Optics Letters*, 28(11):932–934, 2003.

[7] E. Peral, S. Tanelli, Z. Haddad, O. Sy, G. Stephens, and E. Im. Raincube: A proposed constellation of precipitation profiling radars in cubesat. In *2015 IEEE International Geoscience and Remote Sensing Symposium (IGARSS)*, pages 1261–1264, July 2015. doi: 10.1109/IGARSS.2015.7326003.

[8] C. F. Gauss. *Disquisitiones generales circa superficies curvas*. Typis Dietericianis, 1828.

[9] M. Konaković, K. Crane, B. Deng, S. Bouaziz, D. Piker, and M. Pauly. Beyond developable: Computational design and fabrication with auxetic materials. *ACM Transactions on Graphics*, 35(4):89, 2016. doi: 10.1145/2897824.2925944.

[10] F. Wang, X. Guo, J. Xu, Y. Zhang, and C. Q. Chen. Patterning curved three-dimensional structures with programmable kirigami designs. *Journal of Applied Mechanics*, 84(6):061007, 2017. doi: 10.1115/1.4036476.

[11] Y. Zhang, Z. Yan, K. Nan, D. Xiao, Y. Liu, H. Luan, H. Fu, X. Wang, Q. Yang, J. Wang, W. Ren, H. Si, F. Liu, L. Yang, H. Li, J. Wang, X. Guo, H. Luo, L. Wang, Y. Huang, and J. A. Rogers. A mechanically driven form of kirigami as a route to 3D mesostructures in micro/nanomembranes. *Proceedings of the National Academy of Sciences*, 112(38):11757–11764, 2015. doi: 10.1073/pnas.1515602112.

[12] R. Guseinov, E. Miguel, and B. Bickel. Curveups: Shaping objects from flat plates with tension-actuated curvature. *ACM Transactions on Graphics*, 36(4):64, 2017. doi: 10.1145/3072959.3073709.

[13] P. Celli, C. McMahan, B. Ramirez, A. Bauhofer, C. Naify, D. Hofmann, B. Audoly, and C. Daraio. Shape-morphing architected sheets with non-periodic cut patterns. *Soft Matter*, 14(48):9744–9749, 2018. doi: 10.1039/C8SM02082E. URL `http://dx.doi.org/10.1039/C8SM02082E`.

[14] J. Kim, J. A. Hanna, M. Byun, C. D. Santangelo, and R. C. Hayward. Designing responsive buckled surfaces by halftone gel lithography. *Science*, 335(6073): 1201–1205, 2012.

[15] T. H. Ware, M. E. McConney, J. J. Wie, V. P. Tondiglia, and T. J. White. Voxelated liquid crystal elastomers. *Science*, 347(6225):982–984, 2015. doi: 10.1126/science.1261019.

[16] A. S. Gladman, E. A. Matsumoto, R. G. Nuzzo, L. Mahadevan, and J. A. Lewis. Biomimetic 4D printing. *Nature Materials*, 15(4):413–418, April 2016.

[17] D. Raviv, W. Zhao, C. McKnelly, A. Papadopoulou, A. Kadambi, B. Shi, S. Hirsch, D. Dikovsky, M. Zyracki, C. Olguin, et al. Active printed materials for complex self-evolving deformations. *Scientific Reports*, 4, 2014.

[18] A. Kotikian, R. L. Truby, J. W. Boley, T. J. White, and J. A. Lewis. 3D printing of liquid crystal elastomeric actuators with spatially programed nematic order. *Advanced Materials*, 30(10):1706164, 2018. doi: 10.1002/adma.201706164. URL https://www.onlinelibrary.wiley.com/doi/abs/10.1002/adma.201706164.

[19] M. O. Saed, C. P. Ambulo, H. Kim, R. De, V. Raval, K. Searles, D. A. Siddiqui, J. M. O. Cue, M. C. Stefan, M. R. Shankar, and T. H. Ware. Molecularly-engineered, 4D-printed liquid crystal elastomer actuators. *Advanced Functional Materials*, 29(3):1806412, 2019. doi: 10.1002/adfm.201806412. URL https://onlinelibrary.wiley.com/doi/abs/10.1002/adfm.201806412.

[20] C. P. Ambulo, J. J. Burroughs, J. M. Boothby, H. Kim, M. R. Shankar, and T. H. Ware. Four-dimensional printing of liquid crystal elastomers. *ACS Applied Materials & Interfaces*, 9(42):37332–37339, 2017. doi: 10.1021/acsami.7b11851. URL https://doi.org/10.1021/acsami.7b11851. PMID: 28967260.

[21] A. A. Bauhofer, S. Krödel, J. Rys, O. R. Bilal, A. Constantinescu, and C. Daraio. Harnessing photochemical shrinkage in direct laser writing for shape morphing of polymer sheets. *Advanced Materials*, 29(42):1703024, 2017. doi: 10.1002/adma.201703024.

[22] J. W. Boley, W. M. van Rees, C. Lissandrello, M. N. Horenstein, R. L. Truby, A. Kotikian, J. A. Lewis, and L. Mahadevan. Shape-shifting structured lattices via multimaterial 4D printing. *Proceedings of the National Academy of Sciences*, page 201908806, 2019.

[23] J. H. Na, A. A. Evans, J. Bae, M. C. Chiappelli, C. D. Santangelo, R. J. Lang, T. C. Hull, and R. C. Hayward. Programming reversibly self-folding origami with micropatterned photo-crosslinkable polymer trilayers. *Advanced Materials*, 27(1):79–85, 2014. doi: 10.1002/adma.201403510.

[24] P. Plucinsky, B. A. Kowalski, T. J. White, and K. Bhattacharya. Patterning nonisometric origami in nematic elastomer sheets. *Soft Matter*, 14:3127–3134, 2018. doi: 10.1039/C8SM00103K.

[25] L. H. Dudte, E. Vouga, T. Tachi, and L. Mahadevan. Programming curvature using origami tessellations. *Nature Materials*, 15:583–588, 2016. doi: 10.1038/nmat4540.

[26] E. D. Demaine and T. Tachi. Origamizer: A practical algorithm for folding any polyhedron. In *33rd Internaional Symposium on Computational Geometry (SoCG 2017)*, volume 77, pages 34:1–34:16, 2017. doi: 10.4230/LIPIcs.SoCG.2017.34.

[27] A. Kotikian, C. McMahan, E. C. Davidson, J. M. Muhammad, R. D. Weeks, C. Daraio, and J. A. Lewis. Untethered soft robotic matter with passive control of shape morphing and propulsion. *Science Robotics*, 4(33):eaax7044, 2019.

[28] E. Hawkes, B. An, N. M. Benbernou, H. Tanaka, S. Kim, E. D. Demaine, D. Rus, and R. J. Wood. Programmable matter by folding. *Proceedings of the National Academy of Sciences*, 107(28):12441–12445, 2010. doi: 10.1073/pnas.0914069107.

[29] S. Felton, M. Tolley, E. Demaine, D. Rus, and R. Wood. A method for building self-folding machines. *Science*, 345(6197):644–646, 2014. ISSN 0036-8075. doi: 10.1126/science.1252610. URL http://science.sciencemag.org/content/345/6197/644.

[30] Y. Mao, K. Yu, M. S. Isakov, J. Wu, M. L. Dunn, and H. J. Qi. Sequential self-folding structures by 3D printed digital shape memory polymers. *Scientific Reports*, 5:13616, September 2015. URL https://doi.org/10.1038/srep13616. Article.

[31] Y. Tao, J. Gu, B. An, T. Cheng, X. A. Chen, X. Zhang, W. Zhao, Y. Do, T. Zhang, and L. Yao. Demonstrating thermorph: Democratizing 4D printing of self-folding materials and interfaces. In *Extended Abstracts of the 2018 CHI Conference on Human Factors in Computing Systems*, CHI EA '18, pages D405:1–D405:4. ACM, 2018. ISBN 978-1-4503-5621-3. doi: 10.1145/3170427.3186478. URL http://doi.acm.org/10.1145/3170427.3186478.

[32] Y. Liu, B. Shaw, M. D. Dickey, and J. Genzer. Sequential self-folding of polymer sheets. *Science Advances*, 3(3), 2017. doi: 10.1126/sciadv.1602417. URL https://advances.sciencemag.org/content/3/3/e1602417.

[33] B. Springborn, P. Schröder, and U. Pinkall. Conformal equivalence of triangle meshes. *ACM Transactions on Graphics*, 27(3):77:1–77:11, August 2008. ISSN 0730-0301. doi: 10.1145/1360612.1360676. URL http://doi.acm.org/10.1145/1360612.1360676.

[34] R. Guseinov, C. McMahan, J. Pérez, C. Daraio, and B. Bickel. Programming temporal morphing of self-actuated shells. *Nature Communications*, 11(1): 1–7, 2020. doi: 10.1038/s41467-019-14015-2.

Chapter 6

UNTETHERED SOFT ROBOTS WITH PASSIVE CONTROL OF SHAPE MORPHING AND PROPULSION

A. Kotikian*, C. McMahan*, E. C. Davidson, J. M. Muhammad, R. D. Weeks, C. Daraio, and J. A. Lewis. Untethered soft robotic matter with passive control of shape morphing and propulsion. *Science Robotics*, 4(33), 2019. doi: 10.1126/scirobotics.aax7044.

C.M. and A.K. contributed equally to this work. C.M. participated in the conception of the project, in designing the experiments, in material characterization experiments, in the design of the proof-of-concept demonstrations, and in writing and revising the manuscript. C.M. also coded the 3D printer nozzle paths and performed mechanical modeling.

Chapter preamble

In this chapter, micro- and mesoscale patterning are discussed within the context of designing soft robots with easy-to-predict kinematics. The extrusion of liquid crystal elastomer (LCE) inks during a direct ink writing 3D printing process causes the liquid crystal mesogens to be aligned in the direction of the printing path. Self-folding hinges are attained by stacking LCE layers with orthogonal microstructural geometry. These active hinges can then be embedded in larger devices that change shape and self-propel in response to environmental stimuli.

Chapter abstract

There is growing interest in creating untethered soft robots that can repeatedly shape-morph and self-propel in response to external stimuli. Toward this goal, we printed soft programmable materials composed of liquid crystal elastomer (LCE) bilayers with orthogonal director alignment and different nematic-to-isotropic transition temperatures (T_{NI}) to form active hinges that interconnect polymeric tiles. When heated above their respective actuation temperatures, the printed LCE hinges exhibit a large, reversible bending response. Their actuation response is programmed by varying their chemistry and printed architecture. Through an integrated design and additive manufacturing approach, we created passively controlled, untethered soft programmable materials that adopt task-specific configurations on demand, including a self-twisting origami polyhedron that exhibits three stable configurations and

a “rollbot” that assembles into a pentagonal prism and self-rolls in programmed responses to thermal stimuli.

6.1 Introduction

Soft robots are versatile in ways that rigid systems are not. Their compliant nature allows them to safely interact with living organisms [1, 2] and fragile objects [2, 3]. They can perform complex motions as a result of simple actuation inputs [4–6], conform to arbitrary geometries [7], perform multigait propulsion [8], morph into different shapes [8, 9], and withstand large deformation or impact without damage [10]. However, challenges associated with the integration of untethered, fully soft actuation modalities currently limit their broader utilization. To date, soft robots have primarily relied on pneumatic networks embedded within elastomeric matrices for actuation and propulsion [2, 6, 8, 11]. Yet, most pneumatically actuated soft robots must be tethered to rigid power and control systems to generate sufficient forces for locomotion [6, 12]. Recently, active matter that self-actuates in response to external and internal stimuli (e.g., temperature, light, chemical gradients, and electric fields) has been explored as an alternative for soft robots [5, 13–20]. However, active materials also have limitations that must be overcome. For example, electroactive actuators must be tethered to rigid power sources [19, 20], shape-memory polymers require manual reprogramming [17, 21, 22], bilayer strips made of materials that undergo differential growth are volumetrically expensive [18, 23, 24], and hydrogel-based actuators must be paired with pneumatic systems to produce large forces quickly [1, 25].

The creation of untethered, soft robots that perform complex tasks is difficult. For example, pneumatically actuated soft robots typically undergo large deformations across their entire structural frame [8, 10]. Predicting the kinematics of these systems is not straightforward because nonlinear elastic models that satisfy a diverse set of boundary conditions are required. These challenges are compounded when the implementation of control systems is desired. Origami-based strategies offer a compelling alternative for designing soft robots that exhibit large shape changes through a reduced set of predictable motions. One can greatly simplify the design space by localizing deformations to creases within the robotic structure, e.g., using actuating hinges connected to planar facets. Recently, reconfigurable robots with rigid on-board power sources and electronic controls have been constructed by this method [25–29].

Soft robots may also benefit from hinge-based actuation, in which compliant, energy-dense actuators are placed at creases, whereas stiffer structural elements serve as planar facets [30]. Folding patterns can be modeled and predicted geometrically using existing mathematical tools [31–33]. The design and implementation of controls in origami-based untethered systems can be achieved solely through the constitutive response of the actuating hinges, and locomotive gaits can be encoded within their frames via programmable folding sequences. Although controlled folding sequences have been realized in rigid and hybrid (soft/rigid) systems [26, 34], fully soft systems implemented to date are typically irreversible [17, 22, 35], geometrically constrained [36], or tethered to rigid power sources [18, 37]. New advances are needed to generate untethered soft robots that exhibit repeatable actuation [38], self-morphing [25], and self-propulsion in response to external stimuli [39].

Liquid crystal elastomers (LCEs) have recently emerged as a promising class of soft active matter because they generate large, powerful, and repeatable deformations upon heating above their nematic-to-isotropic transition temperature (T_{NI}) [40, 41]. The direction of contractile strain (director) can be programmed by aligning rigid mesogens during fabrication [40, 41]. In addition to thermal stimuli, LCEs that respond to electric [42], light [43, 44], or chemical stimuli [13, 45] have been synthesized. However, despite their remarkable behavior, LCEs have not been widely integrated within untethered robotic structures because of fabrication challenges that relegate them to simple unidirectional actuators [40] or voxelated thin films ($\sim$ 50 μm thick) [45, 46]. Current LCEs are either too compliant to support large loads or lack the capability to output large torques in compact, untethered arrangements [18, 47–49]. Recent attempts to achieve LCE-based untethered locomotion have relied on using small-scale actuators that are not integrated with other functional components [14, 15, 50]. Recently, voxelated LCEs have been produced in thick-film geometries ($\sim$ 1 mm thick) via three-dimensional (3D) printing [51–53]. These 3D LCEs actuate reversibly and exhibit large work capacities. However, the ability to combine multiple LCE actuators with programmed director alignment with soft structural materials has not yet been demonstrated in a single-step fabrication process.

Here, we created untethered, soft programmable materials that can reversibly shape-morph and propel itself in response to thermal stimuli. Specifically, we printed LCE hinges that interconnect structural polymeric tiles to produce active architectures that exhibit large, repeatable deformations. Using this method, the folding orienta-

tion, hinge angles, and actuator geometry are fully programmable. By incorporating LCEs with two different T_{NI}, we created soft programmable materials that exhibit sequential folding and unfolding in response to different temperatures. Through an integrated design and manufacturing method, we demonstrated simple embodiments of origami-inspired soft robots, whose shape morphing and self-propulsion were passively controlled via the constitutive response of the printed matter. As an exemplar, we produced an origami-based architecture that could adopt three different stable configurations, depending on its exposure to varying thermal conditions. Next, we characterized the mechanical response of the active LCE hinges, which generated a torque capable of folding and lifting objects that were more than two orders of magnitude heavier than the hinges themselves. Last, we exploited their torque response to create a printed (flat) structure that was reconfigured to a pentagonal prism and propelled itself by rolling on a hot surface, which we refer to as a "rollbot."

6.2 Results

Printing soft active hinges and structural tiles

The active hinges and structural tiles were fabricated as shown in Fig. 6.1. All inks were formulated with the desired viscoelastic behavior needed to facilitate direct ink writing (Fig. E.1) [54]. The hinges were composed of LCE bilayers that exhibit orthogonally programmed nematic order, which interconnect each structural tile. Two oligomeric LCE inks were synthesized with low and high T_{NI} values of 24° and 94°C and are referred to as LT_{NI} and HT_{NI} inks, respectively. Such differences arise because of disparities in their backbone flexibility and cross-linking chemistry (Fig. E.2). The LT_{NI} ink was composed of a thiol-terminated liquid crystalline oligomer and trivinyl-functionalized cross-linker [52], whereas the HT_{NI} ink was composed of an acrylate-terminated liquid crystalline oligomer analogous to previously reported inks composed of main-chain mesogens (Fig. 6.2a) [45, 51, 53, 55]. To ensure strong adhesion between the printed hinges and tiles, we used a structural ink for printing the tiles that was composed of a photopolymerizable diacrylate resin and an acrylate cross-linker that chemically binds to the reactive LCE groups. The ink rheology was modified by adding fumed silica to achieve the desired yield stress and a shear thinning behavior needed for printing (Fig. E.1).

The LCE inks were printed using high operating temperature direct ink writing (HOT-DIW) [51]. To facilitate director alignment during printing, we printed the LT_{NI} ink at 26°C and the HT_{NI} ink at 50° to 55°C (Fig. E.1) [51]. Ink cross-linking

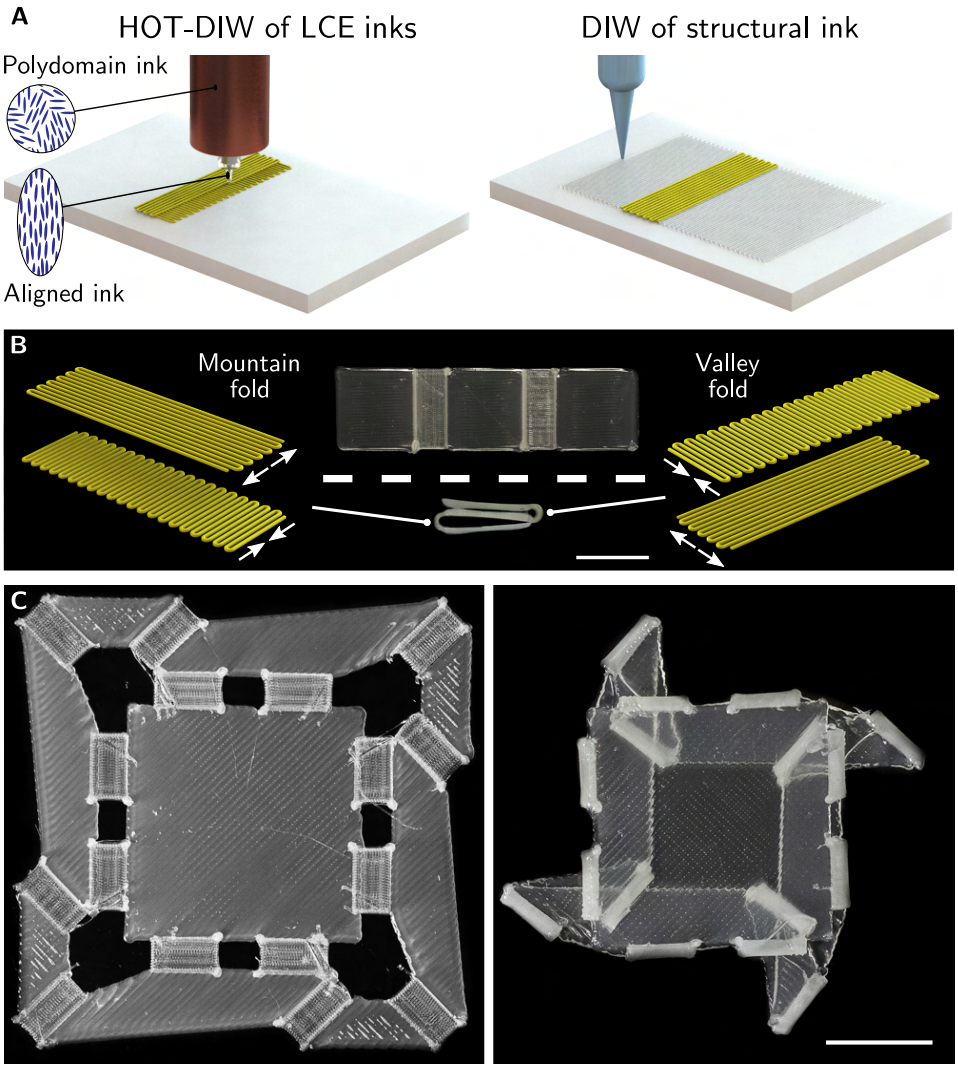

Figure 6.1: 3D printing of soft programmable materials. (a) Active hinges were printed from oligomeric LCE inks, whose rigid mesogens aligned along the print path during HOT-DIW (left). Immediately upon printing, LCE ink cross-linking was photo-initiated to lock in the desired director alignment. Structural tiles were then printed from an ink composed of acrylate resin that chemically bonded to LCE hinges upon photo-initiated cross-linking (right). (b) The LCE hinges were printed in the form of $0^o/90^o$ and $90^o/0^o$ bilayers, which bend into mountain and valley folds, respectively, when actuated above T_{NI}. A simple structure composed of two hinges, with mountain and valley folds, that interconnect three structural tiles is shown as printed (middle and top) and as actuated (middle and bottom). (c) A more complex, square-twist reconfigurable structure was printed (left) and actuated at 125°C (right). The LCE hinges that form the central square and the four LCE hinges that point toward the center of the structure (left) are mountain folds, whereas the other LCE hinges are valley folds. Scale bars, 1 cm.

was photo-initiated immediately upon printing to lock in the programmed director alignment along the print path (Fig. E.3). After printing and cross-linking, the low

T_{NI} LCE structures became fully isotropic at 92°C, and high T_{NI} LCE structures did so at 127°C [51, 53], enabling these structures to sequentially actuate in response to thermal stimuli. We note that LCE actuation can occur over a wide temperature range [52]. Unidirectionally printed HT_{NI} LCE films (0.375 mm thick) exhibited a repeated contraction of $-49.8 \pm 0.9\%$ along the printing direction and an expansion of $41.7 \pm 5.7\%$ perpendicular to that direction, whereas the LT_{NI} LCEs exhibited respective values of $-31.1 \pm 0.6\%$ and $21.5 \pm 0.6\%$ (Fig. E.4). The structural tiles were printed under ambient conditions via DIW. The placement of each structural tile induced a bending axis that is parallel to the LCE hinge interface (Fig. 6.1a, right). Upon curing, the printed tiles exhibited a stiffness of 766 ± 41 MPa, which provided the structural integrity to prevent collapse of the printed architectures under self- and applied loading conditions.

To achieve controlled bending, we fabricated each LCE hinge in a "bilayer" design, in which the bottom half is composed of multiple layers printed along the same direction and the top half is composed of multiple layers printed in the orthogonal direction (Fig. 6.1A, left). A spontaneous strain mismatch caused each hinge to bend when heated above their actuation temperature. We chose an orthogonal bilayer design because the spontaneous strains in each layer favored a single bending direction around a given axis. Consequently, greater curvatures were achieved compared with bilayer hinges composed of a top LCE layer and a bottom inactive layer [47, 48]. The folding orientation of each LCE hinge is defined by the print path. The bilayer (bottom/top) orientation relative to the printing direction determines whether they exhibit mountain ($0^o/90^o$) or valley ($90^o/0^o$) folds (Fig. 6.1b). Because self-folding is reversible, the printed structures could be repeatedly actuated by cycling above and below their respective actuation temperatures. To demonstrate this, we printed both mountain and valley hinges in a simple structure composed of two LCE hinges that interconnected three structural tiles, as shown in Fig. 6.1b (center), which repeatedly folded and unfolded without manual intervention. By varying the specific arrangement of active hinges and structural tiles, we could realize more complex self-folding structures, including the square twist unit cell shown in Fig. 6.1c (movie S1). In both cases, the architectures contained hinges printed using a single LCE ink (HT_{NI}). Below, we demonstrate the broad versatility that arose from the integration of multiple LCE hinges of different T_{NI} values with structural tiles.

Programmed sequential self-folding

Sequential self-folding is essential for untethered origami-inspired structures because this capability enables collision prevention during shape morphing and locomotive gaits with multiple degrees of freedom triggered by distinct stimuli [30, 35]. By printing LCE inks with different actuation temperatures, we created soft materials with programmable sequential folding upon heating (Fig. 6.2a). The unbiased bending angle (where hinges do not bear a load) increases with temperature for both LT_{NI} and HT_{NI} LCE hinges. From direct observations, we found that both the onset and the completion of folding for the LT_{NI} LCE hinges occur at considerably lower temperatures, relative to their HT_{NI} counterparts (Fig. 6.2b). Specifically, the LT_{NI} LCE hinges begin to fold below 40°C, whereas the onset of folding occurs near 60°C for HT_{NI} LCE hinges. Because of the residual stress that arose from cross-linking the LT_{NI} LCE hinges in their isotropic phase [56], these hinges had a negative bending angle under ambient conditions (Fig. E.5). Although both types of hinges could achieve a 180° folding angle, their temperature response depended strongly on their composition and overall dimensions (Figs. E.5 and E.6). Leveraging these capabilities, we printed a simple structure that integrated both LT_{NI} and HT_{NI} LCE mountain hinges, which interconnected three structural tiles and sequentially actuated when heated (Fig. 6.2c). As expected, the LT_{NI} LCE hinge folded completely before the HT_{NI} LCE hinge actuated. The structure unfolded in reverse upon cooling to room temperature; i.e., the HT_{NI} LCE hinge unfolded to its flat configuration first, followed by the LT_{NI} LCE hinge. This demonstration highlights our ability to create soft materials with programmed sequential folding in untethered motifs (movie S2).

Folding temperatures were programmed by the LCE chemistry, and hinge angles were prescribed geometrically by the printing process. We defined the hinge length and width as the in-plane geometric parameters in the directions parallel and perpendicular to the folding axis, respectively. The hinge thickness was defined in the surface normal direction and varied in discrete increments of 0.25 mm, which corresponds to twice the nozzle diameter used during HOT-DIW.By varying the number of printed layers, we produced hinges with thicknesses between 0.25 mm (one layer in each direction) and 1 mm (four layers in each direction). The spontaneous curvature that the actuators assume at temperatures above T_{NI} decreased with hinge thickness (Fig. 6.2d), akin to other bilayer systems [57–59]. We discuss the LCE hinge mechanics in further detail in the Supplementary Materials. HT_{NI} LCE hinges exhibited greater unbiased folding angles compared with LT_{NI} LCE hinges

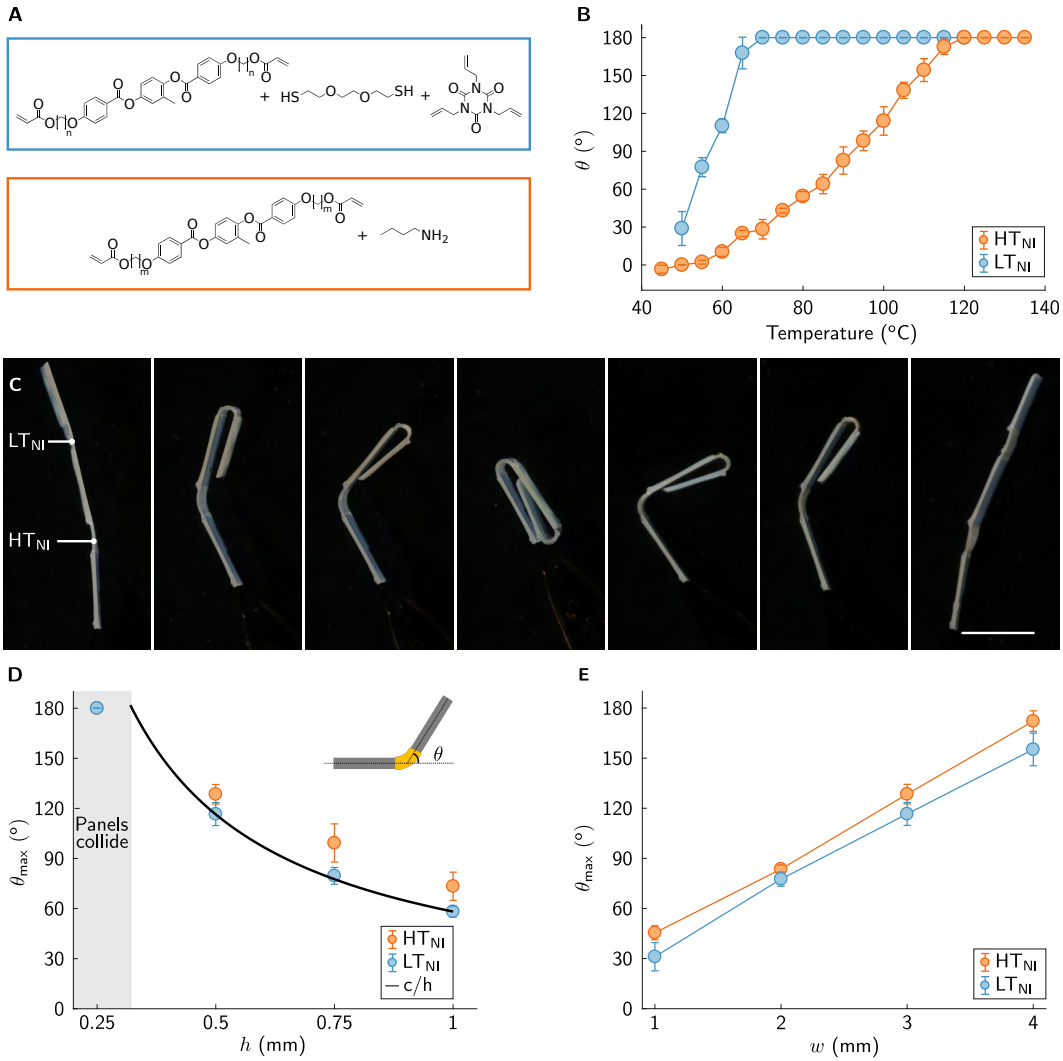

Figure 6.2: Untethered, sequential, and reversible folding of active hinges. (a) Chemical composition of the LT_{NI} (blue) and HT_{NI} (orange) oligomeric LCE inks (where $n = 3$ and 6, and $m = 6$ in the molecular structures). (b) Bending angle θ as a function of temperature for LT_{NI} and HT_{NI} LCE hinges with length of 10 mm, width of 4 mm, and thickness of 0.25 mm. (c) A printed structure composed of LT_{NI} and HT_{NI} LCE hinges with mountain folds that interconnect three structural tiles, which undergo sequential actuation when heated (left to center) and cooled (center to right). Scale bar, 1 cm. (d) Bending angle θ as a function of thickness, h, for LT_{NI} and HT_{NI} LCE hinges of fixed length of 10 mm and width of 3 mm. Their bending angle decreased with thickness. Other bilayer systems display inverse proportionality between curvature and thickness [57–59]. We plot this relationship, where c is a constant, for comparison. Both hinges exhibited a maximum bending angle of 180°, where panels contact one another. (e) Bending angle θ as a function of hinge width, w, for LT_{NI} and HT_{NI} LCE hinges of fixed length of 10 mm and thickness of 0.5 mm. Error bars indicate SD.

of identical geometry, because the strain differential between directions parallel and perpendicular to their director alignment is more pronounced [57, 59]. For a given

hinge thickness, the folding angle increased proportionally with the hinge width (Fig. 6.2e) because the curvature remained constant when their width was varied. Our additive manufacturing approach is both scalable and flexible, so there is no limit on the hinge thickness or geometry. However, the director was misaligned near each edge of the LCE hinges, where the printing nozzle changed direction in a semicircular arc to enable continuous printing of adjacent-aligned filaments. Hence, because of this effect, the minimum LCE hinge width must exceed two nozzle diameters (in this case, 0.25 mm). We note that the minimum hinge width also increased with LCE thickness because the misalignment radius increased when LCE layers were printed on top of one another compared with those printed directly on the underlying glass substrate. This misalignment caused hinges programmed as valley folds to have marginally smaller bending angles compared with those programmed as mountain folds. This is because their top layer is parallel to hinge width, which is a smaller in-plane geometric parameter than hinge length (Fig. E.7). The printed LCE hinges could bend repeatedly without bias weight, and their maximum folding angle remained constant over multiple heating and cooling cycles (Fig. E.8). Their repeatable actuation is an essential feature for untethered soft robotic applications that operate without manual intervention.

Next, we demonstrate that soft programmable materials can be designed and printed with geometric locking mechanisms. As one example, we created the triangulated polyhedron shown in Fig. 6.3, which is based on a well-known origami design [60]. The structure was printed in a planar layout (Fig. 6.3a) before manually joining the edges (Fig. 6.3b) to create an open polyhedron that was stable at room temperature (Fig. 6.3c). The top and bottom sections of the polyhedron were identical, except that different LCE inks were used to print their respective hinges. Specifically, the top section contained LT_{NI} LCE hinges that facilitated folding into a compacted form when heated above 95° C. The bottom section contained HT_{NI} LCE hinges that remained unfolded when the top layer actuated (Fig. 6.3d) yet compact when heated above 155°C (Fig. 6.3e and movie S3). An environment temperature well above the T_{NI} of both materials was used to accelerate the folding process. All hinges were constructed with a 6 mm width and 0.5 mm thickness to ensure 180° folding angles upon actuation. This geometry was stable after each intermediate folding stage, even when the structure returned to room temperature (Fig. E.9). This behavior is similar to what was observed in paper origami structures that locked in intermediate folding states due to bending of the facets between two flat-faceted states [60, 61]. Guest and Pellegrino [60] provided a good overview of these multistable geometries

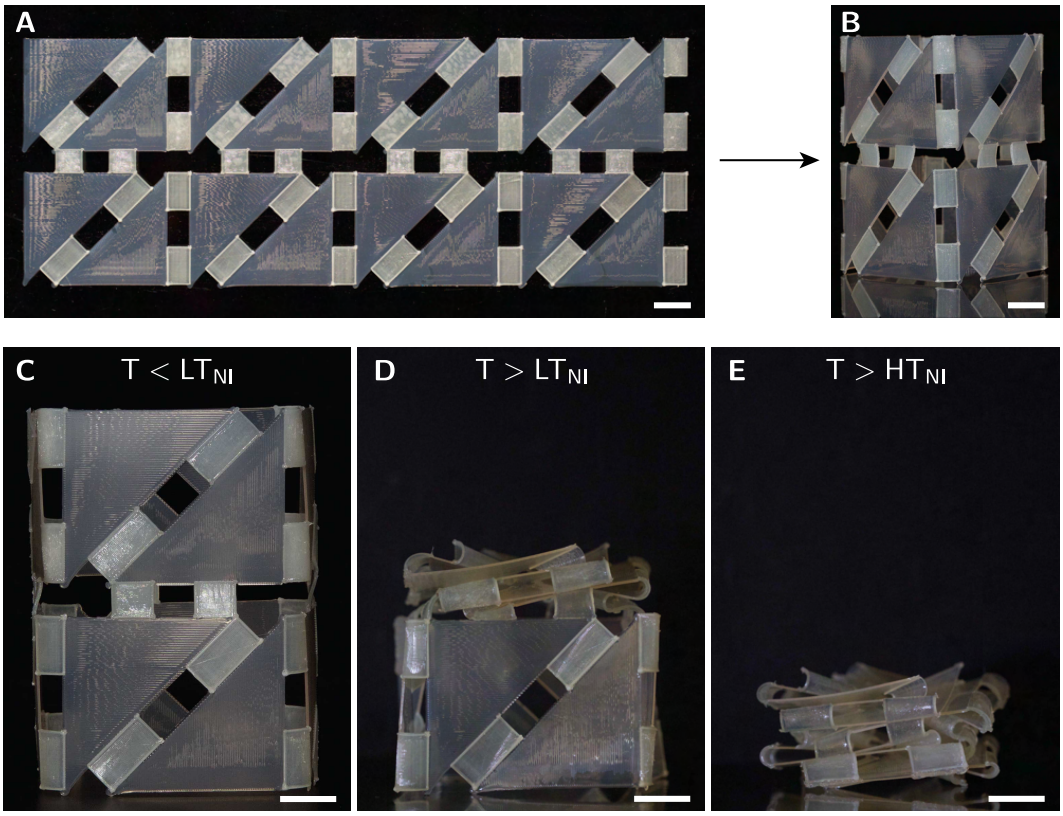

Figure 6.3: Printed soft materials with programmed sequential folding and deformation. (a) A triangulated polyhedron was printed in the form of a flat sheet composed of both LT_{NI} hinges (top section) and HT_{NI} hinges (bottom section) that interconnect the structural tiles. All diagonal LCE hinges are valley folds, whereas all vertical and horizontal LCE hinges are mountain folds. (b) The printed flat sheet was manually assembled into a 3D triangulated structure that exhibited sequential folding upon heating from (c) ambient temperature to (d) 100°C, where the LT_{NI} LCE hinges actuated, and to (e) 150°C, where the HT_{NI} LCE hinges actuated. Scale bars, 1 cm.

and their kinematics. The observed behavior (Fig. E.9) for these printed structures suggests that a variety of multistable architectures can be created by our approach.

Programmed self-propulsion

Untethered self-propulsion is a requirement for autonomous and preprogrammed robotic systems that navigate large distances in uncertain environments [21]. This poses challenges, especially given that untethered operation often requires onboard power and control systems that add mass to the robot [25, 62]. LCE bilayers offer a promising option for these tasks because they are energy dense and are capable of performing multiple loading and unloading cycles in response to external stimuli. However, because of the inherently soft nature of LCE hinges, large external moments induce bending and lead to actuated hinge angles that are different from

the unloaded hinge measurements (Fig. 6.2). As an example, a printed LT_{NI} LCE hinge achieved a 79° bending angle when unbiased (Fig. 6.4a), but when a 10 g mass was suspended 1 cm away from the hinge at room temperature, it deflected to −72° because of its compliance. When heated above T_{NI}, the hinge bent by 55°, and the mass was lifted 6.5 mm (Fig. 6.4b), corresponding to a work output of about 0.6 mJ. This actuation is remarkable for a soft actuator with dimensions 10 mm by 3 mm by 1 mm. It corresponds to an energy density of 29 J/kg when accounting for the combined mass (22 mg) of the LCE hinge and structural panels, which is in good agreement with our earlier work [51]. The mass of the lifted object was more than 450 times greater than the hinge mass.

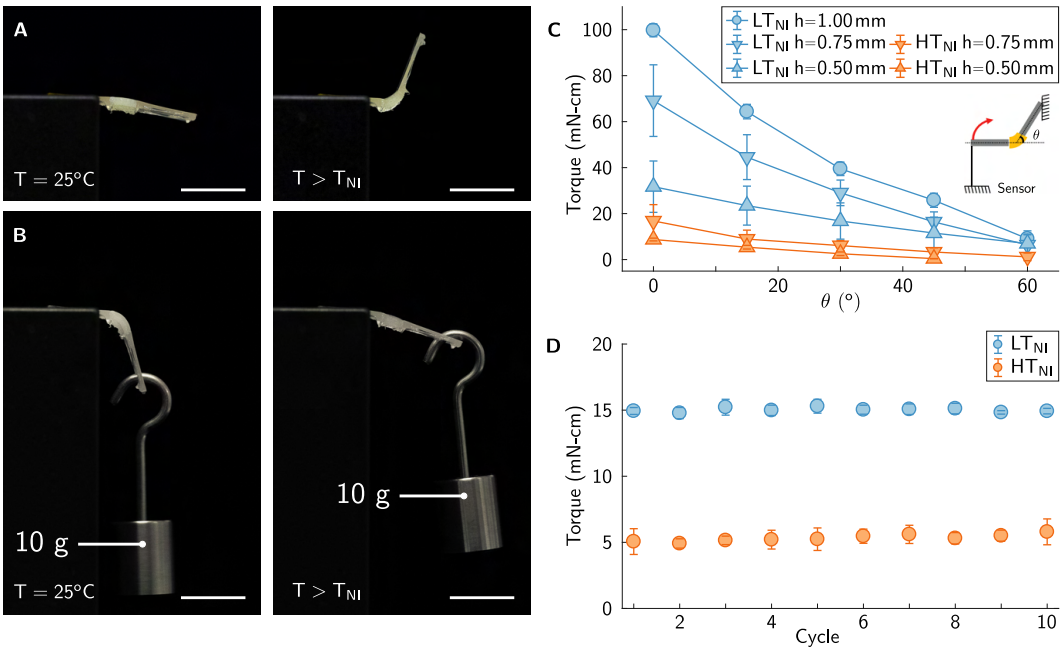

Figure 6.4: Torque capacity of printed active hinges. (a) LT_{NI} LCE hinge (10 mm by 4 mm by 1 mm) folds to a 75° bending angle while unbiased. (b) When a 10 g mass was suspended 1 cm away from the LCE hinge at room temperature, it deflected to −72°. The mass was lifted by about 1 cm when actuated above T_{NI}. (c) Exerted torque as a function of hinge folding angle, θ, as defined by the inset. Hinge composition and thickness, h, are the primary factors that affect torque output. (d) LCE hinges (5 mm by 3 mm by 0.5 mm) undergo multiple actuation cycles with negligible changes in the torque output. Error bars indicate SD. Scale bars, 1 cm.

We quantified the torque output of LCE bilayer hinges to further explore their suitability for reconfigurable and propulsive soft robots. Both types of LCE hinges were tested in different geometries. For a given thickness, LT_{NI} LCE hinges output more torque than their HT_{NI} counterparts (Fig. 6.4c). Torque increases with hinge thickness for both LCE chemistries but diminishes with increasing folding angle.

Consequently, heavier self-assembling and self-propelling structures will require hinges that are capable of greater torque outputs because hinges will only fold until there is equilibrium between external moments and their curvature-dependent torque capacity. Torque output remained constant over multiple heating and cooling cycles (Fig. 6.4d), which is essential for repeatable propulsion in untethered robots. We noticed an asymmetry in the torque produced by the actuators when heated compared with the relatively lower restoration torque exerted by hinges during cooling. This asymmetry is disadvantageous for applications that require large torque outputs in both rotational directions, but leads to energy savings in deployable structures that require a permanent post-actuated configuration, such as the printed structure shown in Fig. 6.3, which remained locked in a post-actuated configuration rather than unfolding under ambient conditions.

We exploited the large torque output by the printed LCE hinges to achieve passive control of self-assembly and propulsion in a rolling architecture (i.e., rollbot) (Fig. 6.5). The entire structure was printed flat with a total mass of 1.67 g. The structural frame was composed of two outer rails that use LT_{NI} LCE hinges to morph from a flat state (Fig. 6.5a) to a pentagonal prism with edge lengths of 15 mm (Fig. 6.5b). These rails were connected by bridges that hold propelling HT_{NI} LCE hinges. A hot plate held at an average surface temperature of 200^{o} C and a convective environment that sustains the ambient temperature at 45^{o} C were used to passively induce the desired assembly and rolling motion. Under these conditions, the LT_{NI} LCE hinges actuated to a $\sim$ 72^{o} hinge angle and remained folded throughout the rolling process because of the modest difference between their T_{NI} and the ambient temperature, even away from the hot plate. The actuated LT_{NI} hinges provided enough torque to allow the structure to maintain a pentagonal shape during rolling, obviating the need for a locking mechanism. A free-body analysis was used to determine the torque requirements for shape reconfiguration and propulsion (Fig. E.10). To transform into a pentagonal prism, the LT_{NI} LCE hinges must have a minimum torque output of 9.9 mN-cm at a 0^{o} hinge angle (flat configuration) and a sustained torque of 0.3 mN-cm when fully folded (Fig. E.11). Given these torque and angle requirements, we printed LT_{NI} LCE hinges with a width of 4 mm and a thickness of 0.75 mm. In the assembled 3D configuration, the HT_{NI} LCE hinges actuated when in contact with the hot plate, rolling the structure over the adjacent vertex and onto the next hinge, which carried out the same action. Propelling the structure over vertices required a 36^{o} tipping angle, and the corresponding torque needed to initiate this action was 6.9 mN-cm exerted by the hinge (Fig. E.11). To

realize this, we printed HT_{NI} LCE hinges that were 2 mm wide and 0.50 mm thick as propelling actuators. These hinges were also printed with a 4 mm offset from the tipping vertex to provide mechanical advantage. Because of this offset, HT_{NI} LCE hinges must fold by 63°. A greater hinge angle was needed for tipping over an open vertex, so 4 mm HT_{NI} LCE hinges were used for propulsion over a small gap. Both LT_{NI} and HT_{NI} LCE hinge dimensions were chosen on the basis of the torque measurements described above, and a pentagonal frame was selected to showcase the torque capabilities of LCE hinges (rolling over vertices requires large torque outputs). Because these hinges unfolded away from the hot surface, their repeated actuation was possible. This allowed temperature gradient-driven propulsion to continue even after the structure completed a full roll without a need for manual reprogramming, traveling ~ 12 cm in 95 s (Fig. 6.5c and movie S4). This simple concept can be expanded upon to passively control soft programmable matter and, ultimately, robots with more sophisticated reversible functions and locomotive gaits.

6.3 Discussion

We have demonstrated a design and additive manufacturing method for integrating LCE bilayer actuators, into shape-morphing and self-propelling structures. We integrated programmable LCE hinges that actuate at different temperatures. The orthogonal orientation of these bilayer hinges induces anticlastic bending (i.e., saddle-like surfaces) and reduces their bending energy [49]. Even so, torque outputs are large enough for lifting objects that are substantially heavier than the hinges themselves and, importantly, for self-propulsion. We envision that given the modular nature of these inks, it would be relatively straightforward to incorporate LCEs that respond to other stimuli (e.g., light, pH, and humidity) within these printed architectures. Through the introduction of multiple stimuli-responsive actuators and more complex folding sequences, we can further expand the functionality of untethered soft robotic systems capable of task-specific reconfiguration and locomotion.

6.4 Materials and methods

Ink synthesis and characterization

The LT_{NI} ink was synthesized by a previously reported thiol-acrylate "click" reaction (52). As-received 2,2'-(ethylenedioxy)diethanethiol (Sigma-Aldrich), 1,4-bis-[4-(6-acryloyloxy-hexyloxy)benzoyloxy]-2-methylbenzene (Wilshire Technologies Inc.), 1,4-bis-[4-(3-acryloyloxypropypropyloxy) benzoyloxy]-2-methylbenzene

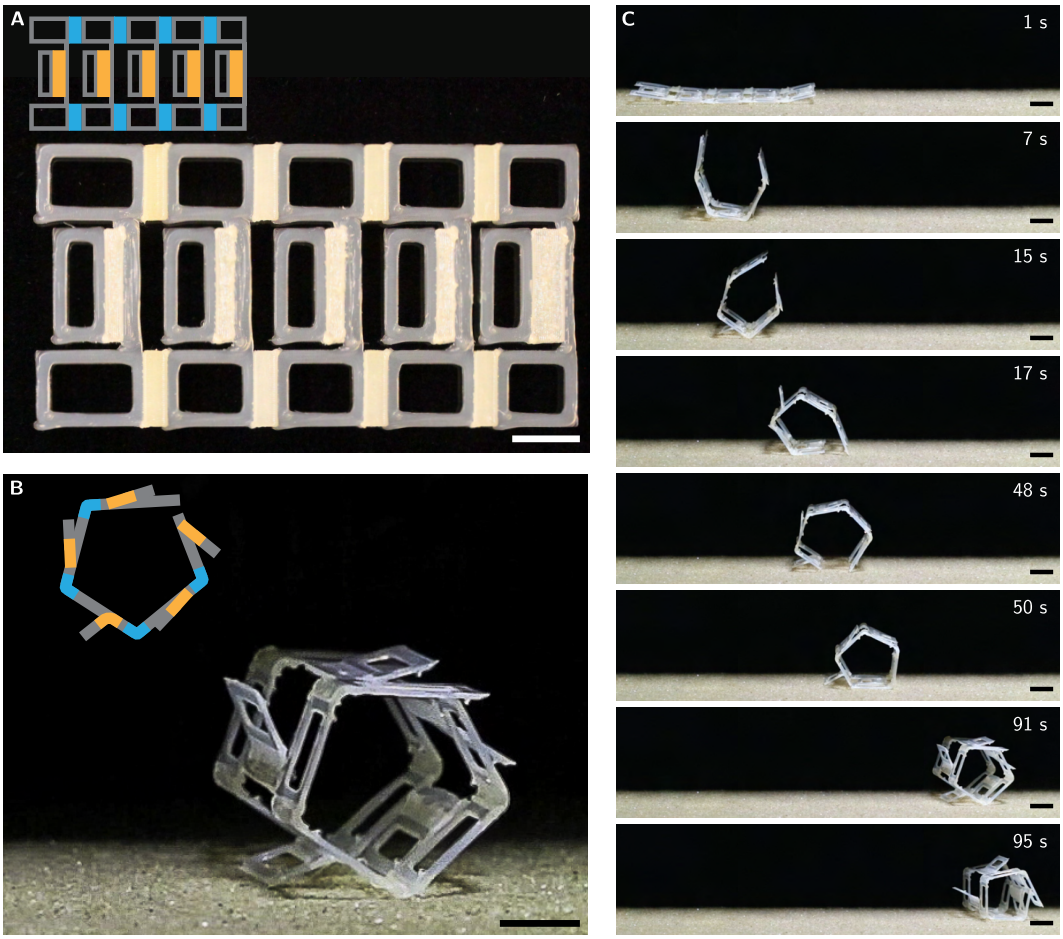

Figure 6.5: Printed self-propelling structure. (a) Self-propelling rollbot is shown in its printed configuration. In the legend (inset), the blue (LT_{NI}) and orange (HT_{NI}) LCE hinges denote valley and mountain folds, respectively, and gray indicates structural tiles. (b) Printed structure in its rolling configuration, in which the LT_{NI} LCE hinges induced folding into a pentagonal prism and the HT_{NI} LCE hinges propelled the rollbot when heated above their actuation temperature. (c) Still images (from movie S4) of the rollbot that show its self-propelling locomotion when heated. The structure self-propels at least six times over the time sequence shown. [The heated surface was held at 200°C, and the average ambient temperature was 45°C. Scale bars, 1 cm.]

(Matrix Scientific), and 1,3,5-triallyl-1,3,5-triazine-2,4,6(1H,3H,5H)-trione (Sigma-Aldrich) in a mole ratio of 1.0:0.6:0.2:0.133, and 1 weight % (wt %) triethylamine (Sigma-Aldrich), 2 wt % butylated hydroxytoluene (Fisher Scientific), and 1.5 wt % Irgacure 651 (BASF) were melted and mixed in an amber scintillation vial with a heat gun (MHT3300, Milwaukee) and vortexed for about 5 min. The reaction was subsequently heated and stirred for 3 hours at 65°C in an oil bath. The HT_{NI} ink was synthesized by a previously reported aza-Michael addition method [51]. A 1.1:1

mole ratio of 1,4-bis-[4-(6-acryloyloxyhexyloxy) benzoyloxy]-2-methylbenzene and n-butyl amine (Sigma-Aldrich), 0.2 wt % butylated hydroxytoluene, and 2 wt % Irgacure 651 were added to a 25 ml round-bottom flask fitted with a condenser. The reaction was stirred at 105°C for 18 hours while protecting it from ambient fluorescent light.

The structural ink was prepared by mixing Ebecryl 8413 resin (Allnex) and pentaerythritol tetraacrylate (TCI Chemicals) in a 1:1 weight ratio with 10 wt % fumed silica (CAB-O-SIL EH-5, Cabot) and 4 wt % Irgacure 651. Irgacure 651 was added as a solution in dichloromethane (Sigma-Aldrich) at a concentration of 750 mg/ml. After each reagent was added, the ink was mixed in a SpeedMixer (FlackTek Inc.) for about 3 min. The solvent was evaporated before printing. An Instron tensile testing machine was used to measure the stiffness of dogbone-shaped structural tiles.

The respective T_{NI} of each oligomeric LCE ink was determined by differential scanning calorimetry (DSC) measurements (TA Q200 calorimeter). Uncross-linked LCE ink samples (10 to 15 mg each) were hermetically sealed inside TZero aluminum pans. Samples were analyzed via a heat-cool-heat cycle between -50^{o} and 150°C with ramp rates of 10°C/min to clear the thermal history on the first heating ramp and to access both the glass transition temperatures and nematic-to-isotropic transition temperatures of the inks. Samples were held isothermally for 1 min at both high and low temperatures. Data from the second heating ramp were analyzed to determine their T_g and T_{NI} values.

The rheological properties of inks were measured using a controlled-stress rheometer (Discovery HR-3 Hybrid Rheometer, TA Instruments) equipped with a 20 mm peltier plate geometry with a 250 μm gap. Before each test, LCE inks were brought to 100°C, then to testing temperature for 300 s to erase structural history of the inks during the loading process. During the viscometry measurements, shear rate was swept from 0.001 to 1000 s^{-1}. During the oscillatory measurements, stress was swept from 0.01 to 1000 Pa at 1 Hz. The rheological properties of the elastomeric ink used to pattern the structural tiles were measured using a 40 mm cone geometry under ambient conditions. During the viscometry measurements, the ink viscosity was measured as the shear rate was swept from 0.0001 to 10,000 s^{-1}. During the oscillatory measurements, its storage and loss moduli were determined by carrying out stress sweeps from 0.0001 to 10,000 Pa at 1 Hz.

Alignment of printed LCE samples was characterized by x-ray scattering measurements on a SAXSLAB system with a Rigaku 002 microfocus x-ray source

(λ = 1.5409 Å) with a sample-to-detector (PILATUS 300K) distance of 109 mm to capture the mesogen-mesogen correlations at $q \sim 1.5$ Å^{-1}. Wide-angle x-ray scattering samples consisted of two-layer printed LCE unidirectional strips (200 to 250 μm thick). Samples were exposed for 300 s. Data reduction was performed using the Nika Macro for Igor Pro. Herman's orientational order parameter $<P_2>$ was calculated by extracting the intensity of the mesogen scattering peak as a function of azimuthal angle, masking low-intensity regions due to the beamstop and gaps in the PILATUS 300K detector and then using a custom MATLAB script. The order parameters of printed LT_{NI} and HT_{NI} LCEs are 0.1707 and 0.2688, respectively.

Unbiased linear actuation of unidirectional LCE as a function of temperature was determined by increasing temperature at 4^{o} C/min with a programmable heating stage (modified HCS302, Instec) on 20 mm–by–5 mm–by–0.375 mm unidirectional samples from 25^{o} to 150^{o} C. The stage was covered in a thin layer of silicone oil to enhance heat transfer and reduce friction. Images were collected from above every 15 s via a Canon EOS Rebel T2i camera with a Canon 100 mm macro lens, and dimensions were analyzed via ImageJ.

Fabrication and operation of programmed soft materials

LCE hinges were printed using a customized HOT-DIW printhead (operating at $T < 100^{o}$ C). The printhead composed of a machined copper block that was designed to couple to a Nordson 3-cc high-pressure adapter (Nordson EFD). For heating control, a resistance temperature detector sensor in the block (Omega) monitored the temperature adjacent to the nozzle, two 100 W 1/4–by–2 in cartridge heaters (Omega) in the copper block provided heating, and a Teflon mounting block provided insulation. Feedback control was provided via an Omega platinum series single-zone temperature controller. The LCE inks were loaded into a custom SS 3-cc syringe with a 250 μm nozzle (TecDia Inc.). LT_{NI} and HT_{NI} inks were printed at 26^{o} C and 50^{o} to 55^{o} C and at print speeds of 25 and 28 mm/s, respectively. Both were printed at a print height of 0.125 mm, a filament spacing of 0.125 mm, and a pressure of 455 psi using a 3-cc high-pressure adapter controlled with a pressure box (Ultimus V, Nordson EFD). On-the-fly ultraviolet (UV) curing (OmniCure S2000) was carried out at 20, 000 μW/cm^2 for LT_{NI} LCE ink and 8000 μW/cm^2 for HT_{NI} LCE ink. Structural tiles were printed by extruding the ink through a 410 μm tapered nozzle (Nordson EFD) at an average speed of 30 mm/s, a print height of 0.25 mm, a filament spacing of 0.2 mm, and a pressure of 60 psi (Ultimus V, Nordson EFD). Inks were printed using our multimaterial 3D printer (customized

ABG 10000, Aerotech Inc.) and G-Code (MeCode). All samples except the shape-morphing element and self-propelling structure were printed on an untreated glass slide (VWR). The triangulated polyhedron and the self-propelling structure were printed on a sacrificial polyvinyl alcohol (99% hydrolyzed; Sigma-Aldrich)–coated glass substrate. After printing, all samples were cross-linked upon exposure to UV light (6000 μW/cm^2) for about 15 min per side.

The triangulated polyhedron was fully printed in a single step in a flat configuration. The 3D configuration was achieved by bonding the edges of outlying LCE hinges to structural tiles with the structural ink. All hinges in the structure were 0.5 mm thick and 6 mm wide. The triangulated polyhedron was actuated in two steps. First, it is placed in an oven at 100^o C to actuate the LT_{NI} LCE hinges. Next, it was placed in an oven at 155^o C to actuate the HT_{NI} LCE hinges (Fig. 6.4 and movie S3). After each actuation in the sequence, the structure was imaged at room temperature (Fig. E.9).

The self-propelling structure (Fig. 6.5) was printed with LT_{NI} LCE hinges that were 0.75 mm thick and 4 mm wide and HT_{NI} LCE hinges that were 0.5 mm thick and 2 mm wide. The last HT_{NI} LCE hinge that propels the structure at the open vertex of the pentagonal prism was 0.5 mm thick and 4 mm wide. The self-propelling structure was tested on a substrate with a sand-covered silicone adhesive (Rutland). The substrate was heated with a hotplate to have a surface temperature of about 200^o C. To provide a heated and convective environment, we placed a space heater (Sunbeam) 4 in away and set at 27^o C. To ensure a thin boundary layer of heat at sand surface, we used a fan. Both the convective heater and the fan were aligned to be parallel to the self-propelling structure.

Characterization of programmed soft materials

Images of actuated samples in Fig. 6.1b-c and movie S1 were taken in an oil bath with a temperature of 125^o C acquired from above. The sample in Fig. 6.4a-b was heated with a heat gun (MHT3300, Milwaukee) until the sample was optically clear, indicating full actuation. All unbiased folding angle measurements were conducted by printing one stiff panel longer than the other to fit in an acrylic holder perpendicular to the panel face. Hinges were printed as mountain folds unless otherwise specified. The hinges were inverted into an oil bath of the temperature of measurement and imaged from above with a camera (Canon EOS 5D Mark III). For repeatable bending measurements (Fig. E.8), hinges were alternated between

room temperature and a hot oil bath. For LT_{NI} and HT_{NI} LCE hinges, the oil bath was at 120^{o} and 150^{o} C, respectively. Images were taken after 30 s in the hot oil bath and after 2 min at room temperature. Sequential folding images (Fig. 6.2c and movie S2) were taken from above, as samples were heated from room temperature to 150^{o}C in an oil bath and cooled passively to room temperature again. The edges of all hinges analyzed for bending angle were colored black with permanent marker (Sharpie) to enhance contrast for image analysis (MATLAB). All images analyzed for bending angle were taken using a Canon EOS 5D Mark III camera from above.

To measure their torque output, we fixed one of the LCE hinges' structural panels to a rotary stage that was used to control hinge angle. The second panel was attached to a thin string 10 mm away from the edge of the LCE. The string, with negligible bending stiffness, was axially stiff and was fixed to a force sensor at the other end. A linear stage was used in conjunction with the near-inextensible string for fine-tuning the target hinge angle, ensuring that the force vector being measured by the sensor was normal to the second hinge panel and to the sensor plate. The actuators were heated using a 24 W metal ceramic heater (Thorlabs Inc.), causing them to bend away from the sensor until reaching the target hinge angle. At this target angle, the string experienced axial forces, which were measured by a Mettler Toledo XS205 scale. The measured force plateaued with the completion of the nematic-to-isotropic phase transition. Torque cycling experiments were carried out at a 0^{o} hinge angle by turning the heater off upon reaching full actuation. See Fig. E.12 for images of the experimental setup and Fig. E.13 for additional torque measurements.

Acknowledgements

We thank Y. Liu for experimental assistance and S. Uzel, W. Boley, K. Korner, P. Celli, S. Injeti, and H. Zhou for useful discussions. We thank L. K. Sanders for technical assistance with imaging and videography. Funding: The work was supported by the Army Research Office (ARO) Grant W911NF-17-1-0147 (to C.D. and C.M.), the Harvard MRSEC (NSF DMR-1420570 to J.A.L. and A.K.), and the ARO MURI Grant W911NF-17-1-0351 (to J.A.L. and E.C.D.). We also acknowledge support from the NASA Space Technology Research Fellowship to C.M. and the National Science Foundation Graduate Research Fellowship to A.K. This work made use of the Shared Experimental Facilities supported in part by the Harvard MRSEC Program under award number DMR-1420570.

Permissions

References

[1] H. Yuk, S. Lin, C. Ma, M. Takaffoli, N. X. Fang, and X. Zhao. Hydraulic hydrogel actuators and robots optically and sonically camouflaged in water. *Nature Communications*, 8(1):1–12, 2017.

[2] F. Ilievski, A. D. Mazzeo, R. F. Shepherd, X. Chen, and G. M. Whitesides. Soft robotics for chemists. *Angewandte Chemie*, 123(8):1930–1935, 2011.

[3] B. T. Phillips, K. P. Becker, S. Kurumaya, K. C. Galloway, G. Whittredge, D. M. Vogt, C. B. Teeple, M. H. Rosen, V. A. Pieribone, D. F. Gruber, et al. A dexterous, glove-based teleoperable low-power soft robotic arm for delicate deep-sea biological exploration. *Scientific Reports*, 8(1):1–9, 2018.

[4] F. Connolly, C. J. Walsh, and K. Bertoldi. Automatic design of fiber-reinforced soft actuators for trajectory matching. *Proceedings of the National Academy of Sciences*, 114(1):51–56, 2017.

[5] E. Hawkes, B. An, N. M. Benbernou, H. Tanaka, S. Kim, E. D. Demaine, D. Rus, and R. J. Wood. Programmable matter by folding. *Proceedings of the National Academy of Sciences*, 107(28):12441–12445, 2010.

[6] M. Wehner, R. L. Truby, D. J. Fitzgerald, B. Mosadegh, G. M. Whitesides, J. A. Lewis, and R. J. Wood. An integrated design and fabrication strategy for entirely soft, autonomous robots. *Nature*, 536(7617):451–455, 2016.

[7] J. R. Amend, E. Brown, N. Rodenberg, H. M. Jaeger, and H. Lipson. A positive pressure universal gripper based on the jamming of granular material. *IEEE Transactions on Robotics*, 28(2):341–350, 2012.

[8] R. F. Shepherd, F. Ilievski, W. Choi, S. A. Morin, A. A. Stokes, A. D. Mazzeo, X. Chen, M. Wang, and G. M. Whitesides. Multigait soft robot. *Proceedings of the National Academy of Sciences*, 108(51):20400–20403, 2011.

[9] W. Hu, G. Z. Lum, M. Mastrangeli, and M. Sitti. Small-scale soft-bodied robot with multimodal locomotion. *Nature*, 554(7690):81–85, 2018.

[10] M. T. Tolley, R. F. Shepherd, B. Mosadegh, K. C. Galloway, M. Wehner, M. Karpelson, R. J. Wood, and G. M. Whitesides. A resilient, untethered soft robot. *Soft Robotics*, 1(3):213–223, 2014.

[11] K. Suzumori, S. Endo, T. Kanda, N. Kato, and H. Suzuki. A bending pneumatic rubber actuator realizing soft-bodied manta swimming robot. In *Proceedings 2007 IEEE International Conference on Robotics and Automation*, pages 4975–4980. IEEE, 2007.

[12] N. W. Bartlett, M. T. Tolley, J. T. B. Overvelde, J. C. Weaver, B. Mosadegh, K. Bertoldi, G. M. Whitesides, and R. J. Wood. A 3D-printed, functionally graded soft robot powered by combustion. *Science*, 349(6244):161–165, 2015.

[13] Y. Liu, B. Xu, S. Sun, J. Wei, L. Wu, and Y. Yu. Humidity-and photo-induced mechanical actuation of cross-linked liquid crystal polymers. *Advanced Materials*, 29(9):1604792, 2017.

[14] S. Palagi, A. G. Mark, S. Y. Reigh, K. Melde, T. Qiu, H. Zeng, C. Parmeggiani, D. Martella, A. Sanchez-Castillo, N. Kapernaum, et al. Structured light enables biomimetic swimming and versatile locomotion of photoresponsive soft microrobots. *Nature Materials*, 15(6):647–653, 2016.

[15] C. Ahn, K. Li, and S. Cai. Light or thermally powered autonomous rolling of an elastomer rod. *ACS Applied Materials & Interfaces*, 10(30):25689–25696, 2018.

[16] A. H. Gelebart, D. J. Mulder, M. Varga, A. Konya, G. Vantomme, E. W. Meijer, R. L. B. Selinger, and D. J. Broer. Making waves in a photoactive polymer film. *Nature*, 546(7660):632–636, 2017.

[17] Q. Ge, C. K. Dunn, H. J. Qi, and M. L. Dunn. Active origami by 4D printing. *Smart Materials and Structures*, 23(9):094007, 2014.

[18] C. Yuan, D. J. Roach, C. K. Dunn, Q. Mu, X. Kuang, C. M. Yakacki, T. J. Wang, K. Yu, and H. J. Qi. 3D printed reversible shape changing soft actuators assisted by liquid crystal elastomers. *Soft Matter*, 13(33):5558–5568, 2017.

[19] N. Kellaris, V. G. Venkata, G. M. Smith, S. K. Mitchell, and C. Keplinger. Peano-hasel actuators: Muscle-mimetic, electrohydraulic transducers that linearly contract on activation. *Science Robotics*, 3(14), 2018.

[20] A. O'Halloran, F. O'Malley, and P. McHugh. A review on dielectric elastomer actuators, technology, applications, and challenges. *Journal of Applied Physics*, 104(7):9, 2008.

[21] T. Chen, O. R. Bilal, K. Shea, and C. Daraio. Harnessing bistability for directional propulsion of soft, untethered robots. *Proceedings of the National Academy of Sciences*, 115(22):5698–5702, 2018.

[22] J. Wu, C. Yuan, Z. Ding, M. Isakov, Y. Mao, T. Wang, M. L. Dunn, and H. J. Qi. Multi-shape active composites by 3D printing of digital shape memory polymers. *Scientific Reports*, 6(1):1–11, 2016.

[23] Q. Zhang, K. Zhang, and G. Hu. Smart three-dimensional lightweight structure triggered from a thin composite sheet via 3D printing technique. *Scientific Reports*, 6(1):1–8, 2016.

[24] C. Wang, K. Sim, J. Chen, H. Kim, Z. Rao, Y. Li, W. Chen, J. Song, R. Verduzco, and C. Yu. Soft ultrathin electronics innervated adaptive fully soft robots. *Advanced Materials*, 30(13):1706695, 2018.

[25] S. I. Rich, R. J. Wood, and C. Majidi. Untethered soft robotics. *Nature Electronics*, 1(2):102–112, 2018.

[26] S. Felton, M. Tolley, E. Demaine, D. Rus, and R. Wood. A method for building self-folding machines. *Science*, 345(6197):644–646, 2014.

[27] D. Rus and M. T. Tolley. Design, fabrication and control of origami robots. *Nature Reviews Materials*, 3(6):101–112, 2018.

[28] J.-S. Koh and K.-J. Cho. Omega-shaped inchworm-inspired crawling robot with large-index-and-pitch (lip) sma spring actuators. *IEEE/ASME Transactions on Mechatronics*, 18(2):419–429, 2012.

[29] W. P. Weston-Dawkes, A. C. Ong, M. R. A. Majit, F. Joseph, and M. T. Tolley. Towards rapid mechanical customization of cm-scale self-folding agents. In *2017 IEEE/RSJ International Conference on Intelligent Robots and Systems (IROS)*, pages 4312–4318. IEEE, 2017.

[30] X. Ning, X. Wang, Y. Zhang, X. Yu, D. Choi, N. Zheng, D. S. Kim, Y. Huang, Y. Zhang, and J. A. Rogers. Assembly of advanced materials into 3D functional structures by methods inspired by origami and kirigami: A review. *Advanced Materials Interfaces*, 5(13):1800284, 2018.

[31] R. J. Lang. A computational algorithm for origami design. In *Proceedings of the Twelfth Annual Symposium on Computational Geometry*, pages 98–105, 1996.

[32] T. Tachi. Freeform variations of origami. *Journal for Geometry and Graphics*, 14(2):203–215, 2010.

[33] E. D. Demaine and T. Tachi. Origamizer: A practical algorithm for folding any polyhedron. In *33rd International Symposium on Computational Geometry (SoCG 2017)*. Schloss Dagstuhl-Leibniz-Zentrum fuer Informatik, 2017.

[34] S Miyashita, S. Guitron, S. Li, and D. Rus. Robotic metamorphosis by origami exoskeletons. *Science Robotics*, 2(10), 2017.

[35] Y. Liu, B. Shaw, M. D. Dickey, and J. Genzer. Sequential self-folding of polymer sheets. *Science Advances*, 3(3):e1602417, 2017.

[36] J.-H. Na, A. A. Evans, J. Bae, M. C. Chiappelli, C. D. Santangelo, R. J. Lang, T. C. Hull, and R. C. Hayward. Programming reversibly self-folding origami with micropatterned photo-crosslinkable polymer trilayers. *Advanced Materials*, 27(1):79–85, 2015.

[37] J. T. B. Overvelde, T. A. De Jong, Y. Shevchenko, S. A. Becerra, G. M. Whitesides, J. C. Weaver, C. Hoberman, and K. Bertoldi. A three-dimensional actuated origami-inspired transformable metamaterial with multiple degrees of freedom. *Nature Communications*, 7(1):1–8, 2016.

[38] S. Kim, C. Laschi, and B. Trimmer. Soft robotics: A bioinspired evolution in robotics. *Trends in Biotechnology*, 31(5):287–294, 2013.

[39] M. A. McEvoy and N. Correll. Materials that couple sensing, actuation, computation, and communication. *Science*, 347(6228), 2015.

[40] J. Küpfer and H. Finkelmann. Nematic liquid single crystal elastomers. *Die Makromolekulare Chemie, Rapid Communications*, 12(12):717–726, 1991.

[41] S. W. Ula, N. A. Traugutt, R. H. Volpe, R. R. Patel, K. Yu, and C. M. Yakacki. Liquid crystal elastomers: An introduction and review of emerging technologies. *Liquid Crystals Reviews*, 6(1):78–107, 2018.

[42] T. Guin, B. A. Kowalski, R. Rao, A. D. Auguste, C. A. Grabowski, P. F. Lloyd, V. P. Tondiglia, B. Maruyama, R. A. Vaia, and T. J. White. Electrical control of shape in voxelated liquid crystalline polymer nanocomposites. *ACS Applied Materials & Interfaces*, 10(1):1187–1194, 2018.

[43] Y. Yao, J. T. Waters, A. V. Shneidman, J. Cui, X. Wang, N. K. Mandsberg, S. Li, A. C. Balazs, and J. Aizenberg. Multiresponsive polymeric microstructures with encoded predetermined and self-regulated deformability. *Proceedings of the National Academy of Sciences*, 115(51):12950–12955, 2018.

[44] B. R. Donovan, V. M. Matavulj, S. Ahn, T. Guin, and T. J. White. All-optical control of shape. *Advanced Materials*, 31(2):1805750, 2019.

[45] T. H. Ware, M. E. McConney, J. J. Wie, V. P. Tondiglia, and T. J. White. Voxelated liquid crystal elastomers. *Science*, 347(6225):982–984, 2015.

[46] T. Guin, M. J. Settle, B. A. Kowalski, A. D. Auguste, R. V. Beblo, G. W. Reich, and T. J. White. Layered liquid crystal elastomer actuators. *Nature Communications*, 9(1):1–7, 2018.

[47] F. Greco, V. Domenici, A. Desii, E. Sinibaldi, B. Zupančič, B. Zalar, B. Mazzolai, and V. Mattoli. Liquid single crystal elastomer/conducting polymer bilayer composite actuator: Modelling and experiments. *Soft Matter*, 9(47): 11405–11416, 2013.

[48] A. Agrawal, T. Yun, S. L. Pesek, W. G. Chapman, and R. Verduzco. Shape-responsive liquid crystal elastomer bilayers. *Soft Matter*, 10(9):1411–1415, 2014.

[49] P. Plucinsky, B. A. Kowalski, T. J. White, and K. Bhattacharya. Patterning nonisometric origami in nematic elastomer sheets. *Soft Matter*, 14(16):3127–3134, 2018.

[50] H. Zeng, O. M. Wani, Piotr W., and A. Priimagi. Light-driven, caterpillar-inspired miniature inching robot. *Macromolecular Rapid Communications*, 39 (1):1700224, 2018.

[51] A. Kotikian, R. L. Truby, J. W. Boley, T. J. White, and J. A. Lewis. 3D printing of liquid crystal elastomeric actuators with spatially programed nematic order. *Advanced Materials*, 30(10):1706164, 2018.

[52] M. O. Saed, C. P. Ambulo, H. Kim, R. De, V. Raval, K. Searles, D. A. Siddiqui, J. M. O. Cue, M. C. Stefan, M. R. Shankar, et al. Molecularly-engineered, 4D-printed liquid crystal elastomer actuators. *Advanced Functional Materials*, 29(3):1806412, 2019.

[53] C. P. Ambulo, J. J. Burroughs, J. M. Boothby, H. Kim, M. R. Shankar, and T. H. Ware. Four-dimensional printing of liquid crystal elastomers. *ACS Applied Materials & Interfaces*, 9(42):37332–37339, 2017.

[54] J. E. Smay, G. M. Gratson, R. F. Shepherd, J. Cesarano III, and J. A. Lewis. Directed colloidal assembly of 3D periodic structures. *Advanced Materials*, 14(18):1279–1283, 2002.

[55] M. López-Valdeolivas, D. Liu, D. J. Broer, and C. Sánchez-Somolinos. 4D printed actuators with soft-robotic functions. *Macromolecular Rapid Communications*, 39(5):1700710, 2018.

[56] N. P. Godman, B. A. Kowalski, A. D. Auguste, H. Koerner, and T. J. White. Synthesis of elastomeric liquid crystalline polymer networks via chain transfer. *ACS Macro Letters*, 6(11):1290–1295, 2017.

[57] S. Timoshenko. Analysis of bi-metal thermostats. *Journal of the Optical Society of America*, 11(3):233–255, 1925.

[58] V. Agostiniani and A. DeSimone. Dimension reduction via γ-convergence for soft active materials. *Meccanica*, 52(14):3457–3470, 2017.

[59] P. Nardinocchi and E. Puntel. Unexpected hardening effects in bilayered gel beams. *Meccanica*, 52(14):3471–3480, 2017.

[60] S. D. Guest and S. Pellegrino. The folding of triangulated cylinders, Part II: the folding process. 1994.

[61] R. J. Lang. *Twists, tilings, and tessellations: Mathematical methods for geometric origami*. CRC Press, 2017.

[62] D. Rus and M. T. Tolley. Design, fabrication and control of soft robots. *Nature*, 521(7553):467–475, 2015.

[63] A. Kotikian, C. McMahan, E. C. Davidson, J. M. Muhammad, R. D. Weeks, C. Daraio, and J. A. Lewis. Untethered soft robotic matter with passive control of shape morphing and propulsion. *Science Robotics*, 4(33), 2019.

Chapter 7

CONCLUSIONS

7.1 Summary of contributions

The global kinematic behaviors of structured media (such as shape-morphing and locomotion) can be "programmed" by designing micro- and mesoscale geometries that energetically favor desired modes of deformation. Methods for programming these media require a sound mechanistic understanding of the interplay between internal geometry and the elastic properties of the bulk materials. The preceding chapters in this thesis describe a series of experimental, numerical, and analytical studies on the mechanics of structured media and outline methods for programming their behavior.

Chapter 2 discusses how the onset of failure in twisted ribbons can be considerably delayed by introducing a periodic undulation in the ribbons' edge geometry. Experimental, analytical, and numerical investigations into the mechanics of bulk metallic glass ribbons establish the bounds for the maximum applied twist that the ribbons can be subjected to without failing before thermoforming. This guides the design of metallic ribbon networks that display interesting stowing and deployment kinematics as a result of the ribbon chirality.

In Chapter 3, we discuss a novel method for attaining three-dimensional objects from initially flat sheets. Namely, we induce out-of-plane buckling by leveraging the kinematic frustrations that arise in non-periodically patterned sheets when they are subjected to tensile loads. We study the mechanics of these buckling systems in more depth in Chapter 4. One of the significant challenges of modeling structured media is that the presence of geometric features at disparate length scales makes it computationally expensive to simulate their behavior using conventional finite element methods that fully resolve the small-scale geometry yet span the entire structure. This motivates our development of an effective continuum model that attributes an energy penalty to deviations from the mesostructure's local quasi-mechanism behaviors. The model enables us to capture the global post-buckling behavior of the system. To the best of our knowledge, this is the first demonstration of an effective continuum model for capturing the behavior of quasi-mechanisms in graded media.

All of the studies mentioned above were conducted on passive materials that do not undergo deformations in response to an environmental stimulus (aside from applied loads). In Chapter 5, we discuss the inverse design of trilayer shells that morph into target smooth surfaces when inserted in warm water. The main novelty of our work stems from introducing a method for controlling the deformation rates in every region of our system. This considerably broadens the design space for smooth morphing surfaces, as it permits sequential actuation steps and the avoidance of self-collisions that would impede reaching the target geometry otherwise. This feat is demonstrated through the inverse design of a doubly-looped spiral and a self-interweaving structure that would be unobtainable without programming deformation sequences.

The final study in this thesis is presented in Chapter 6. It shows that micro- and mesostructural design can be used to induce shape-shifting and self-propulsion in soft robotic media. We created liquid crystal elastomer (LCE) bilayers that fold when heated due to the orthogonal relative alignment of the mesogens in the two layers. Incorporating these LCE hinges into an origami-inspired framework allows us to localize large deformations to desired regions, thus simplifying the kinematic modeling and control of soft systems that often have infinite degrees of freedom. In a given structure, the hinge folding sequence is determined by the LCE chemistry, while the folding angle and torque output are determined from the hinge thickness and width. The LCEs display energy dense, reversible actuation and do not require a tether to external power or control devices, enabling the creation of media that are capable of structural reconfiguration and self-propulsion in response to environmental stimuli.

7.2 Outlook on future research directions

As discussed throughout this thesis, materials synthesis techniques and additive manufacturing technology have led to the creation of novel structured media whose behavior can be "programmed." Based on the lessons learned from the above explorations, there are many natural avenues for future research on these structured media. The following subsections outline some interesting possibilities.

Deployable compliant devices made of engineering materials

There are several methods for morphing structures between two geometries in response to environmental stimuli using soft materials [5, 6, 9, 22]. However, this can be challenging to do in larger structures made of metal or other engineering materials because large strains induced by the morphing process can lead to material

failure. Fig. 7.1 shows a metallic analogue to the structures discussed in Chapters 3 and 4, highlighting that localized plasticity can occur at joints/flexures and impeding morphing structures from reaching their target shapes. This can be avoided if the compliant elements are carefully designed (tools such as topology optimization can help with this) or by working with structured media that undergo relatively small local strains [18, 27].

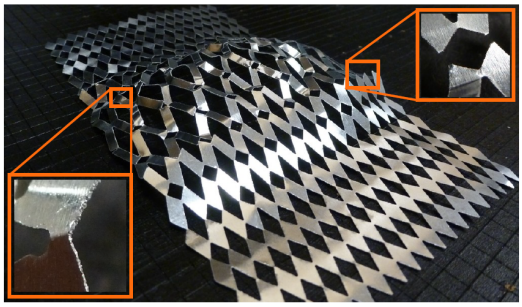

Figure 7.1: Plastic kinking of slender joints in a structured metallic medium.

The research in Chapter 2 discusses an initial effort to address these challenges, where ribbon-based structures rely on the chirality of their constituting elements to undergo extreme and fully reversible compaction/deployment. Within this context, it would be interesting to continue exploring the use of thermoformable metallic ribbons as building blocks for morphing structures in applications such as deployment mechanisms for offset surfaces or woven metallic fabrics.

As highlighted by Chapter 2, the inherent chirality of twisted ribbons allows them to be used as multi-DOF hinges in structures that undergo extreme compaction and deployment cycles. However, in this work we explored the mechanics of individual ribbons in great depth, but the design of networks of these ribbons was left to our engineering intuition. It would be worthwhile to study the mechanics of ribbon assemblages in greater depth and develop reduced order models for these networks to have tools that guide the design of this new class of structures.

Reduced order modeling of structured media

In general, techniques for modeling the behavior of structured media are still fairly limited [46] and usually involve reducing an object to a network of beams, rods, plates, shells, springs, and hinges. These network-based methods could be extended

by creating elements that represent the collective behavior of assemblies [46], to be used in simulations of hierarchical systems.

As alternatives to these network-based approaches, effective continuum models hold promise for analyzing the behavior of structured media. Despite progress by the mechanics community on this front, there is still a significant need to formalize general approaches for describing the behavior of non-periodic systems. The study described in Chapter 4 is an early effort that could be adapted to other classes of structured media, but it is limited to cases that display quasi-mechanisms. Furthermore, it would also be valuable to couple network-based approaches to effective continuum models for modeling and designing non-uniform hierarchical structures.

Additionally, it would be interesting to develop a method for predicting local failure while still capturing global behaviors, including how global mechanical properties are affected by local failure. This could be informed by controlled desktop-scale experiments and through the development of reduced order models that elucidate the effect of topology (i.e. the connectivity of lattices, woven microstructres, ribbon networks, etc.) on macro-scale effective properties. In a similar vein, it is important to understand the impact that local material failure at compliant joints and flexures has on the global properties of these structures, with the goal of developing stochastic models for the phenomena. Inverse design methods would benefit from the inclusion of these models to infer where local failure is likely to happen, and to perform topology optimization in these locations to avert catastrophic damage.

Optimal design of deployable devices

The *optimal design* of complex material properties and behaviors that emerge from micro/mesostructural heterogeneity can be very challenging, especially when multiple design objectives must be met (for example, achieving a desired shape change and then being able to withstand an anticipated loading condition). The coupling of reduced order mechanical modeling frameworks for structured media to optimization techniques would be an interesting approach for overcoming the limitations of engineering intuition. These methods could be used to create devices that attain unprecedented functionalities.

For example, a growing number of industries use 3D printers to manufacture devices that are both resilient to mechanical loads and undergo shape changes when deployed in a new operating environment (e.g. printed NiTi scaffolds for coronary artery stents that expand when heated by the bloodstream). However, it can be com-

putationally expensive to optimally design mesostructures for even moderately large deployable devices if their global dimensions are much larger than their smallest geometric features, especially if the devices have multiple functional needs (e.g. high stiffness-to-weight ratios, multistability, resilience to fracture, etc.). These problems would benefit from a framework that combines discrete differential geometry tools with reduced order modelling and multi-objective optimization techniques. Potential applications include load-bearing deployable structures made of engineering materials geared toward space, architectural and biomedical applications.

Mechanics-informed control of soft robots

As discussed in Chapters 5 and 6, several polymers, metals, and biological materials can be engineered to undergo "programmed" deformations and exertions of mechanical work in response to environmental cues. Their use as *passively* controlled replacements for external power and logic systems (therefore enabling "untethered" soft robots) has been explored recently. However, autonomous and active control are challenging within fully soft systems. In part, this is due to limitations in soft actuator technology (they often lack reversibility, produce small actuation forces, need very specific environments to operate, etc.), but it can also be difficult to predict the extreme elastic deformations that soft robots experience, especially if they are subjected to a diverse set of harsh contact boundary conditions.

In light of this context, the soft robotics community would benefit from methods for optimizing hole patterns or stiffness variations in fully soft robotic frames so that they deform in predictable ways when actuated or squashed. The field would also benefit from improvements to "approximate" elastic body simulation techniques developed for computer graphics applications to create efficient design methods for soft robotic structures. Furthermore, soft robotics will become more broadly applicable to industrial needs with the development of active structured materials that integrate actuation, sensing and communication capabilities more fully. This would permit active control of untethered, work-capable soft structures that operate in a broader set of environmental conditions than what is currently possible.

Appendix A

COMPLIANT MORPHING STRUCTURES FROM TWISTED BULK METALLIC GLASS RIBBONS

A.1 Details on the material properties of BMG

In this Appendix, we report additional results on the characterization of the BMG chosen in this work, the $Zr_{65}Cu_{17.5}Ni_{10}Al_{7.5}$ alloy. The engineering stress-strain response of strips of BMG having identical dimensions (up to the precision of our manual cutting process) is shown in Fig. A.1. We can see that all three specimens

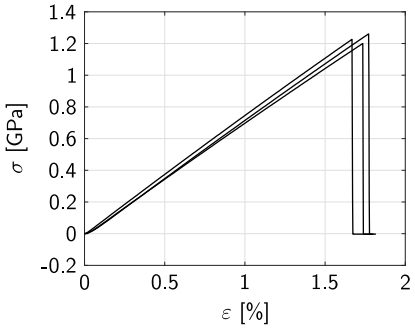

Figure A.1: Stress-strain response of a BMG strip. Each curve corresponds to an experiment carried out under identical conditions on three specimens.

behave linearly until breaking, and no evidence of plastic deformation is observed. The average breaking stress we obtain from these curves is $\sigma_b \approx 1.2\,\text{GPa}$, while the breaking strain (that also represents the elastic strain limit) is $\varepsilon_b \approx 1.7\%$. The breaking strain value is slightly smaller than the nominal one, $\varepsilon_b = 2\%$ [1], since our experiments are performed in tension and since the melt-spinning process introduces cross-sectional irregularities that can accelerate failure.

References

[1] M. Zhou, J. Zhou, J. Wei, M. Yang, and L. Ma. Enhanced glass-forming ability and mechanical properties of $Zr_{65}Al_{7.5}Ni_{10}Cu_{17.5}$ metallic glass by adding fe. *Journal of Non-Crystalline Solids*, 455:1–5, 2017. doi: 10.1016/j.jnoncrysol.2016.05.004.

Appendix B

SHAPE-MORPHING ARCHITECTED SHEETS WITH NON-PERIODIC CUT PATTERNS

B.1 Additional information on the tensile tests

A detail of our tensile experimental setup is shown in Fig. B.1. The insets represent a few stages of the deformation of the specimen studied in Fig. 3.1. To accomodate

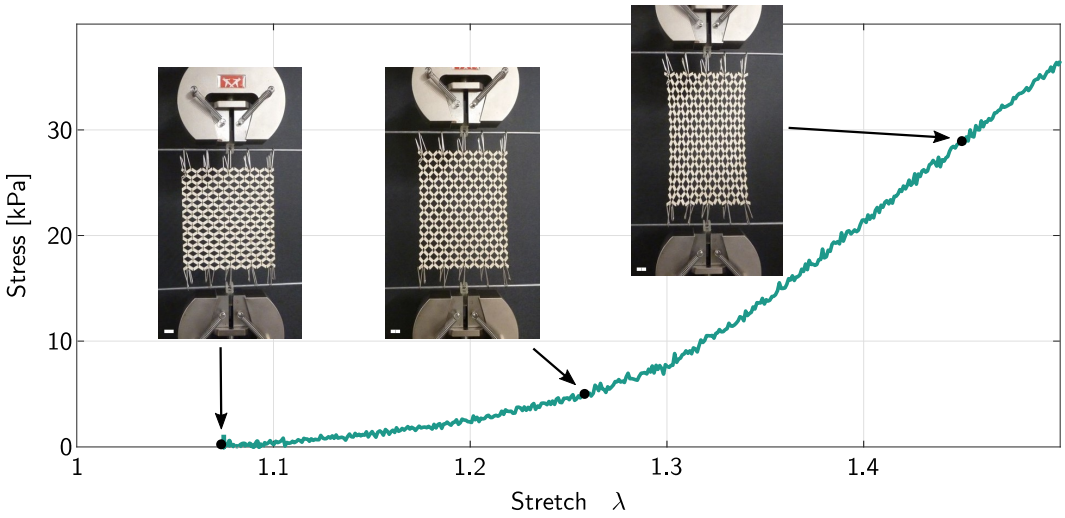

Figure B.1: Response of a 18×18 tile, anisotropic sheet with $\delta/l_x = 1/8$ and $t/l_x \sim 0.26$. The insets depict the experimental setup and the response at three stretch values. (Scale bar, 12 mm)

lateral expansions and/or contractions of the specimens undergoing tensile loads, we employ a fixture where specimens are hung in a curtain-like fashion. We use 3D-printed parts (Formlabs Form 2, clear resin) to connect horizontal steel rods to the Instron's clamps; we then use paper clips as "hooks" to hang the specimens (at 5 locations on each side). Upon pulling, the paper clips can slide on the steel rod; the friction between these components will inevitably affect the response. Note that, due to the very small forces involved in our experiments, we claim that the elasticity of paper clips and steel rods only minimally affects the response. From Fig. B.1, we see that the response is recorded only for values of stretches larger than ~ 1.08. This is due to the fact that, when attached to our fixtures, some of the sheets we consider tend to deform due to their self weight. This self-stretching happens only when specimens feature mechanism-like deformation in the pulling direction. For

example, in Fig. 3.1, the curve corresponding to horizontal stretching starts at 1.08, while the one for vertical stretching starts at 1.

From Fig. 3.1, we can see that the slopes of the elasticity-dominated portions of the experimental curves corresponding to horizontal and vertical stretching are not identical. This is caused by the fact that the size of the vertical and horizontal hinges in our anisotropic specimens are not identical. This is clearly visible from Figure B.2. In particular, the laser cutting process causes vertical hinges to be

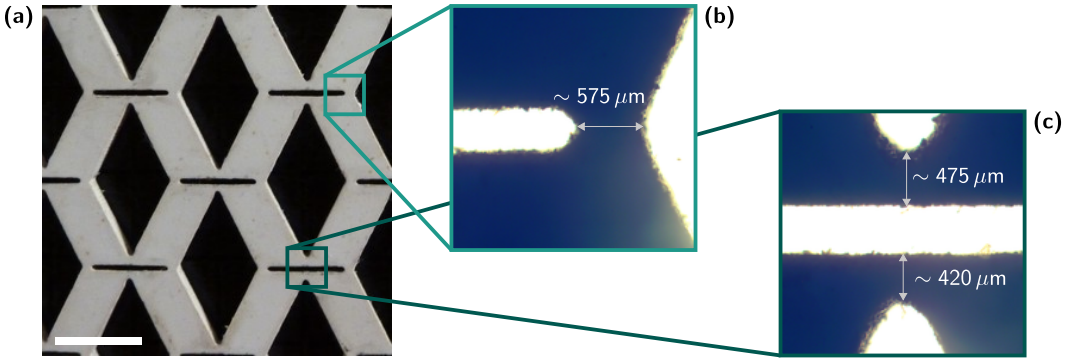

Figure B.2: Size difference between vertical and horizontal hinges in anisotropic specimens. (a) Detail of one of the anisotropic architectures analyzed in this work (Scale bar, 6 mm). (b) and (c) Microscope images (2.5× zoom) representing the details of vertical and horizontal hinges, respectively.

thicker than the horizontal ones. This explains why in Fig. 3.1 the continuous light gray curve is steeper than the elasticity-dominated portion of the continuous black curve.

In Figure B.8, we report the tensile response of the isotropic auxetic architecture displayed in Fig. 3.2(b) and Fig. B.5(a). The two continuous lines, dark and light, represent the experimental curves obtained by pulling the specimen along the horizontal and vertical directions, respectively. The two almost overlap, as expected, due to the isotropic nature of the specimen's response. The dashed line is obtained from FE simulations. The superimposed dash-dot curve represents the mechanism-to-elasticity transition.

B.2 Details on the finite element model

In this work, finite element simulations are carried out using Abaqus/Standard. The investigated sheets present different lengthscales: the hinge in-plane width and length ($\sim$ 1 mm), the length of a tile ($\sim$ 10 mm), and the total size of the sheet ($\sim$ 100 mm). Since the mechanical behavior of the sheets is, to a large extent,

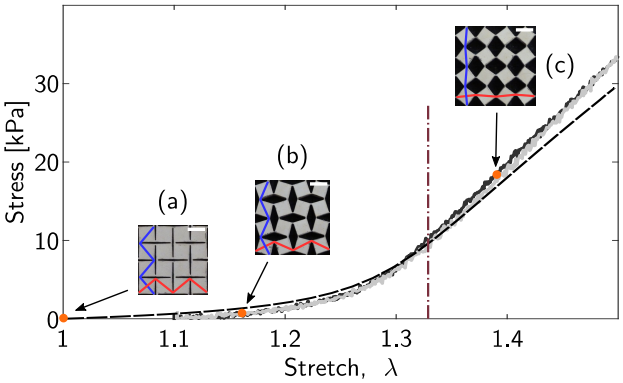

Figure B.3: Tensile response of a periodic sheet featuring the undeformed architecture in (a). Black lines represent the sheet's response to horizontal stretching and light gray lines to vertical stretching. Solid lines are experimental curves. The dashed line represent the numerical response to both horizontal and vertical loading. The vertical dash-dot line shows the theoretically-predicted value for the transition from a mechanism-dominated deformation to an elastic deformation. Insets (a-c) show different stages of the sheet's deformation (Scale bar, 6 mm); the red and blue lines highlight the diagonals of each tile in a given row and column, respectively.

governed by the design of the hinges, a sufficiently fine mesh is required to accurately capture the correct response. Another challenge stems from the large nonlinearities involved and from the large distortions happening at large stretches. In order to efficiently identify regions that are prone to out-of-plane bending, we conduct two-dimensional finite element simulations. In all simulations, we resort to a plane strain assumption, accounting for the fact that the response is primarily determined by the hinge dimensions, and the hinges' in-plane width (~ 0.5 mm) is smaller than their out-of-plane thickness (~ 1.55 mm). Throughout this work, we consider geometric nonlinearities and model the nonlinear material behavior of natural rubber gum with a Neo-Hookean material model. This model is fit to the experimental response of a natural rubber dogbone specimen to tensile loading. Fig. B.4(a) shows a detail of the mesh at one of the hinges. We check mesh convergence for one of the simulations used to obtain the numerical curves in Fig. 3.1. We change the element size and monitor the stress values recorded for a given stretch along a given direction. The errors we obtain for doubling the average element size are below 0.73%.

The results reported in Fig. 3.1 and Figure B.3 show that the numerics capture the features observed experimentally, even though some discrepancies between experiments and numerics arise at large stretches. These discrepancies can be attributed to several factors: 1) the inability of the Neo-Hookean model to capture the correct mechanical behavior at large stretches; 2) the fact that the CAD models

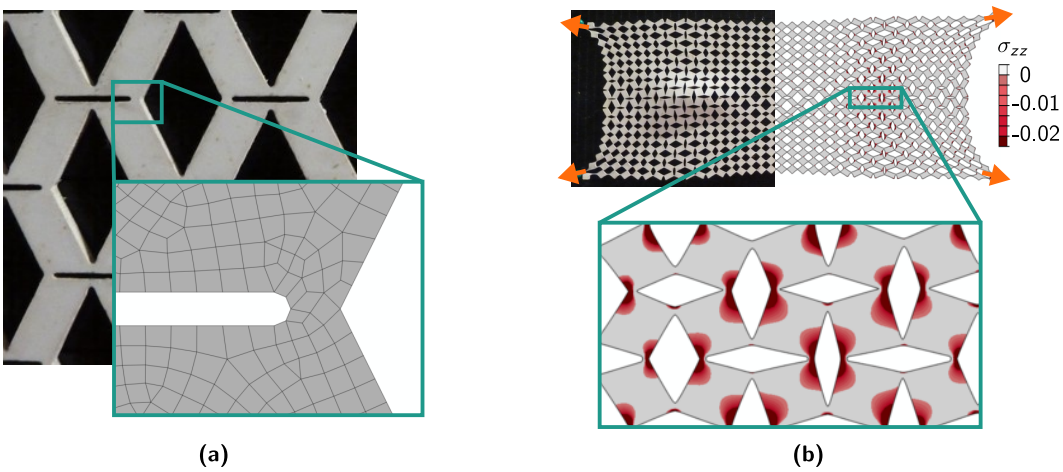

Figure B.4: Details of the FE model. (a) Detail of the mesh used for one of the hinges in the simulation of the anisotropic specimen tensile test. (b) Detail of the stress map for the simulation in Fig. 3.3(b2).

used for our numerical simulations do not account for the exact hinge dimension that results from the laser cutting process; 3) the simulated loads might not be exactly identical to the experimental ones.

The stress maps in Fig. 3.3 represent the out-of-plane stress $\sigma_z = \nu(\sigma_x + \sigma_y)$. The colormap is designed to give relevance only to compressive stresses—those that are responsible for the onset of buckling. The stresses are not averaged over subdomains. Thus, the red areas in Fig. B.4(b) correspond to the compressive stress of the hinges. We also observe that the compressive stresses partially percolate into the tiles. This is likely responsible for out-of-plane buckling. From Fig. 3.3(c2-c3), we can see that the stress maps for the two loading configurations are almost identical. For this reason, the stress maps do not contain enough information to determine the exact shape of the resulting buckling patterns in complex scenarios, but give a useful guideline on where buckling is likely to occur in simple cases like that depicted in Fig. 3.3(b1-b2).

B.3 Kinematic analysis

The sheets discussed in this work are designed to display mechanisms of inextensional deformation, i.e., low energy modes of compliant mechanism-like deformation. In this section, we consider the pin-jointed truss analogs of some of our sheets, and resort to the matrix analysis detailed by Pellegrino & Calladine [3] and Hutchinson & Fleck [2] to determine what these mechanisms are. This analysis consists of the following steps. First, we calculate the equilibrium matrix **A**, that

relates bar tensions $\mathbf{t}$ and joint forces $\mathbf{f}$ according to $\mathbf{A} \cdot \mathbf{t} = \mathbf{f}$, and the kinematic matrix $\mathbf{B}$, relating joint displacements $\mathbf{d}$ and bar elongations $\mathbf{e}$ according to $\mathbf{B} \cdot \mathbf{d} = \mathbf{e}$. Note that equilibrium imposes that $\mathbf{B} = \mathbf{A}^{\mathrm{T}}$. Then, we apply boundary conditions to suppress rigid body motions; in this case, we block the x and y displacements of node (1,1), the node at the bottom left of the specimen, and the y displacement of node (2,1). Finally, we compute the null space of $\mathbf{B}$. If the system is properly constrained, each vector belonging to this null space represents a mode of inextensional deformation. The results of this analysis for two cut patterns are shown in Figure B.5. First, we consider the periodic architecture in Figure B.5(a-b), known

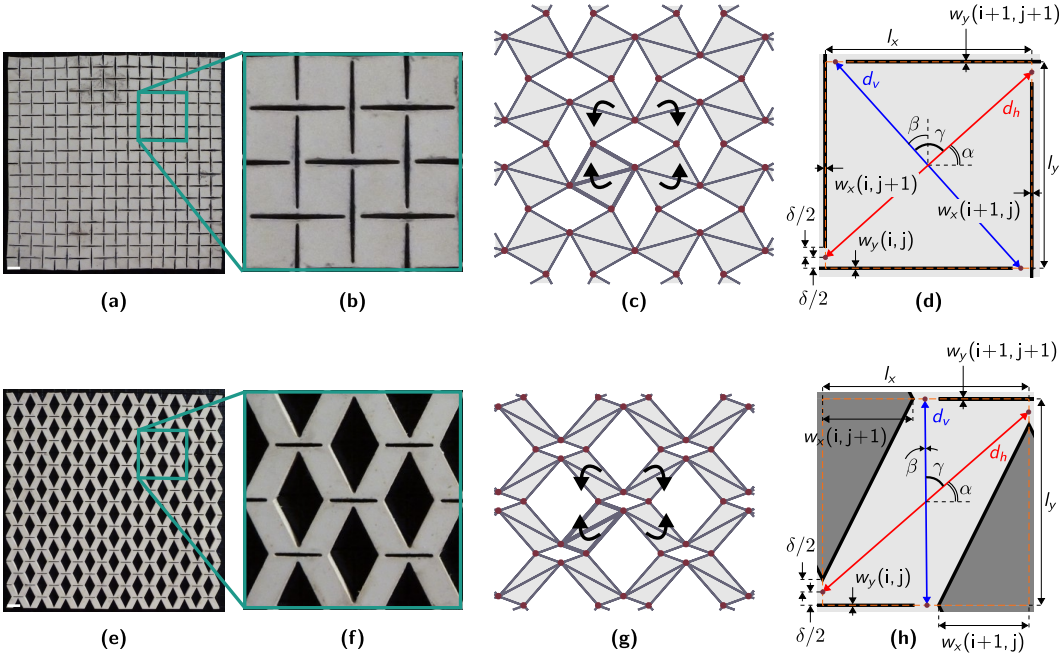

Figure B.5: Kinematic analysis of periodic perforated sheets featuring tiles connected by thin hinges. (a) Isotropic sheet and (b) detail. (c) Mechanism of inextensional deformation for the truss analog of (a), obtained by computing the null space of the kinematic matrix. (d) Detail of one of the tiles of (a), indicating all the quantities necessary for the kinematic analysis. (e-h) Same as (a-d), but for the architecture in (e). (Scale bar, 6 mm)

for its auxeticity [1]. The matrix analysis of the pin-jointed truss analog to this system predicts only one mechanism, shown in Figure B.5(c), and characterized by the tile rotations highlighted by the black arrows. Note that this geometry features no states of self-stress. Thus, even though the analysis assumes small deformations, the same mechanism should extend to large stretch regimes [2]. The periodic sheet in Figure B.5(e) (same as the one shown in Fig. 3.1) features a very similar mechanism of inextensional deformation, characterized by the same relative rotations of the tiles, but with an equivalent positive Poisson's ratio. The tensile tests in Fig. 3.1

and Fig. 3.2 demonstrate that the rubber sheets, despite presenting non-idealities such as finite-sized hinges, deform according to the corresponding mechanisms up to certain stretch values.

Knowing how these periodic sheets deform in plane, we resort to a kinematic model in order to quantify their mechanism-like deformation. The unit cells for these periodic architectures consist of four adjacent tiles. It is sufficient to consider a single tile to determine the whole system's response. In Fig. B.5(d,h) we show a single tile from the sheets in Fig. B.5(a,e), such that $(i + j)/2 \in \mathbb{Z}$, and we indicate all the useful geometric parameters. Here, (i, j) indicates a generic tile, with $i = 1, ..., N_x + 1$, $j = 1, ..., N_y + 1$ and N_x, N_y being the number of tiles along the horizontal and vertical directions. Note that, if we consider a tile such that $(i + j)/2 \notin \mathbb{Z}$, the following formulae will only slightly vary. For the remainder of this section, we assume that we are dealing with periodic architectures; this implies that $w_y(i, j) = w_y(i + 1, j + 1) = w_y$, and $w_x(i + 1, j) = w_x(i, j + 1) = w_x$. The red and blue lines indicate the diagonals of each tile. Their lengths are

$$d_h = \sqrt{l_x^2 + [l_y - 2w_y - \delta]^2} \quad \text{and} \quad d_v = \sqrt{l_y^2 + [l_x - 2w_x - \delta]^2}\,. \tag{B.1}$$

Ideally, tiles can rotate until the diagonal lines corresponding to the selected stretch direction are straightened. With this in mind, we can determine the maximum horizontal and vertical stretches for any periodic architecture designed following our paradigm, as

$$\lambda_x^M = \frac{d_h}{l_x} \quad \text{and} \quad \lambda_y^M = \frac{d_v}{l_y}\,. \tag{B.2}$$

We can also use kinematics to derive formulae for the tangential stretches as functions of λ_x^M or λ_y^M. First, we determine the angle α between d_h and the x-axis in the undeformed configuration, and β between d_v and the y-axis, as

$$\alpha = \arctan\left(\frac{l_y - 2w_y - \delta}{l_x}\right) \quad \text{and} \quad \beta = \arctan\left(\frac{2w_x + \delta - l_x}{l_y}\right)\,. \tag{B.3}$$

Note that we define α to be positive counterclockwise and β to be positive clockwise. We also define $\gamma = \pi/2 - \alpha - \beta$ as the angle between d_h and d_v. During mechanism-like deformation, γ remains fixed since we assume the tiles are rotating rigidly. On the other hand, the inclinations of d_h and d_v with respect to x and y change during the deformation process. To determine the intermediate stages of the sheet's deformation, we define α^* and β^* as angles varying from 0 to α and 0 to β, respectively. Consider now the case of stretching along x. We can write

$$\lambda_x(\alpha^*) = \frac{d_h \cos\alpha^*}{l_x} \quad \text{and} \quad \lambda_y(\alpha^*) = \frac{d_v \sin(\gamma + \alpha^*)}{l_y}\,. \tag{B.4}$$

From the first of the two equations, we obtain $\alpha^*(\lambda_x)$ as

$$\alpha^*(\lambda_x) = \arccos\left(\frac{\lambda_x l_x}{d_h}\right) . \tag{B.5}$$

Substitution leads to the following formula for $\lambda_y(\lambda_x)$:

$$\lambda_y(\lambda_x) = \frac{d_v}{l_y} \sin\left[\gamma + \arccos\left(\frac{\lambda_x l_x}{d_h}\right)\right] . \tag{B.6}$$

This formula is used to determine the analytical curves in Fig. 3.2(e), representing the evolution of the tangential stretch as a function of the applied one. Note that a similar formula can be obtained for $\lambda_x(\lambda_y)$.

In our work, we fix the design parameters l_x, l_y and δ most of the time, and vary w_x and w_y. Different combinations of w_x and w_y allow to span a wide design space in terms of achievable deformations. To get a better idea of the available design space, in Fig. B.6, we report plots for the maximum stretch λ_x^M, and the related tangential stretch $\lambda_y(\lambda_x^M)$, as a function of w_x and w_y. Note that the values in the colormaps are

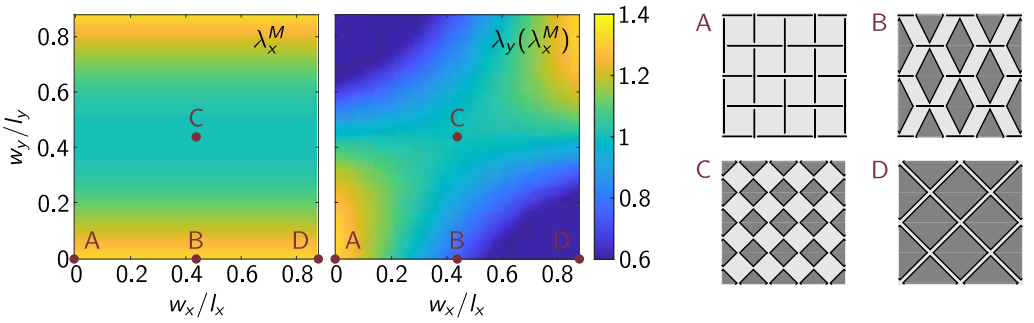

Figure B.6: Design space in terms of maximum stretches, λ_x^M and $\lambda_y(\lambda_x^M)$, as a function of w_x and w_y, with $l_x = l_y = 6$ mm and $\delta = l_x/8$ fixed. Insets A-D represent specific examples extracted from the space.

specific for $l_x = l_y = 6$ mm and $\delta = l_x/8$. We can see that choosing w_x and w_y allows to obtain a wide range of responses to stretching. Some significant examples (A, B, C and D) are extracted from the design space. A, corresponding to $w_x = w_y = 0$, is characterized by $\lambda_x^M = \lambda_y(\lambda_x^M) = 1.33$; B, corresponding to $w_x = (l_x - \delta)/2$ and $w_y = 0$, is characterized by $\lambda_x^M = 1.33$ and $\lambda_y(\lambda_x^M) = 0.75$; C, corresponding to $w_x = (l_x - \delta)/2$ and $w_y = (l_y - \delta)/2$, is kinematically undeformable albeit featuring bulky tiles connected by thin hinges; D, corresponding to $w_x = l_x - \delta$ and $w_y = 0$, does not behave like a mechanism since the rigid tiles assumption does not hold for these specific parameters. From these examples, it is clear that not all the configurations available in the design space allow to obtain the in-plane

mechanism-like deformation behavior we are interested in. Therefore, particular care is needed when choosing the design parameters; in light of this, in this work, we limit ourselves to the ranges $0 \leq w_x \leq (l_x - \delta)/2$ and $0 \leq w_y \leq (l_y - \delta)/2$.

An example of non-periodic sheet is shown in Fig. B.7(a). Non-periodicity leads to

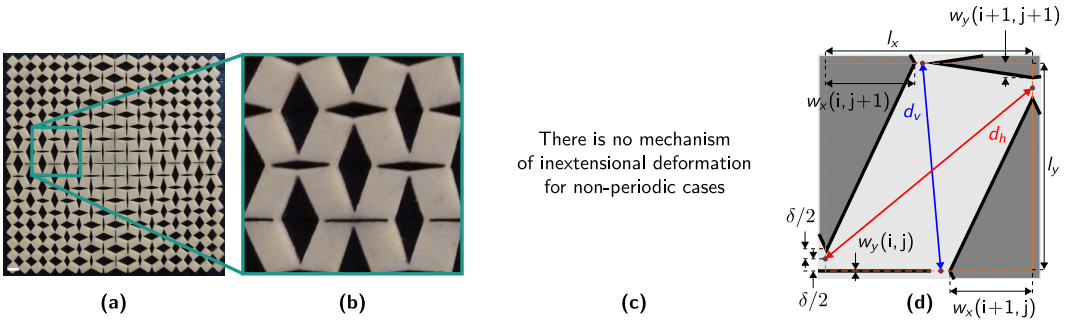

Figure B.7: Kinematic analysis of non-periodic perforated sheets featuring tiles connected by thin hinges. (a) Example of non-periodic sheet. (b) Detail of the sheet in (a). (c) The null space of the kinematic matrix of the pin-jointed truss analog to (a) contains no mechanism. (d) Detail of one of the tiles of the sheet in (a), with all the quantities necessary for the kinematic analysis. (e-h) Same as (a-d), but for the architecture in (e). (Scale bar, 6 mm)

frustration and to the disappearance of mechanisms of inextensional deformation. This is confirmed by the matrix analysis of the pin-jointed truss analog of the architecture in Fig. B.7(a), that has no mechanisms. In these non-periodic cases, we can still use kinematics to infer something about the local deformation of the sheet, even though it cannot be used to quantify global deformations as it did in periodic scenarios. For this reason, in the main article, we sometime consider the maximum stretches that a tile belonging to a non-periodic sheet can undergo. We interpret these stretches as measures of a local ability to deform. The local ability to behave like a mechanism is what makes these systems buckle out of plane. For a generic tile in a non-periodic scenario, whose bottom-left gridpoint (i, j) is such that $(i + j)/2 \in \mathbb{Z}$, the maximum stretches are calculated as in Eq. B.2, with d_h and d_v computed as

$$d_h = \sqrt{l_x^2 + [l_y - w_y(i,j) - w_y(i+1,j+1) - \delta]^2} \quad \text{and} \tag{B.7}$$

$$d_v = \sqrt{l_y^2 + [l_x - w_x(i,j+1) - w_x(i+1,j) - \delta]^2}\,. \tag{B.8}$$

B.4 Cut pattern generation

Our cut patterns are generated and kinematically analyzed using custom MATLAB scripts. The first step of the design process is to generate a grid of points. The grid can be non-Cartesian, as long as it can be mapped to a rectangular one. At each grid

point $(i,\ j)$ with $i = 1, ..., N_x + 1$ and $j = 1, ..., N_y + 1$ with N_x and N_y being the number of tiles along the horizontal and vertical directions, we cut a diamond-shaped hole. For each diamond, we define either its horizontal or vertical half-diagonal, i.e. w_x or w_y. If $(i+j)/2 \in \mathbb{Z}$ we define the diamond's y-oriented half-diagonal $w_y(i,\ j)$. Its x-dimension will be determined by the neighboring diamonds—$l_x - \delta - w_x(i-1, j)$ to the left and $l_x - \delta - w_x(i + 1, j)$ to the right of the grid point. Otherwise, if $(i + j)/2 \notin \mathbb{Z}$, we define $w_x(i,\ j)$ while the diamond's y-dimension follows from the neighboring diamonds. This design paradigm guarantees geometric continuity and that no perforations overlap, even in non-periodic architectures where we let w_x and w_y vary (smoothly or not) from diamond to diamond. In the case of architectures designed to allow for plastic deformations, instead of defining a diamond, we define an octahedron at each gridpoint.

The w_x, w_y functions corresponding to all cut patterns shown throughout this manuscript are listed in the following.

- "Anisotropic" sheet.
  Appearing in Fig. 3.1, Fig. 3.2(c), Fig. B.5(e), Fig. B.4(a), Fig. B.6(b), Fig. B.1, Fig. B.2, Fig. B.8.
  Loading: Uniform horizontal or uniform vertical.
  Material: Natural rubber gum of various thicknesses (1.55, 3.1 mm).
  Parameters: $N_x = N_y = 18$, $l_x = l_y = 6\,\text{mm}$, $\delta = l_x/8$.
  Hole size distribution (with $i = 1, ..., N_x + 1$, $j = 1, ..., N_y + 1$):

$$w_x(i, j) = (l_x - \delta)/2\ , \quad w_y(i, j) = 0\ .$$

- "Isotropic" sheet.
  Appearing in Fig. 3.2(b), Fig. B.5(a), Fig. B.6(a), Fig. B.3.
  Loading: Uniform horizontal or uniform vertical.
  Material: Natural rubber gum, 1.55 mm thick.
  Parameters: $N_x = N_y = 18$, $l_x = l_y = 6\,\text{mm}$, $\delta = l_x/8$.
  Hole size distribution (with $i = 1, ..., N_x + 1$, $j = 1, ..., N_y + 1$):

$$w_x(i, j) = 0\ , \quad w_y(i, j) = 0\ .$$

- "Unstretchable" sheet.
  Appearing in Fig. 3.2(d), Fig. B.6(c).
  Loading: Uniform horizontal or uniform vertical.

Material: Natural rubber gum, 1.55 mm thick.
Parameters: $N_x = N_y = 18$, $l_x = l_y = 6\,\text{mm}$, $\delta = l_x/8$.
Hole size distribution (with $i = 1, ..., N_x + 1$, $j = 1, ..., N_y + 1$):

$$w_x(i,j) = (l_x - \delta)/2 \ , \quad w_y(i,j) = (l_y - \delta)/2 \ .$$

- "Graded" or "Dome" sheet.
  Appearing in Fig. 3.3(a1-a2), Fig. B.9, Fig. B.10, Fig. B.12(a).
  Loading: Horizontal point loads at $y = y^M/2$ along the left and right boundaries.
  Material: Natural rubber gum of various thicknesses (1.55, 3.1 and 0.75 mm).
  Parameters: $N_x = 36$, $N_y = 18$, $l_x = 6\,\text{mm}$, $l_y = 2l_x$, $\delta = l_x/8$.
  Hole size distribution (with $i = 1, ..., N_x + 1$, $j = 1, ..., N_y + 1$):

$$w_x(i,j) = \frac{(l_x - \delta)}{2} \ , \quad w_y(i,j) = \frac{l_y - \delta}{2} \left|\cos \frac{j\pi}{N_y + 2}\right| \ .$$

- "Two bumps" sheet.
  Appearing in Fig. 3.3(b1-b2) and Fig. B.4(b).
  Loading: Point loads at the four corners, directed along $\pm 5^{\text{o}}$ with respect to the horizontal.
  Material: Natural rubber gum, 1.55 mm thick.
  Parameters: $N_x = 37$, $N_y = 18$, $l_x = l_y = 6\,\text{mm}$, $\delta = l_x/8$.
  Hole size distribution (with $i = 1, ..., N_x + 1$, $j = 1, ..., N_y + 1$):

$$w_x(i,j) = \begin{cases} \frac{l_x - \delta}{2} \left|\cos \frac{i\pi}{(N_x+1)/2}\right| & \text{if } i < (N_x+1)/2 + 1 \\ \\ \frac{l_x - \delta}{2} \left|\cos \frac{(i-(N_x+1)/2)\pi}{(N_x+1)/2}\right| & \text{if } i \geq (N_x+1)/2 + 1 \end{cases} \ ,$$

$$w_y(i,j) = \frac{l_y - \delta}{2} \left|\cos \frac{j\pi}{N_y + 2}\right| \ .$$

- "Flower" sheet.
  Appearing in Fig. 3.3(c1-c3).
  Loading: Point loads at the four corners (directed at $\pm 45^{\text{o}}$ with respect to the horizontal), or point loads at the centerpoints of the four edges (and perpendicular to those edges).
  Material: Natural rubber gum, 1.55 mm thick.

Parameters: $N_x = 37$, $N_y = 37$, $l_x = l_y = 6\,\text{mm}$, $\delta = l_x/8$.
Hole size distribution (with $i = 1, ..., N_x + 1$, $j = 1, ..., N_y + 1$):

$$w_x(i,j) = \frac{l_x - \delta}{2}\left|\cos\frac{2i\pi}{N_x+1}\right|\left|\cos\frac{2j\pi}{N_y+1}\right| ,$$
$$w_y(i,j) = \frac{l_y - \delta}{2}\left|\cos\frac{2i\pi}{N_x+1}\right|\left|\cos\frac{2j\pi}{N_y+1}\right| .$$

- "C pattern" sheet.
  Appearing in Fig. 3.3(d1-d2).
  Loading: Point loads at few points along each boundary. All loads are perpendicular to the boundaries.
  Material: Natural rubber gum, 1.55 mm thick.
  Parameters: $N_x = 30$, $N_y = 30$, $l_x = l_y = 6\,\text{mm}$, $\delta = l_x/8$.
  Hole size distribution: We did not use analytical functions of i and j to create this pattern. The w_x, w_y couples we use are $w_x = (l_x - \delta)/2$ and $w_y = (l_y - \delta)/2$ outside the C, and $w_x = 0$, $w_y 0$ inside the C.

- "Bulging tube."
  Appearing in Fig. 3.4(a).
  Loading: Axial loads applied at the ends of the tube through 3D printed rings.
  Material: Natural rubber gum, 1.55 mm thick.
  Parameters: $N_x = 18$, $N_y = 40$, $l_x = l_y = 6\,\text{mm}$, $\delta = l_x/8$.
  Hole size distribution (with $i = 1, ..., N_x + 1$, $j = 1, ..., N_y + 1$):

  $$w_x(i,j) = 0 ,$$
  $$w_y(i,j) = \begin{cases} (l_y - \delta)/2 & \text{if } j \le 6 \,|\, (j \ge 15 \,\&\, j \le 20) \,|\, (j \ge 26 \,\&\, j \le 31) \,|\, j \ge 35 \\ 0 & \text{if } (j \ge 7 \,\&\, j \le 14) \,|\, (j \ge 21 \,\&\, j \le 26) \,|\, (j \ge 32 \,\&\, j \le 34) \end{cases} .$$

- "Petal" sheet.
  Appearing in Fig. 3.4(b).
  Loading: Axial loads applied at the petal's extremities.
  Material: Natural rubber gum, 1.55 mm thick.
  Parameters: We used $w_x = (l_x - \delta)/2$ and $w_y = (l_y - \delta)/2$ along the petal's boundaries and in those regions that we want to remain stiff; we used $w_x = 0$, $w_y = 0$ elsewhere.

- "Plastic chalice."
  Appearing in Fig. 3.4(d).

Loading: Manual forming.
Material: 0.5 mm-thick PETG sheet.
Parameters: $N_x = 36$, $N_y = 18$, $l_x = 6\,\text{mm}$, l_y varies linearly from 6 mm at the bottom of the specimen to 18 mm at the top, $\delta = l_x/10$, $h = l_x/8$.
Hole size distribution (with $i = 1, ..., N_x + 1$, $j = 1, ..., N_y + 1$):

$$w_x(i,j) = \frac{(l_x - \delta)}{2}\ , \quad w_y(i,j) = \frac{l_y - \delta}{2} - \frac{l_y - \delta}{2}\left|\cos\frac{j\pi}{N_y + 2}\right|\ .$$

- "Plastic vase."
  Appearing in Fig. 3.4(c).
  Loading: Manual forming.
  Material: 0.5 mm-thick PETG sheet.
  Parameters: $N_x = 36$, $N_y = 18$, $l_x = 6\,\text{mm}$, l_y varies linearly from 6 mm at the bottom of the specimen to 18 mm at the top, $\delta = l_x/10$, $h = l_x/8$.
  Hole size distribution (with $i = 1, ..., N_x + 1$, $j = 1, ..., N_y + 1$):

$$w_x(i,j) = \frac{(l_x - \delta)}{2}\ , \quad w_y(i,j) = \frac{l_y - \delta}{2} - \frac{l_y - \delta}{2}\left|\cos\frac{j\pi}{2N_y + 4}\right|\ .$$

- "No mechanism" sheet.
  Appearing in Fig. B.7(a).
  Loading: None.
  Material: Natural rubber gum, 1.55 mm thick.
  Parameters: $N_x = 18$, $N_y = 18$, $l_x = l_y = 6\,\text{mm}$, $\delta = l_x/8$.
  Hole size distribution (with $i = 1, ..., N_x + 1$, $j = 1, ..., N_y + 1$):

$$w_x(i,j) = \frac{l_x - \delta}{2}\left|\cos\frac{i\pi}{N_x + 2}\right|\ , \quad w_y(i,j) = \frac{l_y - \delta}{2}\left|\cos\frac{j\pi}{N_y + 2}\right|\ .$$

- "Plastic dome."
  Appearing in Fig. B.12(b).
  Loading: Horizontal point loads at $y = y^M/2$ along the left and right boundaries.
  Material: 0.5 mm-thick PETG sheet.
  Parameters: $N_x = 36$, $N_y = 18$, $l_x = 6\,\text{mm}$, $l_y = 2l_x$, $\delta = l_x/10$, $h = l_x/8$.
  Hole size distribution (with $i = 1, ..., N_x + 1$, $j = 1, ..., N_y + 1$):

$$w_x(i,j) = \frac{(l_x - \delta)}{2}\ , \quad w_y(i,j) = \frac{l_y - \delta}{2}\left|\cos\frac{j\pi}{N_y + 2}\right|\ .$$

B.5 Influence of the design parameters on the in-plane deformation of periodic specimens

To analyze the influence of the design parameters on the in-plane response of perforated sheets, we consider the cut pattern discussed in Figure 1 as reference case. The results of this analysis are reported in Figure B.8. In Fig. B.8(a), we show

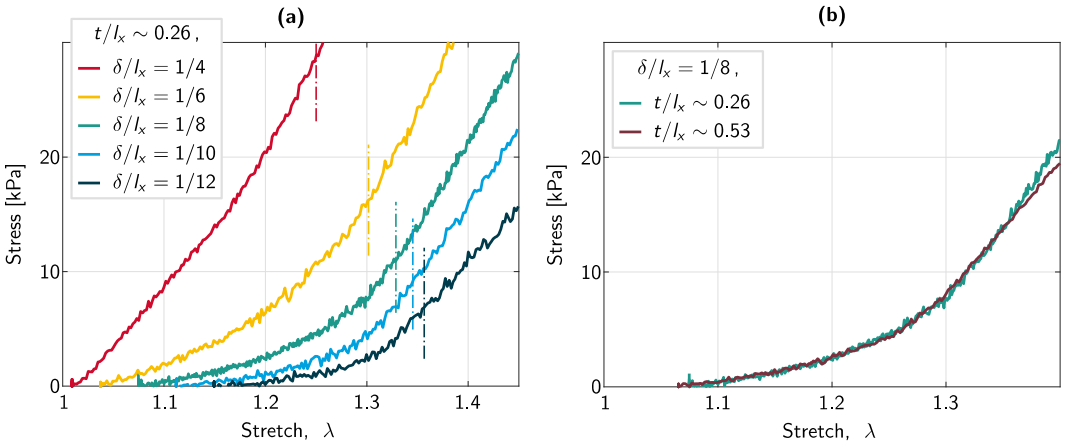

Figure B.8: Influence of design parameters on sheet stiffness. (a) Dependence of the mechanism-like response on the in-plane hinge width, δ. We keep $t/l_x \sim 0.26$ constant, and we vary δ/l_x. The dashed vertical lines represent the mechanism-to-elasticity transitions for all δ/l_x cases. (b) Dependence of the mechanism-like response on the sheet's thickness, t, with $\delta/l_x = 1/8$ constant.

the dependence of the horizontal stretch response on the in-plane width of the hinges δ, for a constant out-of-plane thickness of the sheet $t/l_x \sim 0.26$ (corresponding to $t = 1.55$ mm). If δ is increased, the sheet tends to lose its mechanism-like behavior. This is evident from the fact that the red and yellow continuous curves do not display a clear mechanism-to-elasticity transition. On the other hand, this transition is more pronounced for small δ. Note that the dash-dot lines represent the mechanism-to-elasticity transitions for each δ value. They are different from each other since the lengths of the tile diagonals d_h and d_v differ when we change δ.

In Fig. B.8(b), we superimpose the responses of two specimens featuring the same architecture with $\delta/l_x = 1/8$, and different sheet thicknesses, t. We observe that the two responses overlap in the mechanism region, and in part of the elasticity-dominated regime. The curves deviate for stretches larger than 1.35.

B.6 Influence of the design parameters on the out-of-plane deformation of non-periodic sheets

Fig. B.9 and Fig. B.10 provide information on the influence of δ and t on the doming of an elastic sheet. Figure B.9 is discussed in detail in the main manuscript. Note that these shapes have been obtained by 1) pulling the specimen by hand up to a desired stretch value, 2) nailing it to a wooden board, 3) pinching the center of the specimen to trigger out-of-plane buckling. This guarantees that all the images in Figure B.9 and Figure B.10 are obtained with consistent loading conditions. It also ensures that, if two stable solutions exist for a certain stretch value, we jump on the one that corresponds to out-of-plane deformation. For these reasons, the critical buckling stretches observed in experiments made with tensile test apparati are bound to differ from the results shown here.

In addition to the comments in the main text, we here discuss the influence of δ/t. When t is decreased below the in-plane hinge width δ, the out-of-plane (rather than the in-plane) bending of the hinges becomes favorable: this translates into the formation of localized crease patterns [4, 5]. In our case, this behavior introduces local undulations superimposed to the global three-dimensional profile and concentrated near the loading sites. This is shown in Figure B.10(c).

B.7 Alternative design for stiff materials and plastic deformations

In order to fabricate sheets out of stiff materials, and to have our sheets retain their 3D shape upon load removal, we slightly modify our cut pattern design. To achieve shape retention, we leverage plastic deformations that occur at the hinges when elastic-plastic materials are used. If the same hinge geometry used for soft materials were used for stiff ones, both periodic and non-periodic specimens would shatter at the hinges when pulled open. This is why we modify our hinge design. To do so, we follow the guidelines offered by Shang, Pasini, et al. [6]. This entails defining octahedra-shaped cuts instead of diamond-shaped ones at each grid point. This new design strategy is illustrated in Fig. B.11(b). It represents the compliant mechanism version of the architecture in Fig. B.11(a). As a result, the hinges produced with the new design strategy have a finite length h. Note that the overall response of this alternate geometry is similar to the original one. The requirement is for the hinge length h to be much smaller than the distances between gridpoints, l_x and l_y.

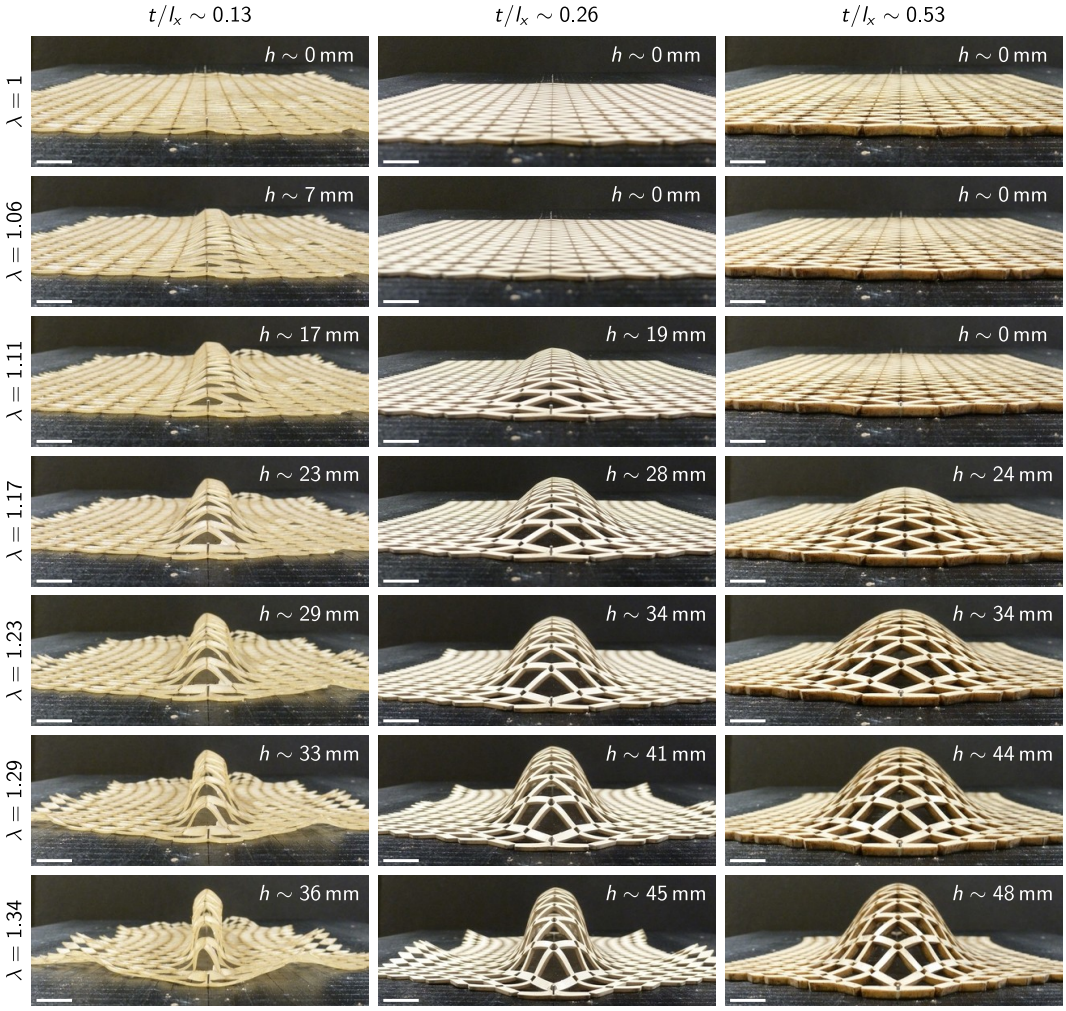

Figure B.9: Out-of-plane deformation of three graded sheets with different thicknesses, for different stretches. Rows of images correspond to specific stretch values. Columns correspond to different thicknesses of the sheets. In each image, h indicates the height of the highest point of the 3D shape with respect to its undeformed position. (Scale bar, 12 mm)

In Fig. B.12, we compare the response of the natural rubber sheet also shown in Fig. 3.3(a1), to the response of a sheet made of PETG, featuring a similar cut pattern albeit modified by selecting $\delta = l_x/10$ and introducing $h = l_x/8$. Upon load removal, the PETG sheet partially retains its deformed, three-dimensional shape, while the rubber one does not.

References

[1] J. N. Grima, V. Zammit, R. Gatt, A. Alderson, and K. E. Evans. Auxetic behaviour from rotating semi-rigid units. *Physica Status Solidi B*, 244(3):866–882, 2007. doi: 10.1002/pssb.200572706.

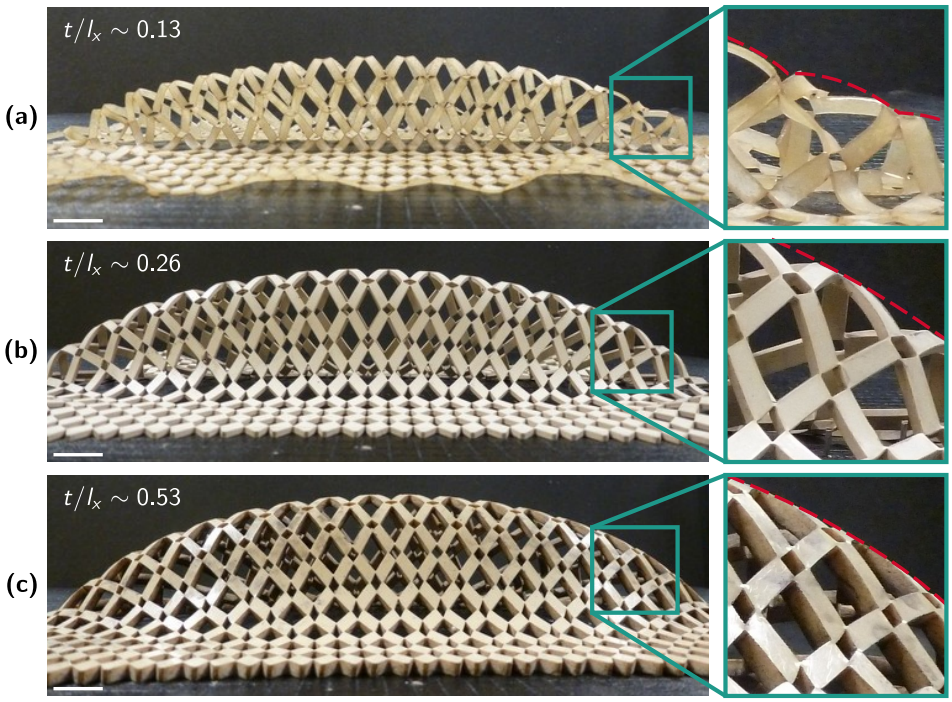

Figure B.10: Out-of-plane deformation of three graded sheets with different thicknesses, for the same stretch value. (a) Corresponds to $t/l_x \sim 0.13$, (b) to $t/l_x \sim 0.26$ and (c) to $t/l_x \sim 0.53$. The left images represent lateral views of the buckled shapes. The details highlight the local deformations of hinges and tiles near the load application points. (Scale bar, 12 mm)

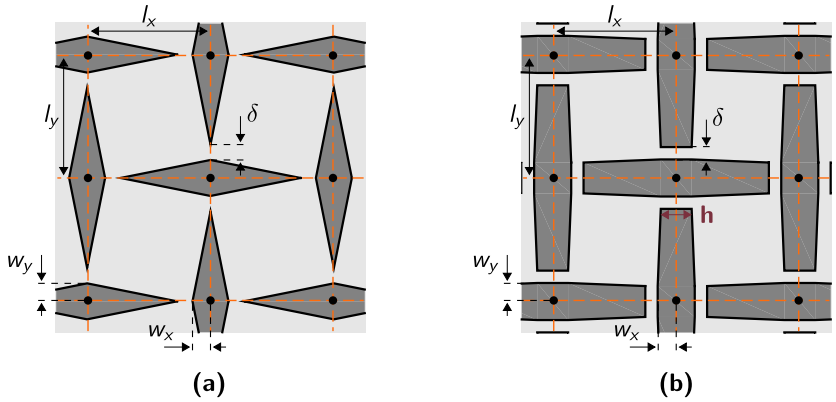

Figure B.11: An alternative design startegy for stiff materials. (a) Detail of an architecture obtained with our initial design strategy. (b) Compliant beam version of the same architecture, where we have introduced the additional parameter h, representing the in-plane hinge length.

[2] R. G. Hutchinson and N. A. Fleck. The structural performance of the periodic truss. *Journal of the Mechanics and Physics of Solids*, 54(4):756–782, 2006. doi: 10.1016/j.jmps.2005.10.008.

[3] S. Pellegrino and C.R. Calladine. Matrix analysis of statically and kinematically

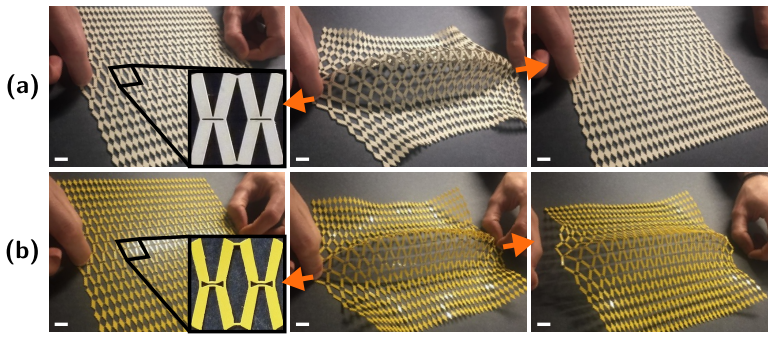

Figure B.12: Plastic dome. (a) Three stages of the deformation of the natural rubber specimen studied in Fig. 3.3(a). (b) Deformation of a similar sheet, made of PETG and featuring the design variation shown in Fig. B.11(b). (Scale bar, 12 mm)

indeterminate frameworks. *International Journal of Solids and Structures*, 22 (4):409–428, 1986. doi: 10.1016/0020-7683(86)90014-4.

[4] A. Rafsanjani and K. Bertoldi. Buckling-induced kirigami. *Physical Review Letters*, 118:084301, 2017. doi: 10.1103/PhysRevLett.118.084301.

[5] A. Rafsanjani, Y. Zhang, B. Liu, S. M. Rubinstein, and K. Bertoldi. Kirigami skins make a simple soft actuator crawl. *Science Robotics*, 3(15), 2018. doi: 10.1126/scirobotics.aar7555.

[6] X. Shang, L. Liu, A. Rafsanjani, and D. Pasini. Durable bistable auxetics made of rigid solids. *Journal of Materials Research*, 33(3):300—-308, 2018. doi: 10.1557/jmr.2017.417.

Appendix C

EFFECTIVE CONTINUUM MODELS FOR THE BUCKLING OF NON-PERIODIC ARCHITECTED SHEETS THAT DISPLAY QUASI-MECHANISM BEHAVIORS

C.1 Strong form of equilibrium

The strong form of the equilibrium relations under the mixed formulation are

$$\begin{aligned} -\nabla \cdot \left(2\mathbf{F}\frac{\partial \Psi_m}{\partial \mathbf{C}} \right) &= 0 \qquad && \text{in } \Omega, \\ -\nabla \cdot \left(2\frac{\partial \Psi_m}{\partial \mathbf{C}}\nabla w \right) + \frac{\partial \Psi_c}{\partial w} + B\Delta v &= 0 \qquad && \text{in } \Omega, \\ B(\Delta w - v) &= 0 \qquad && \text{in } \Omega, \end{aligned} \tag{C.1}$$

with boundary conditions

$$\begin{aligned} \left(2\mathbf{F}\frac{\partial \Psi_m}{\partial \mathbf{C}} \right) \cdot n &= 0 \qquad && \text{on } \partial_f \Omega, \\ u &= u_0 \qquad && \text{on } \partial_u \Omega, \\ w = w_0,\ v &= 0 \qquad && \text{on } \partial\Omega. \end{aligned} \tag{C.2}$$

The first two equations in (C.1) are the in-plane and out-of-plane momentum balance equations, respectively. The last equation is the constraint that $v = \Delta w$.

C.2 Finite element formulation and Solution Procedure

The fields $\mathbf{u}$, w, and v are $H^1(\Omega)$, so we may consider a Galerkin finite element formulation with p = 1 shape functions for them. Therefore,

$$\mathbf{u} = \sum_{i=0}^{n_u} u_i \boldsymbol{\Phi}_i^u, \qquad w = \sum_{i=0}^{n_w} w_i \Phi_i^w, \qquad v = \sum_{i=0}^{n_v} v_i \Phi_i^v, \tag{C.3}$$

where $\{\boldsymbol{\Phi}_i^u\}$ is the set of vector-valued shape functions for the in-plane displacements. $\{\Phi_i^w\}$ and $\{\Phi_i^v\}$ are the scalar-valued sets of shape functions for w and v, respectively. Because we assume homogeneous boundary conditions for both of these fields, we can then consider $\{\Phi_i^w\} = \{\Phi_i^v\}$. Then, using these shape functions for the variations in (4.22), the discrete equilibrium equations can be written as

$$\begin{bmatrix} \mathbf{R}^u \\ \mathbf{R}^w \\ \mathbf{R}^v \end{bmatrix} = \mathbf{R} = \mathbf{0}\,, \tag{C.4}$$

where

$$
\begin{aligned}
R_i^u &= \int_\Omega \left(2\mathbf{F}\frac{\partial \Psi_m}{\partial \mathbf{C}}\right) : \nabla \mathbf{\Phi}_i^u \, dA, \\
R_i^w &= \int_\Omega \left(2\frac{\partial \Psi_m}{\partial \mathbf{C}}\nabla w - B\nabla v\right) \cdot \nabla \Phi_i^w + \frac{\partial \Psi_c}{\partial w}\Phi_i^w \, dA, \\
R_i^v &= \int_\Omega -B\, v\, \Phi_i^v - B\nabla w \cdot \nabla \Phi_i^v \, dA.
\end{aligned} \tag{C.5}
$$

To solve for this equilibrium, we use Newton-Raphson updates of the form

$$
\mathbf{K}(\mathbf{x})\Delta\mathbf{x} = -\mathbf{R}(\mathbf{x}), \tag{C.6}
$$

where $\mathbf{x} = [u_0, \ldots, u_{n_u}, w_0, \ldots, w_{n_w}, v_0, \ldots, v_{n_v}]$ is the vector of degrees of freedom, $\Delta\mathbf{x}$ are their updates, and $\mathbf{K}$ is the tangent stiffness matrix

$$
\mathbf{K} = \begin{bmatrix} \mathbf{K}^{uu} & \mathbf{K}^{uw} & \mathbf{0} \\ \mathbf{K}^{wu} & \mathbf{K}^{ww} & \mathbf{K}^{wv} \\ \mathbf{0} & \mathbf{K}^{vw} & \mathbf{K}^{vv} \end{bmatrix}, \tag{C.7}
$$

where

$$
\begin{aligned}
K_{ij}^{uu} &= \int_\Omega \nabla \mathbf{\Phi}_i^u : \frac{\partial^2 \Psi_m}{\partial \mathbf{F} \partial \mathbf{F}} : \nabla \mathbf{\Phi}_j^u \, dA, \\
K_{ij}^{ww} &= \int_\Omega \nabla \Phi_i^w \cdot \frac{\partial^2 \Psi_m}{\partial \nabla w \partial \nabla w} \cdot \nabla \Phi_j^w \, dA, \\
K_{ij}^{vv} &= \int_\Omega -B\, \Phi_i^v \Phi_j^v \, dA, \\
K_{ij}^{uw} &= K_{ji}^{wu} = \int_\Omega \nabla \mathbf{\Phi}_i^u : \frac{\partial^2 \Psi_m}{\partial \mathbf{F} \partial \nabla w} \cdot \nabla \Phi_j^w \, dA, \\
K_{ij}^{wv} &= K_{ji}^{vw} = \int_\Omega -B\nabla \Phi_i^w \cdot \nabla \Phi_j^v \, dA.
\end{aligned} \tag{C.8}
$$

The displacements $\mathbf{u}_0$ on the boundary are incremented, and Newton-Raphson is used to reach an equilibrium configuration. The previous equilibrium configuration is used as an initial guess for the subsequent iterations.

C.3 Stability analysis with mixed method constraint

To probe the stability of an equilibrium configuration, it is common practice to calculate the eigenvalues of the tangent stiffness matrix. A negative eigenvalue implies an instability, and the equilibrium solution can be perturbed in the direction of the corresponding eigenvector to explore the buckled solution. In our case, we must restrict ourselves to eigenvectors in the subspace where the constraint $v = \Delta w$ is satisfied. To this end, we consider an effective stiffness matrix from

the quadratic form, upon which the constraint is satisfied. Consider the discrete constraint equation:

$$\mathbf{R}^v = \mathbf{K}^{vw}\mathbf{w} + \mathbf{K}^{vv}\mathbf{v} = \mathbf{0}. \tag{C.9}$$

This can also be written in the following form:

$$\mathbf{v} = -\left(\mathbf{K}^{vv}\right)^{-1}\mathbf{K}^{vw}\mathbf{w}. \tag{C.10}$$

We can then use a reduced variable set $\mathbf{x}_r$ under which the constraint is satisfied, as

$$\mathbf{x} = \begin{bmatrix}\mathbf{u}\\ \mathbf{w}\\ \mathbf{v}\end{bmatrix} = \begin{bmatrix}\mathbf{I}_{n_u\times n_u} & \mathbf{0}\\ \mathbf{0} & \mathbf{I}_{n_w\times n_w}\\ \mathbf{0} & -\left(\mathbf{K}^{vv}\right)^{-1}\mathbf{K}^{vw}\end{bmatrix}\begin{bmatrix}\mathbf{u}\\ \mathbf{w}\end{bmatrix} = \mathbf{P}\mathbf{x}_r. \tag{C.11}$$

Then, the quadratic form gives

$$\mathbf{x}^T\mathbf{K}\mathbf{x} = \mathbf{x}_r^T\,\widetilde{\mathbf{K}}\,\mathbf{x}_r, \tag{C.12}$$

where

$$\widetilde{\mathbf{K}} = \mathbf{P}^T\mathbf{K}\mathbf{P} = \begin{bmatrix}\mathbf{K}^{uu} & \mathbf{K}^{uw}\\ \mathbf{K}^{wu} & \left(\mathbf{K}^{ww} - \mathbf{K}^{wv}\left(\mathbf{K}^{vv}\right)^{-1}\mathbf{K}^{vw}\right)\end{bmatrix}. \tag{C.13}$$

Then to assess stability, we probe the eigenvalues of this effective stiffness matrix $\widetilde{\mathbf{K}}$. An eigenvalue passing through zero along the principle deformation path implies an instability. The corresponding eigenvector can then be used to produce a perturbation, using $\mathbf{P}$ to map back to the full variable set. The magnitude of the perturbation is chosen to be on the same order as the displacement increment. The direction of the perturbation is decided such that the w component at the middle of the sheet is positive.

Appendix D

PROGRAMMING TEMPORAL MORPHING OF SELF-ACTUATED SHELLS

D.1 Shell design

Our shells have three layers. Two 3D-printed non-uniform tessellations form the outer layers. These are glued to either side of a pre-stretched latex membrane. This section describes the design of the flat-printed geometries.

Single unit cell design

The shells' outer layers are tessellations of the structures shown in Fig. D.1. Each of these unit cells is bounded by four cylinders of diameter 4 mm and height 2.3 mm, called bases. The bases are connected to their neighbors by two symmetric V-shaped spring elements (called brackets) that form an angle of 37^o relative to the central axis and have a height of 1 mm. At room temperature, brackets are sufficiently stiff to prevent finite deformations due to compression by the pre-stretched elastic membrane that constitutes the shells' mid-planes. The brackets soften when placed in hot water, inducing in-plane contraction. This contraction occurs until the bumpers attached to the bases in the space between the brackets collide. This collision occurs in each unit cell once the target in-plane deformation for that unit is reached. Local curvatures are programmed in a unit cell by setting different bumper lengths for the opposite outer layers. To facilitate aligning the two outer layers with respect to each other during shell fabrication, cylindrical holes are subtracted from several bases (see Appendix D.5 for more information).

The feature dimensions were chosen for the following reasons. Bases interface the membrane to the brackets, so they must have a sufficiently large gluing area to be reliably connected to the membrane, but should be small enough to allow large curvatures in decimeter-scaled specimens. The bracket shape is designed to reduce both in-plane and out-of-plane shearing. In-plane shearing is prevented due to the large (37°) angle between the bracket and the central axis. Out-of-plane shearing is prevented due to the rectangular shape of the bracket section. The 1 mm bracket height is always larger than its thickness ($h \leq 0.65$ mm), which makes in-plane bending energetically favorable.

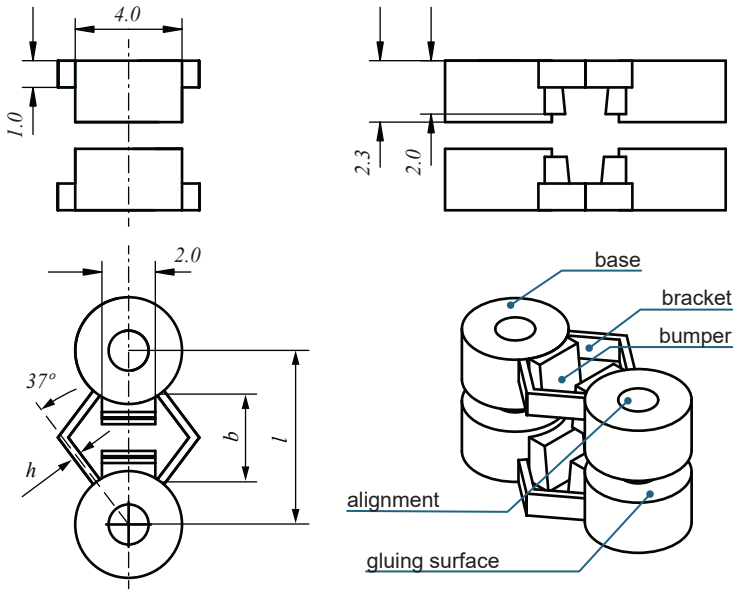

Figure D.1: Unit cell scheme. The configurable parameters are the central length l (constant difference with bracket length b), bracket thicknesses h (which can be different for the two opposite layers), and the bumper cutting plane.

Tessellating unit cells

The design pipeline starts with a user-provided target surface (Fig. D.2), which is isotropically remeshed into a triangular mesh $\mathcal{T}$ with a target number of vertices N [1]. Each pair of adjacent triangles of this mesh represents one unit cell with two bases placed on opposite faces of each triangle, centered on its barycenter. Thus, the whole mesh $\mathcal{T}$ serves as a stencil for our structure's final state, when deformation has completed. It is scaled to ensure there is a minimal bumper length (0.3 mm) to limit bracket deformations in the final state. The actual size of the shell depends on the number of vertices in $\mathcal{T}$.

In order to generate a shell of dimensions close to the input surface, we aim to minimize the required scaling of the stencil. First, we find the best fitting number of vertices of the stencil. It can be coarsely estimated as $N \approx 0.38A/l_{\text{avg}}^2$ where A is total surface area and $l_{\text{avg}} = 7$ mm is the average unit cell length (using heuristic knowledge that the number of triangles is twice the number of vertices, assuming triangles are close to regular, and approximating unit cell lengths as twice the radius of circumscribed circles). Then, N can be varied to find a value leading to minimal stencil scaling.

Given the layout of bases on the stencil, the bumpers are first constructed as boxes that are aligned along the lines connecting the centers of the triangles and projected

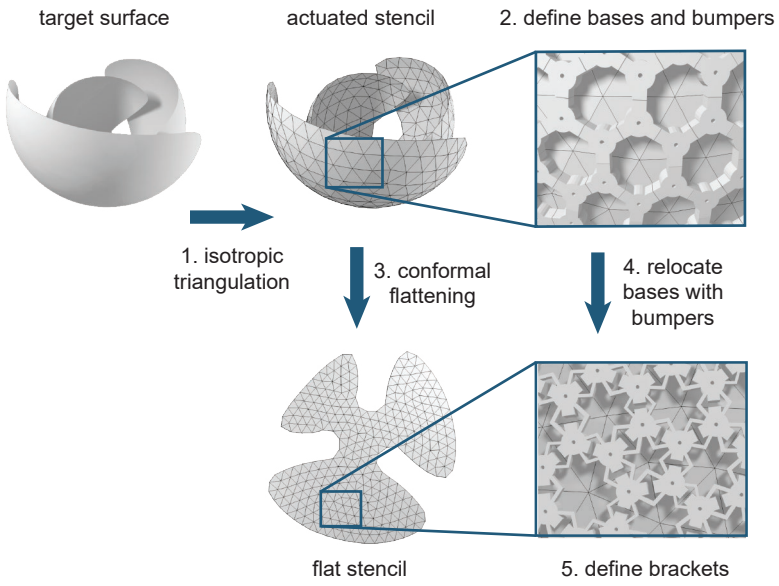

Figure D.2: Shell design pipeline: 1. A target surface is isotropically triangulated. 2. This "actuated" stencil is populated with bases and bumpers touching their corresponding neighbors. 3. The "actuated" stencil is conformally flattened. 4. Bases with bumpers are relocated to the flat stencil. 5. Bracket lengths are set by the distance between bases in this configuration. Bracket thickness is defined later during the temporal programming phase.

onto the corresponding stencil triangle. Matching pairs of boxes are trimmed by the bisector plane between the triangles, defining the interface between neighboring bumpers.

The flat arrangement of bases is then constructed using a minimal distortion conformal map [2] from $\mathcal{T}$ to a resulting 2D mesh, $\mathcal{F}$. We exploit conformal flattening since it circumvents shearing which would result in undesired shear forces in the membrane as it contracts. The mesh $\mathcal{F}$ serves as a stencil for the structure's initial, printed state. We relocate the bases by translation from triangle centers in the final state's stencil to triangle centers in the initial state's stencil. The bases are rotated to align one of its bumper axes in the direction of the corresponding neighbor's center since it is generally not possible to perfectly align all of them. Then, $\mathcal{F}$ is scaled so that the relocated bases with bumpers do not intersect with their neighbors, moreover specifying the minimal gap between them necessary for fabrication (0.1 mm).

Once the flat layout of bases with bumpers is complete, V-shaped brackets that bridge the gaps between bases are generated. This produces a flat structure that fully encodes the target geometry. Conformal flattening may produce overlaps of unit cells, or some of the unit cells may be longer than our upper bound (9.5 mm),

making the target shape impossible to replicate. Large unit cell lengths may occur if the target surface has regions with high curvatures or that require substantial stretching during conformal flattening. It is in certain cases possible to resolve the latter issue by placing cuts across the surface [3] or by editing the input geometry. Morphing times are programmed by configuring the thicknesses of the brackets (see Appendix D.4).

OpenSCAD[1] scripts were used to generate STL meshes for the fabricated structures in this study.

D.2 Simulation

Our framework builds on physical simulation to predict the deformed configuration of the system at a given instant in time. We consider a discrete mechanical model that determines the mechanical behavior of a deformable object based on an elasto-plastic model with elastic energy potential $W(\mathbf{x}, \bar{\mathbf{x}}(t), \boldsymbol{\kappa}(t)) \in \mathcal{R}$ and plastic energy dissipation formulated through the rest configuration update. Here, $\mathbf{x}(t) \in \mathcal{R}^n$ is a vector containing n generalized coordinates that spatially discretize the kinematic state of the shell in different configurations, $\bar{\mathbf{x}}(t)$ refers to the undeformed configuration, $\boldsymbol{\kappa}(t)$ is a vector grouping all material stiffness parameters, and t is the time instant.

Temporal effects are modeled through the explicit dependencies of the undeformed configuration and material stiffness on time. In the next section, we describe how these dependencies are estimated from empirical data. Because our structures morph at low strain rates, we neglect all dynamic effects and take discrete time increments of constant duration, $\delta = 0.5$ s. After each time increment, the undeformed configuration and stiffness parameters are updated quasistatically. We denote the magnitudes corresponding to the k-th time step of the morphing process as $\mathbf{x}^k$, $\bar{\mathbf{x}}^k$, $\boldsymbol{\kappa}^k$. For notation simplicity, we will drop the superscript corresponding to the morphing time step unless specified. Simulating the static behavior of this mechanical system at the k-th morphing time step implies solving the nonlinear system of differential equations defined by net force equilibrium, i.e., $\mathbf{F}(\mathbf{x}^k, \bar{\mathbf{x}}^k, \boldsymbol{\kappa}^k) = -\nabla_{\mathbf{x}} W = \mathbf{0}$, using standard numerical optimization methods.

Our computational model couples a FEM simulation of the membrane, a rigid body model for bases, and a data-driven spring model for the brackets. In the following sections, we describe the kinematics and mechanics of each of these subsystems

[1] http://www.openscad.org

separately, and then specify how we model the coupling between them and solve the numerical problem.

Discrete kinematics

The bases are modeled using N_r prismatic rigid bodies. Each rigid body represents two bases attached to the membrane from the opposite sides. The kinematic state of the i-th rigid body can be determined by the position of the center-of-mass $\mathbf{v}_i \in \mathcal{R}^3$, together with its rotation $\mathbf{r}_i \in \mathcal{R}^3$, expressed in angle-axis format. The corresponding rotation matrix $\mathbf{R}_i$ can be easily computed using the well-known Rodrigues formula

$$\mathbf{R}(\mathbf{r}) = \mathbf{I} + \sin(\theta)[\mathbf{u}]_\times + (1 - \cos(\theta))[\mathbf{u}]_\times^2, \tag{D.1}$$

where $\theta = ||\mathbf{r}||$, $\mathbf{u} = \mathbf{r}/||\mathbf{r}||$ and $[\mathbf{u}]_\times$ is the cross product matrix of $\mathbf{u}$, i.e., the matrix such that $[\mathbf{u}]_\times \mathbf{x} = \mathbf{u} \times \mathbf{x}$. This allows us to express the position of any point $\mathbf{p}_j$ in the local coordinates of the i-th rigid body through the non-linear relation $\mathbf{p}_j = \mathbf{R}_i(\mathbf{r}_i)\mathbf{p}_{ji}^0 + \mathbf{v}_i^k$, where $\mathbf{p}_{ji}^0 = \mathbf{p}_j^0 - \mathbf{v}_i^0$, are the coordinates of the point in the local frame of the rigid body.

Each pair of neighboring bases are joined by two brackets. The N_s brackets are modeled using two types of components: data-driven springs and shear-resisting elements. Both components are composed by line segments denoted $\mathbf{s}_{ij} = (\mathbf{s}_i, \mathbf{s}_j)$, where $\mathbf{s}_i$ and $\mathbf{s}_j$ are a pair of points on the surface of the i-th and j-th bases.

- Data-driven springs (Fig. D.3, left), $\mathbf{c}_{ij}^q$, for $q = 1, \ldots, 4$, are responsible for modeling the time-evolving resistance to deformation as well as bumper collisions.
- Shear-resisting elements (Fig. D.3, center), represented by crossing pairs of segments $\mathbf{s}_{ij}^q = \{\mathbf{s}_{ij}^{qa}, \mathbf{s}_{ij}^{qb}\}$, for $q = 1, \ldots, 4$, are responsible for penalizing undesired in-plane and out-of-plane shearing during the simulation. Resistance to shearing is inherent to the fabricated brackets due to their V-shaped design.

Finally, we represent the elastic membrane as a piecewise linear mesh of triangles (Fig. D.3, right), with N_m vertices. The set of membrane vertices $\mathcal{M} = \{\mathbf{m}_1, \ldots, \mathbf{m}_{N_m}\}$ can be partitioned into two subsets: free vertices, $\mathcal{M}_\mathrm{f} = \{\mathbf{f}_1, \ldots, \mathbf{f}_{N_\mathrm{f}}\}$, and vertices coupled to the bases, $\mathcal{M}_\mathrm{g} = \{\mathbf{g}_1, \ldots, \mathbf{g}_{N_\mathrm{g}}\}$.

All points lying on the surface of a base are coupled to it implicitly. The positions of these points can be expressed in terms of the center-of-mass and rotation of the rigid

bodies following the non-linear expression (D.1). Therefore, the geometric configuration of the shell can be completely determined by the positions and orientations of the rigid bodies together with the membrane vertices that are not coupled to the rigid bodies. This leads to a total of $N_\mathrm{t} = 6N_\mathrm{r} + 3N_\mathrm{f}$ degrees of freedom which we group in the state vector $\mathbf{x} = \{\mathbf{v}_1, \mathbf{r}_1, \ldots, \mathbf{v}_{N_\mathrm{r}}, \mathbf{r}_{N_\mathrm{r}}, \mathbf{f}_1, \ldots, \mathbf{f}_{N_\mathrm{f}}\}$.

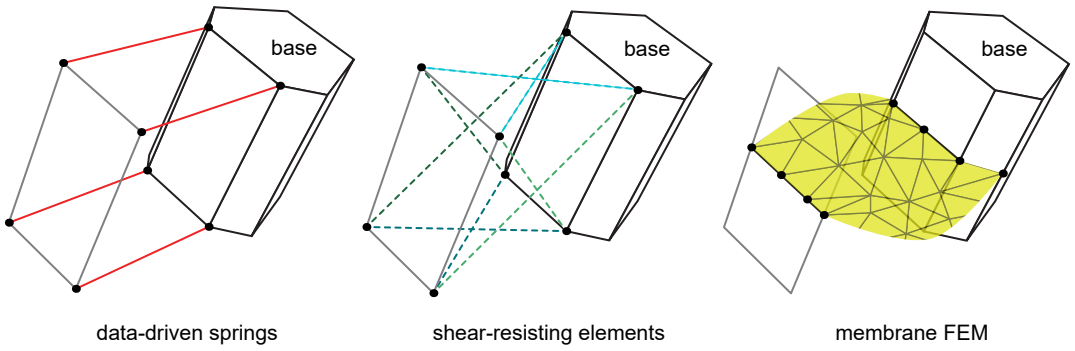

Figure D.3: Discretization elements: *data-driven springs*, representing brackets' time-evolving stiffness and bumper collisions (left); *shear-resisting elements*, representing brackets' resistance to undesired shearing (center); and membrane FEM (right).

Discrete energies

Given this discretization, the mechanical behavior of the shell can be described by a conservative elastic potential W aggregating the contributions of the data-driven springs W_c, shear-resisting energy W_s, and the membrane W_m:

$$W(\mathbf{x}) = \sum_{U_{ij}} \left(\sum_{q=1}^{4} W_\mathrm{c}(\mathbf{c}_{ij}^q) + \sum_{q=1}^{4} W_\mathrm{s}(\mathbf{s}_{ij}^{qa}, \mathbf{s}_{ij}^{qb}) \right) + \sum_{\mathcal{T}_i} W_\mathrm{m}\big(\mathbf{G}_i(\mathbf{m}_{\mathcal{T}_i})\big) \,. \tag{D.2}$$

Here, U_{ij} refers to the unit cell joining the i-th and the j-th bases, $\mathcal{T}_i$ refers to the i-th element of the membrane discretization, and $\mathbf{G}_i$ is the deformation gradient of the membrane evaluated at this element. Let us separately explain each of the energy terms:

- The data-driven spring energy W_c, has the following expression:

$$W_\mathrm{c}(\mathbf{c}_{ij}^q) = \begin{cases} W_\mathrm{d}\Big(b, h, t, \bar{L} - L(\mathbf{c}_{ij}^q)\Big) & \text{if} \quad L(\mathbf{c}_{ij}^q) > L_\mathrm{c}, \\ \frac{\kappa_c}{2}\Big(L(\mathbf{c}_{ij}^q) - L_\mathrm{c}\Big)^2 & \text{if} \quad L(\mathbf{c}_{ij}^q) \leq L_\mathrm{c}, \end{cases} \tag{D.3}$$

  where L_c is the collision distance for the spring determined by the bumpers geometry. Initially, the elastoplastic behavior of the spring follows a data-driven model $W_\mathrm{d}(b, h, t, x)$ for a given bracket length, b, bracket thickness,

h, and time spent under water, t (see next section). It depends on spring deformation, $x = \bar{L} - L(\mathbf{s}_{ij}^q)$, where $\bar{L}$ is the rest length of the spring. To account for plastic effects, the rest length of the spring is updated after each time increment following the scheme $\bar{L}^{k+1} = \min\left(\bar{L}^k, \bar{L}^0 - \eta(\bar{L}^0 - L^k)\right)$ with constant plasticity fraction η. Once the current length of the spring is smaller than the collision distance, the actuation is stopped and the collision distance is enforced using a soft constraint defined through a high stiffness constant, κ_c.

- The shear-resisting energy W_s, has the following expression:

$$W_\mathrm{s}\left(\mathbf{s}_{ij}^{qa}, \mathbf{s}_{ij}^{qb}\right) = \frac{\kappa_s}{2}\left(L(\mathbf{s}_{ij}^{qa}) - L(\mathbf{s}_{ij}^{qb}) - R^0\right)^2, \tag{D.4}$$

  where $L(\mathbf{s}_{ij}) = \|\mathbf{s}_i - \mathbf{s}_j\|$, is the distance between the spring segment end points, R^0 is the difference between distances in the initial morphing time step, and κ_s is a constant.

- For the membrane energy W_m, we use a classical FEM formulation with an incompressible Neo-Hookean material [4]. Continuum magnitudes are interpolated from nodal values using linear basis functions which allows us to discretely approximate the deformation gradient $\mathbf{G} = \nabla_{\bar{\mathbf{m}}}\mathbf{m}$. Here, the undeformed configuration can be computed from the membrane state at the initial configuration $\bar{\mathbf{m}} = \tau^{-1}\mathbf{m}^0$, where τ is the pre-stretch factor.

Coupling and solver

At each time step of the morphing process, we formulate and solve the nonlinear system of differential equations defined by the net force equilibrium $-\nabla_\mathbf{x} W = \mathbf{0}$, by minimizing the discrete elastic potential (D.2). We solve this problem using Newton-Raphson method with Strong Wolfe convergence conditions for step length selection.

Solving this problem efficiently requires analytically computing both the first $\nabla_\mathbf{x} W$ and second $\nabla^2_{\mathbf{xx}} W$ derivatives of the elastic potential. As introduced above, points lying on the surface of the bases, $\mathbf{p}$, are implicitly coupled to the rigid bodies through (D.1). Hence, these derivatives can be easily computed using the chain-rule:

$$\frac{\partial W}{\partial \mathbf{x}} = \frac{\partial W}{\partial \mathbf{f}}\frac{\partial \mathbf{f}}{\partial \mathbf{x}} + \frac{\partial W}{\partial \mathbf{p}}\frac{\partial \mathbf{p}}{\partial \mathbf{x}}, \qquad \frac{\partial^2 W}{\partial \mathbf{x}^2} = \frac{\partial \mathbf{f}}{\partial \mathbf{x}}^T \frac{\partial^2 W}{\partial \mathbf{f}^2}\frac{\partial \mathbf{f}}{\partial \mathbf{x}} + \frac{\partial \mathbf{p}}{\partial \mathbf{x}}^T \frac{\partial^2 W}{\partial \mathbf{p}^2}\frac{\partial \mathbf{p}}{\partial \mathbf{x}}\frac{\partial W}{\partial \mathbf{p}^2}\frac{\partial^2 \mathbf{p}}{\partial \mathbf{x}^2}, \tag{D.5}$$

where $\nabla_{\mathbf{x}}\mathbf{f}$ is a selection matrix of the free membrane vertices and $\nabla_{\mathbf{x}}\mathbf{p}$ and $\nabla^2_{\mathbf{xx}}\mathbf{p}$ can be computed from (D.1). One common technique in rigid-body simulation to simplify this computation is to keep rotational degrees of freedom $\mathbf{r}_i$ close to zero. This is done by updating the local coordinates of the coupled points in the base frame after each successful iteration, i.e., for the j-th point attached to the i-th rigid body, $\mathbf{p}^0_{ji} \leftarrow \mathbf{R}(\mathbf{r}_i)\mathbf{p}^0_{ji}$, $\mathbf{r}_i \leftarrow \mathbf{0}$.

We provide the following data as an example of the simulation scales. Our most complex model with self-interweaving shape (Fig. 5.3d) contains 549 rigid bodies and 7942 membrane elements. The full morphing process simulation (240 time increments) takes 43 minutes in total.

D.3 Material measurement and modeling

As discussed in Section D.2, we represent brackets in simulations by data-driven springs and shear-resisting elements. Here we describe our approach to the mechanical modeling of the data-driven components. The brackets in our structure undergo large deformations and are made of a material with nonlinear elastic properties and time-dependent softening. This combination of material and geometric nonlinearities leads us to a data-driven effective spring model. We performed all measurements in settings that resemble conditions brackets are subjected to in an assembled structure. We first formulate the data-driven elastoplastic spring model $W_{\mathrm{d}}(b, h, t, x)$ (introduced in the previous section) and then describe our fitting strategy. We discuss several polynomial fittings in this section and display their output units in square brackets.

Physical model of brackets

Our elastoplastic bracket model is motivated by a set of material tests described below. The elastic component is expressed through an effective stiffness, and the plastic behavior is described as a dissipation of internal elastic energy due to deformation. We make the approximation of assuming a constant plasticity fraction, η, which we obtained experimentally. The plastic part of the displacement is then given by $x_{\mathrm{pl}} = \eta x$ and the elastic part is $x_{\mathrm{el}} = (1 - \eta)x$.

We aim to obtain elastic energy formulations $W_{\mathrm{d}}(b, h, t, x_{\mathrm{el}})$ that are functions of time t spent in hot water for each valid combination of bracket length b and thickness h. These formulations are modelled as trilinear interpolations between polynomials $p_{b,h,t}(x_{\mathrm{el}})$ that are defined on a regular grid.

Under the assumption of a constant plasticity fraction and with material properties corresponding to time t, we relate elastic energy $W_{\mathrm{d}}(b, h, t, x_{\mathrm{el}})$ to the total external work $\bar{W}$ done through monotonic bracket displacements x in the following manner:

$$W_{\mathrm{d}}(b, h, t, x_{\mathrm{el}}) = (1 - \eta)\bar{W}\Big(b, h, t, \frac{x_{\mathrm{el}}}{1 - \eta}\Big). \tag{D.6}$$

Here, $\bar{W}$ are trilinear interpolations of polynomials $p^{\mathrm{work}}_{b,h,t}(x)$ $[\mathsf{N} - \mathsf{m}]$ that are similarly related to $p_{b,h,t}(x_{\mathrm{el}})$:

$$p_{b,h,t}(x_{\mathrm{el}}) = (1 - \eta)p^{\mathrm{work}}_{b,h,t}\Big(\frac{x_{\mathrm{el}}}{1 - \eta}\Big). \tag{D.7}$$

These polynomials are obtained by integrating force over displacement:

$$p^{\mathrm{work}}_{b,h,t}(x) = \int_0^x p^{\mathrm{load}}_{b,h,t}(\tilde{x})d\tilde{x}\,, \tag{D.8}$$

where $p^{\mathrm{load}}_{b,h,t}(x)$ $[\mathsf{N}]$ are polynomials representing the loads exerted on bracket over applied displacements. The polynomials $p^{\mathrm{load}}_{b,h,t}(x)$ are fourth-order in x with no free term. The fitting methods for obtaining these polynomials are discussed in the following subsection.

It is challenging to measure time-dependent force-displacement relationships directly in an experimental setup since specimen submersion and loading takes a significant amount of time relative to our actuation time ranges. Specimen submersion and loading takes 8 seconds while the target deformations last approximately 30 to 80 seconds. This restrains us from an assumption that material properties are "fixed" at time t for the material measurements. Additionally, we collected a higher density of data in time rather than in displacement due to the capabilities of our experimental setup. This leads us to dividing the fitting problem into simpler components. We first fit (inverted) displacement-force relationships and then use the obtained model to reconstruct the desired force-displacement model $p^{\mathrm{load}}_{b,h,t}(x)$. Our displacement-force model is the following:

$$x(b, h, t, F) = p^{\mathrm{dry}}(b, h, F) + \int_0^t F \exp\big(p^{\mathrm{wet}}(b, h, \tilde{t}, F)\big)d\tilde{t}, \tag{D.9}$$

where p^{dry} $[\mathsf{m}]$ is a third-order polynomial (limited to first order in b and h) for which all terms have F as a multiplier and p^{wet} $[\log\big(\mathsf{m}/(\mathsf{N} - \mathsf{s})\big)]$ is a fourth-order polynomial. Polynomial p^{dry} represents displacement-force relationships before putting into water while p^{wet} is the logarithmic evolution of deformation rates, divided by load, in water. The latter formulation restricts the deformation speed

to be always positive which is a desirable property for our model and assures zero displacement under zero load. The integral does not generally have a simple explicit representation.

We apply the transformation mentioned above to the measured deformation speeds and fit the resulting data

$$p^{\text{wet}}(b, h, t, F) = \log\left(F^{-1}\frac{\partial x}{\partial t}\right). \tag{D.10}$$

The logarithmic function improves the quality of fitting by reducing extreme variation in deformation rates. Note that the formulation of displacement-force relationships is defined as a single continuous function across all parameters in our setup. This allows us to build a consistent model of data collected from all experimental measurements.

Data collection and fitting

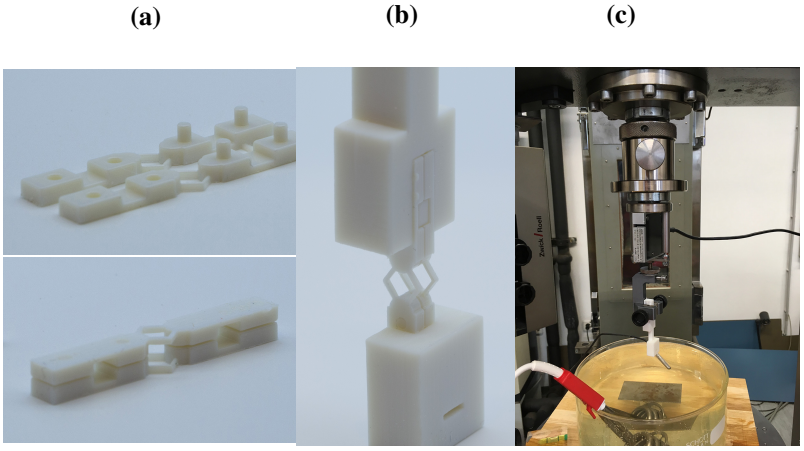

Figure D.4: Experimental setup for characterizing unit cell behaviors. (a) Specimens used for material measurements are assembled from two printed parts to mimic a unit cell. Assembled specimens have holes to ensure consistent boundary conditions in a gripper that was fabricated in-house. (b) Custom-built gripper for quick specimen exchange and a "boot" for firm specimen compression against the floor. (c) Zwick tensile tester for measuring bracket deformations in hot water.

A Zwick tensile tester (shown in Fig. D.4c) was used for all bracket characterization experiments. The specimens tested (shown in Fig. D.4a) were attached to a pair of prismatic grippers (Fig. D.4b) to enforce uniaxial movement.

Three types of experiments were conducted: compression tests in both dry and wet states, as well as effective plasticity measurements. For the dry compression tests, displacement-force relations for brackets that had not been immersed in water were

obtained quasi-statically. For the wet compression tests, we immersed specimens into hot water and immediately applied constant loads. These specimens deformed gradually over time since exposure to hot water causes them to soften. For the effective plasticity tests, we compressed brackets by a prescribed displacement, unloaded them, and measured the restoration to derive the plastic component of the deformation. For all tests we used the same sampling of central lengths l (from Figure 5.1b, it is easy to see that $l = b + 4\cos 37°$) and bracket thicknesses h (in millimeters): $l \in \{5, 6, 7, 8, 9\}$, for $l \leq 7$, we choose $h \in \{0.3, 0.4, 0.5, 0.6\}$ and for $j > 7$, we choose $h \in \{0.35, 0.45, 0.55, 0.65\}$. This set of parameters amounts to 20 total combinations.

Fitting polynomials with constrained derivatives

Empirical knowledge (such as the fact that thicker brackets deform at slower rates) was used to derive constraints on fitted functions. Similar to standard polynomial regression, we solve a quadratic programming problem $y = X\beta + \epsilon$, but instead of $\beta = (X^T X)^{-1} X^T y$, we solve:

$$\begin{aligned} &\texttt{minimize} && \tfrac{1}{2}\beta^T X^T X\beta - y^T X\beta \\ &\texttt{subject to} && A\beta \leq 0\,, \end{aligned} \tag{D.11}$$

where A expresses row-wise derivative constraints per point. By providing sufficiently many points in A we significantly improve fitted curve quality. We impose these constraints at all given data points. All the constraints used for each polynomial fitting are listed below.

Compressive loading of dry specimens

This experiment is conducted once for each specimen by increasing the applied load quasi-statically from 0 to 10 N. We fit to this data a polynomial p^{dry} expressing resulting displacements x given the loading F. Note that displacement is a monotonic function of bracket length b, unlike strain. We impose the following derivative constraints:

$$\frac{\partial p^{\text{dry}}}{\partial b} > 0, \quad \frac{\partial p^{\text{dry}}}{\partial h} < 0, \quad \frac{\partial p^{\text{dry}}}{\partial F} > 0. \tag{D.12}$$

The resulting curves are in Fig. D.5.

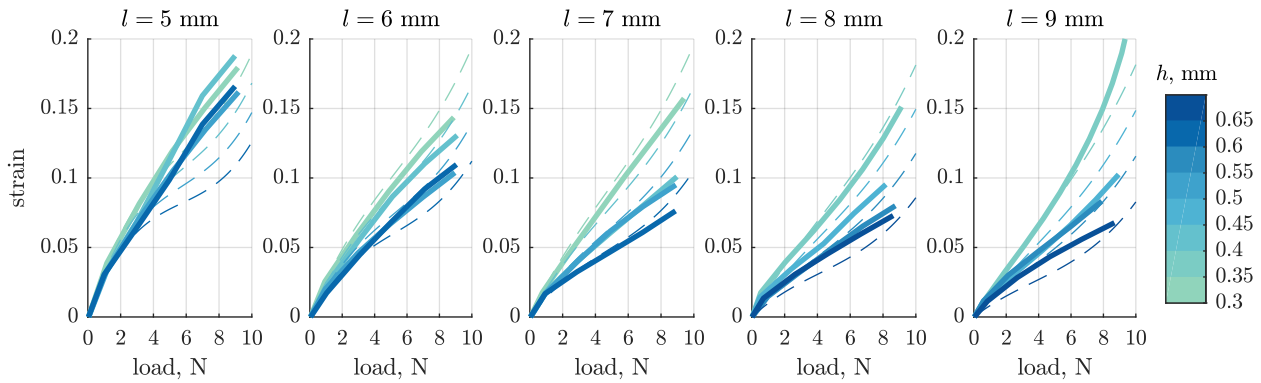

Figure D.5: Compressive loading of dry specimens. Data (solid lines) and fitted curves (dashed lines).

Compressive loading of specimens in water

The next step is to model the evolution of the displacement-force curves over time spent in water. In order to do so, we test the behavior of each specimen under various loads (which are held constant throughout an individual test).

Since the initial force-displacement relationships p^{dry} are known with relatively high precision, we use those curves as our model for $t = 0$. We fit the displacement rate data to reconstruct the time-evolution of bracket behavior in water. We impose the following constraints on the derivatives:

$$\frac{\partial p^{\text{wet}}}{\partial b} > 0, \quad \frac{\partial p^{\text{wet}}}{\partial h} < 0, \quad \frac{\partial p^{\text{wet}}}{\partial t} > 0, \quad \text{and} \quad \frac{\partial p^{\text{wet}}}{\partial F} > 0. \tag{D.13}$$

Then we reconstruct time-evolving displacement-force relationships (D.9). The resulting curves are shown in Fig. D.6. We filter out displacements larger than $2/3$ of the initial length since brackets may be damaged and display inconsistent behavior at that point.

After obtaining a displacement-force relationship, we invert it with respect to displacement. We densely resample our target parameter space of b, h, t and refit force-displacement curves represented by polynomials $p^{\text{load}}_{b,h,t}(x)$ with constrained derivatives:

$$\frac{\partial p^{\text{load}}_{b,h,t}(x)}{\partial x} > 0 \quad \text{and} \quad \frac{\partial^2 p^{\text{load}}_{b,h,t}(x)}{\partial x^2} < 0. \tag{D.14}$$

Effective plasticity tests

In order to properly simulate actuation of the structure, we examine elastic energy dissipation during bracket compression. We approximate this phenomenon through

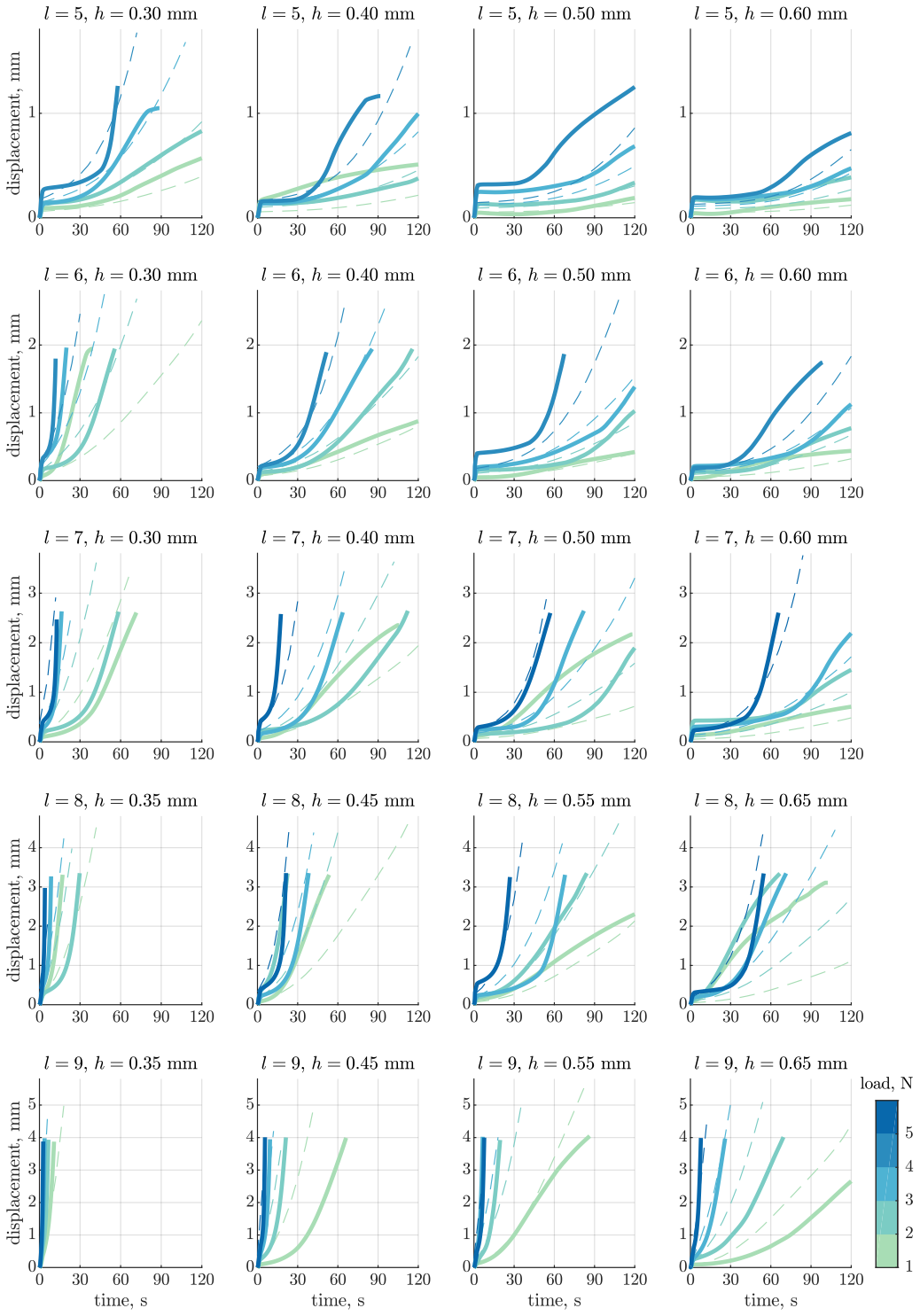

Figure D.6: Compressive loading of specimens in water. Data (solid lines) and fitted curves (dashed lines).

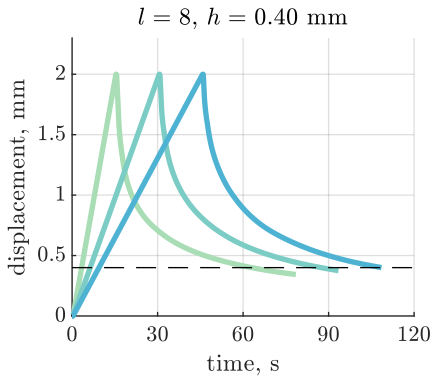

Figure D.7: Plasticity does not depend on deformation rates. Three different deformation rates are shown for a unit cell specimen of length $l = 8$ mm and thickness $h = 0.4$ mm. Dashed line represents 20% of maximal deformation which we use as a constant plasticity fraction in our simulations.

an elasto-plastic model. We do not study the dependence of plasticity on temperature because all experiments occur at 56 ^oC. Thus, we analyze the dependence of plasticity on deformation rates. This experiment is done for specimens with fixed chosen parameters $l = 8$ mm and $h = 0.45$ mm. We do multiple loading tests with different deformation rates and measure the restored strain after unloading. We observed that there is no significant dependence on deformation rates (see Fig. D.7). We did not observe consistent strain restoration across different bracket thicknesses and lengths, with mean plastic fractions in a range 15%–25%. We use a constant mean plasticity fraction $\eta = 20\%$ in our simulations.

D.4 Temporal programming

In our design pipeline, the user specifies a time landscape. This is a smooth scalar field over the target surface that represents the desired deformation completion time at each point. In our implementation, we define it as a piecewise linear function on top of the flat stencil triangulation. For each unit cell, we compute the average desired actuation time, t^*, using values specified at the ends of the associated stencil edge. Then we use t^* to configure the thicknesses of the brackets associated with the unit cell. This computation is based on the effective force-displacement curves modelled by trilinear interpolation of polynomials $p^{\text{load}}_{b,h,t}(x)$, which we denote as $F(b, h, t, x)$. Each unit cell's deformation is consistent with its neighbors' so long as the time landscape is sufficiently smooth.

Both pairs of brackets on the opposite sides of the unit cell have the same initial length b_0 by construction. We first compute their length in the fully actuated state

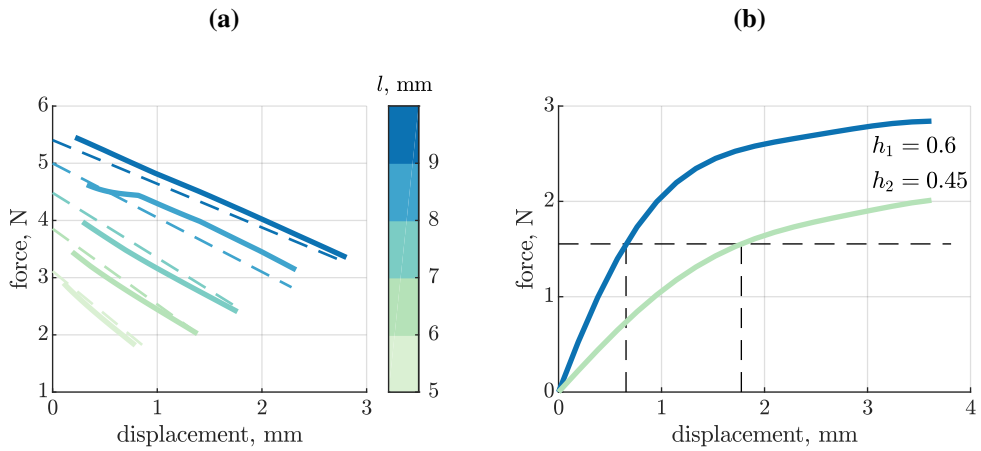

Figure D.8: Predicting applied tractions and selecting bracket thicknesses. (a) Linearized model of the membrane (dashed lines) in comparison to FEM membrane (solid lines) for a set of unit cells of various initial lengths. The membrane tractions decrease with displacement as the pre-stretch is relaxed. (b) Configuring thicknesses for two pairs of brackets on opposite sides of a unit cell. Note that the one requiring larger target displacement is thinner to finish deformation at the same time as the one with smaller target deformation. The dashed horizontal line shows a sample approximation to the target membrane traction.

b_1 (in general, different for different sides). Then, for the target actuation time t^*, we can formulate the bracket thickness h configuration problem as follows:

$$F(b_0, h, t^*, b_0 - b_1) = F^{\text{mem}}(b_0, d_1), \tag{D.15}$$

where F^{mem} is an approximation of the traction generated by the membrane dependent on the initial unit cell length, b_0, and on a parameter describing membrane deformation, d_1 with its value at the actuated state. Here we use the force balance between the brackets and the membrane at the target deformation after time t^* spent in water, ignoring plasticity (Fig. D.8b).

We build a linearized model of the membrane, representing it as a segment spring connecting the centroids of the end points of all brackets in a unit cell, and setting $F^{\text{mem}}(b, d)$ as a first-order polynomial in each of the variables. Here b mimics an initial membrane spring length and d is its displacement. We fit this model by sampling initial bracket lengths and deformations. It captures membrane forces well in our setting (Fig. D.8a).

Our approach to finding the thickness h is a binary search through our interpolated model of $F(b_0, h, t^*, b_0 - b_1)$ to match a known value of $F^{\text{mem}}(b, d)$.

We need a specific treatment of boundary unit cells since the membrane ends there and has less stretch initially. To account for this, we reduce the force evaluation by a

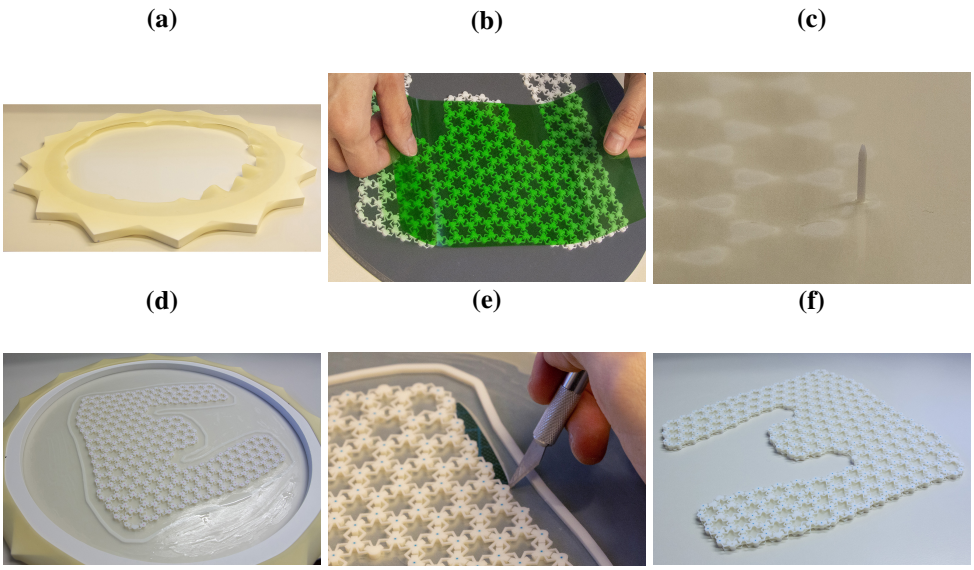

Figure D.9: Fabrication process landmarks. (a) Star-shaped membrane stretching device back side up. Bottom part of the membrane is uniformly stretched due to markers. (b) Transferring glue from a plastic foil to the bases of the shell. (c) Passing a pin through one of the bases and the membrane to align with the second lattice. (d) Membrane surplus is covered by glue in order to "freeze" it and enable its easy removal. (e) Cutting out the shell from the membrane surplus by a scalpel. (f) Flat-fabricated shell ready for actuation in water.

factor of 0.6 which was empirically found by comparing simulations of our examples with the membrane represented by linear springs to FEM membrane simulations.

Once the desired time landscape is specified and bracket thicknesses are computed accordingly, we start the simulation process described in Appendix D.2. Unit cells' actuation completion might deviate from the specified time landscape due to imperfections in the linearized membrane force estimation and plastic effects. Apart from that, the resulting morphing process might not reach the final goal, for example there might be collisions on the way. In these cases time landscape has to be edited and the simulation of morphing has to be recomputed until the goal is achieved.

D.5 Fabrication procedure

We developed a custom fabrication procedure for the shells. It is described in detail in this section.

1. 3D print the outer layers of the shells using a Stratasys J750 printer. We also printed an outer frame to reduce undesired deformation of the structure during fabrication. Printing time for all of our shells is approximately 2 hours

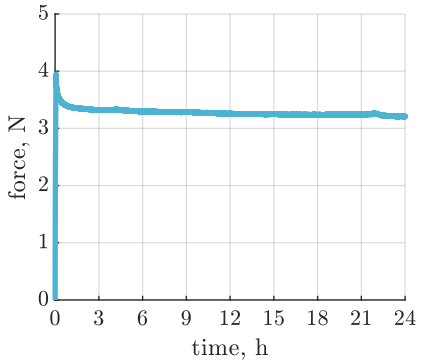

Figure D.10: Membrane stress relaxation over the course of 24 hours. Evolution of the force generated by a dog-bone membrane specimen under a constant stretch factor of 3.

(it mostly depends on the number of layers, which is fixed). It is twice as long for the first petalled shape (Fig. 5.1c) since both sides do not fit on a single printing tray. We remove all overhangs, which does not affect shape replication but makes the cleaning process drastically easier: we only quickly remove almost all support material by several shaving movements with a sharp scraper and airflow the lattice to erase the rest.

2. Use a star-shaped device to manually stretch a latex sheet uniformly by gradually wrapping it around and fixing at the device's teeth (Fig. D.9a). Friction between the membrane and the device is sufficient to keep the membrane stretched without any additional clamps. A stretch factor of 3 (900% the area) is enforced by matching markers on the sheet to the tips of the device's teeth. Note that large deformations of the membrane lead to slight stress relaxation in the long run. Given the variability of the rest of the system and our simplified membrane model, we neglect this effect. It is however possible to take it into account since after approximately 1.5 hours stress relaxation does not progress much further (Fig. D.10).

3. Clean both surfaces of the sheet with 2-Propanol for better gluing. Apply super glue on a plastic film and distribute it uniformly with a brush. Transfer glue from the film to the 3D printed structures through contact with the plastic film (Fig. D.9b).

4. Glue one lattice to the membrane and pass push pins through the alignment holes on the lattice and through the latex membrane (Fig. D.9c). The membrane does not rip since we pinch it through an isolated area.

5. Glue the opposite side to the latex sheet matching the holes with corresponding alignment pins.

6. Distribute additional super glue on the latex membrane in the region surrounding the lattice perimeter (Fig. D.9d).

7. Wait 5 minutes and then release the latex sheet to a stretch factor near 2. Then using a scalpel cut out the structure, keeping a tiny amount of degenerated latex at the border to prevent membrane ripping (Fig. D.9e).

8. Submerge the structure in 56° C water and wait for morphing to complete.

9. Take out the deformed shape and let it dry. Under normal conditions, the drying process may take roughly 15 minutes.

The whole fabrication process after 3D printing and before drying takes 30–50 minutes.

D.6 Mechanical measurements of shells

We performed a set of mechanical measurements of the shells for estimation of their load-bearing capabilities. We fabricated flat regularly tessellated shells composed of identical unit cells of length 7 mm, bracket thickness 0.5 mm, and bumpers 0.3 mm with total dimensions 60×55 mm. Since the shell structure is not isotropic, we performed the tests aligning the deformation to one of the three axes parallel to the edges of the hexagonal pattern. The resulting plots are shown in Fig. D.11. In all tests the deformation speed was approximately 1 mm/min. It is intuitive that the shells have higher resistance to pure in-plane compression due to the bumper contacts in contrast to the other cases when only the membrane and the brackets are loaded.

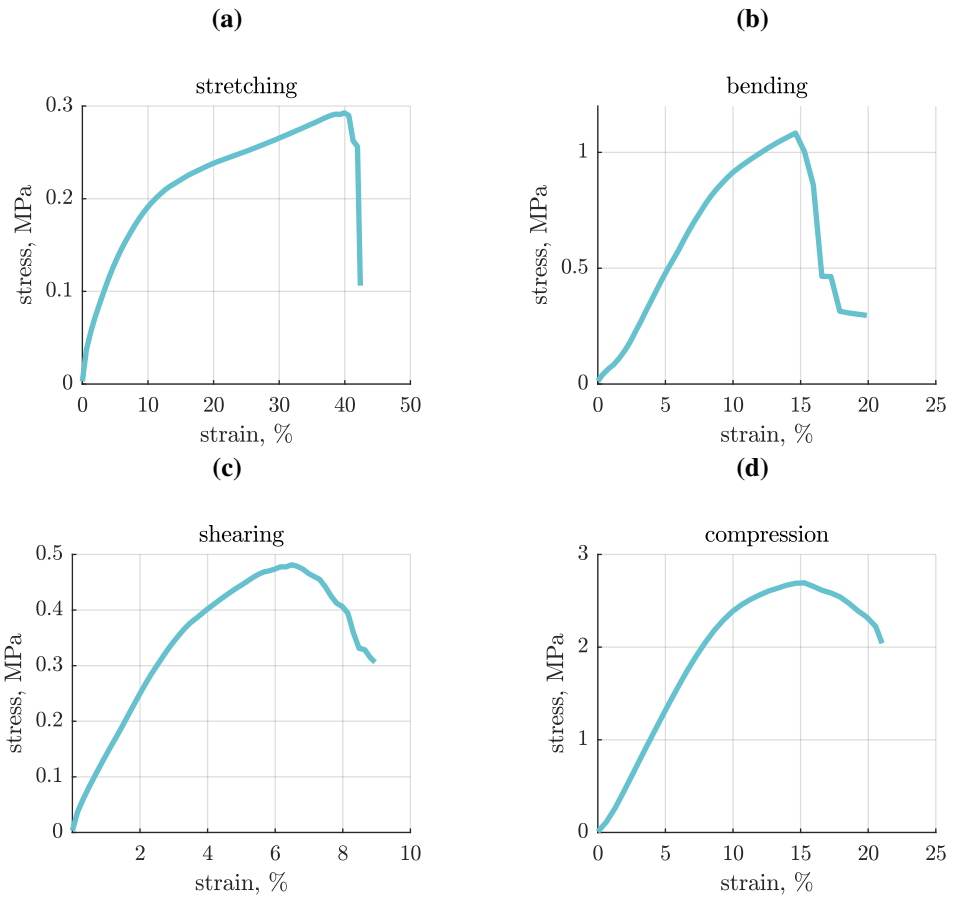

Figure D.11: Mechanical tests of a flat regularly tessellated shell. Since our shells have cross-sections with a complex geometry, we provide the effective stress values (assuming shell homogeneity). (a) Stretching, (b) bending, (c) shearing, and (d) compression tests.

D.7 Supplementary movies

Supplementary Movies 1-5 can be found at the following URL:

`https://www.nature.com/articles/s41467-019-14015-2#Sec10`

References

[1] Y. Liu, W. Wang, B. Lévy, F. Sun, D.-M. Yan, L. Lu, and C. Yang. On centroidal voronoi tessellation–Energy smoothness and fast computation. *ACM Transactions on Graphics*, 28(4):Article 101, August 2009. doi: 10.1145/1559755.1559758. URL `https://hal.inria.fr/inria-00547936`.

[2] B. Springborn, P. Schröder, and U. Pinkall. Conformal equivalence of triangle meshes. *ACM Transactions on Graphics*, 27(3):77:1–77:11, August 2008. ISSN 0730-0301. doi: 10.1145/1360612.1360676. URL `http://doi.acm.org/10.1145/1360612.1360676`.

[3] R. Guseinov, E. Miguel, and B. Bickel. Curveups: Shaping objects from flat plates with tension-actuated curvature. *ACM Transactions on Graphics*, 36(4): 64, 2017. doi: 10.1145/3072959.3073709.

[4] R. D. Ogden. *Non-linear elastic deformations*. Dover Publications, 1997.

Appendix E

UNTETHERED SOFT ROBOTS WITH PASSIVE CONTROL OF SHAPE MORPHING AND PROPULSION

E.1 Mechanics of thin nematic elastomer bilayers

In this section, we discuss the mechanics of nematic elastomer bilayers. In particular, we show that the model developed by Agostiniani and DeSimone [1] for *thin* nematic elastomer bilayers yields an inverse proportionality between curvature, κ, and thickness, h, as what is observed in our experiments. This relation is observed in our specimens (particularly for LT_{NI} hinges), even though the majority of our specimens are thick plates. For a more relevant comparison between our experimental results and the calculation of κ discussed below, we highlight the direct proportionality between curvature and hinge angle, θ, in specimens with near-homogeneous curvature (such as ours). Namely, $\theta \approx \kappa w$, where w is hinge width.

Their model is derived based on the condition that there is an isometry constraint on the midplane of thin bilayers due to kinematic frustration (i.e. there is no stretching, and only deformed configurations with zero Gaussian curvature can be achieved). This constraint is an approximation that can be rationalized by contrasting the scaling of stretching and bending energies with regards to plate thickness, h. While the former is linear with h, the latter scales with h^3. This means that bending deformations are heavily favored as structures become increasingly slender, hence the inclusion of the midplane isometry constraint.

Some of the LCEs we fabricate are thin and behave in accordance with this regime, but most of our samples are thick because they yield higher torque outputs. In this case, anticlastic bending is observed at the free edges of the hinges, meaning that midplane isometry is not preserved. Because we have limited data on thin LCE actuators, we do not directly compare our results to fittings of parameters used in their model. However, we note that the decreasing curvature with increasing thickness observed in our experiments is characteristic to other bilayer growth systems [2, 3] and is consistent with the behavior predicted by their model for thin nematic elastomers. We offer an intuition for the mechanics that govern our hinges by summarizing a calculation based on their model, which illustrates that sheet thickness is the characteristic length scale that determines curvature in the

thin specimen limit. It is beyond the scope of this study to develop a theory for the curving of thick LCE bilayers.

Kinematics

Denote the coordinate frame for an initially flat midsurface as $\mathbf{X} = \{X, Y\}$. The deformed configuration is $\boldsymbol{\chi} = \{x(X,Y),\ y(X,Y),\ z(X,Y)\}$. The unit-normal to the deformed surface is

$$\mathbf{n} = \frac{\partial \boldsymbol{\chi}}{\partial X} \wedge \frac{\partial \boldsymbol{\chi}}{\partial Y} \Bigg/ \left\| \frac{\partial \boldsymbol{\chi}}{\partial X} \wedge \frac{\partial \boldsymbol{\chi}}{\partial Y} \right\| .$$

The second fundamental form of the midsurfaces is given by:

$$\mathrm{A}_y = -\nabla \boldsymbol{\chi}\ \nabla \mathbf{n} = -\frac{\partial \chi_k}{\partial X_i} \frac{\partial n_k}{\partial X_j} .$$

We re-express this form through the following identity:

$$\nabla \boldsymbol{\chi} \cdot \mathbf{n} = 0 \Rightarrow \nabla (\nabla \boldsymbol{\chi} \cdot \mathbf{n}) = 0 .$$

In Einstein summation notation, this can be written as:

$$\frac{\partial}{\partial X_j} \left(\frac{\partial \chi_k}{\partial X_i}\ n_k \right) = 0 \Rightarrow \frac{\partial^2 \chi_k}{\partial X_i \partial X_j} n_k + \frac{\partial \chi_k}{\partial X_i} \frac{\partial n_k}{\partial X_j} = 0 \Rightarrow \mathrm{A}_{ij} = \frac{\partial^2 \chi_k}{\partial X_i \partial X_j} n_k .$$

Thus, the second fundamental form can be expressed as follows:

$$\mathrm{A}_y = \begin{bmatrix} \boldsymbol{\chi}_{,XX} \cdot \mathbf{n} & \boldsymbol{\chi}_{,XY} \cdot \mathbf{n} \\ \boldsymbol{\chi}_{,XY} \cdot \mathbf{n} & \boldsymbol{\chi}_{,YY} \cdot \mathbf{n} \end{bmatrix} .$$

At a fixed point on the surface, given an orthonormal tangent vector basis, the principal curvatures are the eigenvalues of A_y.

Summary of the Agostiniani & DeSimone model

Consider a nematic elastomer sheet with a small thickness h_0 and reference configuration domain $\omega^\varepsilon \times (-h_0/2,\ h_0/2)$. The material has a shear modulus $\mu > 0$, energy per unit volume $c > 0$, and a dimensionless material parameter $\alpha_0 > 0$ which couples the magnitude of spontaneous in-plane strains in each layer to the nematic director, n. Taking $(\mathsf{n} \otimes \mathsf{n})^{\check{}}$ as the 2×2 upper left part of $\mathsf{n} \otimes \mathsf{n}$, the symmetric tensor $\check{M}$ is a function of $\alpha_0,\ h_0,\ \mathsf{n}$:

$$\check{M} \;=\; \frac{1}{2}\frac{\alpha_0}{h_0}\left[(\mathsf{n}\otimes\mathsf{n})\check{}\,-\,\frac{\mathbf{I}_2}{3}\right]\,,$$

and is related to the spontaneous linear strain in each layer $\mathbf{E}$ as follows:

$$\check{M} \;=\; -\frac{\mathbf{E}}{h_0}\,.$$

Agostiniani and DeSimone's model for LCE bilayers gives the following functional for the limiting 2D plate theory. The isometric deformation $y \in \mathrm{W}^{2,2}_{\mathrm{iso}} : (\nabla' y)^T \nabla' y = I_2$ which minimizes this functional corresponds to equilibrium.

$$\widehat{\mathscr{F}}^{\varepsilon}_{h_0}(v_{h_0}) \;\cong\; \min_{y\in \mathrm{W}^{2,2}_{\mathrm{iso}}(\omega^{\varepsilon},\mathbb{R}^3)} \frac{h_0^3}{2}\int_{\omega^{\varepsilon}} \overline{Q}_2\left(\mathrm{A}_y(x')\right)\mathrm{d}x'\,.$$

In this functional, $\overline{Q}_2$ is a doubly-relaxed energy density that is related to $\check{M}$ through the following set of functions:

- A volumetric term, W_{vol}:

$$W_{vol}(t) = c(t^2 - 1 - 2\log t) \Rightarrow W''_{vol}(t) = 2c\left(1 + \frac{1}{t^2}\right).$$

- An effective bulk modulus, γ:

$$\gamma := \frac{W''_{vol}(1)}{2\mu + W''_{vol}(1)}. \Rightarrow \gamma = \frac{4c}{2\mu + 4c}\,.$$

- The relaxed energy density, Q_2:

$$Q_2(D) = 2\mu\,\left(|\mathbf{sym}(D)|^2 + \gamma\,\mathbf{tr}^2 D\right),$$

where $|A| = \sqrt{\mathbf{tr}(AA^T)}$.

- The doubly-relaxed energy density $\overline{Q}_2$:

$$\overline{Q}_2(G) \;=\; \frac{1}{12}Q_2\left(G + \frac{3}{2}(\check{M}_1 - \check{M}_2)\right) - \frac{1}{16}Q_2(\check{M}_1 + \check{M}_2)\,.$$

Calculation for orthogonal bilayer

To compare the results of this model to a *thin* bilayer with same director as our fabricated samples, we consider a bilayer where $\mathsf{n}_1 = (1,0,0)$ in the top layer defined by $Z \in [0, h_0/2)$, and $\mathsf{n}_2 = (0,1,0)$ in the bottom layer $Z \in (-h_0/2, 0)$. Then,

$$\check{M}_1 = \frac{\alpha_0}{6h_0}\begin{bmatrix} 2 & 0 \\ 0 & -1 \end{bmatrix}, \quad \check{M}_2 = \frac{\alpha_0}{6h_0}\begin{bmatrix} -1 & 0 \\ 0 & 2 \end{bmatrix}.$$

Inserting into the strain energy, we have

$$\overline{Q}_2(\mathrm{A}_y) = \frac{\mu}{72}\left[12\left(a_{11}^2 + a_{22}^2 + \gamma(a_{11}+a_{22})^2\right) + 18\frac{\alpha_0}{h_0}(a_{11}-a_{22}) + \frac{\alpha_0^2(13-\gamma)}{h_0^2}\right],$$

where a_{ij} are the elements of A_y. We seek to minimize

$$\widehat{\mathscr{F}}^{\varepsilon}_{h_0}(v_{h_0}) \cong \min_{y \in \mathrm{W}^{2,2}_{\mathrm{iso}}(\omega^{\varepsilon},\mathbb{R}^3)} \frac{h_0^3}{2}\int_{\omega^{\varepsilon}} \overline{Q}_2\left(\mathrm{A}_y(x')\right) \mathrm{d}x' .$$

under the constraint of isometric deformations $y \in \mathrm{W}^{2,2}_{\mathrm{iso}} : (\nabla' y)^T \nabla' y = I_2$ over the entire domain. The sheet's flat initial configuration, nematic order symmetry, and the isometric deformation constraint require solutions of the form

$$\mathrm{A}_y = \begin{bmatrix} k & 0 \\ 0 & 0 \end{bmatrix} \text{ or } \mathrm{A}_y = \begin{bmatrix} 0 & 0 \\ 0 & k \end{bmatrix}.$$

The boundary conditions impose $y_{,YY} \cdot \mathbf{n} = 0$ at the edges located at $X = 0$ and $X = \epsilon$ (in the reference configuration), so we restrict ourselves to deformations which result in curvatures of the form

$$\mathrm{A}_y = \begin{bmatrix} k & 0 \\ 0 & 0 \end{bmatrix}.$$

Assuming homogeneous curvature in the deformed configuration, the minimization problem becomes:

$$\widehat{\mathscr{F}}^{\varepsilon}_{h_0}(v_{h_0}) \;\cong\; \min_{y\in \mathrm{W}^{2,2}_{\mathrm{iso}}(\omega^{\varepsilon},\mathbb{R}^3)} \frac{\mu|\omega^{\epsilon}|h_0}{144}\Big(12h_0^2(1+\gamma)k^2 + 18\alpha_0 h_0 k + (13-\gamma)\alpha_0^2\Big) \quad .$$

This has the solution

$$\widehat{\mathscr{F}}^{\varepsilon}_{h_0}(v_{h_0}) \;\cong\; \frac{\mu\alpha_0^2|\omega^{\epsilon}|h_0\big(25+4\gamma(12-\gamma)\big)}{576(1+\gamma)} \quad ,$$

with

$$k = -\frac{3\alpha_0}{4(1+\gamma)h_0} \; .$$

Since $\gamma = 4c/(2\mu+4c)$, we get:

$$k = -\frac{3\alpha_0(2c+\mu)}{(16c+4\mu)h_0} \; .$$

Remembering that α_0, c and μ are material parameters, this is consistent with the inverse proportionality between curvature and thickness that is observed in many systems with differential growth across bilayers, including our experiments. We remind the reader that hinge angle is directly proportional to curvature for homogeneously-curved specimens. As such, the Agostiniani & DeSimone model predicts the following relation between hinge angle and thickness for thin LCEs:

$$\theta \propto \frac{1}{h_0} \; .$$

Our experiments show that this prediction may extend to thicker specimens. We believe this model provides an intuition for the mechanics that govern our hinges, but remind readers that the observation of anticlastic bending in our thicker samples shows that the isometric assumption should not be maintained in a rigorous theory for thick LCE bilayers.

E.2 Supplemental figures

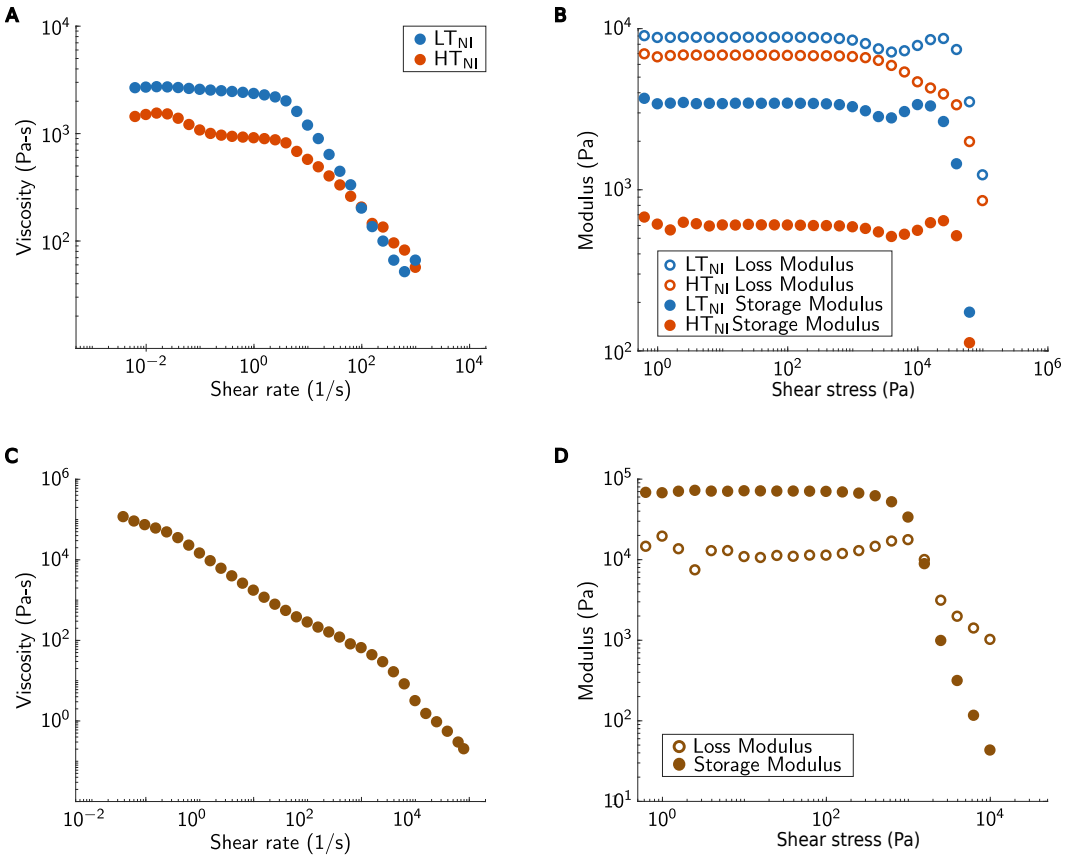

Figure E.1: LCE and structural tile ink rheology. (a) Apparent viscosity as a function of shear rate for LT_{NI} and HT_{NI} LCE inks at printing temperature 26°C and 55°C, respectively. (c) Storage (G') and loss (G'') moduli as a function of shear stress at 1 Hz for LT_{NI} and HT_{NI} LCE inks at the respective printing temperatures of 26°C and 55°C. (c) Apparent viscosity as a function of shear rate for the structural polymer ink under ambient conditions. (d) Storage (G')and loss (G'') moduli as a function of shear stress at 1 Hz for the structural polymer ink under ambient conditions.

References

[1] V. Agostiniani and A. DeSimone. Dimension reduction via γ-convergence for soft active materials. *Meccanica*, 52(14):3457–3470, 2017.

[2] S. Timoshenko. Analysis of bi-metal thermostats. *Journal of the Optical Society of America*, 11(3):233–255, 1925.

[3] P. Nardinocchi and E. Puntel. Unexpected hardening effects in bilayered gel beams. *Meccanica*, 52(14):3471–3480, 2017.

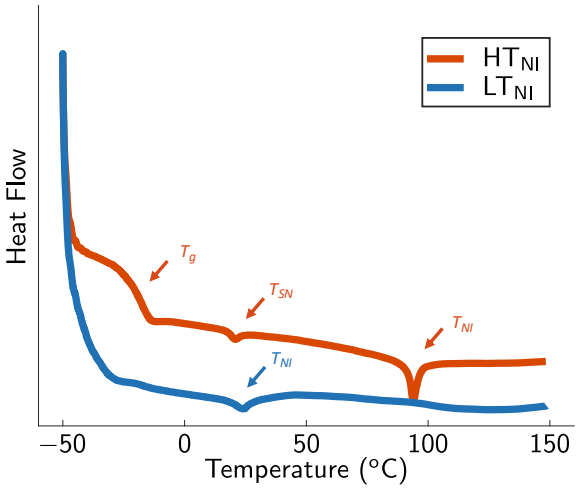

Figure E.2: Differential scanning calorimetry curves for the LCE inks. The two oligomeric LCE inks exhibit LT_{NI} and HT_{NI} values of approximately 24°C and 94°C, respectively. [Note: From this data, the T_g and smectic-to-nematic transition temperature (T_{SN}) for the HT_{NI} ink are approximately −20°C and 20°C, respectively.]

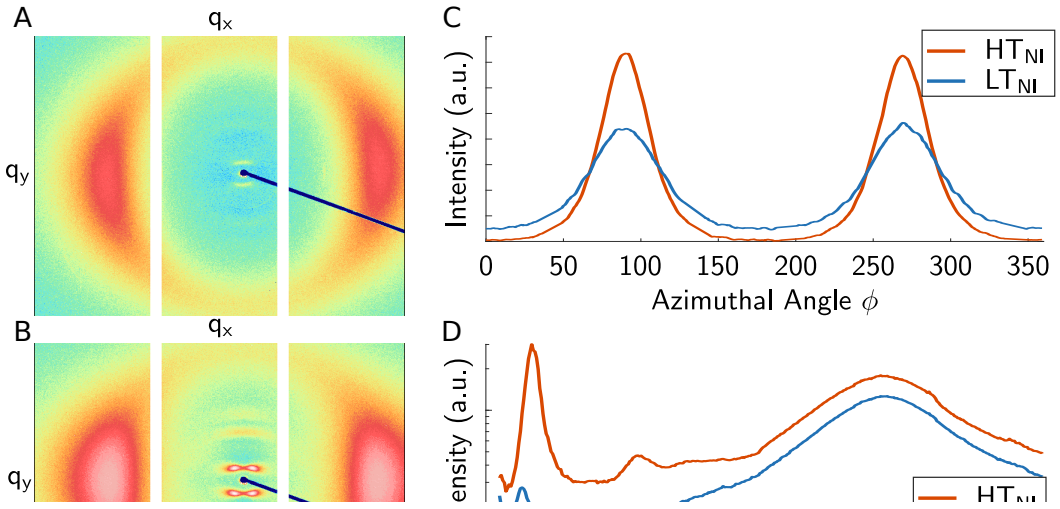

Figure E.3: LCE alignment.2D wide angle X-Ray scattering patterns of unidirectional printed (a) LT_{NI} and (b) HT_{NI} LCEs. (c) Normalized intensity as a function of azimuthal angle. (d) Normalized radial intensity as a function of the momentum transfer vector $q = (4\pi/\lambda)\sin\theta$.

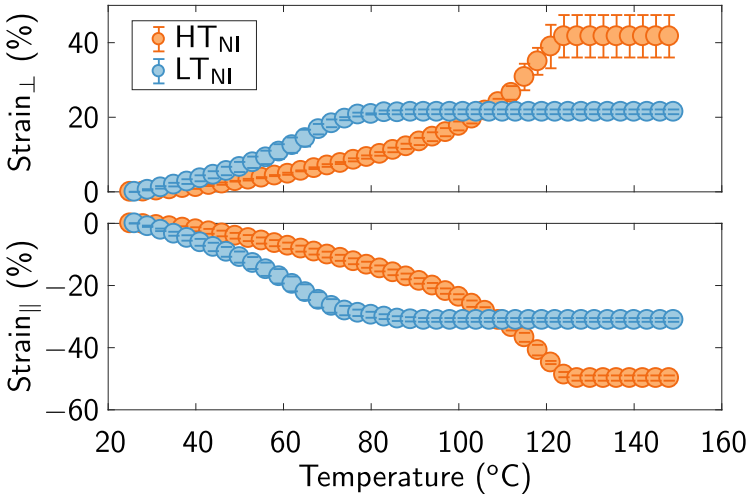

Figure E.4: Actuation response of unidirectional printed LCEs.The measured contractile and expansion strain observed perpendicular and parallel to the print direction, respectively, as a function of temperature for unidirectional aligned LCE actuators printed from LT_{NI} and HT_{NI} inks. [Note: Sample dimensions are approximately 20 mm × 5 mm × 0.375 mm.]

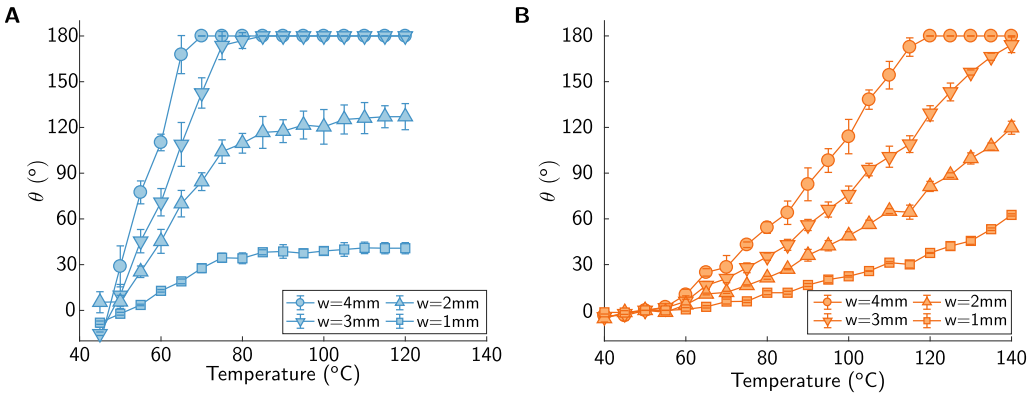

Figure E.5: Bending angle as a function of temperature. Bending angles θ of (a) LT_{NI} and (b) HT_{NI} LCE hinges (0.25 mm thick) with varying width ($w = 1 - 4$ mm) as a function of temperature. Due to residual stress that arises from printing and cross-linking the LT_{NI} LCE hinges in the isotropic phase, their measured bending angle is negative at low temperatures.

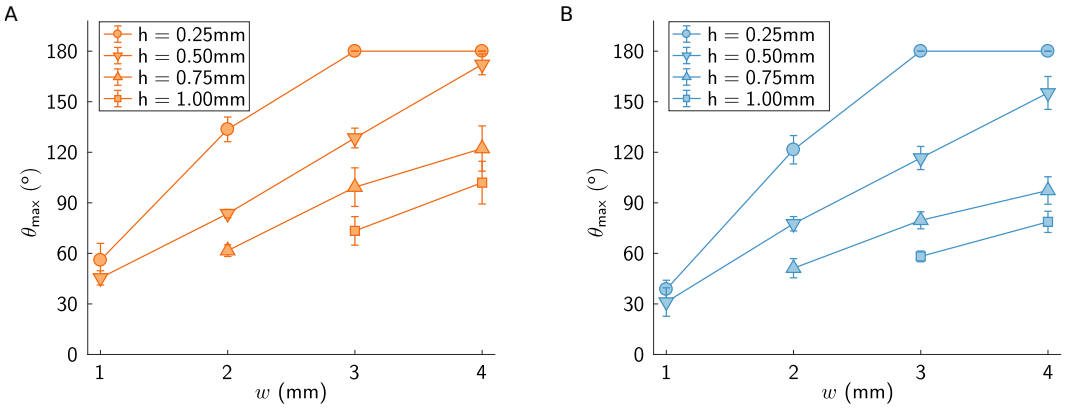

Figure E.6: Bending angle as a function of hinge dimensions. Bending angles of LCE hinges of varying thickness (h) and width (w), when actuated above their T_{NI}. Hinge angles θ are measured at 120°C and 150°C for the LT_{NI} and HT_{NI} LCE hinges, respectively. Maximum bending angle is 180° due to panel collision.

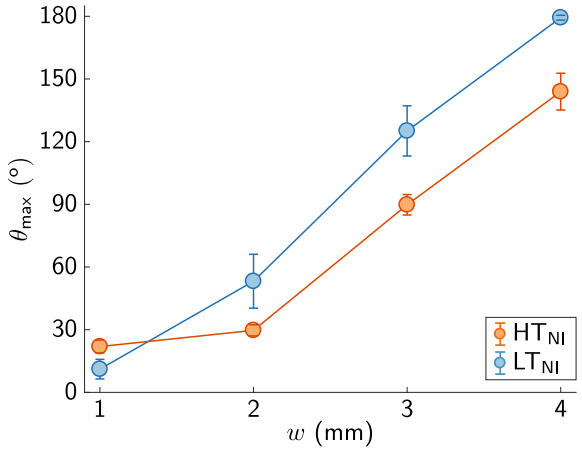

Figure E.7: Valley fold bending angles. Printed LCE hinges (0.25 mm thick) of varying width w exhibit valley folds with smaller bending angles θ than their mountain fold counterparts.

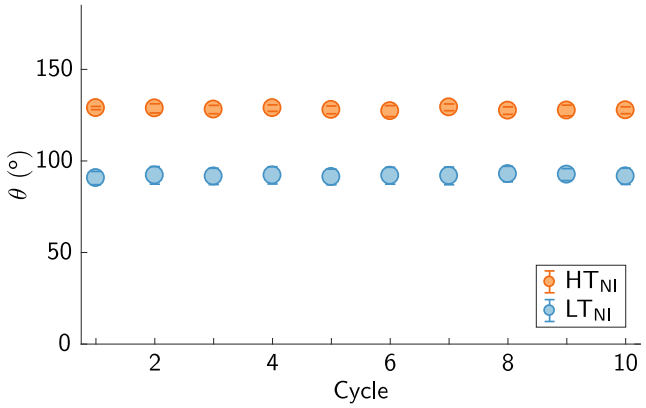

Figure E.8: Repeatable hinge folding. Bending angles θ of LT_{NI} and HT_{NI} LCE hinges (0.25 mm thick and 2 mm wide) when cycled above and below T_{NI}.

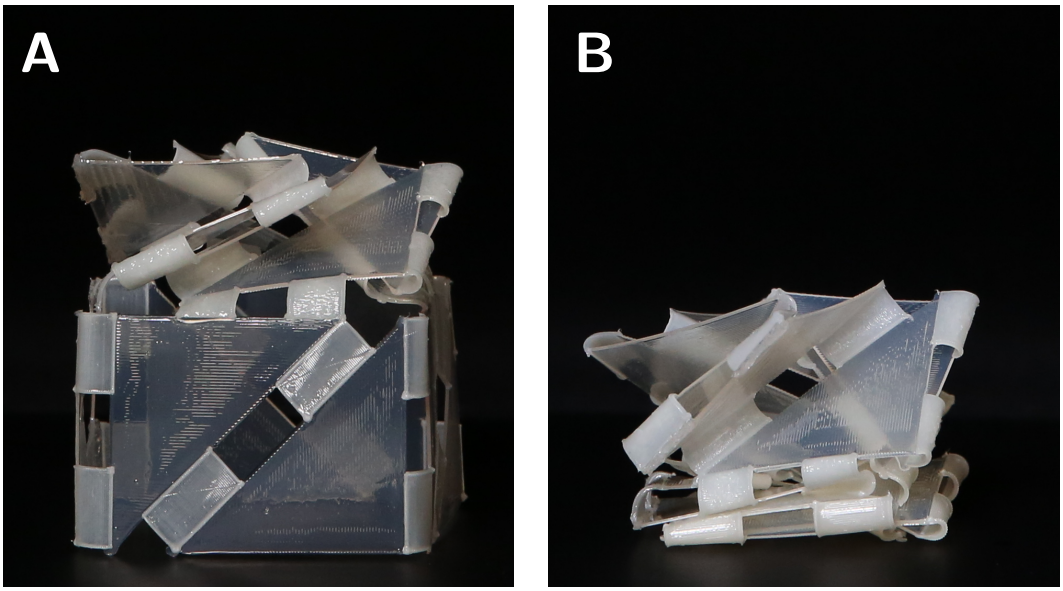

Figure E.9: Triangulated polyhedron actuation sequence at ambient temperature. (a) The triangulated polyhedron in its second, partially folded configuration after heating to actuate the top LT_{NI} section. (b) The triangulated polyhedron in its third, fully folded configuration after heating to actuate the bottom HT_{NI} section. All images are taken under ambient conditions.

A

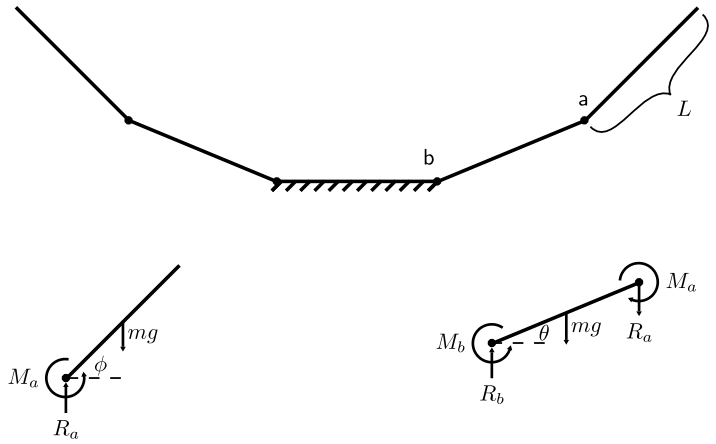

Force balance: $R_a = mg$

Moment balance: $M_a = \frac{mgL}{2}\cos(\phi)$

Force balance: $R_b = R_a + mg$

Moment balance: $M_b = \frac{mgL}{2}\cos(\theta) + R_a L\cos(\theta) + M_a$

Hinge torque: $M_b = \frac{3mgL}{2}\cos(\theta) + mgL\cos\phi$

B

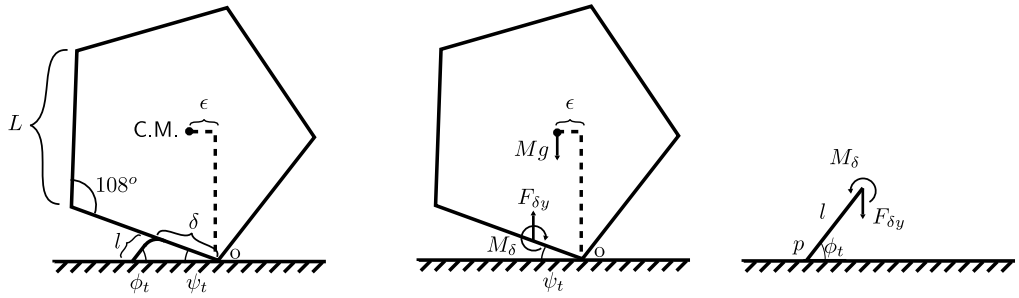

$\epsilon = \frac{L\cos(54^o+\psi_t)\cos(54^o)}{2}$

$\frac{l}{\sin(\psi_t)} = \frac{\delta}{\sin(\phi_t)}$

Hinge angle: $\theta_t = \psi_t + \phi_t$

Moment about o: $F_{\delta y}\delta\cos(\psi_t) + M_\delta - Mg\epsilon = 0$

Moment about p: $M_\delta - F_{\delta y} l\cos(\phi_t) = 0$

Hinge torque: $M_\delta = \frac{Mgel\cos(\phi_t)}{l\cos(\phi_t)+\delta\cos(\psi_t)}$

Figure E.10: Free body diagrams of self-propelling rollbot. (a) Moment diagrams for calculating the torque at the LT_{NI} LCE hinge (b) that requires the greatest torque for self-reconfiguration into a pentagonal prism. Here, m is the mass of each panel, g is gravitational acceleration, L is the length of each panel. (b) Moment diagrams for calculating the torque requirements of HT_{NI} LCE hinges that induce self-propulsion. Here, M is the entire mass of the structure, ϵ is the offset of the center of mass $C.M.$ from the tipping point, l is the length of the propelling plate, δ is the offset of the hinge from the tipping vertex, o. A no-friction assumption is taken for the contact between the structure and the ground. Only forces that affect a torque about the tipping point are shown for clarity in the image.

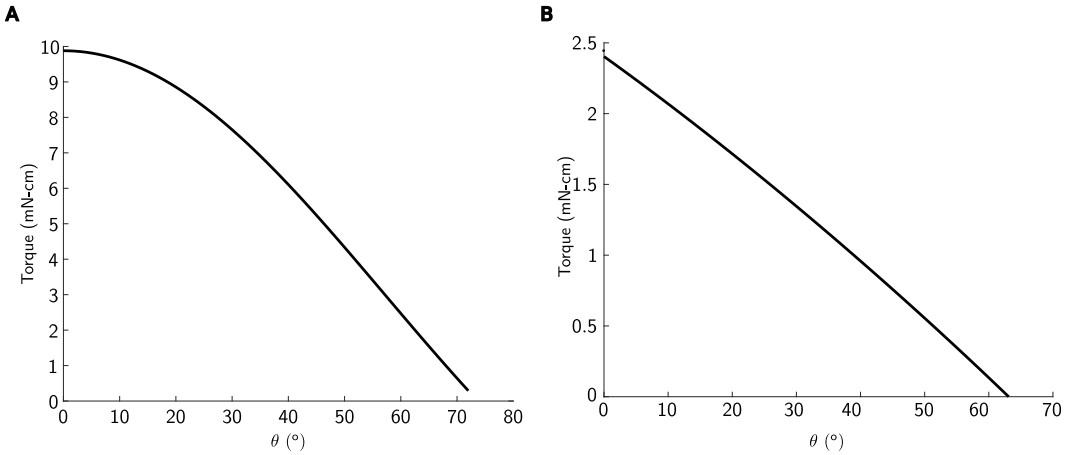

Figure E.11: Torque requirements of hinges for self-propelling rollbot. (a) Torque required from LT_{NI} LCE hinges for self-assembly into a pentagon as a function of folding angle θ. (b) Torque required from HT_{NI} LCE hinges as a function of hinge angle for self-propulsion. The required moment is zero at the tipping point. A 63^{o} hinge angle induces a 36^{o} tipping angle about the vertex.

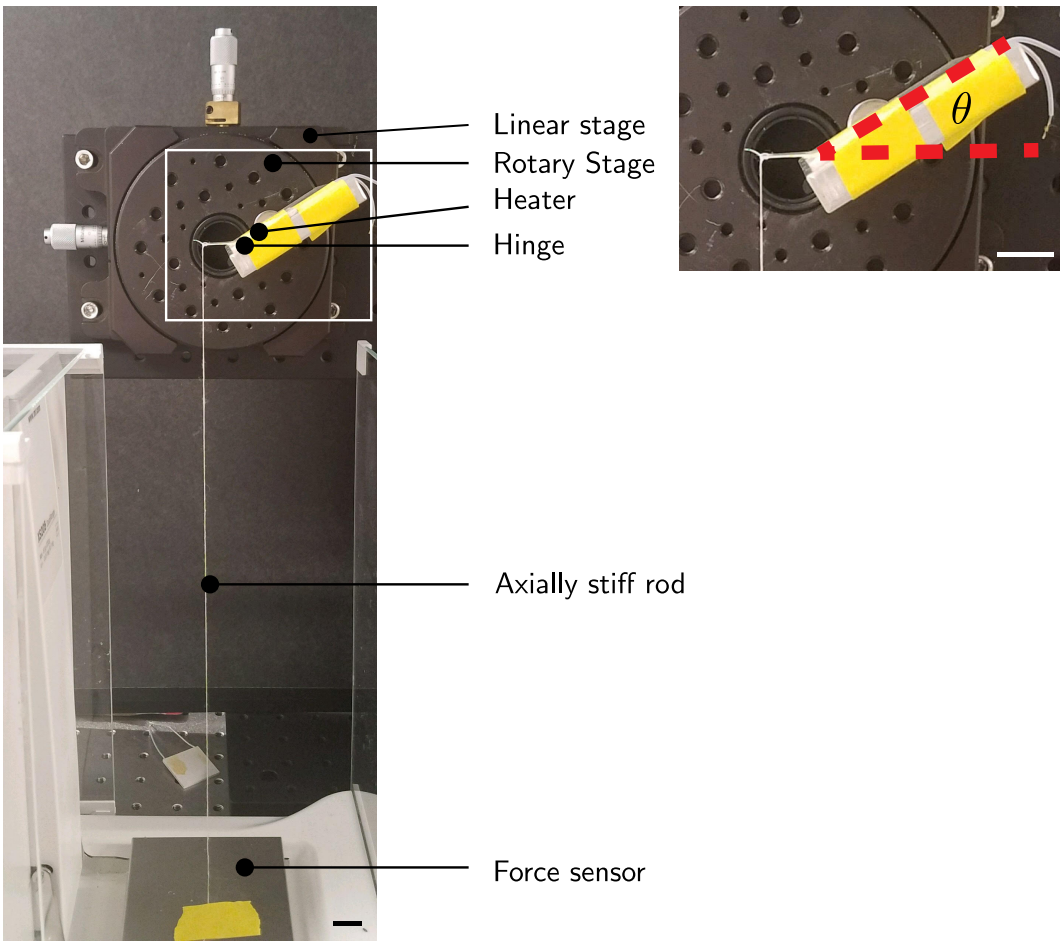

Figure E.12: Torque measurement experimental setup. Torque of the LCE hinges can be measured (left) as a function of angle θ by rotating a rotary stage (right). The force sensor is attached to the hinge at the end of the panel, approximately 1 cm from the edge of the LCE component, which is in contact with a thin heater. A linear stage is used to ensure that the hinge tile attached to the force sensor is parallel to the sensor surface. Scale bars are 1 cm.

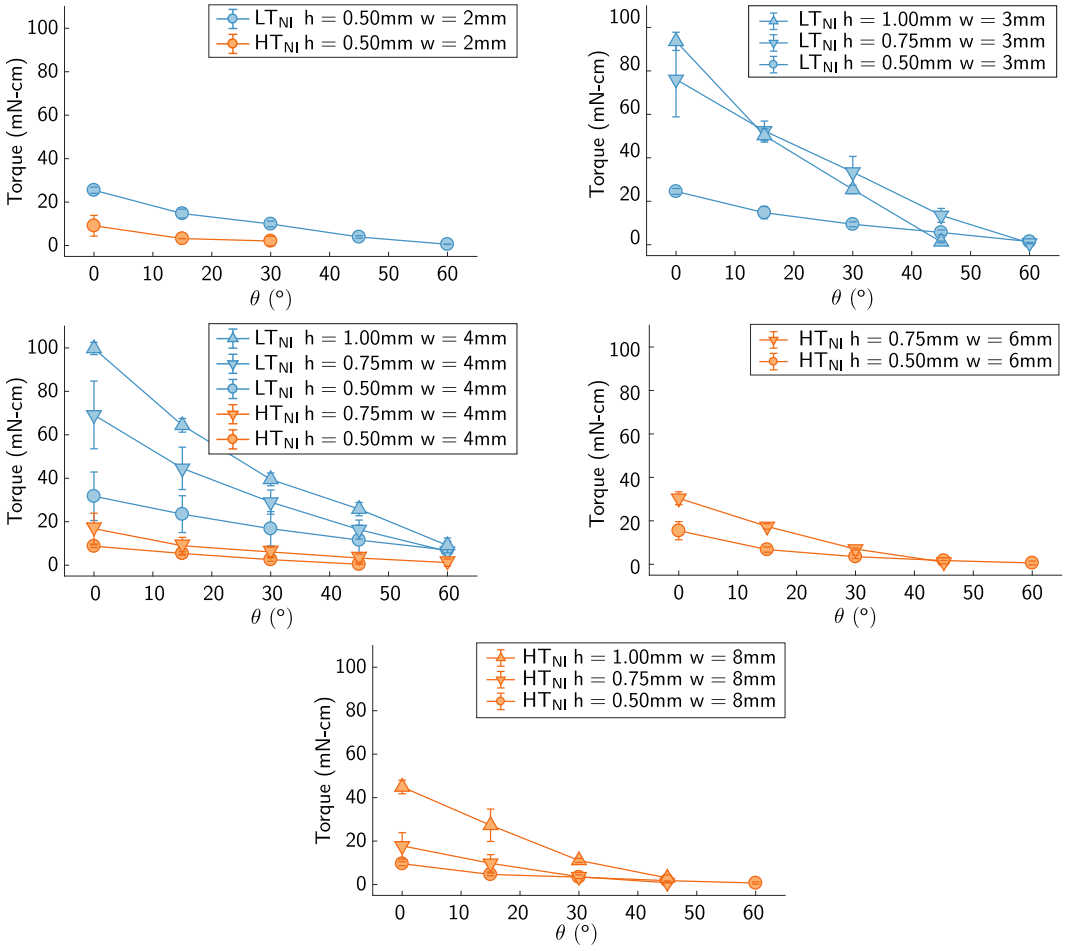

Figure E.13: Torque measurements for hinges of varied dimensions. h indicates hinge thickness in mm, w indicates hinge width in mm, and θ is the folding angle.

LIST OF ILLUSTRATIONS

Number *Page*

1.1 Examples of how deformations can be "programmed" via mesostructural patterning. (a) A miura-ori crease pattern that leads to the kinematic behavior shown in (b) [4]. (c) An inverse design framework is used to create the mesostructure of an initially flat beam network that (d) morphs into the shape of Gauss's face [9]. (e) Hygromorphic wooden bilayers [17] are used to shape the panels that compose (f) the 14m tall Urbach Tower [18]. (g) Pneumatic cavities in the limb of (h) a locomoting soft robot enable complex locomotive gaits in response to pressurization and depressurization cycles [8]. 3

1.2 A time-lapse overlay showing untethered shape-reconfiguration and locomotion by a programmed structured medium. The mesogen orientation in the liquid crystal elastomer bilayers cause the hinges to fold in response to a thermal stimulus [63]. 4

1.3 M is defined as an embedding m of a region of the plane U into $\mathbb{R}^3$. Image reproduced from [20]. 9

1.4 Discrete conformal flattening tools take 3D surface meshes as inputs and output conformally equivalent flat meshes. In this example, the user also has the option of prescribing the flattened boundary. Image sourced from [62]. 10

2.1 Twisting ribbons to create structural elements with an expanded set of bending axes. (a) Original ribbon configuration, where $\{\mathbf{e}_i\}$ are the orthonormal basis vectors of a coordinate system aligned with the centerline of the ribbon. (b) Ribbon configuration after a $\theta = 3\pi$-degree twist about $\mathbf{e}_1$, viewed from two different directions. In a twisted configuration, we call "faces" those regions that can bend about $\mathbf{e}_2$ or $\mathbf{e}_3$. 23

2.2 Undulated ribbon characterized by thin necks and wide faces, with all the relevant geometrical parameters. The gray extremities/tabs of the ribbon are not part of the model, but facilitate clamping of the fabricated specimens. θ_t is the target twisting angle to align all necks with the $\mathbf{e}_1$–$\mathbf{e}_3$ plane and all faces with the $\mathbf{e}_1$–$\mathbf{e}_2$ plane. 24

2.3 Material characterization. (a) BMG roll ($Zr_{65}Cu_{17.5}Ni_{10}Al_{7.5}$). The micrograph shows the irregular cross section of the roll (Scale bar: 10 μm). (b) Tensile test setup to characterize the BMG sheets. (c) Load-time curve indicating our testing procedure; the specimen is pulled and the force is held constant at various force values to record images for the DIC procedure. The insets show the DIC-computed axial strain field. 24

2.4 Numerical (FE) results on twisting. (a) Initial and deformed configurations for an initially-straight ribbon subjected to pre-stretch and torsion. Darker colors indicate regions of higher maximum principal strain, and serve the sole purpose of qualitatively showing where the strains are largest. (b) Same as (a), but for an undulated ribbon with $n = 3$ and $A = w/6$. The circular markers in the undeformed configurations indicate the locations where strains are the largest. (c) Logarithmic strain versus twist angle for a straight ribbon. The crosses indicate when the ribbon reached an unwanted self-folded configuration. (d) Logarithmic strain versus twist angle for an undulated ribbon with $n = 3$ and $A = w/6$. (e) Effects of the number of necks n on the maximum strain, with $A = w/6$ fixed. Recall that the breaking strain for this material is $\varepsilon_b = 1.7\%$. 27

2.5 Experimental validation of the numerical predictions on twisting. (a) Axial reaction force versus twist angle for a straight ribbon. The dark gray line is the mean and the shaded light gray area indicates the standard deviation of measurements performed on three specimens. The cross marker indicates the θ angle at which the simulation indicates self-folding. (b), (c) Same as (a), but for a 3-neck and 5-neck ribbon, respectively. Both cases feature $A = w/6$. A sharp drop in the experimental curve indicates failure. 29

2.6 Comparison between analytical and numerical results. (a) Schematic diagram of a straight ribbon. (b) Principal logarithmic strains at the free edges of a straight ribbon. (c) Schematic diagram of a ribbon with undulated edges and $A = w/6$. (d) Principal logarithmic strains at the free edges of a "neck" region. In (b), (d), the strains are plotted as a function of total relative twist of the clamped edges. (e) Analytical prediction of the axial stress resultant as a function of twist and normalized lateral position in ribbons with straight edges and ribbons with three neck regions. For the undulated-edge ribbon, we plot the stresses at a neck cross-section, where the stresses are greatest. (f) Analytical prediction of the lateral stress resultant as a function of twist and normalized lateral position in ribbons with straight edges and ribbons with three neck regions. The greatest lateral compressive stresses (plotted here) in undulated-edge ribbons emerge in the center of the neck regions. 38

2.7 Extended parametric analysis. All curves are obtained using our analytical model. The dots are numerical data points and are useful to understand the limitations of the analytical model. (a) Effects of the amplitude of undulation A on the maximum principal strain, for various n and with $L/w = 20$ fixed. (b) Effects of L/w for various n, with $A = w/6$ fixed. 39

2.8 BMG ribbon thermoforming. (a) Sketch illustrating the various steps of the thermoforming process, from an initial planar ribbon to a final twisted and stress-free configuration. (b) Thermoforming setup. (c) BMG ribbon before and after thermoforming, with insets illustrating how wide faces and neck regions can be bent about $\mathbf{e}_2$ and $\mathbf{e}_3$, respectively. 41

2.9 Numerical (FE) bending response of different regions of the same twisted ribbon (with $n = 3$ and $A = w/6$). (a) Snapshots of the bending deformation of the neck about $\mathbf{e}_3$. All dimensions are in mm. (b) Performance of the neck region as a joint, indicating the maximum strain involved and the moment about the rotation axis. (c) Snapshots illustrating how a wide face bends about $\mathbf{e}_2$. (d) Bending performance of the wide face. 42

2.10 Elastic stowage and deployment of twisted ribbons. In all cases, deformations are reversible and do not induce any plastic deformation. Note that we use tape to keep together the stowed configurations for illustration purposes. (a) A twisted ribbon can be compacted by folding it about the necks/hinges, and by finally bending the wide faces. (b) Assembling four ribbons in a circle leads to a ring structure that can be compacted following the same procedure shown in (a). (c) The chirality of the ribbons can be leveraged to create a sphere that can be compacted by applying a twisting load, similarly to Hoberman's Twist-O. (d) Planar auxetic lattice made of twisted ribbons. The dashed lines highlight the global curvature achievable by taping together selected pairs of necks. 43

3.1 Uniaxial tension test of a periodic sheet whose undeformed geometry is shown in (a). The plot in the background shows the loading curve when the applied tension is either along the horizontal direction (black lines) or along the vertical direction (grey lines), both from experiments (solid lines) and from finite element simulations (dashed lines). The vertical dash-dot line shows the maximum stretch predicted by the kinematic analysis, where a geometric-to-elastic transition takes place. Insets (a-d) show snapshots of a 4×4-tile portion of the sheet at different levels of deformation (scale bar is 6 mm). The red and blue overlaid lines are obtained by joining the diagonals in a particular row and column of tiles, respectively, and are used to predict the maximum stretch by a kinematic analysis. 55

3.2 Unit cell generalization. (a) Sketch of a generic periodic architecture parameterized by design variables. (b-d) Digital images of details of three periodic undeformed specimens, corresponding to different values of (w_x, w_y) listed in Appendix B.4; scale bar is 6 mm. (e) Transverse stretch λ_y as a function of the axial stretch λ_x for simple traction along the x-direction, and for the same set of specimens: experiments (open symbols) versus predictions of the kinematic model (solid curves). 57

3.3 Out-of-plane morphing of sheets with non-periodic cut patterns. (a1) Cut pattern with gradient in the y direction. The inset to the right of the undeformed configuration highlights the tile diagonals (in red), that are inextensible by the local kinematic analysis, as well as a plot of the corresponding maximum stretch $\lambda_x^M(y)$: this shows that the sheet is highly stretchable in the center, but inextensible along its upper and lower edges. (a2) A dome shape obtained when the sheet is pulled from two boundary points. (b1) Undeformed configuration of a specimen featuring two soft and auxetic regions in its interior, which give rise to two localized bumps upon pulling at the four corners (b2). (c1-c3) Undeformed and deformed configurations of another specimen, highlighting the influence of the boundary loading on the pattern of wrinkles. The right-halves of (b2), (c2) and (c3) are the stress maps of $\sigma_{zz} = \nu(\sigma_{xx}+\sigma_{yy})$ (under the plane strain assumption); negative values of the average in-plane stress $(\sigma_{xx} + \sigma_{yy})$ are taken as an indicator for buckling. (d1-d2) Shaping wrinkles: a C-shaped soft and auxetic region is embedded in a sheet by a suitable choice of the maps of w_x and w_y in the reference configuration (d1). The wrinkles localize upon the application of boundary loads (d2). The orange arrows indicate the boundary loads. Scale bar: 12 mm. 59

3.4 Cylindrical structures and extension to plastic sheets. (a) An architected tube can expand or contract radially based on an initial stripe pattern. Beyond a critical tensile load, an azimuthal buckling pattern appears in the expanded regions. (b) Petal-shaped specimen generated from a non-rectangular grid. This sheet morphs into a pea pod-shaped object when pulled from its ends. (c-d) Sculpting axisymmetric shapes from a sheet made of an elastic-plastic material; the shapes are obtained by using graded cut patterns and by stretching out the sheets locally by hand. Scale bars: 12 mm. 60

4.1 The mechanical behaviors of periodic and non-periodic architected sheets. (a-b) A sheet with a periodic cut pattern that displays a quasi-mechanism mode of deformation: rotation of tiles about slender elastic joints. As the tiles rotate, the unit cell dimensions change from L_α^i to L_α^f. Although tile rotations are low-energy kinematic modes compared to other deformations, the energetic cost associated with the deformation of the joints is not negligible. (c) Introducing a gradient in the cut pattern modulates the quasi-mechanism kinematics over the sheet. The scale bar represents 3 cm. (d) The mesostructural non-uniformity shown in (c) affects the extent to which tiles can rotate in different regions of the sheet, creating kinematic incompatibilities between the quasi-mechanism behaviors of different regions. Here, λ_x is the maximum stretch a unit cell can attain in the direction of loading through quasi-mechanism behaviors. (e) These in-plane kinematic incompatibilities lead to out-of-plane buckling. The design of the buckling sheets shown in (c-e) was first discussed in our prior work [16]. 71

4.2 Quasi-mechanism kinematics. (a) An example of a sheet with a uniform pattern of diamond-shaped cuts. (b) A unit cell (shaded) consists of four tiles (boxed). (c) The quasi-mechanism kinematics consist of tile rotations about the slender elastic joints. This deformation mode can be entirely described by the projection of the tile diagonals onto the fixed orthogonal coordinate frame. This rotational mode has a non-negligible energetic cost, but one that is still much lesser than deformations where the joints are under tension or shear. (d) The reference configuration of the boxed tile shown in (b). Five parameters define the geometry of a unit cell: l_1 and l_2 are the reference configuration lengths of the unit cell grid spacing in the e_1 and e_2 directions, δ is the width of the slender joints, and w_1 and w_2 are the half-widths of the two diamond-shaped cuts that define the tiles' inclinations. The diagonals d_v and d_h and the angle γ between these two can be computed from those parameters. Finally, θ is the angle between the red diagonal, d_h, and the e_1 direction. As the tile rotates from one configuration to another, this angle varies (as shown in b-c). The projected lengths of the tile's deformed configuration in the e_1 and e_2 directions are $d_h \cos(\theta)$ and $d_v \sin(\gamma + \theta)$, respectively. This allows us to compute the unit cell stretches: only the rotation of one tile about a joint needs to be analyzed to determine the quasi-mechanism kinematics of the unit cell. (a-d) Adapted from [16] by permission of The Royal Society of Chemistry. 73

4.3 An example of a domain and of a set of boundary conditions used in our simulations. In-plane displacements are prescribed on a portion of the boundary and in-plane traction-free edges are observed on the remainder. Additionally, we constrain out-of-plane displacements and have no applied moments on the entire boundary. This drawing displays the boundary conditions used to model the sheet with non-uniform cut patterns shown in Fig 4.1c-e. 78

4.4 Effective stress vs. stretch for a sheet with a periodic cut pattern. The insets show four unit cells of this structure, see Fig. 4.2a for an image of the entire sheet. We compare our effective continuum model (solid red and blue lines) represented by (4.17) to experiments (solid black lines) and fine-grain finite element simulations (gray dashes) that fully resolve the small geometric features in our sheets. These experiments and the fine-grain simulations (using Abaqus/Standard) were conducted in our prior work [16]). The experimental curve for the soft loading direction does not start at $\lambda = 1$ due to the effect of gravity in a vertically loaded tensile testing machine. The inset on the bottom left of the figure shows a small region of the mesh used in the Abaqus simulations to capture the geometry of the elastic joints. The large number of elements needed for these fine grain simulations motivates the usage of effective continuum models. The insets in this image were adapted from [16] by permission of The Royal Society of Chemistry. 81

4.5 Buckling behavior of sheets with non-uniform cut patterns. (a) Up to a certain stretch λ, point displacements lead to in-plane deformations. (b) Following a critical value of λ, the in-plane kinematic incompatibilities will lead to out-of-plane buckling. The scale bar represents 3 cm. (c) Comparison of dome height between effective continuum simulations (solid lines) and experiments (dots) for sheets of three aspect ratios. Here, h_{mid} is the height of a sheet's center point, λ is the stretch of the sheet's center line in the e_1 direction, t is the sheet thickness, and l_1 is the length of the unit cell grid spacing in the e_1 direction. 83

4.6 Post-buckling behavior of sheets with three thickness-to-width ratios. These are the same three sheets represented in Fig. 4.5c. Here, t is the sheet thickness, l_1 is the length of the unit cell grid spacing in the e_1 direction, and λ is the applied stretch at the midpoint of the sheet edge. In each entry of the stretch vs. aspect ratio grid, the laser scans are plotted directly above the simulated deformed meshes. As expected, we see that sheets with higher thickness-to-width ratios will nucleate at larger stretches and will buckle into wider domes relative to the overall sheet width. 84

5.1 Encoding spatial and temporal shape evolution in a flat shell mesostructure. (a) A user-specified target surface and actuation time landscape (a field of deformation completion times) are inputs to an inverse design procedure that defines the mesostructure of flat-fabricated shells that morph into the target geometries. The shells are composed of inhomogeneous tessellations of unit cells with an interior pre-stretched membrane. (b) Each unit cell has an initial central length l. Brackets control actuation time through their softening rate, which is controlled by their thickness, h, and a set of bumpers prescribe final local curvatures upon collision. (c) Morphing of a petalled structure with an actuation time landscape ensuring that larger petals cover their smaller neighbors avoiding collisions on the way. Simulation and experiments are compared at 3, 30, 50, and 80 seconds in water. The structure replicates the encoded actuation time landscape shown in (a). Scale bars, 3 cm. 94

5.2 Modeling bracket softening and prescribing an actuation time landscape. (a) Load-controlled tensile tests were used to determine the deformation rates of unit cells in 56° C water. (b) Average deformation rates for specimens subject to constant loads of 4 N for $l < 7$ and 5 N for $l \geq 7$ N. These values are close to the inner membrane tractions on each unit cell in real shells. (c) Deformation rate measurements (solid lines) are fit (dashed lines) to produce a model of bracket softening. Here we show the fit for $l = 6$ mm, $h = 0.4$ mm. (d) The model is interpolated and queried to infer the mesostructure that yields target curvatures and deformation completion times in each section of the shell. Here, we show deformations of unit cells with central length $l = 6$ mm and a range of bracket thicknesses from 0.3 mm to 0.65 mm. (e) Smooth actuation time landscape that induces the sequential deformation process demonstrated in Fig. 5.1c. (f) Bracket thickness fields for both sides of the petalled shape. Though the prescribed time landscape is smooth, the field of bracket thickness is highly irregular because bracket thicknesses also depend on initial unit cell lengths and their target deformations. 97

5.3 Spatio-temporally programmed shells. Each panel shows a real shell (top), its actuation time landscape (bottom-left), and its corresponding simulated shell (bottom-right). (a) Doubly-curved shell where petals morph synchronously to cover each other in a cyclic manner. One corner of each petal is programmed to morph slower to increase the distance between petals during morphing. (b) A double spiral that approximates a developable surface. A gradient time landscape enables the inner spiral to curl first. (c) A saddle shape with negative curvature. (d) A shell with a complex self-interweaving shape prone to multiple collisions in the course of its morphing process. Scale bars, 3 cm. 99

6.1 3D printing of soft programmable materials. (a) Active hinges were printed from oligomeric LCE inks, whose rigid mesogens aligned along the print path during HOT-DIW (left). Immediately upon printing, LCE ink cross-linking was photo-initiated to lock in the desired director alignment. Structural tiles were then printed from an ink composed of acrylate resin that chemically bonded to LCE hinges upon photo-initiated cross-linking (right). (b) The LCE hinges were printed in the form of $0^o/90^o$ and $90^o/0^o$ bilayers, which bend into mountain and valley folds, respectively, when actuated above T_{NI}. A simple structure composed of two hinges, with mountain and valley folds, that interconnect three structural tiles is shown as printed (middle and top) and as actuated (middle and bottom). (c) A more complex, square-twist reconfigurable structure was printed (left) and actuated at 125°C (right). The LCE hinges that form the central square and the four LCE hinges that point toward the center of the structure (left) are mountain folds, whereas the other LCE hinges are valley folds. Scale bars, 1 cm. 110

6.2 Untethered, sequential, and reversible folding of active hinges. (a) Chemical composition of the LT_{NI} (blue) and HT_{NI} (orange) oligomeric LCE inks (where $n = 3$ and 6, and $m = 6$ in the molecular structures). (b) Bending angle θ as a function of temperature for LT_{NI} and HT_{NI} LCE hinges with length of 10 mm, width of 4 mm, and thickness of 0.25 mm. (c) A printed structure composed of LT_{NI} and HT_{NI} LCE hinges with mountain folds that interconnect three structural tiles, which undergo sequential actuation when heated (left to center) and cooled (center to right). Scale bar, 1 cm. (d) Bending angle θ as a function of thickness, h, for LT_{NI} and HT_{NI} LCE hinges of fixed length of 10 mm and width of 3 mm. Their bending angle decreased with thickness. Other bilayer systems display inverse proportionality between curvature and thickness [1–3]. We plot this relationship, where c is a constant, for comparison. Both hinges exhibited a maximum bending angle of 180°, where panels contact one another. (e) Bending angle θ as a function of hinge width, w, for LT_{NI} and HT_{NI} LCE hinges of fixed length of 10 mm and thickness of 0.5 mm. Error bars indicate SD. 113

6.3 Printed soft materials with programmed sequential folding and deformation. (a) A triangulated polyhedron was printed in the form of a flat sheet composed of both LT_{NI} hinges (top section) and HT_{NI} hinges (bottom section) that interconnect the structural tiles. All diagonal LCE hinges are valley folds, whereas all vertical and horizontal LCE hinges are mountain folds. (b) The printed flat sheet was manually assembled into a 3D triangulated structure that exhibited sequential folding upon heating from (c) ambient temperature to (d) 100°C, where the LT_{NI} LCE hinges actuated, and to (e) 150°C, where the HT_{NI} LCE hinges actuated. Scale bars, 1 cm. 115

6.4 Torque capacity of printed active hinges. (a) LT_{NI} LCE hinge (10 mm by 4 mm by 1 mm) folds to a 75° bending angle while unbiased. (b) When a 10 g mass was suspended 1 cm away from the LCE hinge at room temperature, it deflected to −72°. The mass was lifted by about 1 cm when actuated above T_{NI}. (c) Exerted torque as a function of hinge folding angle, θ, as defined by the inset. Hinge composition and thickness, h, are the primary factors that affect torque output. (d) LCE hinges (5 mm by 3 mm by 0.5 mm) undergo multiple actuation cycles with negligible changes in the torque output. Error bars indicate SD. Scale bars, 1 cm. 116

6.5 Printed self-propelling structure. (a) Self-propelling rollbot is shown in its printed configuration. In the legend (inset), the blue (LT_{NI}) and orange (HT_{NI}) LCE hinges denote valley and mountain folds, respectively, and gray indicates structural tiles. (b) Printed structure in its rolling configuration, in which the LT_{NI} LCE hinges induced folding into a pentagonal prism and the HT_{NI} LCE hinges propelled the rollbot when heated above their actuation temperature. (c) Still images (from movie S4) of the rollbot that show its self-propelling locomotion when heated. The structure self-propels at least six times over the time sequence shown. [The heated surface was held at 200°C, and the average ambient temperature was 45°C. Scale bars, 1 cm.] 119

7.1 Plastic kinking of slender joints in a structured metallic medium. . . . 132

A.1 Stress-strain response of a BMG strip. Each curve corresponds to an experiment carried out under identical conditions on three specimens. 135

B.1 Response of a 18 × 18 tile, anisotropic sheet with $\delta/l_x = 1/8$ and $t/l_x \sim 0.26$. The insets depict the experimental setup and the response at three stretch values. (Scale bar, 12 mm) 136

B.2 Size difference between vertical and horizontal hinges in anisotropic specimens. (a) Detail of one of the anisotropic architectures analyzed in this work (Scale bar, 6 mm). (b) and (c) Microscope images (2.5× zoom) representing the details of vertical and horizontal hinges, respectively. 137

B.3 Tensile response of a periodic sheet featuring the undeformed architecture in (a). Black lines represent the sheet's response to horizontal stretching and light gray lines to vertical stretching. Solid lines are experimental curves. The dashed line represent the numerical response to both horizontal and vertical loading. The vertical dash-dot line shows the theoretically-predicted value for the transition from a mechanism-dominated deformation to an elastic deformation. Insets (a-c) show different stages of the sheet's deformation (Scale bar, 6 mm); the red and blue lines highlight the diagonals of each tile in a given row and column, respectively. 138

B.4 Details of the FE model. (a) Detail of the mesh used for one of the hinges in the simulation of the anisotropic specimen tensile test. (b) Detail of the stress map for the simulation in Fig. 3.3(b2). 139

B.5 Kinematic analysis of periodic perforated sheets featuring tiles connected by thin hinges. (a) Isotropic sheet and (b) detail. (c) Mechanism of inextensional deformation for the truss analog of (a), obtained by computing the null space of the kinematic matrix. (d) Detail of one of the tiles of (a), indicating all the quantities necessary for the kinematic analysis. (e-h) Same as (a-d), but for the architecture in (e). (Scale bar, 6 mm) 140

B.6 Design space in terms of maximum stretches, λ_x^M and $\lambda_y(\lambda_x^M)$, as a function of w_x and w_y, with $l_x = l_y = 6\,\text{mm}$ and $\delta = l_x/8$ fixed. Insets A-D represent specific examples extracted from the space. . . . 142

B.7 Kinematic analysis of non-periodic perforated sheets featuring tiles connected by thin hinges. (a) Example of non-periodic sheet. (b) Detail of the sheet in (a). (c) The null space of the kinematic matrix of the pin-jointed truss analog to (a) contains no mechanism. (d) Detail of one of the tiles of the sheet in (a), with all the quantities necessary for the kinematic analysis. (e-h) Same as (a-d), but for the architecture in (e). (Scale bar, 6 mm) 143

B.8 Influence of design parameters on sheet stiffness. (a) Dependence of the mechanism-like response on the in-plane hinge width, δ. We keep $t/l_x \sim 0.26$ constant, and we vary δ/l_x. The dashed vertical lines represent the mechanism-to-elasticity transitions for all δ/l_x cases. (b) Dependence of the mechanism-like response on the sheet's thickness, t, with $\delta/l_x = 1/8$ constant. 148

B.9 Out-of-plane deformation of three graded sheets with different thicknesses, for different stretches. Rows of images correspond to specific stretch values. Columns correspond to different thicknesses of the sheets. In each image, h indicates the height of the highest point of the 3D shape with respect to its undeformed position. (Scale bar, 12 mm) 150
B.10 Out-of-plane deformation of three graded sheets with different thicknesses, for the same stretch value. (a) Corresponds to $t/l_x \sim 0.13$, (b) to $t/l_x \sim 0.26$ and (c) to $t/l_x \sim 0.53$. The left images represent lateral views of the buckled shapes. The details highlight the local deformations of hinges and tiles near the load application points. (Scale bar, 12 mm) 151
B.11 An alternative design startegy for stiff materials. (a) Detail of an architecture obtained with our initial design strategy. (b) Compliant beam version of the same architecture, where we have introduced the additional parameter h, representing the in-plane hinge length. 151
B.12 Plastic dome. (a) Three stages of the deformation of the natural rubber specimen studied in Fig. 3.3(a). (b) Deformation of a similar sheet, made of PETG and featuring the design variation shown in Fig. B.11(b). (Scale bar, 12 mm) 152
D.1 Unit cell scheme. The configurable parameters are the central length l (constant difference with bracket length b), bracket thicknesses h (which can be different for the two opposite layers), and the bumper cutting plane. 157
D.2 Shell design pipeline: 1. A target surface is isotropically triangulated. 2. This "actuated" stencil is populated with bases and bumpers touching their corresponding neighbors. 3. The "actuated" stencil is conformally flattened. 4. Bases with bumpers are relocated to the flat stencil. 5. Bracket lengths are set by the distance between bases in this configuration. Bracket thickness is defined later during the temporal programming phase. 158
D.3 Discretization elements: *data-driven springs*, representing brackets' time-evolving stiffness and bumper collisions (left); *shear-resisting elements*, representing brackets' resistance to undesired shearing (center); and membrane FEM (right). 161

D.4 Experimental setup for characterizing unit cell behaviors. (a) Specimens used for material measurements are assembled from two printed parts to mimic a unit cell. Assembled specimens have holes to ensure consistent boundary conditions in a gripper that was fabricated in-house. (b) Custom-built gripper for quick specimen exchange and a "boot" for firm specimen compression against the floor. (c) Zwick tensile tester for measuring bracket deformations in hot water. 165
D.5 Compressive loading of dry specimens. Data (solid lines) and fitted curves (dashed lines). 167
D.6 Compressive loading of specimens in water. Data (solid lines) and fitted curves (dashed lines). 168
D.7 Plasticity does not depend on deformation rates. Three different deformation rates are shown for a unit cell specimen of length l = 8 mm and thickness h = 0.4 mm. Dashed line represents 20% of maximal deformation which we use as a constant plasticity fraction in our simulations. 169
D.8 Predicting applied tractions and selecting bracket thicknesses. (a) Linearized model of the membrane (dashed lines) in comparison to FEM membrane (solid lines) for a set of unit cells of various initial lengths. The membrane tractions decrease with displacement as the pre-stretch is relaxed. (b) Configuring thicknesses for two pairs of brackets on opposite sides of a unit cell. Note that the one requiring larger target displacement is thinner to finish deformation at the same time as the one with smaller target deformation. The dashed horizontal line shows a sample approximation to the target membrane traction. 170
D.9 Fabrication process landmarks. (a) Star-shaped membrane stretching device back side up. Bottom part of the membrane is uniformly stretched due to markers. (b) Transferring glue from a plastic foil to the bases of the shell. (c) Passing a pin through one of the bases and the membrane to align with the second lattice. (d) Membrane surplus is covered by glue in order to "freeze" it and enable its easy removal. (e) Cutting out the shell from the membrane surplus by a scalpel. (f) Flat-fabricated shell ready for actuation in water. 171

D.10 Membrane stress relaxation over the course of 24 hours. Evolution of the force generated by a dog-bone membrane specimen under a constant stretch factor of 3. 172

D.11 Mechanical tests of a flat regularly tessellated shell. Since our shells have cross-sections with a complex geometry, we provide the effective stress values (assuming shell homogeneity). (a) Stretching, (b) bending, (c) shearing, and (d) compression tests. 174

E.1 LCE and structural tile ink rheology. (a) Apparent viscosity as a function of shear rate for LT_{NI} and HT_{NI} LCE inks at printing temperature 26°C and 55°C, respectively. (c) Storage (G') and loss (G'') moduli as a function of shear stress at 1 Hz for LT_{NI} and HT_{NI} LCE inks at the respective printing temperatures of 26°C and 55°C. (c) Apparent viscosity as a function of shear rate for the structural polymer ink under ambient conditions. (d) Storage (G')and loss (G'') moduli as a function of shear stress at 1 Hz for the structural polymer ink under ambient conditions. 181

E.2 Differential scanning calorimetry curves for the LCE inks. The two oligomeric LCE inks exhibit LT_{NI} and HT_{NI} values of approximately 24°C and 94°C, respectively. [Note: From this data, the T_g and smectic-to-nematic transition temperature (T_{SN}) for the HT_{NI} ink are approximately -20°C and 20°C, respectively.] 182

E.3 LCE alignment.2D wide angle X-Ray scattering patterns of unidirectional printed (a) LT_{NI} and (b) HT_{NI} LCEs. (c) Normalized intensity as a function of azimuthal angle. (d) Normalized radial intensity as a function of the momentum transfer vector $q = (4\pi/\lambda)\sin\theta$. 182

E.4 Actuation response of unidirectional printed LCEs.The measured contractile and expansion strain observed perpendicular and parallel to the print direction, respectively, as a function of temperature for unidirectional aligned LCE actuators printed from LT_{NI} and HT_{NI} inks. [Note: Sample dimensions are approximately 20 mm $\times$ 5 mm $\times$ 0.375 mm.] 183

E.5 Bending angle as a function of temperature. Bending angles θ of (a) LT_{NI} and (b) HT_{NI} LCE hinges (0.25 mm thick) with varying width ($w = 1 - 4$ mm) as a function of temperature. Due to residual stress that arises from printing and cross-linking the LT_{NI} LCE hinges in the isotropic phase, their measured bending angle is negative at low temperatures. 183

E.6 Bending angle as a function of hinge dimensions. Bending angles of LCE hinges of varying thickness (h) and width (w), when actuated above their T_{NI}. Hinge angles θ are measured at 120°C and 150°C for the LT_{NI} and HT_{NI} LCE hinges, respectively. Maximum bending angle is 180° due to panel collision. 184

E.7 Valley fold bending angles. Printed LCE hinges (0.25 mm thick) of varying width w exhibit valley folds with smaller bending angles θ than their mountain fold counterparts. 184

E.8 Repeatable hinge folding. Bending angles θ of LT_{NI} and HT_{NI} LCE hinges (0.25 mm thick and 2 mm wide) when cycled above and below T_{NI}. 185

E.9 Triangulated polyhedron actuation sequence at ambient temperature. (a) The triangulated polyhedron in its second, partially folded configuration after heating to actuate the top LT_{NI} section. (b) The triangulated polyhedron in its third, fully folded configuration after heating to actuate the bottom HT_{NI} section. All images are taken under ambient conditions. 185

E.10 Free body diagrams of self-propelling rollbot. (a) Moment diagrams for calculating the torque at the LT_{NI} LCE hinge (b) that requires the greatest torque for self-reconfiguration into a pentagonal prism. Here, m is the mass of each panel, g is gravitational acceleration, L is the length of each panel. (b) Moment diagrams for calculating the torque requirements of HT_{NI} LCE hinges that induce self-propulsion. Here, M is the entire mass of the structure, ϵ is the offset of the center of mass $C.M.$ from the tipping point, l is the length of the propelling plate, δ is the offset of the hinge from the tipping vertex, o. A no-friction assumption is taken for the contact between the structure and the ground. Only forces that affect a torque about the tipping point are shown for clarity in the image. 186

E.11 Torque requirements of hinges for self-propelling rollbot. (a) Torque required from LT_{NI} LCE hinges for self-assembly into a pentagon as a function of folding angle θ. (b) Torque required from HT_{NI} LCE hinges as a function of hinge angle for self-propulsion. The required moment is zero at the tipping point. A 63^{o} hinge angle induces a 36^{o} tipping angle about the vertex. 187

E.12 Torque measurement experimental setup. Torque of the LCE hinges can be measured (left) as a function of angle θ by rotating a rotary stage (right). The force sensor is attached to the hinge at the end of the panel, approximately 1 cm from the edge of the LCE component, which is in contact with a thin heater. A linear stage is used to ensure that the hinge tile attached to the force sensor is parallel to the sensor surface. Scale bars are 1 cm. 188

E.13 Torque measurements for hinges of varied dimensions. h indicates hinge thickness in mm, w indicates hinge width in mm, and θ is the folding angle. 189